

Free Elastic Plate Impact into Water

Moritz Volkmar Reinhard

A thesis submitted to the University of East Anglia
in fulfilment of the requirements for the degree of
Doctor of Philosophy



School of Mathematics
Norwich, NR4 7TJ England

January 2013

© This copy of the thesis has been supplied on condition that anyone who consults it is understood to recognise that its copyright rests with the author and that use of any information derived therefrom must be in accordance with current UK Copyright Law. In addition, any quotation or extract must include full attribution.

Abstract

The Wagner theory, developed 80 years ago, is an analytical method for solving problems where a body with small deadrise angle impacts onto an undisturbed water surface of infinite depth. In this study, two-dimensional impact models based on the Wagner theory are developed which account for the elasticity of the body, for large horizontal speed of the body and flow separation from the body.

In chapter 3, the problems of inclined rigid and elastic plates, impacting the fluid vertically, are solved. The elastic plate deflection is governed by Euler's beam equation, subject to free-free boundary conditions. In chapter 4 and 5, impact problems of rigid and elastic plates and blunt bodies with high horizontal speed are considered. A smooth separation of the free surface flow from the body is imposed by Kutta's condition and the Brillouin-Villat condition. In chapter 6, we account for fluid separation from the body in the free vertical fall of a rigid plate and a blunt body. In all problems considered in this thesis, the rigid and elastic plate motions, the fluid flow, and the positions of the turnover regions and the separation points are coupled.

We found that hydrodynamic forces on an elastic body can be significantly different from those on a rigid body. In particular, the elasticity of the body can promote cavitation and ventilation. It is shown that horizontal speed of the body increases the hydrodynamic forces on the body and the jet energy significantly. For free-fall problems at high horizontal speed, the body can exit the fluid after entering if the forward speed is large enough. It is illustrated that the hydrodynamic forces on the body and the motion of the body strongly depend on the separation model. For the Brillouin-Villat separation criterion, we found that the position of the separation point is sensitive to the body vibration.

Acknowledgements

I am greatly indebted to my supervisors Prof Alexander A. Korobkin and Dr Mark J. Cooker for all the help and assistance on this exciting project they have provided. I also would like to thank my colleague Dr Alan Tassin for his help and advice, especially during the final stage of my project. Finally, this thesis would not have been possible without my partner Evelyn, whose support and encouragement have been invaluable during the last years.

This work was supported by a UEA studentship and by the EPSRC and I am very grateful for the opportunity provided. Conference expenses were also paid by the Tuck Fellowship and by the Camina-Glauert Fund.

Contents

1	Introduction	1
1.1	Wagner’s model for impact problems	2
1.2	Wagner’s model for the impact of elastic structures	3
1.3	Numerical vs. analytical methods in impact problems	3
1.4	The hydrodynamic model for impact problems	4
1.4.1	Modelling assumptions	4
1.4.2	Basic hydrodynamic equations	5
1.5	Objectives and the structure of this thesis	6
2	Mixed boundary-value problems	8
2.1	The homogeneous problem	9
2.2	MBVP-solutions for boundary values of polynomial type	11
2.3	Particular solutions of inhomogeneous problems	12
2.4	Solutions for singular $c(x)$	14
2.5	An integral relation	15
2.6	Summary	16
3	Wagner model of vertical plate impact	17
3.1	Impact of a rigid plate at constant vertical speed	17
3.1.1	The non-dimensional nonlinear hydrodynamic problem	18
3.1.2	The linearised hydrodynamic problem	21
3.1.3	The MBVP in terms of the complex velocity	23
3.1.4	The MBVP in terms of the displacement potential	24
3.1.5	Inner solution in the jet region	26
3.1.6	The flow in the splash region	29
3.2	Euler’s beam equation and normal modes	30
3.3	Free fall of an inclined elastic plate	37
3.3.1	Mathematical formulation	37
3.3.2	Solution of the coupled problem	39
3.3.3	Numerical results	43
3.3.4	Fluid structure interaction when the plate is fully wetted	46
3.3.5	Discussion	48
3.4	Conclusion	48

4	Water entry of a rigid body at high horizontal speed	50
4.1	Impact of general-shaped bodies at high horizontal speed	51
4.1.1	Non-dimensional and linearised hydrodynamic problem	51
4.1.2	The complex velocity and complex acceleration potential	53
4.1.3	The complex displacement and Wagner's condition	56
4.1.4	Kutta's condition	60
4.1.5	Energy of the flow	61
4.2	Oblique impact of a rigid plate at constant speed	62
4.2.1	Mathematical formulation	63
4.2.2	Solution of the problem	63
4.2.3	Comparison with experiments and numerical solutions	67
4.3	The Brillouin-type separation	68
4.4	Free fall of a rigid plate with high horizontal speed and ventilation	72
4.4.1	Mathematical formulation	73
4.4.2	Solution of the coupled problem	74
4.4.3	Numerical implementation	77
4.4.4	Numerical results	78
4.4.5	Long time planing after impact with gravity	82
4.4.6	The plate and flow behaviour for large time	85
4.4.7	Summary	86
4.5	Bouncing of a blunt body from a water surface at high horizontal speed	86
4.5.1	Mathematical formulation	87
4.5.2	Wagner stage	89
4.5.3	Separation stage	92
4.5.4	Local behaviour of the complex velocity in the separation stage	94
4.5.5	Numerical results	95
4.5.6	Discussion	97
4.6	Conclusion	98
5	Free fall of elastic plates at high horizontal speed	99
5.1	Separation of the fluid at the trailing edge	100
5.1.1	Mathematical formulation	100
5.1.2	Solution of the coupled problem	102
5.1.3	An account of work and energy	103
5.1.4	The hydrodynamic loads on the plate	105
5.1.5	Numerical results	106
5.2	Fluid separation from the plate surface	114
5.2.1	Structural problem	114
5.2.2	Hydrodynamic problem	115
5.2.3	Implementation and the switch between the flow regimes	117
5.2.4	Numerical results	119
5.3	Discussion	123

6	Free-fall problems with flow separation	124
6.1	Free vertical fall of a rigid plate with flow separation	124
6.1.1	Mathematical formulation	125
6.1.2	Wagner stage	128
6.1.3	Separation stage	132
6.1.4	Vertical impact without rotation	135
6.1.5	Numerical results	138
6.2	Free vertical fall of a blunt body with cavitation	140
6.2.1	Mathematical formulation	141
6.2.2	Wagner stage	142
6.2.3	Cavitation stage	143
6.2.4	Numerical results	149
6.3	Discussion	151
7	Conclusions and further work	153
7.1	Conclusions	153
7.2	Future work	154
A	The norm of the eigenmodes	156
B	Coefficients in the final equations for impact problems of elastic plates	158
B.1	The symmetry of $\Lambda(v, w_x)$	159
B.2	An analytical expression for $\Lambda(e^{sx}, e^{r\xi})$	160
B.3	Expressions for $\Lambda(f, g)$ for specific f and g	161
B.4	Expressions for $\Gamma^{(1)}(f)$ and $\Gamma^{(2)}(f)$ for specific f	162
C	Some specific Cauchy principal-value integrals	163
D	An integral relation	165

Chapter 1

Introduction

On the 15th January 2009 an Airbus A320-214 lost full engine power due to a bird strike shortly after take-off. Since the airplane was still over New York, the pilot was forced to carry out an emergency landing of the aircraft into the Hudson River in Manhattan and all 155 passengers survived (Hersman et al., 2010). This emergency landing has been described as the most successful water landing in aviation history and is also known as the Hudson River Miracle.

The controlled emergency landing into water, also known as ditching, is a risky process and usually involves fatalities. According to Bertorelli (1999), the overall chance of surviving such an airplane accident is about 90%. For a successful ditching, the pilot has to follow ditching instructions: For example the Boeing 737 Flight Crew Training Manual (The Boeing Company, 1999) allows only a very low speed of descent of 1 to 1.5ms^{-1} and a forward speed of about 50ms^{-1} shortly before ditching. If these instructions are not followed, the forces caused during the aircraft impact into water can be so high that the aircraft breaks into pieces, as happened to a Boeing 767-200ER in the accident of Ethiopian Airlines Flight 961 on 23th November 1996 (Hamilton, 1998).

Ditching of aircraft is a problem where a body hits the free water surface at high horizontal speed. Such impacts also occur in slamming of high-speed vessels (Faltinsen, 2005) causing unexpected vessel motions and damage to the vessel hull. Seal systems at the bow and the stern of surface-effect ships can be damaged, since they are exposed to water impact even in low sea states (Ulstein, 1995).

In slamming of light bodies at high enough speed, it can be observed that the impacting body bounces out of the water after entry. Body bouncing can be a hazard for planing of high-speed vessels and for the safe landing of aircraft on the water surface. On the other hand, this effect can be utilised for the bounce of missiles on the free surface for military purposes. For example a ‘bouncing bomb’ was used by the British Army in the Second World War to destroy dams (see Johnson, 1998).

Body slamming into water with low or zero horizontal speed occurs in the dropping of lifeboats from ships and offshore platforms. A prediction of the hydrodynamic loads is necessary to assess the risk of injury to the passengers. Slamming can be also fatal when waves hit structures, such as the wetdecks of catamarans and the decks of ships (Faltinsen, 2005). In high sea states, the bow-flare of ships can slam onto the water surface which is also known as whipping (Kapsenberg, 2011). Whipping can cause, together with the global

bending of the ships known as springing, serious stresses leading to material fatigue or even cracks in the structure.

Understanding the interactions between structures and the water during impact can help manufacturers to find the right design for aircraft, ships and lifeboats, and can help to develop guidelines facilitating safe emergency landing into water and sustainable ship maneuvering.

1.1 Wagner's model for impact problems

High loads on the structure can be experienced during impact when the angle between the tangent to the profile and the undisturbed free surface, also known as the deadrise angle, is small. Pioneering works for such impact problems were written by von Karman (1929) and Wagner (1932). In both models, the problem is solved using potential flow theory, where the boundary conditions of the potential flow are linearised and imposed onto the undisturbed free surface. Von Karman neglected the water surface elevation during impact so that his model underestimated the impact loads. The account for the pile-up of the free surface in Wagner's model during impact improved the prediction of the loads. Zhao and Faltinsen (1993) solved the impact problem for the fully nonlinear hydrodynamic model and showed that the theoretical predictions of the hydrodynamic loads on the wedge in Wagner's model have an error of less than 10% for a range of deadrise angles of less than 10° . Wagner's model has received a lot of attention since the hydrodynamic loads are simple to calculate and analytical, also for other body shapes (Howison et al., 1991), and are conservative predictions. Excellent reviews of the Wagner theory are given by Korobkin (1988), Howison et al. (1991) and Oliver (2002).

Modifications of the original Wagner theory were introduced to improve the predictions of the hydrodynamic impact loads acting on different shapes entering water, most notably the modified Logvinovich model in Korobkin (2004). Other modified Wagner models are given in Zhao et al. (1996), Vorus (1996) and Cooker (1996). The original Wagner model solves the impact problem in the leading order of the small deadrise angle. Second-order extensions have been presented by Oliver (2007) and Korobkin (2007). They also found significant improvements in the predictions of the hydrodynamic loads. However, the second order models give hardly any improvements for the prediction of the size of the contact region.

Much less work has been done on the Wagner model for three-dimensional problems, since their solutions are much more complicated to achieve. Analytical solutions have only been published for axisymmetric bodies and elliptic paraboloids (see Scolan and Korobkin, 2001; Korobkin and Scolan, 2006). Recently, Moore et al. (2012b) presented results for the impact of axisymmetric bodies with horizontal speed. Numerical evaluations of the three dimensional Wagner model have been given by Takagi (2004) for elliptical paraboloids and Tassin et al. (2012) for bodies of general convex shapes. It should be mentioned that problems of slender-body impact can be solved by the strip theory (Wagner, 1932; Oliver, 2002). This method reduces the three-dimensional problem to two-dimensional impact problems in transversal cross-sections of the body.

1.2 Wagner’s model for the impact of elastic structures

Impact loads on the body during water impact can be extremely high, but they do not directly imply high stresses on the body. To account for the stresses on a structure, its elasticity has to be taken into account. If the stresses exceed the yield stress of the material the body starts to deform permanently. Repeated impacts lead to material fatigue with a decrease of the yield stress. The interactions of an elastic structure with the fluid flow are coupled, which means that the elastic deformations of the body depend on the hydrodynamic forces and vice versa. This subject of coupling is also known as hydroelasticity (Korobkin et al., 2011).

The simplicity of Wagner’s model makes it possible to couple directly the hydrodynamic model with the elastic deflection of an impacting body. Such a coupled model was first studied by Meyerhoff (1965a), (1965b), who discussed the vertical entry of an elastic wedge with small deadrise angle. The wedge material consisted of two simply supported beams modelled by Euler’s beam equation (see Donnell (1976)). To couple the hydrodynamic loads with the elastic deflection of the wedge, Meyerhoff used the normal-mode method. His results showed that the flexibility of the plate first reduces the hydrodynamic forces compared to the forces of a rigid wedge, but the hydrodynamic forces on the elastic wedge can be significantly larger than for a rigid wedge later on during the impact. After Meyerhoff’s pioneering work Kvåsvold and Faltinsen (1993) picked up his idea for the discussion of the problem of water impact against an elastic wet-deck. They showed that the hydrodynamic loads are smaller than those occurring at a rigid plate if the wet-deck is flexible enough. Further work on wave impact onto an elastic plate, simply supported at its ends, followed, most notably by Korobkin (1998). He reduced the problem to an ordinary differential equation system by formulating the hydrodynamic problem in terms of the displacement potential. Unsymmetrical problems of wave impact on an elastic plate have been discussed by Korobkin and Khabakhpasheva (2006).

1.3 Numerical vs. analytical methods in impact problems

Nowadays computers with high processing power are available to solve impact problems with Computational Fluid Dynamic (CFD) techniques. But the numerical solution of water-impact related problems remains difficult because of moving boundaries, localised high-pressure zones and small-scale phenomena such as thin spray jets and coupled physical processes such as in hydroelasticity. Numerical algorithms are not perfect, as they exhibit numerical noise and one must overcome problems at the start of impact with a zero-wetted body, in the fluid far-field, in the jet region and at points where the fluid separates from the body.

Analytical methods in impact problems are limited in their application since results can only be found for simplified shapes of the impacting body or give only asymptotic solutions for shapes satisfying extreme conditions. However, we require analytical models to understand coupled effects in the fluid-structure interaction, and the behaviour of the fluid in the jet, fluid turnover region and the fluid separation region. Furthermore, the flow at the time of initial contact of the body with the fluid free surface can only be found with the help of analytical models.

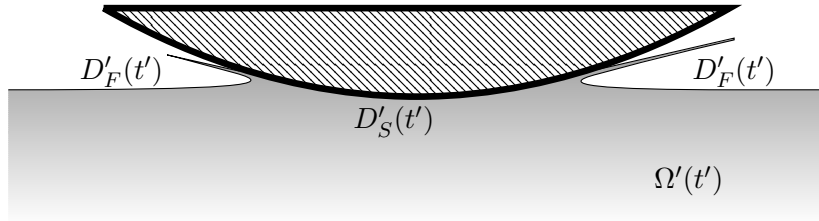


Figure 1.1: An example of a body impact onto deep water. The fluid region $\Omega'(t')$ is bounded by the free surface line $D'_F(t')$ and by the wetted body surface $D'_S(t')$ at time t' .

1.4 The hydrodynamic model for impact problems

1.4.1 Modelling assumptions

We are concerned with impact problems of large bodies, where the contact region of water and body is of the order of 1m and the vertical speed of the body is of order 1ms^{-1} . In particular, for such impact problems surface tension can be neglected. Water has a low kinematic viscosity of $10^{-6}\text{m}^2\text{s}^{-1}$, so that in our problems the Reynolds-number is of order 10^6 . Hence, viscosity will be neglected in our models.

The presence of air between the water surface and the impacting body can be important if the shape of the bottom of the body is of low curvature as air can be trapped and influence the hydrodynamic loads on the body. A two dimensional model of impact of bodies of general shape with account for air-cushioning was introduced by Wilson (1991). He showed that air entrapment between body and fluid is more likely, the ‘blunter’ the body is at its bottom. Experiments of a sphere impacting onto a water surface have been done by Hicks et al. (2012). In particular, they showed that a thin air-layer is trapped, whose shape is almost axisymmetrical. Their experiments and numerical calculations showed that the initial radius of the air pocket decreases with the impact speed V of the body, as $V^{-1/3}$.

The density of air is much smaller than the density of water, so that air cushions are very thin and restricted to a small region under the bottom of the body. In the case of wedge impact, air cushion effects were reported to have no significant effects on the hydrodynamic loads for deadrise angle larger than 3° (see e.g. Chuang (1966)). For these reasons air cushion effects are not included in the models presented in this thesis.

Compressibility effects are important if the vertical velocity of an impacting body is very large. In weakly compressible fluids, like water, the impact of a body into the fluid generates a shock wave at the initial contact region which propagates with the speed of sound to the far-field (Lesser and Field, 1983). Korobkin (1992) uses the acoustic approximation to model compressibility effects in slamming problems for weakly compressible fluids. However, for the problems discussed in this thesis we assume that the impact velocity is of order 1ms^{-1} , and the deadrise angle of the body is not too small, say about 10° , so that the Mach number is small and compressibility effects can be neglected.

In summary, in this thesis we only consider two-dimensional problems of body impact into fluid, where the fluid is assumed inviscid and incompressible, and where the presence of air and surface tension are neglected.

1.4.2 Basic hydrodynamic equations

Here we give an outline of the basic equations which are used to analyse the fluid-body interaction when a body penetrates the fluid free surface. These equations are basic and can be found in most textbooks about fluid mechanics (see e.g. Lamb, 1945; Milne-Thomson, 1968). Initially the fluid is at rest. We introduce a Cartesian coordinate system $x'Oy'$, so that the x' -axis points along the undisturbed free surface and the y' -axis vertically upwards. The Cartesian coordinate system is fixed such that the fluid in the far-field is at rest. Throughout the thesis, dimensional variables are primed. We will drop the primes for non-dimensional variables. Since we assume that the fluid is inviscid and initially at rest, it follows from Kelvin's theorem that the liquid flow is irrotational. For incompressible fluid in irrotational flow, a velocity potential $\tilde{\varphi}'(x', y', t')$ exists, whose gradient $\nabla\tilde{\varphi}'(x', y', t')$ describes the velocity field of the fluid at time t' , and $\tilde{\varphi}'$ satisfies Laplace's equation

$$\nabla^2\tilde{\varphi}' = 0 \quad ((x', y') \in \Omega'(t')), \quad (1.1)$$

where we define $\Omega'(t')$ as the fluid domain at time t' (see Figure 1.1). In potential flow theory for inviscid, incompressible fluid, the pressure in the fluid flow, $\tilde{p}'(x', y', t')$, is given by Bernoulli's equation

$$\frac{1}{\varrho_F}\tilde{p}' + \tilde{\varphi}'_{t'} + \frac{1}{2}|\nabla\tilde{\varphi}'|^2 + gy' = C'(t') \quad ((x', y') \in \Omega'(t')), \quad (1.2)$$

where ϱ_F is the constant density of the fluid, g is the acceleration due to gravity and C' is an unknown function that only depends on time. Here $\tilde{\varphi}'_{t'}$ is the partial time derivative of $\tilde{\varphi}'$. Similarly, we will use the indices x' and y' for the partial derivatives in terms of x' and y' .

The water is in contact with the body along $D'_S(t')$ and the position of the free surface is described by $D'_F(t')$ (see Figure 1.1). We assume that the pressure on $D'_F(t')$ is equal to the constant atmospheric pressure p'_{atm} . This assumption is also known as the dynamic boundary condition. We introduce the normalised velocity potential φ' and the normalised pressure p' defined as

$$\varphi' = \tilde{\varphi}' + \frac{p'_{\text{atm}}}{\varrho_F}t' - \int_0^{t'} C'(\tau') d\tau, \quad p' = \tilde{p}' - p'_{\text{atm}}. \quad (1.3)$$

Note that $\nabla\varphi' = \nabla\tilde{\varphi}'$, so that φ' is also a potential of the fluid velocity. Equations (1.1) and (1.2) in terms of φ' and p' are given by

$$\nabla^2\varphi' = 0 \quad ((x', y') \in \Omega'(t')), \quad (1.4)$$

$$\frac{1}{\varrho_F}p' + \varphi'_{t'} + \frac{1}{2}|\nabla\varphi'|^2 + gy' = 0 \quad ((x', y') \in \Omega'(t')). \quad (1.5)$$

For a unique solution Laplace's equation (1.4) has to be supplemented by boundary conditions. The dynamic boundary condition and equation (1.5) imply the following equation on the free surface $(x', y') \in D'_F(t')$:

$$\varphi'_{t'} + \frac{1}{2}|\nabla\varphi'|^2 + gy' = 0 \quad ((x', y') \in D'_F(t')). \quad (1.6)$$

The kinematic boundary condition assumes that fluid on the free surface is not able to leave the fluid free surface and is given by

$$\varphi'_{y'} = \eta'_{x'} \varphi'_{x'} + \eta'_{t'} \quad ((x', y') \in D'_F(t')), \quad (1.7)$$

where the multi-valued function $y' = \eta'(x', t')$ describes the position of the free surface, $(x', y') \in D'_F(t')$. We assume that the fluid on the contact region $D'_S(t')$, described by the function $y' = \omega'(x', t')$, cannot leave the contact region. Similar to equation (1.7), we find the body boundary condition

$$\varphi'_{y'} = \omega'_{x'} \varphi'_{x'} + \omega'_{t'} \quad ((x', y') \in D'_S(t')). \quad (1.8)$$

Since the fluid in the far-field is at rest, the free surface elevation $\eta'(x', t')$ tends to zero as $|x'| \rightarrow \infty$ due to equation (1.7), and the initial condition $\eta'(x', 0) \equiv 0$. Hence, it follows from equation (1.6) that $\varphi'_{t'}$ tends to zero in the far-field along the free surface. We can conclude from the initial condition $\varphi'(x', y', 0) \equiv 0$ and the far-field condition $\nabla \varphi'(x', y', t') \rightarrow 0$ as $x'^2 + y'^2 \rightarrow \infty$, that φ' satisfies the far-field condition

$$\varphi' \rightarrow 0 \quad (x'^2 + y'^2 \rightarrow \infty). \quad (1.9)$$

Hence, to find the fluid flow, we have to solve Laplace's equation (1.4) subject to the boundary conditions (1.6) – (1.8) and the far-field condition (1.9). The pressure in the fluid is obtained by Bernoulli's equation (1.5).

1.5 Objectives and the structure of this thesis

The main objective of this thesis is to give novel two-dimensional models for plate and blunt body impact with small deadrise angle into deep water within the Wagner theory. In these models, we account for the elasticity of the body, the horizontal speed of the body, separation of the fluid and a wake region generated due to detachment of the fluid from the body. The separation and cavitation models suggested avoid unphysical low-pressure zones. In these models, we couple together the fluid flow, the hydrodynamic loads and the motion of the body, including the vibration of the body and the position of the mobile separation points and turnover regions.

To achieve these objectives, we will solve mixed boundary-value problems in terms of the acceleration potential, velocity potential and displacement potential to find solutions of the impact problems. To couple the impact of an elastic plate into water, we use the normal-modes method. Results in this thesis will be analytical and semi-analytical depending on the complexity of the problem. As to the semi-analytical results, their final equations are straightforward for numerical evaluations. In particular, this work will illustrate the importance of the elasticity of the body and the choice of the separation criterion for the hydrodynamic loads. We will show interesting scenarios due to the free vertical component of motion of the body along with its fixed horizontal component of velocity.

The structure of the thesis is as follows. We start with a mathematical analysis of a certain class of mixed boundary-value problems on the lower half plane in chapter 2. To

obtain unique solutions, we permit only certain behaviours of the solutions at the points where the type of boundary condition changes and in the far-field. The solution of these mixed boundary-value problems will be used in the subsequent chapters to solve the linearised hydrodynamic part of the impact problems in terms of the acceleration potential, velocity potential and displacement potential.

In chapter 3, we introduce the Wagner model for the vertical impact of a plate with small inclination onto an undisturbed water surface. The Wagner model consists of the linearised hydrodynamic problem and the Wagner condition to determine the size of the contact region. We will show that the linearised hydrodynamic model breaks down at the initial penetration point and at the fluid turnover region. Here we will only present the inner flow at the turnover region and analyse the energy in the jet. Finally, we analyse the problem of an elastic plate vertically entering the fluid where the plate elasticity is modelled by Euler's beam equation.

In chapter 4, we present a model for the impact of a body with small deadrise angle at high horizontal speed using the Wagner theory and including a wake region behind the body. If the fluid separates at the rear contact point, we impose Kutta's condition and the condition that the fluid boundary is continuous at the separation point. The forward contact point is modelled by Wagner's condition. We identify the energy in the jet and in the rest of the fluid. In the first case study, we solve the problem of oblique impact of a rigid plate at constant speed, where the separation point is fixed at the trailing edge. For general body shapes we derive a formula for the position of the separation point along the smooth body, which is shown to be equivalent to the Brillouin-Villat criterion. This criterion will be used to determine the position of the separation point in the free impact of a rigid plate with constant angle of attack. If the mass of the plate is small enough, the plate exits the fluid after entry. In the case of plate planing after impact we analyse the long time behaviour of the fluid flow and of the plate motion. Finally, we discuss the impact of a blunt body at high speed and analyse the body behaviour in terms of different separation criteria. The work for the impact of a blunt body has been published in Reinhard et al. (2012a).

In chapter 5, we analyse the impact of an elastic plate onto the water surface at high horizontal speed. In the first section, we fix the position of the contact point at the trailing edge. In particular, in this model we will identify the energy in the fluid and in the plate, and analyse the possible plate-motion scenarios in detail. In the second section, the position of the rear contact point is determined by the Brillouin-Villat criterion. We have to distinguish between three flow regimes at the rear contact point since the motion of the separation point is sensitive to the plate vibration. The work in the first section is under review for the *Journal of Fluid Mechanics* (see Reinhard et al., 2013). The work in the second section has been published in Reinhard et al. (2012b).

In chapter 6, we discuss two vertical impact problems where the fluid separates from a part of the contact region. In the first problem, we consider the free impact of a rigid plate. Due to the vertical deceleration and the rotation of the plate, the fluid can separate at the lower edge of the plate or inside the wetted region. In the second problem, we discuss the symmetric problem of vertical impact of a light blunt body with account for a cavity under the body.

In chapter 7, conclusions are drawn and future work is suggested.

Chapter 2

Mixed boundary-value problems

Mixed boundary-value problems (MBVPs) for Laplace's equation arise in many applications and are described for example in Duffy (2008) for various two dimensional and three-dimensional problems mainly on strips, spheres and half-spaces, in Sneddon (1966) specifically for three-dimensional axisymmetric problems on the half space and in Gakhov (1966) for two-dimensional problems. Here, we will mainly refer to Gakhov (1966). A typical definition of a two-dimensional MBVP in terms of a function $\varphi(x, y)$, twice continuously differentiable on an open domain Ω , is given by

$$\nabla^2 \varphi = 0 \quad ((x, y) \in \Omega), \quad (2.1)$$

$$\varphi = u_1 \quad ((x, y) \in \partial\Omega_1), \quad (2.2)$$

$$\frac{\partial \varphi}{\partial \mathbf{n}} = u_2 \quad ((x, y) \in \partial\Omega_2), \quad (2.3)$$

where the boundary of the domain Ω is decomposed into $\partial\Omega_1$ and $\partial\Omega_2$. The functions u_1 and u_2 are prescribed on $\partial\Omega_1$ and $\partial\Omega_2$. Here \mathbf{n} denotes the exterior normal to the boundary $\partial\Omega_2$. The two-dimensional problem (2.1) – (2.3) can be related to a boundary problem of the complex function $f(z) = \varphi_x(x, y) - i\varphi_y(x, y)$, $z = x + iy$. Equation (2.1) implies that $f(z)$ is analytic, which means that it satisfies the Cauchy-Riemann equations $\frac{\partial}{\partial x} \operatorname{Re}(f) = \frac{\partial}{\partial y} \operatorname{Im}(f)$ and $\frac{\partial}{\partial x} \operatorname{Im}(f) = -\frac{\partial}{\partial y} \operatorname{Re}(f)$.

Many important electrostatic problems, diffusion problems, and problems in potential flow theory can be formulated as MBVPs of the form (2.1) – (2.3). The two-dimensional problems in this study, where a body with small deadrise angle impacts onto an initially flat water surface, can be approximately described as MBVPs on the lower half-plane (see e.g. Howison et al., 1991). In the following, we discuss such MBVPs in terms of analytic functions.

In our problems, an analytic function $f(z) = u(x, y) + iv(x, y)$ defined on $y < 0$, satisfies the following conditions for given integers k_1, k_2, l and given smooth enough functions $u_0(x)$ for $x < d_1$ and $x > d_2$ and $v_0(x)$ for $d_1 < x < d_2$ (see also Figure 2.1):

- (i) $f(z)$ can be continually extended on $y = 0$, excluding the points $z = d_1$ and $z = d_2$.
- (ii) $f(z) = O(z^{l-1})$ as $|z| \rightarrow \infty$.
- (iii) $|f(z)| = O(|z - d_1|^{-k_1-1/2})$ as $z \rightarrow d_1$ and $|f(z)| = O(|z - d_2|^{-k_2-1/2})$ as $z \rightarrow d_2$.
- (iv) $\operatorname{Re}(f(x - i0)) = u_0(x)$ for $x < d_1$ and $x > d_2$.

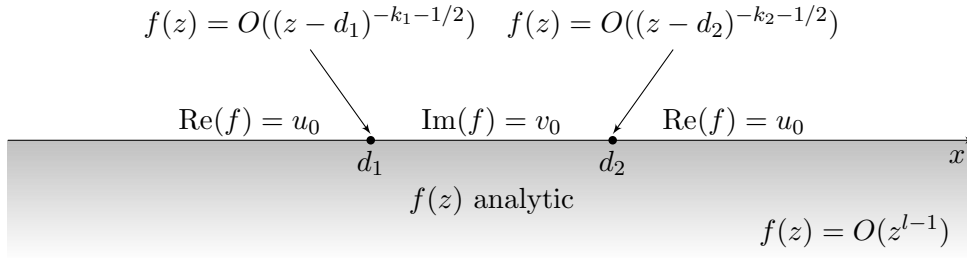


Figure 2.1: MBVP for the lower-half plane.

(v) $\text{Im}(f(x - i0)) = v_0(x)$ for $d_1 < x < d_2$.

We only consider boundary functions $u_0(x)$ and $v_0(x)$ which are consistent with conditions (ii) and (iii). Condition (i) implies that $u_0(x)$ and $v_0(x)$ are continuous functions. For solutions f satisfying (i) – (v), which will be presented in section 2.3, we require stronger conditions on the regularity of $u_0(x)$ and $v_0(x)$, which will be specified later. The solution of this boundary value problem is linear with respect to $u_0(x)$ and $v_0(x)$. Any possible solution of (i) – (v) can be obtained by adding eigensolutions to a particular solution of the inhomogeneous problem. The eigensolutions are the solutions of the homogeneous problem, where $u_0(x) = 0$ and $v_0(x) = 0$. Hence, the dimension of the space of solutions of (i) – (v) is given by the maximum number of independent eigensolutions. We introduced conditions (ii) and (iii) to control this dimension. The smaller the parameters k_1 , k_2 and l the smaller is the dimension of the solution space. If the parameters k_1 , k_2 and l are too small, the problem may have no solution. We will also address the question of the existence and uniqueness of solutions in the following subsections.

Here we remark that the problem (i) – (v) can be transformed into the Riemann-Hilbert problem (Gakhov (1966), King (2009) and Gillow (1998)), where the analytic function $f(z)$ is given by the relation

$$f(x - i0) + G(x)\overline{f(x - i0)} = g(x). \quad (2.4)$$

Here $\overline{f(x - i0)}$ is the complex conjugate of $f(x - i0)$. In our problem, the functions G and g are specified by $G(x) = -1$ and $g(x) = 2iv_0(x)$ for $d_1 < x < d_2$ and $G(x) = 1$ and $g(x) = 2u_0(x)$ for $x < d_1$ and $x > d_2$. Solutions of equation (2.4) can be obtained using the Plemelj-Sokhotski formula (see equation (2.21)). However, in this thesis we will solve the MBVP (i) – (v) directly by reducing it to a Dirichlet problem.

2.1 The homogeneous problem

In the homogeneous problem we seek all possible solutions f satisfying conditions (i) – (v) with $u_0(x) = 0$ for $x < d_1$ and $x > d_2$, and $v_0(x) = 0$ for $d_1 < x < d_2$ in (iv) and (v). The MBVP can be transformed into a Dirichlet problem by multiplying $f(z)$ with the characteristic function

$$g(z) = (z - d_1)^{k_1+1/2}(z - d_2)^{k_2+1/2} \quad (y < 0), \quad (2.5)$$

where k_1 and k_2 are the integers given in (iii). In equation (2.5) we consider the branch of $g(z)$, for which $g(x - i0)$ is positive for $x > d_2$. In particular, $g(z)$ is analytic in $y < 0$. Note that $g(z)$ behaves in the far-field as $g(z) = z^{k_1+k_2+1} + O(z^{k_1+k_2})$. The values of $g(z)$ on the boundary $y = 0$ are

$$g(x - i0) = (-1)^{k_1+k_2+1}(d_1 - x)^{k_1+1/2}(d_2 - x)^{k_2+1/2} \quad (x < d_1) \quad (2.6)$$

$$g(x - i0) = i(-1)^{k_2+1}(x - d_1)^{k_1+1/2}(d_2 - x)^{k_2+1/2} \quad (d_1 < x < d_2) \quad (2.7)$$

$$g(x - i0) = (x - d_1)^{k_1+1/2}(x - d_2)^{k_2+1/2} \quad (x > d_2). \quad (2.8)$$

We introduce the product $h(z) = if(z)g(z)$, which is analytic in $y < 0$, since $f(z)$ and $g(z)$ are analytic in $y < 0$. It follows from (2.6) – (2.8) and $u_0(x) \equiv 0$, $v_0(x) \equiv 0$ in conditions (iv) and (v) that $\text{Im}(h(x - i0)) = 0$. Furthermore it follows from conditions (i) – (iii) that $h(z)$ inherits the following properties:

- (a) $h(z)$ can be continually extended on $y = 0$, excluding the points $z = d_1$ and $z = d_2$.
- (b) $h(z) = O(z^{k_1+k_2+l})$ as $|z| \rightarrow \infty$.
- (c) $h(z) = O(1)$ as $z \rightarrow d_1$ and $z \rightarrow d_2$.

Since $h(x - i0)$ is real-valued and satisfies condition (a), it can be analytically continued onto $\mathbb{C} \setminus \{d_1, d_2\}$ by Schwarz's reflection principle (see Lang, 1993). Since condition (c) is satisfied, Riemann's theorem (Lang (1993)) implies that $h(z)$ can be further analytically defined at $z = d_1$ and $z = d_2$. Since $h(z)$ can be analytically continued on the entire complex plane and is real-valued on $y = 0$ and satisfies condition (b), it follows from the generalised Liouville's theorem (see Gakhov (1966)) that $h(z)$ can be written as the following polynomial on the complex plane:

$$h(z) = \sum_{j=0}^{k_1+k_2+l} a_j z^j, \quad (2.9)$$

with real coefficients a_j . In particular, if $k_1 + k_2 + l < 0$ we obtain that $h(z) \equiv 0$ so that $f(z) \equiv 0$. For $k_1 + k_2 + l \geq 0$, we find the following formula $f(z)$ by using the definition of $h(z)$ and equation (2.9):

$$f(z) = -i(z - d_1)^{-k_1-1/2}(z - d_2)^{-k_2-1/2} \sum_{j=0}^{k_1+k_2+l} a_j z^j. \quad (2.10)$$

The function $f(z)$ in (2.10) is an eigensolution of the homogeneous problem of (i) – (v) for any real a_j . Hence, the dimension of the solution space is $k_1 + k_2 + l + 1$. This is in agreement with the Riemann-Hilbert theory: If we formulate the MBVP (i) – (v) as the Riemann-Hilbert problem (2.4), then $\kappa = k_1 + k_2 + l$ is known as the index of the problem, where $\kappa + 1$ is the dimension of the solution space if $\kappa \geq 0$.

Equation (2.10) shows that the eigensolutions $f(z)$ can only have asymptotic forms $f(z) \sim iC_1 z^{l^*-1}$ as $|z| \rightarrow \infty$, $f(z) \sim C_2(z - d_1)^{-k_1^*-1/2}$ as $z \rightarrow d_1$ and $f(z) \sim iC_3(z - d_2)^{-k_2^*-1/2}$ as $z \rightarrow d_2$ for integers $k_1^* \leq k_1$, $k_2^* \leq k_2$ and $l^* \leq l$ where $k_1^* + k_2^* + l^* \geq 0$ and C_1, C_2, C_3 are real and non-zero coefficients.

At the beginning of this chapter we assumed that k_1 , k_2 and l are integers. In general, for real k_1 , k_2 and l in (ii) and (iii), it can be shown that they can be replaced by the integers $\lfloor k_1 \rfloor$, $\lfloor k_2 \rfloor$ and $\lfloor l \rfloor$ to obtain all possible solutions. Here $\lfloor x \rfloor$ is the integer lying in the interval $x - 1 < \lfloor x \rfloor \leq x$.

2.2 MBVP-solutions for boundary values of polynomial type

Here we consider the complex function $f(z)$ satisfying (i) – (v) with the following boundary functions in (iv) and (v):

$$u_0(x) = 0 \quad (x < d_1 \text{ and } x > d_2), \quad (2.11)$$

$$v_0(x) = \sum_{j=0}^m b_j x^j \quad (d_1 < x < d_2). \quad (2.12)$$

The function $v_0(x)$ in (2.12) is a polynomial of degree m . Note that $v_0(x)$ in (2.12) has to be consistent with the conditions (ii) and (iii). We introduce the function

$$f^*(z) = f(z) - i \sum_{j=0}^m b_j z^j, \quad (2.13)$$

which is analytic for $y < 0$. Consequently, $f^*(z)$ satisfies the boundary conditions $\operatorname{Re}(f^*(x)) = 0$ for $x < d_1$ and $x > d_2$ and $\operatorname{Im}(f^*(x)) = 0$ for $d_1 < x < d_2$. Conditions (i) – (iii) for $f(z)$ imply that:

(a*) $f^*(z)$ can be continually extended on $y = 0$, excluding the points $z = d_1$ and $z = d_2$,

(b*) $f^*(z) = O(z^{l_0-1})$ as $|z| \rightarrow \infty$ where $l_0 = \max\{l, m + 1\}$,

(c*) $|f^*(z)| = O(|z - d_1|^{-k_1-1/2})$ as $z \rightarrow d_1$ and $|f^*(z)| = O(|z - d_2|^{-k_2-1/2})$ as $z \rightarrow d_2$.

It follows that the function $f^*(z)$ is given by equation (2.10). Correspondingly, $f(z)$ can be written as

$$f(z) = i \left(\sum_{j=0}^m b_j z^j - (z - d_1)^{-k_1-1/2} (z - d_2)^{-k_2-1/2} \sum_{j=0}^{k_1+k_2+l_0} a_j z^j \right), \quad (2.14)$$

where the real coefficients a_j have to be chosen in such a way that $f(z)$ satisfies condition (ii). If $l \geq m + 1$ where m is the degree of the polynomial $v_0(z)$, condition (ii) is satisfied for any a_j . However, if $l < m + 1$, we arrive at $m - l + 1$ equations for a_j . This is illustrated by the following example:

We consider a function $f(z)$ satisfying (i) – (v) for $k_1 = k_2 = l = 0$ and the boundary functions $u_0(x) \equiv 0$ for $x < d_1$ and $x > d_2$, $v_0(x) = x - \frac{1}{2}(d_1 + d_2)$ for $d_1 < x < d_2$. Formula (2.14) with $l_0 = 2$ yields:

$$f(z) = i \left(z - \frac{d_1 + d_2}{2} - \frac{a_2 z^2 + a_1 z + a_0}{\sqrt{(z - d_1)(z - d_2)}} \right), \quad (2.15)$$

where a_0 , a_1 and a_2 are real. The far-field condition, $f(z) = O(z^{-1})$ as $|z| \rightarrow \infty$, implies that $a_2 = 1$ and $a_1 = -(d_1 + d_2)$. In this example the coefficient a_0 is still undetermined.

In this subsection, we derived the solutions of (i) – (v) where $u_0(x) = 0$ and $v_0(x)$ is a polynomial. A similar approach can be used to obtain a solution if both boundary functions $u_0(x)$ and $v_0(x)$ are polynomials. However, if either $u_0(x)$ or $v_0(x)$ is not a polynomial, then we need a different approach to solve the MBVP (i) – (v). This will be shown in the next subsection.

2.3 Particular solutions of inhomogeneous problems

This subsection will give a particular solution of the MBVP (i), (iii), (iv) and (v). It will depend on the choice of l , if this particular solution will also satisfy condition (ii). First, we define the function $c(x)$ by the following values:

$$c(x) = (-1)^{k_1+k_2+1}(d_1 - x)^{k_1+1/2}(d_2 - x)^{k_2+1/2}u_0(x) \quad (x < d_1) \quad (2.16)$$

$$c(x) = (-1)^{k_2}(x - d_1)^{k_1+1/2}(d_2 - x)^{k_2+1/2}v_0(x) \quad (d_1 < x < d_2) \quad (2.17)$$

$$c(x) = (x - d_1)^{k_1+1/2}(x - d_2)^{k_2+1/2}u_0(x) \quad (x > d_2) \quad (2.18)$$

where $u_0(x)$ and $v_0(x)$ are the prescribed boundary functions in (iv) and (v). Here the functions $u_0(x)$ and $v_0(x)$ are supposed to be such that $c(x)$ satisfies the following conditions:

(I) $c(x)$ is absolute integrable, so that $\int_{-\infty}^{\infty} |c(\xi)| d\xi < \infty$.

(II) $c(x)$ is Hölder-continuous with index $0 < \lambda \leq 1$, i.e. a constant $B > 0$ exists such that

$$|c(x_2) - c(x_1)| < B|x_2 - x_1|^\lambda \quad (2.19)$$

for all real x_1, x_2 .

Note that the Hölder index is not related to the index of a Riemann-Hilbert problem. Since $c(x)$ satisfies condition (I), the Cauchy-type integral

$$h_0(z) = \frac{i}{\pi} \int_{-\infty}^{\infty} \frac{c(\xi)}{\xi - z} d\xi \quad (2.20)$$

is well defined and analytic in $y < 0$. The behaviour of $h_0(z)$ in the far-field is $O(z^{-1})$ as $|z| \rightarrow \infty$. Since $c(x)$ is Hölder-continuous (condition (II)), the function $h_0(z)$ can be continuously extended to the real axis using the Plemelj-Sokhotski formula (see Gakhov, 1966)

$$\lim_{\substack{y \rightarrow 0 \\ y < 0}} \int_{-\infty}^{\infty} \frac{c(\xi)}{\xi - z} d\xi = -\pi i c(x) + \int_{-\infty}^{\infty} \frac{c(\xi)}{\xi - x} d\xi, \quad (2.21)$$

where the integral on the right-hand side of (2.21) is understood as a Cauchy principal-value integral, which is defined as

$$\int_{-\infty}^{\infty} \frac{c(\xi)}{\xi - x} d\xi = \lim_{\varepsilon \rightarrow 0} \left(\int_{-\infty}^{x-\varepsilon} \frac{c(\xi)}{\xi - x} d\xi + \int_{x+\varepsilon}^{\infty} \frac{c(\xi)}{\xi - x} d\xi \right). \quad (2.22)$$

Hence, for $y = 0$ the real and imaginary parts of $h_0(z)$ are given by:

$$\operatorname{Re}(h_0(x)) = c(x), \quad (2.23)$$

$$\operatorname{Im}(h_0(x)) = \frac{1}{\pi} \int_{-\infty}^{\infty} \frac{c(\xi)}{\xi - x} d\xi. \quad (2.24)$$

Equation (2.24) is known as Hilbert's formula. Since $c(x)$ is Hölder-continuous, it can be shown that $\operatorname{Im}(h_0(x))$ in (2.24) is also Hölder-continuous (see Gakhov, 1966).

A particular solution $f_0(z)$ of the MBVP (i) – (v) can be obtained by introducing $f_0(z) = h_0(z)/g(z)$, where the characteristic function $g(z)$ is given by equation (2.5). Hence $f_0(z)$ can be written as

$$f_0(z) = \frac{i}{\pi} (z - d_1)^{-k_1-1/2} (z - d_2)^{-k_2-1/2} \int_{-\infty}^{\infty} \frac{c(\xi)}{\xi - z} d\xi \quad (y < 0). \quad (2.25)$$

where k_1 and k_2 are the integers given in (iii). Note that $h_0(z)$ in (2.20) is analytic in $y < 0$, and continuous in $y \leq 0$, so that the function $f_0(z)$ in (2.25) satisfies the conditions (i) and (iii). It follows from (2.6) – (2.8), (2.16) – (2.18) and (2.21) that $f_0(z)$ in (2.25) satisfies the boundary conditions (iv) and (v). As to condition (ii), it is satisfied for $l \geq -k_1 - k_2 - 1$, since the function $f_0(z)$ in (2.25) behaves in the far-field as

$$f_0(z) \sim \frac{i}{\pi} \int_{-\infty}^{\infty} c(\xi) d\xi z^{-k_1-k_2-2} \quad (|z| \rightarrow \infty). \quad (2.26)$$

Hence, $f_0(z)$ in (2.25) is the required particular solution satisfying conditions (i) – (v), if $l \geq -k_1 - k_2 - 1$. However, formula (2.25) cannot be used for arbitrary boundary functions $u_0(x)$ and $v_0(x)$ and integers k_1 and k_2 , because $c(x)$ in (2.16) – (2.18) has to satisfy conditions (I) and (II). In particular, condition (II) implies that for all $\varepsilon > 0$ the function $u_0(x)$ for $x < d_1 - \varepsilon$ and $x > d_2 + \varepsilon$ and the function $v_0(x)$ for $d_1 + \varepsilon < x < d_2 - \varepsilon$ have to be Hölder-continuous. It is possible for $k_1 \geq 0$ and $k_2 \geq 0$ to use formula (2.25) for functions $u_0(x)$ and $v_0(x)$ which are singular at $x = d_1$ and $x = d_2$, as long (I) and (II) are satisfied.

In many problems in this thesis we will not be interested in $f_0(z)$ for $y < 0$ given in (2.25), but in $f_0(x-i0)$. For obtaining the limit $y \rightarrow 0$ in (2.25) we use the Plemelj-Sokhotski formula (2.21), so that the unknown parts on the x -axis are given by:

$$\operatorname{Im}(f_0(x - i0)) = (-1)^{k_1+k_2+1} (d_1 - x)^{-k_1-1/2} (d_2 - x)^{-k_2-1/2} I(x) \quad (x < d_1), \quad (2.27)$$

$$\operatorname{Re}(f_0(x - i0)) = (-1)^{k_2+1} (x - d_1)^{-k_1-1/2} (d_2 - x)^{-k_2-1/2} I(x) \quad (d_1 < x < d_2), \quad (2.28)$$

$$\operatorname{Im}(f_0(x - i0)) = (x - d_1)^{-k_1-1/2} (x - d_2)^{-k_2-1/2} I(x) \quad (x > d_2), \quad (2.29)$$

$$I(x) = \frac{1}{\pi} \int_{-\infty}^{\infty} \frac{c(\xi)}{\xi - x} d\xi. \quad (2.30)$$

where $c(x)$ is given by (2.16) – (2.18).

In this subsection we derived a particular solution of the MBVP given by (i) – (v), such that we are able to find the general solution with the help of the eigensolutions (2.10). A particular solution of the MBVP (i) – (v) exists, if $l + k_1 + k_2 \geq -1$ and $c(x)$ in (2.16) – (2.18) satisfies (I) and (II). A solution of the MBVP (i) – (v), if it exists, is unique for $l + k_1 + k_2 \leq -1$ as we have seen in subsection 2.1. A solution of (i) – (v) may not exist for

$l + k_1 + k_2 < -1$.

Note that formulas (2.25) and (2.27) – (2.29) are also valid for boundary functions $u_0(x)$ and $v_0(x)$ with discontinuities at x_1, \dots, x_N where the resulting $c(x)$ in (2.16) – (2.18) is supposed to be piecewise Hölder-continuous. In this case we have to modify the continuity condition in (i) at x_1, \dots, x_N , so that we account for the logarithmic singularities of $f_0(z)$ in (2.25) at x_1, \dots, x_N .

2.4 Solutions for singular $c(x)$

If the boundary values $u_0(x)$ and $v_0(x)$ do not tend to zero as $x \rightarrow d_1$ and $x \rightarrow d_2$, the function $c(x)$ in (2.16) – (2.18) can only be Hölder-continuous for $k_1 \geq 0$ and $k_2 \geq 0$. However, it is possible to use $f_0(z)$ in (2.25) for $k_1 = -1$ and $k_2 = -1$, also if $u_0(x) \neq 0$, $v_0(x) \neq 0$ at $x = d_1, d_2$. To do this we weaken condition (II) to the following alternative condition:

(II*) For all $\varepsilon > 0$ the function $c(x)$ is Hölder-continuous on the intervals $(-\infty, d_1 - \varepsilon)$, $(d_1 + \varepsilon, d_2 - \varepsilon)$ and $(d_2 + \varepsilon, \infty)$.

If $c(x)$ satisfies condition (I) and (II*) it can be shown that $f_0(z)$ in (2.25) still satisfies conditions (i), (iv), (v), since we do not have to apply the Plemelj-Sokhoski formula (2.21) to $x = d_1$ and $x = d_2$. The only drawback of condition (II*) is that it does not guarantee that $f_0(z)$ in (2.25) satisfies condition (iii), so that we still have to find the asymptotic behaviour of $f_0(z)$ as $z \rightarrow d_1$ and $z \rightarrow d_2$.

Below, we identify the behaviour of $f_0(z)$ in (2.25) at $z = d_1$ and $z = d_2$ for $k_1 = -1$ or $k_2 = -1$ for functions $u_0(x)$ and $v_0(x)$ in (2.16) – (2.18) satisfying Hölder's condition with Hölder-index $\frac{1}{2} < \lambda \leq 1$. In particular, for $k_1 = -1$ or $k_2 = -1$ the resulting function $c(x)$ given by (2.16) – (2.18) satisfies condition (II*) but not (II). We use the following result from Gakhov (1966):

Let $\varphi(x)$ be a real valued function which satisfies Hölder's condition for $a < x < b$ with index $\frac{1}{2} < \lambda \leq 1$. Then there exists a complex number β and an analytic function $\Phi_0(z)$ in the vicinity of $z = d$, $a \leq d \leq b$, such that

$$\int_a^b \frac{\varphi(\xi)}{|\xi - d|^{1/2}(\xi - z)} d\xi = \beta(z - d)^{-1/2} + \Phi_0(z) \quad (2.31)$$

in the vicinity of $z = d$.

Then equation (2.31) implies that $f_0(z)$ in (2.25) with $k_1 = -1$ is continuously extendable at $z = d_1$, where conditions (iv) and (v) infer that $f_0(d_1) = u_0(d_1) + iv_0(d_1)$. Similarly, $f_0(z)$ can be continuously extended at $z = d_2$ for $k_2 = -1$, where $f_0(d_2) = u_0(d_2) + iv_0(d_2)$.

In the following we derive the fundamental identity

$$\int_{d_1}^{d_2} \frac{d\xi}{(\xi - x)\sqrt{(\xi - d_1)(d_2 - \xi)}} = 0. \quad (2.32)$$

First, we consider an analytic function $f(z)$ satisfying the boundary conditions $u_0(x) \equiv 0$ for $x < d_1$, $y = 0$, and $x > d_2$, $y = 0$, and $v_0(x) \equiv 1$ for $d_1 < x < d_2$, $y = 0$, which is bounded in

the far-field and at $z = d_1, d_2$. This problem has no eigensolutions (see equation (2.10)), so the solution of the problem is unique. The solution of this problem is $f(z) \equiv i$. Moreover, the solution of the problem is also given by the formula in (2.25) with $k_1 = k_2 = -1$ where $c(x)$ is obtained by (2.16) – (2.18). Hence

$$f(z) = -\frac{i}{\pi} \sqrt{(z-d_1)(z-d_2)} \int_{d_1}^{d_2} \frac{1}{\sqrt{(\xi-d_1)(d_2-\xi)(\xi-z)}} d\xi. \quad (2.33)$$

It follows from equation (2.33) with $f(z) = i$ that:

$$\int_{d_1}^{d_2} \frac{d\xi}{(\xi-z)\sqrt{(\xi-d_1)(d_2-\xi)}} = -\frac{i\pi}{\sqrt{(z-d_1)(z-d_2)}}. \quad (2.34)$$

Consequently, for $d_1 < x < d_2$, $y = 0$, we obtain from equations (2.21) and (2.34) the identity (2.32).

Equation (2.32) helps us to reduce Cauchy principal-value integrals to regular integrals by the following identity for $d_1 < x < d_2$:

$$\int_{d_1}^{d_2} \frac{F(\xi)}{\sqrt{(\xi-d_1)(d_2-\xi)(\xi-x)}} d\xi = \int_{d_1}^{d_2} \frac{1}{\sqrt{(\xi-d_1)(d_2-\xi)}} \frac{F(\xi) - F(x)}{\xi - x} d\xi, \quad (2.35)$$

where the quotient $(F(\xi) - F(x))/(\xi - x)$ does not have a singularity at $\xi = x$, if $F(\xi)$ is differentiable in x . For example if $F(\xi)$ is a polynomial in ξ , the value $(F(\xi) - F(x))/(\xi - x)$ is a polynomial in ξ . Hence, we can find an analytical solution of the right-hand side of equation (2.35). For arbitrary but smooth functions $F(x)$, the right-hand side of equation (2.35) is suitable for numerical evaluation.

This section discussed the particular solution $f_0(z)$ in (2.25) for square-root singular $c(x)$ and we investigated the asymptotic behaviour of $f_0(z)$ at $z = d_1$ and $z = d_2$.

2.5 An integral relation

In this subsection, we consider an analytic function $f(z) = u(x, y) + iv(x, y)$ which is defined in $y < 0$. We specify the behaviour of $f(z)$ at $z = d_1, d_2$ and in the far-field by $f(z) = O((z-d_i)^{-1/2})$ as $z \rightarrow d_i$, $i = 1, 2$ and by $f(z) = O(z^{-2})$ as $z \rightarrow \infty$. The aim of this section is to derive a formula which expresses the integral $\int_{d_1}^{d_2} r(x)u(x, 0) dx$ in terms of $v(x, 0)$ for $d_1 < x < d_2$ and $u(x, 0)$ for $x < d_1$ and $x > d_2$ for a prescribed Hölder-continuous function $r(x)$ with index $\lambda > \frac{1}{2}$.

We define an auxiliary analytic function $g(z) = \tilde{u}(x, y) + i\tilde{v}(x, y)$ in the lower half-plane given by the mixed boundary value problem

$$\tilde{u} = 0 \quad (y = 0, x < d_1 \text{ and } x > d_2), \quad (2.36)$$

$$\tilde{v} = r(x) \quad (y = 0, d_1 < x < d_2), \quad (2.37)$$

$$g(z) = O(1) \quad (z = d_1 \text{ and } z = d_2), \quad (2.38)$$

$$g(z) = O(1) \quad (|z| \rightarrow \infty), \quad (2.39)$$

where $r(x)$ is a prescribed Hölder-continuous function with index $\lambda > \frac{1}{2}$. In particular, it can be shown that the MBVP (2.36) – (2.39) has no eigensolutions, so its solution is unique.

Since $f(z)g(z)$ decays as $O(z^{-2})$ in the far field and may be only square-root singular at $z = d_1$ and $z = d_2$, we obtain from Cauchy's integral theorem that

$$\int_{-\infty}^{\infty} f(z)g(z) dz = 0. \quad (2.40)$$

The real part of equation (2.40) is given by the following equation by substituting $f(z) = u + iv$ and $g(z) = \tilde{u} + i\tilde{v}$:

$$\int_{d_1}^{d_2} r(x)u(x, 0) dx = - \left(\int_{-\infty}^{d_1} + \int_{d_2}^{\infty} \right) u(x, 0)\tilde{v}(x, 0) dx - \int_{d_1}^{d_2} \tilde{u}(x, 0)v(x, 0) dx. \quad (2.41)$$

Solutions for $\tilde{u}(x, 0)$ for $d_1 < x < d_2$ and $\tilde{v}(x, 0)$ for $x < d_1$ and $x > d_2$ are determined by (2.36) – (2.39) and are given by equations (2.27) – (2.29). Hence, if $u(x, 0)$ is unknown for $d_1 < x < d_2$, the left-hand side of (2.41) can be expressed by integrals, whose integrands are known. Formula (2.41) will be used in sections 4.4 and 6.1 for $r(x) = x$ and $r(x) = \frac{1}{2}x^2 - d_1x$.

2.6 Summary

This chapter discussed several particular types of MBVPs in the lower-half plane which will be used in the chapters below. The behaviour at the points, where the boundary condition changes, and in the far-field has to be restricted to obtain a finite-dimensional space of solutions. We presented formulas for the particular solution on the lower-half plane in (2.25) and along the x -axis in (2.27) – (2.29). The behaviour of these particular solutions in the far-field and at $z = d_1$, $z = d_2$ depend on the choice of k_1 and k_2 . We showed that under certain conditions also the choice $k_1 = -1$ and $k_2 = -1$ is allowed. To obtain all possible solutions of the MBVP we have to add the eigensolutions of the problem, given by equation (2.10), to the particular solution. In subsection 2.5 we presented an integral relation.

Chapter 3

Wagner model of vertical plate impact

This chapter will give the reader an introduction to the original Wagner model (Wagner, 1932). The Wagner model gives an asymptotic solution for problems where a body with small deadrise angle impacts onto an initially flat water free surface. We discuss the problem of an inclined rigid plate vertically impacting onto the free surface in section 3.1, where we introduce and solve the linearised hydrodynamic model. In particular, it will be shown that the linearised hydrodynamic model is not valid in the turnover region, where a thin jet is thrown off, and in the region of the initial penetration point, where a splash occurs. We present an approach to find the local flow in the turnover region. We also calculate the kinetic energy of the fluid and the portion of kinetic energy in the jet. In section 3.2 we introduce the normal modes of a dry elastic beam governed by Euler's beam equation subject to free-free boundary conditions. These normal modes will be used in section 3.3 to discuss the free fall of an elastic plate onto the free surface. In this problem we discuss both the impact stage, where the fluid overturns under the plate, and the stage after the plate is fully wetted (without the jet).

3.1 Impact of a rigid plate at constant vertical speed

The most popular shapes for impacting bodies in the literature are wedges and parabolas (e.g. Wagner, 1932; Howison et al., 1991; Oliver, 2002). However, also bodies with sharp edges can be exposed to slamming. In this section, we consider the two-dimensional unsteady water flow due to an inclined rigid plate, which is vertically moving onto the initially flat surface of deep water with constant speed (see Figures 3.1 and 3.2). We are interested in the pressure distribution, the water flow on the underside of the plate, the motion of the turnover region and the shape of the free surface during the initial impact stage. Although there are many impact experiments of wedges and cylinders, we are not aware of impact experiments of inclined plates.

The impact of a semi-infinite rigid plate with constant velocity onto a flat free surface is self-similar, since the problem does not have a lengthscale. Faltinsen and Semenov (2008) presented a method to obtain semi-analytic solutions for this problem, and they showed numerical results for vertical impact alongside results where the plate enters the fluid obliquely.

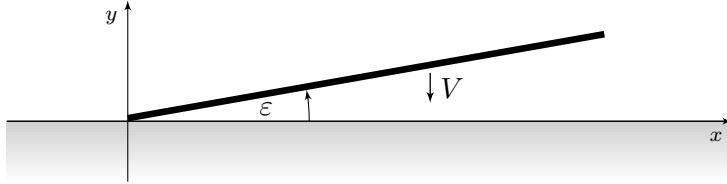


Figure 3.1: The left edge of the rigid plate initially touches the free surface at the origin, is inclined by the angle ε and has the initial vertical velocity V .

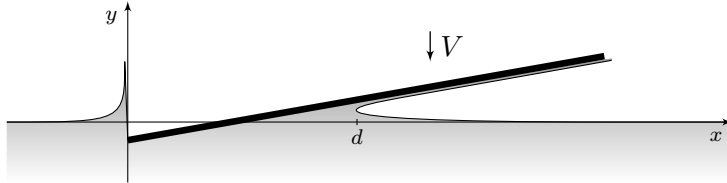


Figure 3.2: The inclined plate penetrates the free surface vertically with constant speed V . At $x = d$ the fluid overturns and a thin jet is thrown off. A splash occurs close to the initial penetration point $x = 0$.

During the impact of an inclined plate a splash occurs to the left of the sharp impacting edge (see Figure 3.2). Note that in Faltinsen and Semenov (2008) the fluid separates tangentially from the plate edge. A similar condition has been used in Iafrati and Korobkin (2004), where the profile of the splash has been analysed for the vertical impact of a horizontal plate onto a flat water surface. The asymptotic model presented in this section will not resolve the splash formation. In particular, we will experience an unphysical singular free-surface elevation at the initial penetration point. More insight into the splash flow can be achieved by investigating the inner flow structure.

3.1.1 The non-dimensional nonlinear hydrodynamic problem

We start with the formulation of the nonlinear problem and the scaling of the variables for the plate impact problem. Initially, the fluid is at rest and covers the lower half plane, $y' < 0$, described by a Cartesian coordinate system $x'Oy'$ at time $t' = 0$. The coordinate system $x'Oy'$ is fixed such that the fluid in the far-field is at rest during the fluid-plate interaction. Initially, the rigid flat plate of length L touches the free surface with its left edge at a single point, which is taken as the origin O (see Figure 3.1). The plate is inclined to the liquid free surface at a small angle ε . At time $t' = 0$ the plate starts to penetrate the liquid with constant vertical speed. The position of the lower plate surface is given by

$$y' = \omega'(x', t'), \quad \omega'(x', t') = x' \tan(\varepsilon) - Vt' \quad (0 < x' < L \cos(\varepsilon)). \quad (3.1)$$

We assume the fluid to be inviscid and incompressible, and we neglect surface tension and the presence of air (see subsection 1.4.1). Then the fluid flow is governed by equations (1.4) – (1.9) and (3.1). We only consider the impact stage from the initial touchdown of the plate with the fluid until the turnover region reaches the right edge of the plate. The impact stage is completed before $t' = \varepsilon L/V$ when the entire plate is below the initial equilibrium position of the free surface. Note that during the impact stage the length of wetted region

(without the jet) is of order L . This lengthscale is much larger than the vertical displacement of the body, which is of order εL . We use the following scalings of x' , y' and t' :

$$x' = Lx, \quad y' = Ly, \quad t' = \frac{\varepsilon L}{V}t, \quad (3.2)$$

where we drop the primes for the corresponding non-dimensional variables.

During the impact stage the free-surface elevation from the equilibrium position, $y' = \eta'(x', t')$, is of the same order as the vertical displacement of the body, which is of order εL . For convex shaped bottoms without sharp edges this can be explained by the fact that the free-surface elevation during impact is above its equilibrium position and below the surface of the impacting body: $0 \leq \eta'(x', t') \leq \omega'(x', t')$. For the impact of an inclined plate, a splash occurs behind the sharp edge, with the free surface elevation being much larger than εL in the splash region for small inclination angles of the plate. However, this splash is localised at the initial penetration point and is shown to be thin in Iafrati and Korobkin (2004). The horizontal extent of the splash region is of the order $(Vt'/L)^{2/3}L$ which is much smaller than the lengthscale L during the stage of impact. In Faltinsen and Semenov (2008), the free surface elevation in the splash region is of order εL for plates with inclination angle $\varepsilon \geq 5^\circ$. For the global flow, we scale the free-surface elevation and the vertical displacement as

$$\eta' = \varepsilon L \eta, \quad \omega' = \varepsilon L \omega. \quad (3.3)$$

Accordingly, the non-dimensional shape of the body surface and the position of the free surface are given by $y = \varepsilon \omega(x, t)$ and $y = \varepsilon \eta(x, t)$, respectively.

We use the following scaling for the velocity potential $\varphi'(x', y', t')$, since the fluid velocity can be estimated by the impact speed of the plate into water, V :

$$\varphi' = VL\varphi. \quad (3.4)$$

The flow velocity is much larger than V in the splash region close to the sharp edge of the plate, in the turnover region and in the jet developed in the turnover region. However, Wagner (1932) and Howison et al. (1991) showed for the problem of a wedge with small deadrise angle impacting the free surface that the size of the turnover region and the thickness of the jet are small. The scaling of the pressure $p'(x', y', t')$ in the fluid is provided by Bernoulli's equation (1.2):

$$p' = \varepsilon^{-1} \rho_F V^2 p. \quad (3.5)$$

Let us assume that the fluid occupies the region $(x', y') \in \Omega'(t')$ at time t' . The fluid is in contact with the body along $D'_S(t')$ and the part of the boundary given by the free surface is denoted $D'_F(t')$ as defined in section 1.4. Then equations (1.4), (1.6) – (1.9) can be written

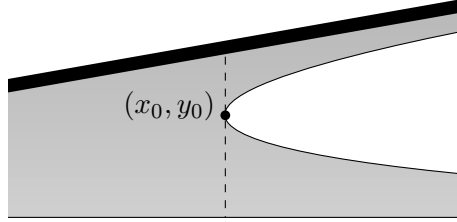


Figure 3.3: The turnover region of the fluid, where a thin low-pressure jet is thrown off. The position of the bend in the turnover region, (x_0, y_0) , is marked by a black dot.

in the following non-dimensional form with respect to the scalings in (3.2) – (3.5):

$$\nabla^2 \varphi = 0 \quad ((x, y) \in \Omega), \quad (3.6)$$

$$\varphi_y = \omega_t + \varepsilon \omega_x \varphi_x \quad ((x, y) \in D_S), \quad (3.7)$$

$$\varphi_y = \eta_t + \varepsilon \eta_x \varphi_x \quad ((x, y) \in D_F), \quad (3.8)$$

$$\varphi_t = -\frac{\varepsilon}{2} (\varphi_x^2 + \varphi_y^2) - \frac{\varepsilon}{\text{Fr}^2} y \quad ((x, y) \in D_F), \quad (3.9)$$

$$\varphi(x, y, t) \rightarrow 0 \quad (x^2 + y^2 \rightarrow \infty), \quad (3.10)$$

where the Froude number in equation (3.9) is defined as $\text{Fr} = V/\sqrt{gL}$. The initial conditions for the system (3.6) – (3.10) are

$$\eta \equiv 0, \quad \varphi \equiv 0 \quad (t = 0). \quad (3.11)$$

Once φ and η have been determined, we obtain the hydrodynamic pressure by Bernoulli's equation (1.5), which is in non-dimensional form

$$p = -\varphi_t - \frac{\varepsilon}{2} (\varphi_x^2 + \varphi_y^2) - \frac{\varepsilon}{\text{Fr}^2} y \quad ((x, y) \in \Omega). \quad (3.12)$$

Note that the solution of the unknown functions φ and η depend on the parameter ε . We will consider the problem (3.6) – (3.11) in the leading order for $\varepsilon \rightarrow 0$.

Equations (3.6) – (3.12) have been analysed for the model problem of a wedge entering the fluid at constant speed. This problem is also self-similar and can be reduced to a single nonlinear integral equation (see e.g. Dobrovol'skaya, 1969). Fraenkel and McLeod (1997) showed for the impact of a wedge that the limit of φ , η and p in (3.6) – (3.12) exists for $\varepsilon \rightarrow 0$. For small ε the jets thrown off at the two turnover-regions are thin and have low pressure. Wagner (1932) and Howison et al. (1991) showed that the thicknesses of the spray jets and the size of the turnover regions are proportional to ε^2 for small ε . Numerical calculations (e.g. Zhao and Faltinsen, 1993) and experiments (e.g. Greenhow, 1987) confirm for the impact of a wedge that the size of the turnover region is very small and the jet is very thin for small deadrise angles. Hence, the contribution of the jet onto the hydrodynamic loads acting on the plate is negligible for small deadrise angle. We define the point $(x_0(t), y_0(t))$ to be the turnover point on the free surface, where $\eta_x(x_0(t), t) = -\infty$ (see Figure 3.3). The analysis described in Wagner (1932) and Howison et al. (1991) suggests that this point approaches

the surface of the wedge as $\varepsilon \rightarrow 0$, such that for fixed non-dimensional time t we obtain

$$\eta(x_0, t) - \omega(x_0, t) \rightarrow 0 \quad (\varepsilon \rightarrow 0). \quad (3.13)$$

However, a strict justification of (3.13) has not been done yet. The limit in (3.13) as $\varepsilon \rightarrow 0$ was exploited by Wagner (1932) to determine the position of the turnover region within the linearised hydrodynamic model, which is derived in the next subsection for the impact of an inclined plate.

We distinguish between an outer region where equations (3.6) – (3.10) can be linearised in the leading order for small ε , and inner regions where the leading order analysis breaks down. The problem in the outer region will be discussed for the impact of an inclined plate in the next subsection. In an a posteriori analysis it will be shown that the inner regions are very localised in a zone close to the initial penetration point and at the turnover region including the jet. An inner solution for the turnover region will be given in subsection 3.1.5. An inner solution of the splash at the initial penetration point and of the jet region will not be discussed in this thesis.

3.1.2 The linearised hydrodynamic problem

In this subsection, we derive the linearised hydrodynamic problem in the outer region and introduce Wagner's condition. We only consider impact speeds where the Froude number Fr satisfies

$$\frac{\varepsilon}{\text{Fr}^2} = O(1). \quad (3.14)$$

It follows that the hydrostatic term in equation (3.9) is of order ε . The hydrostatic term in Bernoulli's equation (3.12) is only of order ε in the part of the fluid domain where $y = O(\varepsilon)$. In the outer region, we expand the velocity potential, $\varphi = \varphi_0 + \varepsilon\varphi_1 + O(\varepsilon^2)$, the free surface elevation, $\eta = \eta_0 + \varepsilon\eta_1 + O(\varepsilon)$, the body displacement $\omega = \omega_0 + \varepsilon\omega_1 + O(\varepsilon^2)$, and the hydrodynamic pressure $p = p_0 + \varepsilon p_1 + O(\varepsilon^2)$ as asymptotic series in terms of ε . In the leading order for small ε the boundary conditions (3.7) – (3.9) are linearised. Since the non-dimensional free-surface elevation is of order ε , we can project the linearised boundary conditions and the wetted part of the body onto the equilibrium position of the free surface, $y = 0$. Equations (3.6), (3.7), (3.9) and (3.10) together with (3.1) form the following mixed boundary value problem in terms of the velocity potential $\varphi_0(x, y, t)$ (see Figure 3.4):

$$\nabla^2 \varphi_0 = 0 \quad (y < 0), \quad (3.15)$$

$$\varphi_{0y} = -1 \quad (y = 0, 0 < x < d), \quad (3.16)$$

$$\varphi_{0t} = 0 \quad (y = 0, x < 0 \text{ and } x > d), \quad (3.17)$$

$$\varphi_0 \rightarrow 0 \quad (x^2 + y^2 \rightarrow \infty). \quad (3.18)$$

Within this model, the thin jet formed in the turnover region is not taken into consideration. The jet belongs to the inner flow and the parameters of this jet can be determined after the flow in the outer region has been obtained (see Howison et al., 1991). Equations (3.15) – (3.18) are written for impact problems, where the region in contact with the moving plate

corresponds to the interval $0 \leq x \leq d$ on $y = 0$. Throughout the thesis we will call the region $0 \leq x \leq d$, $y = 0$ the ‘contact region’ or the ‘wetted part of the plate’, although we are aware that the fluid in the problem (3.6) – (3.10) is also in contact with the body in the jet region. In some literature $0 \leq x \leq d$, $y = 0$, is also called the ‘contact set’ (see e.g. Howison et al., 1997). The point $x = 0$, $y = 0$, corresponds to the left edge of the plate, and $x = d$, $y = 0$, corresponds to the turnover region in the jet (see Figure 3.2). These two points are called the ‘contact points’. The point $x = d$, $y = 0$, whose position is not prescribed, is also known as a ‘free point’ (Howison et al., 1997).

Since the plate moves downwards and the free surface piles up in front of the turnover region, we expect the contact region to grow, so that $\dot{d} > 0$. Hence, integrating equation (3.17) in time, using the initial condition (3.11) for φ , and differentiating with respect to x leads to (see Figure 3.4):

$$\varphi_{0x} = 0 \quad (y = 0, x < 0 \text{ and } x > d). \quad (3.19)$$

Note that time-derivatives of φ_0 are not involved in the problem (3.15), (3.16), (3.18), (3.19), so that d is here only a parameter. The uniqueness of the solution (3.15), (3.16), (3.18), (3.19) for a given d is obtained by demanding that the kinetic energy in the fluid is finite (Wilson, 1991; Oliver, 2002):

$$\frac{1}{2} \int_{\{y < 0\}} (\varphi_{0x}^2 + \varphi_{0y}^2) \, dV < \infty. \quad (3.20)$$

The non-dimensional energy on the left-hand side of (3.20) is scaled by $\rho_F V^2 L^2$. This term only accounts for the kinetic energy in the fluid bulk, which is the fluid domain without the jet region. The energy in the bulk and jet will be calculated later in subsection 3.1.5.

The position $x = d$ cannot be determined by the linearised problem (3.15) – (3.18). The x -position of the contact point, $x = d$, is defined as the limit of the x -position of the turnover point $x = x_0$ (see Figure 3.3) as ε tends to zero. It follows from (3.13) that the position of the free surface is equal to the position of the body at $x = d$ as $\varepsilon \rightarrow 0$:

$$\eta_0(d, t) = d - t. \quad (3.21)$$

Condition (3.21) was first introduced in Wagner (1932) and is also known as Wagner’s condition. The free surface elevation η_0 in equation (3.21) is obtained from equations (3.8) and (3.11):

$$\eta_{0t} = \varphi_{y0} \quad (y = 0, x < 0 \text{ and } x > d), \quad (3.22)$$

$$\eta_0 \equiv 0 \quad (t = 0). \quad (3.23)$$

Note that it follows from (3.21) and (3.23) that $d(0) = 0$, which implies together with equations (3.6) – (3.10) that $\varphi_0 \equiv 0$ for $t = 0$. The leading order hydrodynamic pressure p_0 is obtained from Bernoulli’s equation (3.12):

$$p_0 = -\varphi_{0t} + \frac{\varepsilon}{\text{Fr}^2} y \quad (y \leq 0). \quad (3.24)$$

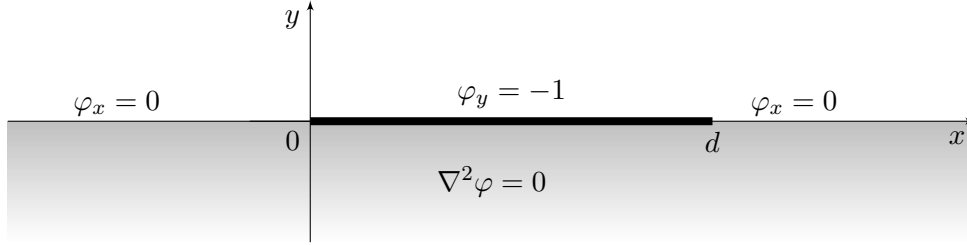


Figure 3.4: Mixed boundary value problems on the lower half plane

Note that for the region $d_1 < x < d_2$, $y = 0$, corresponding to the wetted part of the body, the hydrostatic term in equation (3.24) is zero. In the following we skip the indices in φ_0 , η_0 and p_0 .

The equations (3.15) – (3.24) give us an asymptotic solution of the impact problem in the outer region. The solution of the problem (3.15) – (3.24) will be determined in the next two sections. Even though the hydrodynamic problem is linearised, the problem (3.15) – (3.20) is nonlinear due to Wagner’s condition (3.21). Note that no condition is needed at the left edge of the plate. A condition at this edge would be necessary if the impact were oblique, as will be shown in chapter 4.

3.1.3 The MBVP in terms of the complex velocity

In this subsection, we solve the linearised hydrodynamic problem (3.15) – (3.18) in order to determine the fluid flow and the hydrodynamic pressure. However, the position of the forward contact point, $x = d$, appears as a unknown parameter here, which will be determined in the next subsection.

Since $\varphi(x, y, t)$ satisfies the far-field condition (3.18) there exists a stream function $\psi(x, y)$, such that the so-called complex velocity potential

$$F_t(z, t) = \varphi(x, y, t) + i\psi(x, y, t), \quad z = x + iy, \quad (3.25)$$

is analytic in z for $y < 0$ (see Lang (1993), p. 254) and satisfies the far-field condition $F_t(z, t) \rightarrow 0$ as $x^2 + y^2 \rightarrow \infty$. The index t in $F_t(z, t)$ denotes the time-derivative of the complex displacement potential $F(z, t)$, which will be introduced in the next section. The function $F_t(z, t)$ can be analytically extended onto the complex plane with a cut at $x \leq d \leq 1$, $y = 0$. Hence, the far-field behaviour of $F_t(z, t)$ is given by a MacLaurin series. Since $\text{Re}(F_t(x - i0, t)) = 0$ for $x < 0$, $y = 0$, and $x > d$, $y = 0$ (see equation (3.19)), the behaviour of $F_t(z, t)$ in the far-field is

$$F_t(z, t) = iA(t)z^{-1} + O(z^{-2}) \quad (|z| \rightarrow \infty), \quad (3.26)$$

where A is a real-valued function depending only on time. It will be shown later that $A(t) \neq 0$ for $t > 0$. The complex velocity $f_t(z, t) = \varphi_x(x, y, t) - i\varphi_y(x, y, t)$, which is the z -derivative of the complex potential $F_t(z, t)$, is also analytic on the lower half plane with the far-field behaviour

$$f_t(z, t) = -iA(t)z^{-2} + O(z^{-3}) \quad (|z| \rightarrow \infty). \quad (3.27)$$

Since the kinetic energy in the fluid is finite (see condition (3.20)), the solution $f_t(z, t)$ has no poles. Then the solution of the problem (3.15) – (3.18) is given by the solution (2.14) for $k_1 = 0$, $k_2 = 0$, $l_0 = 1$, $b_0(t) = 1$ leading to

$$f_t(z, t) = i \left(1 - \frac{a_1(t)z + a_0(t)}{\sqrt{z(z-d)}} \right), \quad (3.28)$$

where a_0 and a_1 are determined by condition (3.27). We obtain $a_0(t) = -\frac{1}{2}\dot{d}(t)$ and $a_1(t) \equiv 1$. Eigensolutions of the problem (3.15) – (3.18) are not included in (3.28), because they have stronger singularities at the contact points $x = 0$ and $x = d(t)$, which are not permitted by condition (3.20). Note that $f_t(z, t)$ has square-root singularities at $z = 0$ and $z = d$. This confirms that the linearised hydrodynamic problem (3.15) – (3.18) breaks down at these points. Due to the weak singularities of $f_t(z, t)$, the complex velocity potential $F_t(z, t)$ is continuous at 0 and d . By integrating $f_t(z, t)$ in z and by taking into account, that $F_t(z, t) \rightarrow 0$ as $z \rightarrow \infty$ we obtain

$$F_t(z, t) = -i \left(-z + \frac{d}{2} + \sqrt{z(z-d)} \right). \quad (3.29)$$

By differentiating $F_t(z, t)$ in time we obtain $F_{tt}(z, t) = \varphi_t + i\psi_t$ where

$$F_{tt}(z, t) = -\frac{i}{2}\dot{d} \left(1 - \sqrt{\frac{z}{z-d}} \right). \quad (3.30)$$

The real part of $F_{tt}(z, t)$ in the contact region, together with the linearised Bernoulli equation (3.24), give us the hydrodynamic pressure acting on the plate:

$$p(x, 0, t) = \frac{\dot{d}}{2} \sqrt{\frac{x}{d-x}} \quad (0 < x < d). \quad (3.31)$$

In particular, equation (3.31) shows that the dimensional pressure on the underside of the plate decreases to atmospheric value as the square-root of the distance from the sharp left edge. At the contact point $x = d$, $y = 0$, the pressure is square-root singular, with the horizontal velocity of the right contact point as a factor. This characteristic behaviour will be also observed in other impact problems in this thesis. The non-dimensional vertical hydrodynamic force acting on the plate, $\mathcal{F}(t) = \int_0^d p(x, 0, t) dx$ and the moment about the left edge $\mathcal{M}(t) = \int_0^d xp(x, 0, t) dx$ are given by

$$\mathcal{F}(t) = \frac{\pi}{4}\dot{d}d, \quad \mathcal{M}(t) = \frac{3\pi}{16}\dot{d}d^2. \quad (3.32)$$

In the next section, the position of the contact point $x = d$ and the free surface elevation are determined using Wagner's condition (3.21) and reformulating (3.15) – (3.18) in terms of the displacement potential.

3.1.4 The MBVP in terms of the displacement potential

To employ Wagner's condition (3.21), we need to know the free surface elevation $\eta(x, t)$. We could evaluate $\eta(x, t)$ by using $\varphi_y(x, 0, t)$ given by the imaginary part of $f_t(z, t)$ in (3.28) and integrating the kinematic boundary condition (3.22) with respect to t . However, it is more convenient to find the free surface by introducing the displacement potential $\Phi(x, y, t)$

defined by (see Korobkin, 1982)

$$\Phi(x, y, t) = \int_0^t \varphi(x, y, \tau) d\tau \quad (y < 0). \quad (3.33)$$

Integrating the kinematic boundary condition (3.22) in time and using $\eta(x, 0) \equiv 0$, the free surface elevation is given by

$$\eta(x, t) = \Phi_y(x, 0, t) \quad (x < 0 \text{ and } x > d). \quad (3.34)$$

To obtain $\Phi(x, y, t)$ we reformulate the hydrodynamic problem (3.15) – (3.18) with respect to this potential (see Howison et al., 1991). Integrating the body boundary condition (3.16) in time, using Wagner’s condition (3.21) and equation (3.34) we obtain

$$\Phi_y(x, 0, t) = \int_0^{G(x)} \eta_t(x, \tau) d\tau + G(x) - t = x - t, \quad (3.35)$$

where $t = G(x)$ is the time when $d(t) = x$. In (3.35) we also used the assumption that $\dot{d} > 0$. Equations (3.34) and (3.35) show that the derivative $\Phi_y(x, 0, t)$ provides the component of vertical displacement of a liquid particle. In general $(\Phi_x(x, y, t), \Phi_y(x, y, t))$ describes the displacement of a liquid particle from its initial position. For large enough $|z|$, the velocity potential $\varphi(x, y, t)$ is bounded by

$$|\varphi(x, y, t)| \leq |F_t(z, t)| = \frac{d^2}{4|z - \frac{d}{2} + \sqrt{z(z-d)}|} \leq \frac{d^2}{2|z|} \quad (|z| > d, y < 0), \quad (3.36)$$

where $F_t(z, t)$ is given by (3.29). The inequality (3.36) implies the following far-field behaviour of Φ :

$$|\Phi(x, y, t)| \leq t \max_{\tau \in [0, t]} |\varphi(x, y, \tau)| \leq \frac{td(t)^2}{2|z|}. \quad (3.37)$$

By integrating equations (3.15) and (3.19) in time, together with equation (3.35) and the far-field condition (3.37), we obtain the following mixed boundary value problem in terms of the displacement potential:

$$\nabla^2 \Phi = 0 \quad (y < 0), \quad (3.38)$$

$$\Phi_y = x - t \quad (y = 0, 0 < x < d), \quad (3.39)$$

$$\Phi_x = 0 \quad (y = 0, x < 0 \text{ and } x > d), \quad (3.40)$$

$$\Phi = O((x^2 + y^2)^{-1/2}) \quad (x^2 + y^2 \rightarrow \infty). \quad (3.41)$$

We define the complex displacement $f(z, t) = \Phi_x(x, y, t) - i\Phi_y(x, y, t)$. The time derivative of $f(z, t)$ is the complex velocity $f_t(z, t)$. Now, $\Phi(x, y, t)$ satisfies condition (3.41), we have assumed $\dot{d} > 0$, and $f_t(z, t)$ is square-root singular at $z = 0$ and $z = d$, so it follows that

$$f(z, t) = O(z^{-1/2}) \quad (z \rightarrow 0), \quad (3.42)$$

$$f(z, t) = O(1) \quad (z \rightarrow d), \quad (3.43)$$

$$f(z, t) = O(z^{-2}) \quad (|z| \rightarrow \infty). \quad (3.44)$$

We seek the solution $f(z, t)$ satisfying the conditions (3.38) – (3.44). The solution is given by equation (2.14) with $k_1 = 0$, $k_2 = -1$, $l_0 = 2$, $b_0(t) = -t$, $b_1(t) = 1$, so that we obtain

$$f(z, t) = i \left(-z + t - \sqrt{\frac{z-d}{z}} \left(-z + \frac{t}{3} \right) \right), \quad (3.45)$$

$$d(t) = \frac{4}{3}t, \quad (3.46)$$

where the position of the contact point is determined by equation (3.46) to guarantee that $f(z, t)$ in (3.45) satisfies the far-field condition (3.44). Hence, the position of the contact point $x = d(t)$ increases linearly in time, which is obvious due to the self-similarity of the problem. Equation (3.46) confirms that $x = d(t)$ is beyond $x = t$. Note that $x = t$ is the intersection between the initial position of the free surface and the plate surface, which was introduced as the endpoint of the contact region by von Karman (1929). Substituting equation (3.46) into (3.28), (3.31) and (3.32) provides explicit solutions of the fluid flow, the hydrodynamic pressure along the contact region, the vertical hydrodynamic force and the moment.

The free surface elevation of the fluid is given by the real part of $f(z, t)$ in equation (3.45) according to (3.34):

$$\eta(x, t) = x - t - \sqrt{\frac{x - \frac{4}{3}t}{x}} \left(x - \frac{t}{3} \right) \quad (x < 0 \text{ and } x > \frac{4}{3}t) \quad (3.47)$$

where d in (3.46) has been substituted. Equation (3.47) together with $\omega(x, t) = x - t$ verifies the continuity of the fluid boundary at $x = d$ as required by Wagner's condition (3.21). However, the present linearised hydrodynamic model leads to a singular free-surface elevation at $x = 0$. Note that the free surface elevation given by equation (3.47) is the outer solution and is obtained without any further conditions at the left contact point $x = 0$, $y = 0$. However, an inner solution of the splash region needs to satisfy a tangential detachment of the fluid from the left edge of the plate as it was done in Iafrati and Korobkin (2004) and Faltinsen and Semenov (2008). We will give a brief discussion of the inner solution in the splash region in subsection 3.1.6.

The functions $\eta(x, t)$, $\varphi(x, y, t)$ and $p(x, y, t)$ in equations (3.47), (3.29) and (3.31) can be written in the self-similar forms $\eta^*(x^*) = \eta/t$, $\varphi^*(x^*, y^*) = \varphi/t$, $p^*(x^*, y^*) = p$ where $x^* = x/t$, $y^* = y/t$. Moreover, we confirm that the non-dimensional functions $\eta(x, t)$, $p(x, y, t)$, $\varphi(x, y, t)$ are of order 1 on the lower half plane except close to the origin, where the plate penetrates the fluid initially, and except close to $x = d(t)$, $y = 0$. An inner solution for the turnover region corresponding to $x = d(t)$, $y = 0$, will be presented in the next subsection.

3.1.5 Inner solution in the jet region

In this section we consider the flow in the turnover region. During the early stage of impact the flow in the turnover region can be approximated by a quasi-steady Kelvin-Helmholtz cavity flow as shown in Howison et al. (1991) and Oliver (2002) (see Figure 3.5). We introduce the inner variables $\tilde{x} = (x - d)/\varepsilon^2$, $\tilde{y} = (y - \varepsilon\omega(d, t))/\varepsilon^2$ and the inner velocity potential $\tilde{\varphi}(\tilde{x}, \tilde{y}) = \varepsilon^{-1}\varphi(x, y)/\dot{d} - \tilde{x}$, where here $\varphi(x, y)$ corresponds to the quasi-steady solution of the

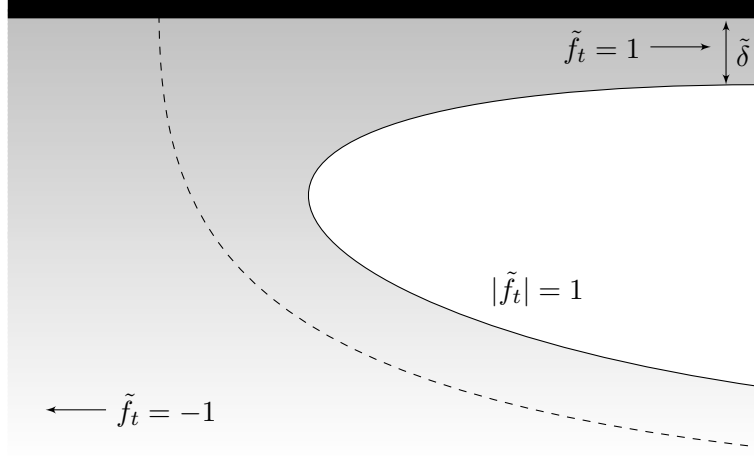


Figure 3.5: Kelvin-Helmholtz cavity flow as inner flow region with a free stream flow velocity $\tilde{f}_t = -1$. The flow in the jet in the far-field is $\tilde{f}_t = 1$. The jet has thickness $\tilde{\delta}$. The dashed curve is the dividing stream line.

nonlinear hydrodynamic problem (3.6) – (3.10) in the turnover region. The inner complex velocity is defined by $\tilde{f}_t = \tilde{\varphi}_x - i\tilde{\varphi}_y$. Then the free stream velocity for the cavity flow is $\tilde{f}_t = -1$ and the velocity in the jet tends to $\tilde{f}_t = 1$. The speed of the fluid on the free surface is 1. A solution of the Kelvin-Helmholtz flow can be obtained using the hodograph method (see Birkhoff and Zarantonello, 1957). The inner complex potential of the nonlinear flow, $\tilde{F}_t = \tilde{\varphi} + i\tilde{\psi}$, where $\tilde{\psi}$ is the stream function, is given by

$$\tilde{F}_t = -\frac{\tilde{\delta}}{\pi} \left(\frac{4\tilde{f}_t}{(\tilde{f}_t + 1)^2} + \log \left[\left(\frac{1 - \tilde{f}_t}{1 + \tilde{f}_t} \right)^2 \right] \right). \quad (3.48)$$

Here $\tilde{f}_t = \tilde{\varphi}_x - i\tilde{\varphi}_y$ is the complex velocity and $\tilde{\delta}$ is the thickness of the jet (see Figure 3.5). Equation (3.48) shows that $\tilde{F}_t = 0$ at the stagnation point. The point $\tilde{z} = \tilde{x} + i\tilde{y}$, where the fluid has the complex velocity \tilde{f}_t , is given by the following complex integral

$$\tilde{z} = \int_0^{\tilde{f}_t} \frac{1}{\omega} \frac{d\tilde{F}_t}{d\tilde{f}_t} d\omega = -\frac{\tilde{\delta}}{\pi} \left(4 \frac{\tilde{f}_t + 2}{(\tilde{f}_t + 1)^2} + \log \left[\left(\frac{1 - \tilde{f}_t}{1 + \tilde{f}_t} \right)^2 \right] - 8 \right). \quad (3.49)$$

The pressure in the inner region is given by $\tilde{p} = \frac{1}{2}(1 - |\tilde{f}_t|^2)$, where the pressure in the inner region is scaled by $\tilde{p} = \varepsilon p/d^2$. It follows from equation (3.49) that the complex velocity in the jet behaves as $\tilde{f}_t(\tilde{z}) - 1 \sim -2e^{-\pi\tilde{z}/(2\tilde{\delta})+5/2}$ as $\tilde{x} \rightarrow \infty$, $-\tilde{\delta} \leq \tilde{y} \leq 0$. Hence, the hydrodynamic pressure in the jet along the plate decays exponentially to zero as \tilde{x} increases. This confirms that the forces on the plate in the forward jet are negligible.

Equation (3.49) also implies that the complex velocity in the far-field of the inner region, $|\tilde{z}| \rightarrow \infty$, $\tilde{y} \leq 0$ (excluding the jet branch) is

$$\tilde{f}_t(\tilde{z}) = -1 - 2i\sqrt{\frac{\tilde{\delta}}{\pi\tilde{z}}} + O\left((- \tilde{z})^{-3/2}\right) \quad (|\tilde{z}| \rightarrow \infty, \tilde{y} < 0), \quad (3.50)$$

where the square-root is positive when its argument is a positive real number. We introduce the intermediate region where the variables $\hat{x} = \varepsilon\tilde{x}$ and $\hat{y} = \varepsilon\tilde{y}$ are of order 1. In this region,

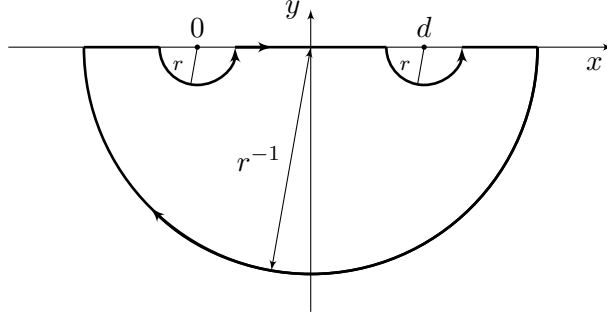


Figure 3.6: The contour C_r .

we compare equation (3.50) with the outer flow velocity given by equation (3.28). Matching their leading order terms determines the jet thickness (see Howison et al., 1991; Oliver, 2002)

$$\delta = \varepsilon^2 \frac{\pi t}{16} \quad (3.51)$$

where $\delta = \varepsilon^2 \tilde{\delta}$ is the jet thickness in the scaling of the outer region. Equation (3.51) confirms that the thickness of the jet is proportional to ε^2 .

It is well known that the law of energy conservation is not satisfied within the classical Wagner theory if the kinetic energy of the jet is not accounted for (see Scolan and Korobkin, 2003). The jet energy is not small and can be determined within our local analysis of the flow in the turnover region. In the problem of the vertical water entry of a sphere at constant speed, Cointe et al. (2004) showed that half of the work done by the sphere on the fluid is expressed in the spray jet and the other half is the kinetic energy of the bulk of the fluid domain. The corresponding two-dimensional problem of a parabolic body entering water at constant speed was investigated by Korobkin (1994), who arrived at the same equipartition of energy.

The non-dimensional jet velocity in the reference frame moving with the turnover region is \dot{d} , so the jet velocity in the global frame of reference xOy is $2\dot{d}$, hence the energy flux in the jet is (see Cointe et al., 2004):

$$\frac{d}{dt} E_{\text{jet}} = \frac{1}{2} \delta \times \dot{d} \times (2\dot{d})^2 = 2\delta \dot{d}^3. \quad (3.52)$$

For the impact of an inclined plate onto the water surface at constant speed, δ is given by equation (3.51), so that we obtain the jet energy $E_{\text{jet}} = \frac{\pi}{9} t^2$. By using equation (3.15) and the divergence theorem on a contour C_r shown in Figure 3.6 and by letting $r \rightarrow 0$, the kinetic energy of the fluid bulk (excluding that in the jet) can be written as

$$E_{\text{bulk}} = \frac{1}{2} \int_{y < 0} (\varphi_x^2 + \varphi_y^2) dV = \frac{1}{2} \int_0^d \varphi(x, 0, t) \varphi_y(x, 0, t) dx. \quad (3.53)$$

Substituting equation (3.16) and the velocity potential $\varphi(x, 0, t)$, given by equation (3.29), into (3.53) leads to $E_{\text{bulk}} = \frac{\pi}{9} t^2$. Hence, the energy in the fluid bulk is equal to the kinetic energy transferred into the jet. It can be shown that the equipartition of kinetic energy holds for vertical impact of general shaped bodies of small deadrise angle, $y = \varepsilon \omega(x, t)$, if $\omega_{tt} \equiv 0$ is satisfied at any time t . Since the vertical speed of the inclined plate is -1 , the

non-dimensional work, which has been done by the plate onto the fluid is

$$W = \int_0^t \mathcal{F} dt = \frac{2\pi}{9} t^2, \quad (3.54)$$

where the force \mathcal{F} is given by (3.32). This confirms the conservation of energy in the linearised hydrodynamic model:

$$W = E_{\text{jet}} + E_{\text{bulk}}. \quad (3.55)$$

Equation (3.55) shows that in the leading order for small ε there is no additional source of energy in the splash. This is due to the fact that the contact point is fixed at $x = 0, y = 0$ implying a square-root behaviour of the pressure at this point. However, the fluid velocity is inverse-square-root singular at the origin indicating a significant amount of fluid kinetic energy in this region, which we discuss in the next subsection.

3.1.6 The flow in the splash region

We start with quantifying the fluid kinetic energy close to the origin. We define Ω_r as the lower half of the disk around the origin with radius r . It can be shown using Reynolds transport theorem that, in the leading order for small ε , the time-derivative of the kinetic energy in Ω_r is given by

$$\frac{d}{dt} E_{\text{kin}}^{(r)}(t) = \int_{\partial\Omega_r} p \varphi_n ds \quad (3.56)$$

where φ_n is the fluid speed normal to $\partial\Omega_r$. It follows from equations (3.28) and (3.30) that $E_{\text{kin}}^{(r)} \sim \frac{\pi}{6} r t$ as $r \rightarrow 0$. For example we obtain the energy $E_{\text{kin}}^{(0.1)}(0.5) = 0.026$, which is about 15% of the total kinetic energy in the fluid.

The presence of an inverse-square-root singularity in $f_t(z, t)$ at $z = 0$ indicates the existence of an inner region, whose solution describes the local flow structure. Note that during the impact stage, when $0 < d(t) < 1$, the nonlinear hydrodynamic problem (3.6) – (3.10) is self-similar. Hence, the inner flow in the splash region has to be described by the fully nonlinear problem which has been solved by Faltinsen and Semenov (2008) exploiting the self-similarity. They showed that the contour of the splash has a corner point moving along the y -axis. The speed of the corner point is of the same order as the speed of the plate for $\varepsilon \geq 5^\circ$. However, for plates with almost zero inclination angle ε , say where $\sqrt{\varepsilon} \ll 1$, the flow structure of the splash region is roughly given by the vertical impact of a rigid horizontal plate after the plate is fully wetted. Here we only outline the ideas in Iafrati and Korobkin (2004) for obtaining a local solution. In order to derive a local formulation of the problem at the left plate edge, we introduce the stretched non-dimensional variables

$$t' = \frac{L}{V} \tau, \quad x' = L\tau^{2/3} u, \quad y' = L\tau^{2/3} v, \quad \phi' = LV\tau^{1/3} \phi, \quad \eta' = L\tau^{2/3} \zeta. \quad (3.57)$$

Substituting the scalings (3.57) into the nonlinear problem (1.4), (1.6) – (1.8), we find close

to the left edge

$$\nabla^2 \phi = 0 \quad \text{in the fluid,} \quad (3.58)$$

$$\phi_v = -\tau^{1/3} \quad (y = -\tau^{1/3}, u > 0), \quad (3.59)$$

$$\phi_v = \frac{2}{3}\zeta + \tau\zeta_\tau - \frac{2}{3}\zeta_u u + \zeta_u \phi_v \quad (v = \zeta(u, \tau), u < 0), \quad (3.60)$$

$$\frac{1}{3}\phi + \tau\phi_\tau = -\frac{1}{2}(\phi_u^2 + \phi_v^2) + \frac{2}{3}(u\phi_u + v\phi_v) \quad (v = \zeta(u, \tau), u < 0), \quad (3.61)$$

$$\phi \sim -\text{Re}(\sqrt{u+iv}) \quad (u^2 + v^2 \rightarrow \infty). \quad (3.62)$$

Equation (3.62) is obtained by enforcing the matching between the inner solution and the inner limit of the outer solution given by equation (3.28) where we set the wetted length $d = 1$. Here we apply a continuous and tangential detachment of the fluid from the plate which is given by

$$\zeta(0, \tau) = -\tau^{1/3}, \quad \zeta_u(0, \tau) = 0. \quad (3.63)$$

During the initial stage, $\tau \ll 1$, several terms in (3.58) – (3.61) can be neglected in the leading order. In the leading order, all ϕ_τ and ζ_τ vanish for $\tau \rightarrow 0$, implying that ϕ and ζ are approximatively independent of time. However, the analysis of the resulting equations remains difficult. Iafrati and Korobkin (2004) gave numerical results of the leading-order equations and showed the contour of the splash. The jet forming at the left plate edge is detached from the plate surface and its flow direction is approximately vertical upwards at about $u = 0.5$. The jet is of infinite length and it narrows quickly for increasing distance from the origin. Note that the jet forming in the turnover region is of uniform thickness.

3.2 Euler's beam equation and normal modes

In the next section we will model the impact of an elastic plate onto the water surface. Since hydrodynamic loads are very high for small plate inclination ε , the flexibility of the plate plays a significant role in the impact stage. We consider a plate, which has length L and relatively small thickness h , such that $h/L \ll 1$. The plate material has constant density ϱ_S , Young's modulus E and Poisson's ratio ν . The position of the plate at time t is described by the equation $y' = \omega'(x', t')$ for $0 \leq x' \leq L$, which includes both the rigid body motions of the plate and its elastic deflection. For $h/L \ll 1$ the rigid and elastic body motion can be modelled by Euler's beam equation as long as $\omega'_{x'}(x', t')$ is small for $0 < x' < L$ (see Donnell (1976)). Here Euler's beam equation is formulated as

$$\varrho_S h \frac{\partial^2 \omega'}{\partial t'^2} + D \frac{\partial^4 \omega'}{\partial x'^4} = q'(x', t') \quad (0 < x' < L), \quad (3.64)$$

where $D = Eh^3/(12(1 - \nu^2))$ is the flexural rigidity and $q'(x', t')$ is the pressure acting on the underside of plate at time t' . Equation (3.64) is written in the coordinate system with the longitudinal coordinate along the plate being approximated as x' , which is correct in the leading order for small inclinations of the plate. Only the bending stresses and the normal shear forces are taken into consideration in Euler's beam model in (3.64). The vertical forces due to plate bending in equation (3.64), $D \frac{\partial^4 \omega'}{\partial x'^4}$, are obtained by the x' -derivative of the

vertical shear stresses in the plate, S' . These shear stresses are given in terms of the bending moment, M' , by

$$S' = \frac{\partial M'}{\partial x'}, \quad \text{where} \quad M' = D \frac{\partial^2 \omega'}{\partial x'^2}. \quad (3.65)$$

The plate model (3.64) has also been used in the wave impact onto an elastic plate in Kvåsvold and Faltinsen (1993), Korobkin (1998) and Korobkin and Khabakhpasheva (2006) where the ends of the plate were simply supported. Here the ends of the plate are modelled to be free of stresses and moments, so equation (3.64) is subject to the free-free boundary conditions

$$\frac{\partial^2 \omega'}{\partial x'^2}(x', t') = \frac{\partial^3 \omega'}{\partial x'^3}(x', t') = 0 \quad (x' = 0 \text{ and } x' = L). \quad (3.66)$$

We formulate the problem (3.64) and (3.66) in terms of non-dimensional coordinates given in (3.2), (3.3) and (3.5). Then the position of the plate is $y = \varepsilon \omega(x, t)$ where the plate motion is governed by the non-dimensional problem

$$\mu \frac{\partial^2 \omega}{\partial t^2} + \theta \frac{\partial^4 \omega}{\partial x^4} = q(x, t) \quad (0 \leq x \leq 1), \quad (3.67)$$

$$\frac{\partial^2 \omega}{\partial x^2} = \frac{\partial^3 \omega}{\partial x^3} = 0 \quad (x = 0 \text{ and } x = 1), \quad (3.68)$$

$$\omega(x, 0) = \omega_0(x), \quad \frac{\partial \omega}{\partial t}(x, 0) = \omega_1(x) \quad (0 \leq x \leq 1). \quad (3.69)$$

where $\mu = \rho_S h \rho_F^{-1} L^{-1}$ is a ratio of plate mass and fluid mass below the plate and $\theta = \varepsilon^2 D L^{-3} V^{-2} \rho_F^{-1}$ is the kinematic rigidity. Equations in (3.69) are the initial conditions. The external forces, $q(x, t)$, will be given by the hydrodynamic loads during impact of the plate. Note that they are inverse-square-root singular at the position of the Wagner contact point, $x = d(t)$ (see 3.1). In this case, equation (3.67) is only valid for $0 \leq x < d$ and $d < x \leq 1$ instead of $0 \leq x \leq 1$. Then we further require the conditions

$$[\omega] = [\omega_x] = [\omega_{xx}] = [\omega_{xxx}] = 0, \quad (3.70)$$

where $[\omega] = \lim_{\delta \rightarrow 0} (\omega(d - \delta) - \omega(d + \delta))$. Formulations of Euler's beam equation in the subsequent chapters will be given in the form of (3.67) – (3.69) and we will implicitly assume condition (3.70) wherever we have a inverse-square root singularity in $q(x, t)$. The rigid position of the plate and its elastic deflection can be decomposed into normal modes. The normal modes will be discussed in detail in this section before we consider the impact of an elastic plate into water in the next section.

For $q(x, t) = 0$ solutions of (3.67) and (3.68) are given by $\omega(x, t) = \sigma(t)\psi(x)$ where $\psi(x)$, $0 < x < 1$, is a dry normal mode of a free-free elastic plate and $\sigma(t)$ is the corresponding eigenoscillation. Then a dry normal mode is given by the eigensolution of the boundary value problem

$$\frac{\partial^4 \psi}{\partial x^4} = \nu \psi \quad (0 \leq x \leq 1), \quad (3.71)$$

$$\frac{\partial^2 \psi}{\partial x^2} = \frac{\partial^3 \psi}{\partial x^3} = 0 \quad (x = 0 \text{ and } x = 1), \quad (3.72)$$

where the complex number ν is the corresponding eigenvalue. The eigenoscillation is given by

$$\frac{\partial^2 \sigma}{\partial t^2} = -\frac{\theta}{\mu} \nu \sigma \quad (t \geq 0). \quad (3.73)$$

First we find the dry normal modes given by equations (3.71) and (3.72). Note that we only consider non-trivial solutions $\psi \neq 0$. We understand the fourth derivative in equation (3.71) as an operator $T = \frac{\partial^4}{\partial x^4}$. For sufficiently smooth functions ψ , satisfying the conditions in (3.72), the operator T is self-adjoint and non-negative to the inner product $(\psi, \chi) = \int_0^1 \psi(x) \overline{\chi(x)} dx$. Here $\overline{\chi(x)}$ is the complex conjugate of $\chi(x)$. An operator is self-adjoint if $(T\psi, \chi) = (\psi, T\chi)$ for all considered ψ, χ and is non-negative if $(T\psi, \psi) \geq 0$ for all considered ψ . For a self-adjoint and non-negative operator all eigenvalues have to be real and non-negative. Self-adjointness also implies that eigensolutions corresponding to distinct eigenvalues are orthogonal. For $\nu = 0$ the space of solutions of (3.71) and (3.72) consists of linear polynomials. We choose the two representative modes

$$\psi_0(x) = 1 \quad \text{and} \quad \psi_1(x) = \sqrt{3}(2x - 1), \quad (3.74)$$

which are orthonormal and describe the vertical translation and rotation of the plate, respectively. For $\nu > 0$ the solution of (3.71) can be written as

$$\psi(x) = b_1 \cosh(\lambda x) + b_2 \sinh(\lambda x) + b_3 \cos(\lambda x) + b_4 \sin(\lambda x) \quad (3.75)$$

where $\lambda = \nu^{1/4}$ with constants b_1, b_2, b_3, b_4 to be specified by the boundary conditions in (3.72). An eigensolution $\psi \neq 0$ in (3.75) only satisfies the conditions in (3.72) if λ satisfies the characteristic equation

$$\cosh(\lambda_k) \cos(\lambda_k) = 1 \quad (k \geq 2), \quad (3.76)$$

where we assign λ_k to the interval $(\pi k - \frac{\pi}{2}, \pi k)$ for $k \geq 2$, k even, and to $(\pi(k-1), \pi k - \frac{\pi}{2})$ for $k \geq 3$, k odd. The eigenvalues λ_k in the given intervals are uniquely determined and solutions of (3.76) outside these intervals do not exist. The space of eigensolutions for each λ_k , $k \geq 2$, is one-dimensional and we choose the representation

$$\psi_k(x) = \cosh(\lambda_k x) + \gamma_k \sinh(\lambda_k x) + \cos(\lambda_k x) + \gamma_k \sin(\lambda_k x), \quad (3.77)$$

$$\gamma_k = -\frac{\cosh(\lambda_k) - \cos(\lambda_k)}{\sinh(\lambda_k) - \sin(\lambda_k)}. \quad (3.78)$$

The functions ψ_k in (3.77) are called elastic modes, since they describe the elastic deflection from the rigid plate position. It is shown in appendix A, that the modes $\psi_k(x)$, $k \geq 2$, given by (3.77) and (3.78) are normalised. It follows that the complete set of eigensolutions, $\{\psi_k\}$, given by (3.74) and (3.77) is an orthonormal system, i.e.

$$\int_0^1 \psi_k(x) \psi_l(x) dx = \delta_{kl}, \quad (3.79)$$

where $\delta_{kl} = 1$ for $k = l$ and $\delta_{kl} = 0$ for $k \neq l$. Nariboli (1965) proved that $\{\psi_k\}$ is an

orthonormal basis in the Lebesgue space $L^2(0, 1)$ by converting the expansion of a function $f(x)$ in terms of the normal modes,

$$\sum_{k=0}^{\infty} a_k \psi_k(x), \quad a_k = \int_0^1 \psi_k(x) f(x) dx, \quad (3.80)$$

to a Fourier series of f .

We investigate the behaviour of the eigenvalue λ_k for increasing k . It follows from (3.76) that $\cos(\lambda_k) \rightarrow 0$ as $k \rightarrow \infty$, so that we obtain

$$\lambda_k - \left(\frac{\pi}{2} + \pi k\right) \rightarrow 0 \quad (k \rightarrow \infty). \quad (3.81)$$

Now, we derive a formula for the convergence speed of $\lambda_k - (\pi k - \frac{\pi}{2})$ for even k for $k \rightarrow \infty$. For k even, $\cos(\lambda_k)$ is bounded by the first and third order Taylor-series of $\cos(x)$ about $\pi k - \frac{\pi}{2}$, so that we get the inequalities

$$\lambda_k - \pi k + \frac{\pi}{2} - \frac{1}{6}(\lambda_k - \pi k + \frac{\pi}{2})^3 < \cos(\lambda_k) < \lambda_k - \pi k + \frac{\pi}{2} \quad (\pi(k - \frac{1}{2}) < \lambda_k < \pi k). \quad (3.82)$$

We conclude from the first inequality in (3.82) and from equation (3.76) that

$$\begin{aligned} (\lambda_k - \pi k + \frac{\pi}{2})e^{\pi k} &= \cos(\lambda_k)e^{\pi k} + (\lambda_k - \pi k + \frac{\pi}{2} - \cos(\lambda_k))e^{\pi k} \\ &\leq \frac{e^{\pi k}}{\cosh(\lambda_k)} + \frac{1}{6}(\lambda_k - \pi k + \frac{\pi}{2})^3 e^{\pi k}. \end{aligned} \quad (3.83)$$

Rearranging (3.83) and using (3.81) provides

$$(\lambda_k - \pi k + \frac{\pi}{2})e^{\pi k} \leq \frac{e^{\pi k}}{[1 - \frac{1}{6}(\lambda_k - \pi k + \frac{\pi}{2})^2] \cosh(\lambda_k)} \rightarrow 2e^{\pi/2} \quad \text{as } k \rightarrow \infty. \quad (3.84)$$

Using the second inequality in (3.82) and the characteristic equation (3.76) we obtain

$$(\lambda_k - \pi k + \frac{\pi}{2})e^{\pi k} \geq \cos(\lambda_k)e^{\pi k} = \frac{e^{\pi k}}{\cosh(\lambda_k)} \rightarrow 2e^{\pi/2} \quad \text{as } k \rightarrow \infty. \quad (3.85)$$

It follows from inequalities in (3.84) and (3.85) that

$$\lim_{\substack{k \rightarrow \infty \\ k \text{ even}}} \left(\lambda_k - \pi k + \frac{\pi}{2}\right) e^{\pi k} = 2e^{\pi/2}. \quad (3.86)$$

A similar derivation of the convergence speed can be given for odd n . In this case we obtain

$$\lim_{\substack{k \rightarrow \infty \\ k \text{ odd}}} \left(\lambda_k - \pi k + \frac{\pi}{2}\right) e^{\pi k} = -2e^{\pi/2}. \quad (3.87)$$

Hence, for both odd and even k , the series $\lambda_k - \pi k + \frac{\pi}{2}$ tends to zero exponentially. Formulas (3.86) and (3.87) provide excellent approximations $\lambda_k^* = \pi(k - \frac{1}{2}) + e^{-\pi(k-1/2)}$ for k even and $\lambda_k^* = \pi(k - \frac{1}{2}) - e^{-\pi(k-1/2)}$ for k odd for the eigenvalues λ_k , even for small k . For example, for $k = 2$ we obtain $\lambda_2^* = 4.73036$, which is an relative error of about 0.007% of

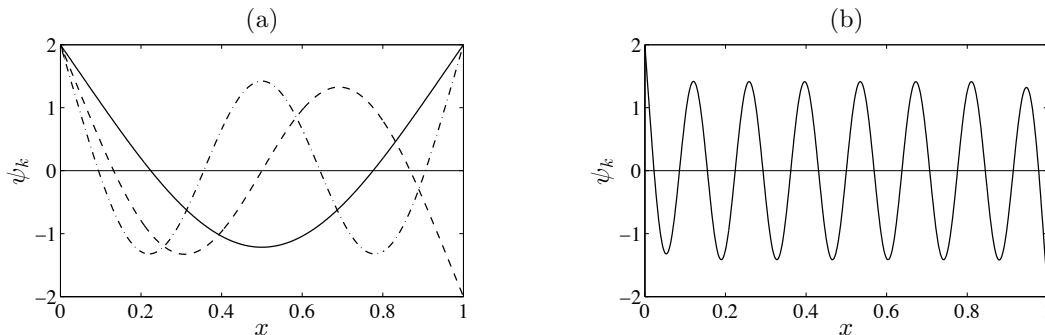


Figure 3.7: (a) The dry normal modes $\psi_k(x)$ given by equations (3.71) and (3.72) for $k = 2$ (solid line), $k = 3$ (dashed line) and $k = 4$ (dashed-dotted line), (b) $\psi_k(x)$ for $k = 15$.

$\lambda_2 = 4.73004$. The approximation $\lambda_3^* = 7.85320$ starts to differ from λ_3 at the sixth digit behind the decimal point. Note that λ_k is found from equation (3.76) numerically by using Newton's method.

The linear increase of λ_k for growing k implies that γ_k in (3.78) converges to -1 exponentially as $k \rightarrow \infty$. For large k the first two terms of the right-hand side of (3.77) are exponentially large in absolute values and they cancel each other for $0 < x \leq 1$, so equation (3.77) is not suitable for numerical evaluation of $\psi_k(x)$ for large k . To derive an alternative formula for $\psi_k(x)$ we use the following identities derived from equation (3.76):

$$(\cos(\lambda_k) \sinh(\lambda_k))^2 = \cos^2(\lambda_k)(\cosh^2(\lambda_k) - 1) = \sin^2(\lambda_k), \quad (3.88)$$

$$(\sin(\lambda_k) \cosh(\lambda_k))^2 = (1 - \cos^2(\lambda_k)) \cosh^2(\lambda_k) = \sinh^2(\lambda_k), \quad (3.89)$$

Note that $\cos(\lambda_k)$ is positive and $\sin(\lambda_k)$ is negative for k even, whereas both $\cos(\lambda_k)$ and $\sin(\lambda_k)$ are positive for k odd. With the help of the identities (3.88) and (3.89) we find from equation (3.78) the two alternative formulas

$$\gamma_k = \begin{cases} -\tanh(\frac{1}{2}\lambda_k), & (k \text{ even}) \\ -\coth(\frac{1}{2}\lambda_k), & (k \text{ odd}) \end{cases} \quad \text{and} \quad \gamma_k = \begin{cases} \tan(\frac{1}{2}\lambda_k), & (k \text{ even}) \\ -\cot(\frac{1}{2}\lambda_k), & (k \text{ odd}) \end{cases} \quad (3.90)$$

Substituting these formulas into equations (3.77) gives us

$$\psi_k(x) = \frac{\cosh((\frac{1}{2} - x)\lambda_k)}{\cosh(\frac{1}{2}\lambda_k)} + \frac{\cos((\frac{1}{2} - x)\lambda_k)}{\cos(\frac{1}{2}\lambda_k)} \quad (k \text{ even}), \quad (3.91)$$

$$\psi_k(x) = \frac{\sinh((\frac{1}{2} - x)\lambda_k)}{\sinh(\frac{1}{2}\lambda_k)} + \frac{\sin((\frac{1}{2} - x)\lambda_k)}{\sin(\frac{1}{2}\lambda_k)} \quad (k \text{ odd}). \quad (3.92)$$

Equations (3.91) and (3.92) show that $\psi_k(x)$ is symmetric about $x = \frac{1}{2}$, if k is even, and ψ_k is antisymmetric about $x = \frac{1}{2}$ with $\psi_k(\frac{1}{2}) = 0$, if k is odd. We also can read off the values $\psi_k(0) = \psi_k(1) = 2$ for k even and $\psi_k(0) = 2$, $\psi_k(1) = -2$ for k odd. The second summands on the right-hand side of (3.91) and (3.92) dominate for x close to $\frac{1}{2}$, so that we find regular oscillations there with angular frequency λ_k and amplitude of about $\sqrt{2}$. The dry normal modes for $k = 2$, $k = 3$, $k = 4$ and $k = 15$ are shown in Figures 3.7(a) and (b).

As to the corresponding eigenoscillations $\sigma_k(t)$ satisfying equation (3.73) its period is

given by

$$T_k = 2\pi\lambda_k^{-2}\left(\frac{\mu}{\theta}\right)^{1/2}. \quad (3.93)$$

The values T_k are also known as the natural period of the dry normal modes $\psi_k(x)$. As k increases the period decreases as $T_k \sim \frac{2}{\pi}(\mu/\theta)^{1/2}k^{-2}$.

In general, if the pressure $q(x, t)$ in (3.67) is non-zero the plate position can be described as an expansion of the dry normal modes,

$$\omega(x, t) = \sum_{k=0}^{\infty} a_k(t)\psi_k(x), \quad (3.94)$$

where the values $a_k(t)$ are called principal coordinates. The values of the principal coordinates depend on the pressure $q(x, t)$ and we do not know a priori if the series (3.94) converges in $L^2(0, 1)$. Substituting (3.94) in (3.67) and projecting the result onto each individual mode $\psi_k(x)$ with the help of orthonormality relation (3.79) and equation (3.71), we obtain a system of ordinary differential equations for the principal coordinates:

$$\mu\ddot{a}_k(t) + \theta\lambda_k^4 a_k(t) = \int_0^1 q(x, t)\psi_k(x) dx. \quad (3.95)$$

Here we have interchanged infinite summation and differentiation as well as infinite summation and integration. This is valid if the principal coordinates and its first and second time-derivatives, a_k , \dot{a}_k , \ddot{a}_k , decay to zero quickly enough as $k \rightarrow \infty$. The analysis of decay rate of a_k , \dot{a}_k , \ddot{a}_k can be investigated a posteriori. If the external force is decoupled from the plate motion and we have initial conditions

$$a_k(0) = 0, \quad \dot{a}_k(0) = 0 \quad (k \geq 0), \quad (3.96)$$

the principal coordinates are given by

$$a_k(t) = \frac{1}{\beta_k} \left(\int_0^t \cos(\beta_k\tau)b_k(\tau) d\tau \sin(\beta_k t) - \int_0^t \sin(\beta_k\tau)b_k(\tau) d\tau \cos(\beta_k t) \right) \quad (3.97)$$

$$b_k(t) = \frac{1}{\mu} \int_0^1 q(x, t)\psi_k(x) dx, \quad \beta_k = \lambda_k^2 \sqrt{\theta/\mu}. \quad (3.98)$$

For $q(x, t)$ continuous in both variables it follows that $b_k(t) = O(k^{-1})$ as $k \rightarrow \infty$, which implies $a_k(t) = O(k^{-5})$, $\dot{a}_k(t) = O(k^{-3})$, $\ddot{a}_k(t) = O(k^{-1})$ as $k \rightarrow \infty$. It can be shown that these decay rates are large enough to justify the normal mode expansions and Euler's beam equation in the form (3.95).

In the following we discuss Euler's beam model (3.67) – (3.69) for inverse-square-root behaviour of the external force. Such a behaviour is given for the leading-order hydrodynamic pressure for a plate impacting a fluid free-surface in section 3.1. Then interchanging of infinite summation and differentiation as well as infinite summation and integration to derive equation (3.95) may be not valid. A singular forcing term in (3.67) can be avoided by reformulating Euler's beam model (3.67) – (3.69) in terms of the function $W(x, t) = \int_0^t \omega(x, \tau) d\tau$.

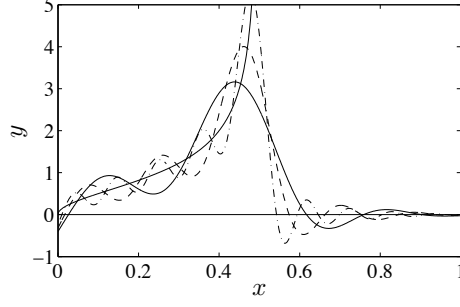


Figure 3.8: The function $f(x) = \sqrt{x/(1/2-x)}$ (thin solid line), and the normal-mode approximations $S_7(f)$ (thick solid line), $S_{11}(f)$ (dashed line) and $S_{19}(f)$ (dashed-dotted line), where $S_n(f) = \sum_{k=0}^n a_k \psi_k(x)$, $a_k = \int_0^1 f(u) \psi_k(u) du$.

Integrating equations (3.67) – (3.69) with respect to time we obtain

$$\mu \frac{\partial^2 W}{\partial t^2} + \theta \frac{\partial^4 W}{\partial x^4} = \int_0^t q(x, \tau) d\tau - \omega_1(x) \quad (0 \leq x \leq 1), \quad (3.99)$$

$$\frac{\partial^2 W}{\partial x^2} = \frac{\partial^3 W}{\partial x^3} = 0 \quad (x = 0 \text{ and } x = 1), \quad (3.100)$$

$$W(x, 0) = 0, \quad \frac{\partial W}{\partial t}(x, 0) = \omega_0(x) \quad (0 \leq x \leq 1). \quad (3.101)$$

In particular, $W(x, t)$ also satisfies the free-free boundary condition (3.100). Hence, we can expand $W(x, t)$ in terms of the normal modes (3.74) and (3.77):

$$W(x, t) = \sum_{k=0}^{\infty} A_k(t) \psi_k(x). \quad (3.102)$$

If $q(x, t)$ is given by the hydrodynamic pressure, it follows from the linearised Bernoulli's equation (see equation (3.24)) that $\int_0^t q(x, \tau) d\tau = -\varphi(x, 0, t)$, where $\varphi(x, y, t)$ is the velocity potential of the fluid flow. Hence, the right-hand side of equation (3.99) is continuous and we can write equation (3.99) in the following form using the expansion (3.102):

$$\mu \ddot{A}_k(t) + \theta \lambda_k^4 A_k(t) = - \int_0^1 \varphi(x, 0, t) \psi_k(x) dx - \int_0^1 \omega_1(x) \psi_k(x) dx. \quad (3.103)$$

Note that if we differentiate (3.103) in time we obtain equation (3.95). We found it more convenient to work with equation (3.95), so that in this thesis we will use equation (3.95) to investigate impact problems of elastic plates.

We briefly discuss the decay of the normal modes and its time-derivatives obtained from the system (3.95) and (3.96) applying the external force $q(x, t) = \sqrt{x/(t-x)}$, $0 \leq x < t$, and $q(x, t) = 0$, $t \leq x \leq 1$, for $0 \leq t < 1$. Note that in this example the external force is decoupled from the plate vibration. It can be shown that $b_k(t)$ in (3.98) decays as $O(k^{-1/2})$, and oscillates in t with period $2\pi/\lambda_k$. Equation (3.97) guarantees that the principal coordinates and its derivatives decay at least as $a_k(t) = O(k^{-9/2})$, $\dot{a}_k(t) = O(k^{-5/2})$, $\ddot{a}_k(t) = O(k^{-1/2})$ as $k \rightarrow \infty$. However, computations indicate that the decay of $\dot{a}_k(t)$ and $\ddot{a}_k(t)$ is quicker. We found for the first 50 modes that $\dot{a}_k(t) = O(k^{-7/2})$ and $\ddot{a}_k(t) = O(k^{-2})$.

In impact problems, the hydrodynamic pressure depends on the elastic deflection of the plate. Hence the problem is coupled and we have to be careful with the evaluation of equation (3.95). After computing $a_k(t)$, $\dot{a}_k(t)$ and $\ddot{a}_k(t)$, the pressure can be computed by substituting $a_k(t)$, $\dot{a}_k(t)$ and $\ddot{a}_k(t)$ directly into the pressure formula as shown in the next subsection. It is not reliable to compute the hydrodynamic pressure via the partial sums of the normal-mode expansion, $\sum_{k=0}^N b_k(t)\psi_k(x)$ where b_k is given in (3.98). To demonstrate this we computed the partial sums of the normal-mode expansions for the function $f(x) = \sqrt{x/(1/2 - x)}$. Figure 3.8 illustrates that the partial sums converge to $f(x)$ very slowly.

3.3 Free fall of an inclined elastic plate

In this section we analyse the interactions that occur when an inclined elastic plate falls onto the free surface of deep water (see Figure 3.9). If the initial inclination angle of the plate is small, the hydrodynamic loads are very high and the flexibility of the plate significantly influences the interaction between fluid and body. To date it is simply supported plates that have mostly been considered (see Meyerhoff (1965a); Kvåsvold and Faltinsen (1993); Korobkin (1998); Korobkin and Khabakhpasheva (2006)). In the present problem the ends of the plate are not attached to an external structure and are free of stresses. Furthermore, the plate is free to move, i.e. it is free in vertical translation and rotation. To show certain hydroelastic features we will determine simultaneously the hydrodynamic loads acting on the plate, the size of the contact region between the plate and the fluid, the rigid body motions, and the elastic deflections of the plate.

3.3.1 Mathematical formulation

The elastic plate is initially undeformed, inclined to the liquid free surface at a small angle ε and touches the surface at a single point, the origin of the fixed $x'Oy'$ coordinate system. We consider a plate, which has length L and relatively small thickness h , such that $h/L \ll 1$. The plate material has constant density ρ_S , Young's modulus E and Poisson's ratio ν . The plate position $y' = \omega'(x', t')$ is unknown in advance and must be determined together with the liquid flow and the hydrodynamic pressure. We assume that the rigidity of the plate is large enough, so that in the early stage of interaction $\omega'_{x'}(x', t')$ is small in the region where the fluid is in contact with the body.

We formulate the impact problem in terms of non-dimensional coordinates given in (3.2) – (3.5). The boundary conditions (3.7) – (3.9) can be linearised and imposed on the original position of the liquid boundary, $y = 0$, in the leading order for small ε as shown in subsection 3.1.2. Within the linearised hydrodynamic model the spatial interval $0 < x < d(t)$ on $y = 0$ corresponds to the contact region of the moving plate with the fluid. The point $x = 0$, $y = 0$ corresponds to the left edge of the plate, and the point $x = d(t)$, $y = 0$ is the Wagner contact point. The function $d(t)$ is unknown in advance and is determined as part of the solution. For very flexible plates $\dot{d}(t)$ can become negative. Here we consider only plates and initial configurations, where $\dot{d}(t)$ is positive during the impact stage. Then the velocity potential

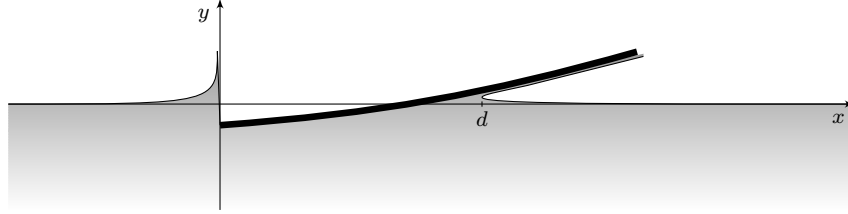


Figure 3.9: Vertical free fall of an elastic plate onto deep water.

$\varphi(x, y, t)$ satisfies the following equations:

$$\nabla^2 \varphi = 0 \quad (y < 0), \quad (3.104)$$

$$\varphi_y = \omega_t \quad (y = 0, 0 < x < d), \quad (3.105)$$

$$\varphi_x = 0 \quad (y = 0, x < 0 \text{ and } x > d), \quad (3.106)$$

$$\varphi = O((x^2 + y^2)^{-1/2}) \quad (x^2 + y^2 \rightarrow \infty). \quad (3.107)$$

In contrast to the problem (3.15), (3.16), (3.19), (3.18), equations (3.104) – (3.107) are for general body motion $y = \omega(x, t)$. As in section 3.1, the velocity field has square-root singularity behaviours at the left edge of the plate $x = 0, y = 0$ and at the Wagner contact point $x = d(t), y = 0$. The solution $\varphi(x, y, t)$ in (3.104) – (3.107) depends on the length of the wetted part, $d(t)$. The function $d(t)$ is determined by the following equations:

$$\eta(d, t) = \omega(d, t) \quad (0 \leq d \leq 1), \quad (3.108)$$

$$\eta_t = \varphi_y \quad (y = 0, x < 0 \text{ and } x > d), \quad (3.109)$$

$$\eta \equiv 0 \quad (t = 0). \quad (3.110)$$

Equation (3.108) is Wagner's condition (see equation (3.13)) where the free-surface elevation $\eta(x, t)$ is obtained from the linearised kinematic boundary condition (3.109) and the initial condition (3.110).

The problem (3.104) – (3.110) can be readily solved if the body position $y = \varepsilon\omega(x, t)$ in equations (3.105) and (3.108) is known. But this is not the case, as the motion of the plate will be determined by Euler's beam equation with free-free boundary conditions given by equations (3.67) and (3.68). In section 3.2 we showed that Euler's beam equation can be reformulated as equations (3.95) in terms of the principal coordinates $a_k(t)$ of the normal modes $\psi_k(x)$ given in (3.91) and (3.92). The function $q(x, t)$ in (3.95) is given by the hydrodynamic pressure together with the gravity force on the plate:

$$q(x, t) = \begin{cases} p(x, 0, t) - \mu\kappa & 0 \leq x < c, \\ -\mu\kappa & x \geq c, \end{cases} \quad (3.111)$$

where $\mu = \rho_S h / (\rho_F L)$ and $\kappa = \varepsilon g L V^{-2}$. The initial conditions are given by

$$\omega(x, 0) = x, \quad \omega_t(x, 0) = -1. \quad (3.112)$$

The pressure $p(x, 0, t)$ in (3.111) is determined by the linearised Bernoulli's equation (3.24)

through the velocity potential $\varphi(x, y, t)$, where $\varphi(x, 0, t)$ is given by (3.104) – (3.108) depending on $\omega(x, t)$. This implies that the problem is coupled: the flow, the pressure distribution, the motions of the plate and its elastic deflections have to be determined simultaneously along with the size of the contact region and the shape of the free surface (see Korobkin and Khabakhpasheva, 2006). A direct numerical solution is difficult because the problem is nonlinear and unknown functions could be singular. The solution of the coupled problem (3.24), (3.94) – (3.112) depends on four parameters χ , μ , θ and κ .

3.3.2 Solution of the coupled problem

In the hydrodynamic part of the problem we seek the horizontal velocity $\varphi_x(x, 0, t)$ for $0 < x < d$ and the hydrodynamic pressure $p(x, 0, t)$ for $0 < x < d$. With the help of formula (2.28) for $k_1 = k_2 = 0$, we obtain the following horizontal velocity of the fluid along the plate from the MBVP (3.104) – (3.107):

$$\varphi_x(x, 0, t) = \frac{1}{\pi \sqrt{x(d-x)}} \int_0^d \frac{\sqrt{\xi(d-\xi)}}{\xi-x} \omega_t(\xi, t) d\xi. \quad (3.113)$$

Eigensolutions of the problem (3.104) – (3.107) with $\omega_t(x, t) \equiv 0$ are not included in (3.113) because they have stronger singularities.

To find the hydrodynamic pressure $p(x, 0, t)$ we solve the following mixed boundary-value problem for the complex acceleration potential $F_{tt}(z) = \varphi_t + i\psi_t$:

$$F_{tt}(z) \text{ analytic} \quad (y < 0), \quad (3.114)$$

$$\text{Im}(F_{tt}) = -\hat{\omega}_{tt} + C(t) \quad (y = 0, 0 < x < d), \quad (3.115)$$

$$\text{Re}(F_{tt}) = 0 \quad (y = 0, x < 0 \text{ and } x > d), \quad (3.116)$$

$$F_{tt}(z) = O(z^{-1}) \quad (|z| \rightarrow \infty), \quad (3.117)$$

where $\hat{\omega}_{tt}(x, t) = \int_0^x \omega_{tt}(\xi, t) d\xi$ and $C(t)$ is an undetermined term due to integration of (3.105) with respect to x . Equations (3.114) – (3.117) are derived from the problem (3.104) – (3.107). The function $F_{tt}(z)$ has an inverse square-root singularity at $z = d$ and is bounded at $z = 0$ (see subsection (3.1.3)). Formula (2.25) with $k_1 = -1$ and $k_2 = -1$ gives us a particular solution $F_{tt}^*(z)$ of (3.114) – (3.116) where $F_{tt}^*(z) = O(1)$ as $|z| \rightarrow \infty$ and $F_{tt}^*(z) = O(1)$ as $z \rightarrow 0$ and $z \rightarrow d$. To obtain $F_{tt}(z)$ we add the corresponding eigensolutions to $F_{tt}^*(z)$ (see equation (2.10)):

$$F_{tt}(z) = \frac{i}{\pi} \sqrt{z(z-d)} \int_0^d \frac{\hat{\omega}_{tt}(\xi, t) - C(t)}{(\xi-z)\sqrt{\xi(d-\xi)}} d\xi + B(t) \sqrt{\frac{z}{z-d}}. \quad (3.118)$$

A relation between $B(t)$ and $C(t)$ is obtained by the far-field behaviour of $F_{tt}(z)$ given in (3.117):

$$C(t) = \frac{1}{\pi} \int_0^d \frac{\hat{\omega}_{tt}(\xi, t)}{\sqrt{\xi(d-\xi)}} d\xi + iB(t). \quad (3.119)$$

To specify $B(t)$, we investigate the asymptotic behaviour of $\text{Re}(F_{tt}(z))$ at $z = d$ in detail.

Equation (3.113) shows that the asymptotic behaviour of $\varphi_x(x, 0, t)$ at $x = d$ is given by

$$\varphi_x(x, 0, t) = -\frac{1}{\pi\sqrt{d}} \int_0^d \sqrt{\frac{\xi}{d-\xi}} \omega_t(\xi, t) d\xi (d-x)^{-1/2} + O(1) \quad (x \rightarrow d^-). \quad (3.120)$$

We have assumed that $\dot{d} > 0$, so that differentiating of (3.120) with respect to time and integrating the resulting equations in x afterwards gives us the asymptotic behaviour of $\varphi_t(x, 0, t)$ at $x = d$:

$$\varphi_t(x, 0, t) = \frac{\dot{d}}{\pi\sqrt{d}} \int_0^d \sqrt{\frac{\xi}{d-\xi}} \omega_t(\xi, t) d\xi (d-x)^{-1/2} + O(1) \quad (x \rightarrow d^-). \quad (3.121)$$

The function $B(t)$ in equations (3.118) and (3.119) is specified by the asymptotic behaviour in (3.121):

$$B(t) = \frac{\dot{d}}{\pi d} \int_0^d \sqrt{\frac{\xi}{d-\xi}} \omega_t(\xi, t) d\xi, \quad (3.122)$$

The real part of $F_{tt}(z)$ gives us together with the linearised Bernoulli's equation (3.24) the hydrodynamic pressure along the contact region, $0 < x < d$, $y = 0$:

$$p(x, 0, t) = -\frac{1}{\pi} \sqrt{x(d-x)} \int_0^d \frac{\hat{\omega}_{tt}(\xi, t)}{(\xi-x)\sqrt{\xi(d-\xi)}} d\xi - \frac{\dot{d}}{\pi d} \sqrt{\frac{x}{d-x}} \int_0^d \sqrt{\frac{\xi}{d-\xi}} \omega_t(\xi, t) d\xi. \quad (3.123)$$

Now, we reformulate the problem (3.104) – (3.107) with respect to the displacement potential, $\Phi(x, y, t)$ as was done in subsection 3.1.4. We use equations (3.108) – (3.110) to obtain

$$\nabla^2 \Phi = 0 \quad (y < 0), \quad (3.124)$$

$$\Phi_y = \omega(x, t) \quad (y = 0, 0 < x < d), \quad (3.125)$$

$$\Phi = 0 \quad (y = 0, x < 0 \text{ and } x > d), \quad (3.126)$$

$$\Phi = O((x^2 + y^2)^{-1/2}) \quad (x^2 + y^2 \rightarrow \infty). \quad (3.127)$$

The solution for the vertical displacement of the fluid along the free surface is given by

$$\Phi_y(x, 0, t) = \pm \frac{1}{\pi\sqrt{x(x-d)}} \int_0^d \frac{\sqrt{\xi(d-\xi)}}{\xi-x} \omega(\xi, t) d\xi. \quad (3.128)$$

The plus sign in equation (3.128) applies for $x > d$ and the minus sign for $x < 0$. Note that $\Phi_y(x, 0, t)$ in (3.128) is also the free surface elevation of the fluid due to equation (3.34). The complex displacement $f(z) = \Phi_x(x, y, t) - i\Phi_y(x, y, t)$ has a square-root singularity at $z = 0$ and does not have a singularity at $z = d$ (see also section 3.1.4). Hence, the integral in (3.128) becomes zero for $x \rightarrow d$, so that we obtain the following equation:

$$\int_0^d \sqrt{\frac{\xi}{d-\xi}} \omega(\xi, t) d\xi = 0. \quad (3.129)$$

Equation (3.129) will be used to determine the position of the contact point $x = d(t)$. For the case $\omega(x, t) = x - t$, discussed in section 3.1, we obtain the solution (3.46) from equation (3.129).

The structural part of the problem is calculated from (3.95) where $q(x, t)$ is given by equation (3.111) together with the hydrodynamic pressure in (3.123) and the shape of the elastic plate in (3.94). Equations (3.95) are written in matrix form as

$$(M(d) + \mu I)\ddot{\mathbf{a}} = -\frac{1}{\pi}d\dot{d}D(d)\dot{\mathbf{a}} - \theta S\mathbf{a} - \mu\kappa\mathbf{e}_0, \quad (3.130)$$

where $\mathbf{a}(t) = (a_0(t), a_1(t), a_2(t), \dots)^T$ and $\mathbf{e}_0 = (1, 0, 0, \dots)^T$. Here S is a diagonal matrix, $S = \text{diag}(\lambda_0^4, \lambda_1^4, \lambda_2^4, \dots)$, and the elements of the matrix D are $D_{kn}(d) = \Gamma_k(d)\Gamma_n(d)$ where $\Gamma_k(d)$ is defined by

$$\Gamma_k(d) = \int_0^1 \sqrt{\frac{u}{1-u}} \psi_k(du) du. \quad (3.131)$$

The inertia matrix on the left-hand side of the system (3.130) consists of the non-dimensional structural mass matrix of the dry plate, μI , where I is the identity matrix, and the added mass matrix $M(d)$ defined by

$$M_{kl}(d) = \frac{d}{\pi} \int_0^1 \int_0^1 \frac{\sqrt{u(1-u)} \psi_l(du) \Psi_k(dv)}{\sqrt{v(1-v)} (v-u)} dv du. \quad (3.132)$$

where $\Psi_k(x) = \int_0^x \psi_k(u) du$. The matrix $M(d)$ accounts for the presence of the fluid in contact with the plate (see Newman (1977)). The elements of the added mass matrix are zero when $d = 0$ and are increasing with the increase of the contact region $0 < x < d$. The concept of added mass is helpful to arrive at a suitable form of the equations describing coupled structural and hydrodynamic parts of the problem by numerical means. It is shown in appendix B, that the matrix M defined in (3.132) is symmetric. The system of second-order differential equations (3.130) involves a damping term. It can be shown that half of the energy leaving the plate due to the damping term is transferred into the jet. In particular, this is the only mechanism to extract energy from the plate vibration. The right-hand side of (3.130) depends on \dot{d} . We obtain the following equation for \dot{d} by differentiating equation (3.129) with respect to t and using the expansion of $\omega(x, t)$ in (3.94):

$$\dot{d} = -\frac{(\dot{\mathbf{a}}, \mathbf{\Gamma}(d))}{(\mathbf{a}, \frac{d}{da}\mathbf{\Gamma}(d))}. \quad (3.133)$$

where the elements of $\mathbf{\Gamma}(d) = (\Gamma_k(d))$ are defined by (3.131) and $(\mathbf{v}_1, \mathbf{v}_2)$ is the scalar product of the vectors \mathbf{v}_1 and \mathbf{v}_2 . Substituting (3.133) into (3.130) gives an ODE system whose right-hand side depends on \mathbf{a} , $\dot{\mathbf{a}}$ and d but not on t . Therefore it is convenient to take the quantity d as a new independent variable with $0 \leq d \leq 1$. Dividing the system of equations (3.130)

by \dot{d} and taking into account (3.133), we find the ODE system

$$\frac{d\mathbf{a}}{dd} = -\frac{(\mathbf{a}, \frac{d}{dd}\boldsymbol{\Gamma})}{(\mathbf{b}, \boldsymbol{\Gamma})}\mathbf{b}, \quad (3.134)$$

$$\frac{d\mathbf{b}}{dd} = (M + \mu I)^{-1} \left[-\frac{d}{\pi} D\mathbf{b} + \frac{(\mathbf{a}, \frac{d}{dd}\boldsymbol{\Gamma})}{(\mathbf{b}, \boldsymbol{\Gamma})}(\theta S\mathbf{a} + \mu\kappa\mathbf{e}_0) \right], \quad (3.135)$$

$$\frac{dt}{dd} = -\frac{(\mathbf{a}, \frac{d}{dd}\boldsymbol{\Gamma})}{(\mathbf{b}, \boldsymbol{\Gamma})}, \quad (3.136)$$

where we defined $\mathbf{b} := \dot{\mathbf{a}}$. Note that (3.134) follows from $\mathbf{b} = \dot{\mathbf{a}}$ and equation (3.133). The initial conditions for the system of ordinary differential equations (3.134) – (3.136) are

$$\mathbf{a} = \left(\frac{1}{2}, \frac{1}{6}\sqrt{3}, 0, 0, 0, \dots \right), \quad \mathbf{b} = (-1, 0, 0, 0, \dots), \quad t = 0 \quad (d = 0). \quad (3.137)$$

Here equation (3.136) recovers, together with the initial conditions in (3.137) and $\Gamma_0(0) = \frac{\pi}{2}$, $\frac{d}{dd}\Gamma_0(0) = 0$, $\frac{d}{dd}\Gamma_1(0) = \frac{3\pi}{8}$, the initial contact point velocity $\dot{d}(0) = \frac{4}{3}$, which agrees with the one for the impact of a rigid plate at constant speed (see equation (3.46)). The system (3.134) – (3.136) is suitable for the start of numerical calculations at $t = 0$. This will be different for the system of differential equations arising from the plate impact at high horizontal speed (see sections 4.4, 5.1 and 5.2), where we have to replace the initial time integration by the results of a simpler impact model.

The replacement of d as the integration variable for t is justified only while $dt/dd > 0$. Hence, the behaviour of dt/dd in equation (3.136) has to be monitored in numerical calculations. We stop the calculation if dt/dd becomes zero, which corresponds to an infinite velocity of the turnover point $x = d(t)$. Note that $dt/dd > 0$ is satisfied for small d , since we start with $\dot{d}(0) = \frac{4}{3}$. However, $dt/dd = 0$ is possible later, since the plate rotates during impact, so that the inclination may become very small during impact, which corresponds to large \dot{d} . On the other hand, the unlimited growth of the derivative dt/dd means that the velocity of the contact point can decrease to zero and the contact point may change its direction, which cannot be accounted for in the present model. A shrinking contact region indicates a partial exit of the plate from water. Both cases $dt/dd \rightarrow 0$ and $dt/dd \rightarrow \infty$ were only found for small θ ($\theta < 0.02$), when the inclination angle of the plate becomes very small during impact (e.g. $dt/dd \rightarrow 0$ for $\mu = 0.01$, $\theta = 0.01$ and $dt/dd \rightarrow \infty$ for $\mu = 0.01$, $\theta = 0.02$). These cases are of interest and may have specific effects on the fluid and on the plate behaviour at the contact point.

We are also interested in computing the hydrodynamic pressure along the surface of an elastic plate. If the plate is light and very flexible ($\mu \ll 1$ and $\theta \ll 1$) we expect that the hydrodynamic pressure in (3.95) to depend strongly on the plate deflection, and the problem is then strongly coupled. Furthermore, we should monitor the regions where the pressure is negative, since fluid may separate from the body in these zones of low pressures with the development of vapour cavities or air may be sucked under the plate. These phenomena are known as cavitation and as ventilation, correspondingly. Both phenomena are important issues and were reported in drop tests of horizontal elastic plates on a flat water surface (Faltinsen, 1997). In particular, cavitation can cause serious damage to structures since shock waves appear during the collapse of such cavities. In this section, cavitation and

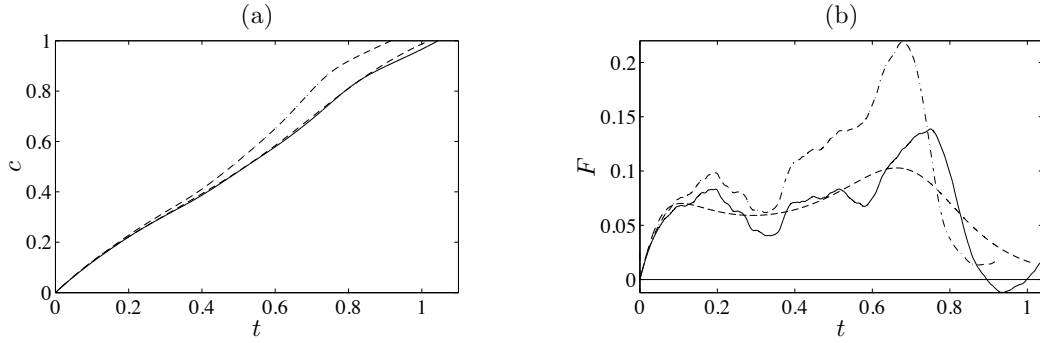


Figure 3.10: (a) Contact point motions for rigid plate without gravity (dashed line), for elastic plate without gravity (solid line) and for elastic plate with gravity (dashed-dotted line), (b) vertical force evolutions for plate configuration as described in (a).

ventilation are not considered. The fluid is attached to the plate from the left edge to the turnover region, so that suction forces of the fluid contribute to the dynamics of the plate. The pressure is obtained from (3.94) and (3.123) which give

$$p(x, 0, t) = -\frac{1}{\pi} \sqrt{x(d-x)} (\ddot{\mathbf{a}}, \mathbf{F}^{(d)}(x)) + \frac{1}{\pi} \sqrt{\frac{x}{d-x}} \frac{(\dot{\mathbf{a}}, \mathbf{\Gamma}(d))^2}{(\mathbf{a}, \frac{d}{dd} \mathbf{\Gamma}(d))}, \quad (3.138)$$

where the elements of the vector $\mathbf{F}^{(d)}(x) = (F_1^{(d)}(x), F_2^{(d)}(x), \dots)$ are defined by

$$F_k^{(d)}(x) = \int_0^d \frac{\Psi_k(\xi)}{(\xi-x)\sqrt{\xi(d-\xi)}} d\xi. \quad (3.139)$$

The functions $F_k^{(d)}(x)$ in terms of the quickly converging series given in appendix C. Note that the functions $F_k^{(d)}(x)$ depend on the size of the contact region but not on the impact conditions. This implies that these functions can be pre-computed for $0 \leq d \leq 1$.

3.3.3 Numerical results

We use the discretisation $d_n = n\Delta d$ with constant integration step Δd . The number of modes is limited in computations. We set $a_k = 0$ for $k \geq M$ and we only retain the first M equations $k = 0, \dots, M-1$ in (3.134) and (3.135). By comparing the results obtained for various M we can draw conclusions to the number of modes that give sufficiently accurate results for the plate motion and the elastic deflections. However, the integration step Δd has to be small enough, so that the maximum of the corresponding timesteps, given by $\Delta d \max_d \frac{dt}{dd}$, has to be much smaller than the period of the highest mode, T_{M-1} , retained in our calculations. We expect that the periods T_k are about the natural periods of a dry Euler beam given by equation (3.93).

The problem (3.134) – (3.137) is solved by the fourth order Runge-Kutta method. In each step it is necessary to calculate the elements of the matrix $M(d)$ and the vectors $\mathbf{\Gamma}(d)$, $\frac{d}{dd} \mathbf{\Gamma}(d)$ for equations (3.134) – (3.136), (3.138). Their analytical expressions in terms of d are presented in appendix B.

Numerical results are presented in Figures 3.10 – 3.13 for the impact of a steel plate onto water. We fix the plate length $L = 2\text{m}$, plate thickness $h = 2\text{cm}$, density $\rho_S = 8000\text{kg m}^{-3}$,

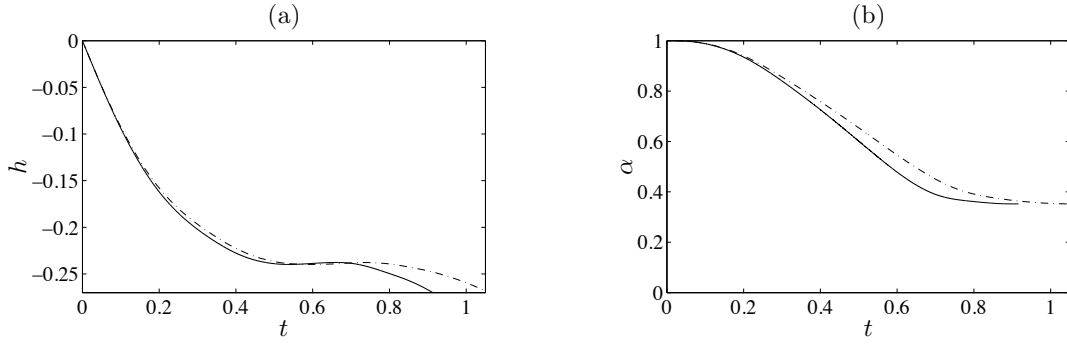


Figure 3.11: (a) The depth $h(t) := a_0(t) - 2\sqrt{3}a_1(t)$ and (b) the instantaneous inclination angle, $\alpha(t) := a_1(t)/(2\sqrt{3})$ for the rigid plate with gravity (solid line) and without gravity (dashed-dotted line).

flexural rigidity $D = 145 \times 10^3 \text{kN m}$ and initial vertical velocity $V = 3 \text{m s}^{-1}$. The gravity acceleration $g = 9.81 \text{m s}^{-2}$ acts on the plate. We select an initial inclination angle of 10° , so that $\varepsilon = 0.175$. Then the non-dimensional parameters are $\mu = 0.080$, $\theta = 0.061$ and $\kappa = 0.38$. We compare the results of the elastic plate, where we use the first eight elastic modes ($M = 10$), with the rigid plate impact. The computations for $M = 10$ were performed with step size 2.5×10^{-4} of the wetted length d , which can be shown to be sufficiently small, as they correspond to non-dimensional time steps not exceeding 3.8×10^{-4} . The step size is 26 times smaller than the natural period of the eighth elastic mode, which is the highest elastic mode retained for the calculations. It was verified numerically that the relative accuracy of d with eight elastic modes is better than 0.2% for the configuration described above. To evaluate the free fall of a rigid plate, we set all principal coordinates a_k corresponding to the elastic modes equal to zero ($M = 2$). Note that we will give analytic solutions for the problem of rigid plate impact in section 6.1. To see the influence of gravity acting on the plate, we also show results with and without the gravity term of equation (3.135).

The motion of the contact point for the rigid and the elastic plate, without gravity, are shown in Figure 3.10(a). The two contact point motions hardly differ. However, the elasticity of the plate notably increases the speed of the contact point for $0.7 < t < 0.8$, which leads to an increase of the hydrodynamic loads (see equation (3.123)). Figure 3.10(a) also shows that the contact point increases more quickly, if the gravity term in Newton's second law is included.

Figure 3.10(b) shows the vertical hydrodynamic forces acting on rigid and elastic plates. For the rigid plate we find two local maxima. The first maximum is due to the initial increase of the wetted region of the plate. This leads to strong deceleration of the vertical motion and a decrease in the inclination angle of the plate. By the time of the second peak, the angle is rather small and the vertical speed of the right edge of the plate is large. This forces the contact point to move faster towards the right edge, increasing quickly the wetted area of the plate and the hydrodynamic force acting on it. The forces on elastic and rigid plates are different in amplitude but are similar in behaviour. Due to the faster contact point motion of the elastic plate during the stage where the inclination angle is small, the maximum vertical force acting on the elastic plate are about 40% higher than that acting on the rigid plate. The difference in the force is explained by the higher speed of the contact

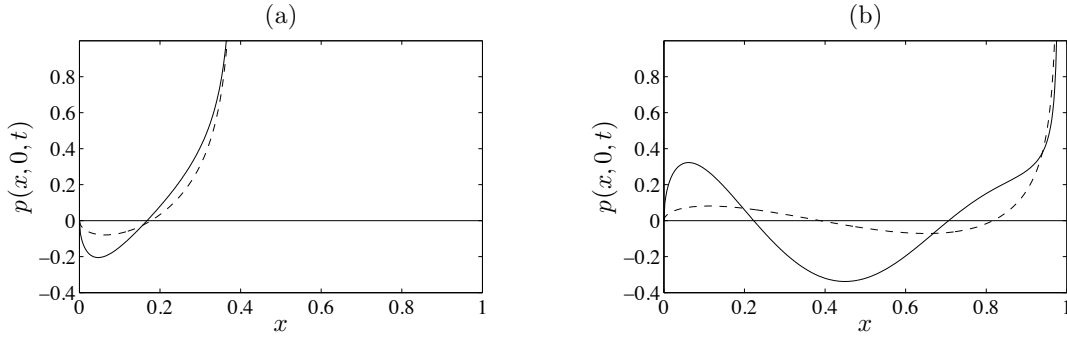


Figure 3.12: (a) Pressure distributions along the elastic plate (dashed line) and along the rigid plate (solid line), (a) at $t = 0.38$ and (b) at $t = 0.89$.

point at $t \approx 0.7$, when the elastic plate bends towards the liquid. Just after the second peak the force drops sharply below zero with the plate being completely wetted at the end of the computations. The inclusion of gravity increases the vertical speed of the right edge towards the free surface, resulting in larger forces shortly before the plate is fully wetted. However, the behaviour of the hydrodynamic force is similar to that when gravity is not taken into account.

Figures 3.11(a) and (b) indicate the rigid body motion of the plate through the penetration depth of the left edge $h := a_0(t) - 2\sqrt{3}a_1(t)$, and the inclination angle of the plate $\alpha := a_1(t)/(2\sqrt{3})$, respectively, with and without gravity included. The motion of the rigid plate and the rigid motion of the elastic plate hardly differ, so that we only plotted h and α for the rigid plate. The inclusion of gravity increases the angular velocity of the plate, resulting in larger forces shortly before the plate is fully wetted. Figure 3.11(b) indicates that the angular velocity is zero when $d = 1$. This applies for any rigid plate ($\theta \rightarrow \infty$) and will be shown later in section (6.1).

The pressure distributions of rigid and elastic plates differ strongly during the impact stage as shown in Figure 3.12(a) and (b) for times $t = 0.38$ and $t = 0.89$. A negative-pressure zone initially appears close to the left edge and later moves along the plate with the negative pressure being captured between positive-pressure zones. For an elastic plate the pressure oscillates, so that the negative pressures are more pronounced, where the negative pressure zone moves around quickly. On the other hand, the pressure in the contact region is rather uniform for the rigid plate. Hence fluid cavitation and ventilation is more likely for elastic plates than for rigid ones.

The maximum amplitude of the principal coordinates, $a_k(t)$, and their derivatives are defined by

$$r_k^{(i)} = \max_{0 < t < t_e} \left| \frac{d^i}{dt^i} a_k(t) \right|, \quad (3.140)$$

which indicate how many modes have to be taken into account in the calculations. The maximum amplitude of the principal coordinates $r_k^{(0)}$ quickly decreases for large k , as shown in Figure 3.13(a). We found that $r_k^{(0)}$ decays approximately as $O(k^{-9/2})$, so that only few normal modes need to be taken into account to get reasonable results for the elastic plate deflection. We found that the order of convergence of $r_k^{(1)}$ is about $O(k^{-7/2})$ as k increases.

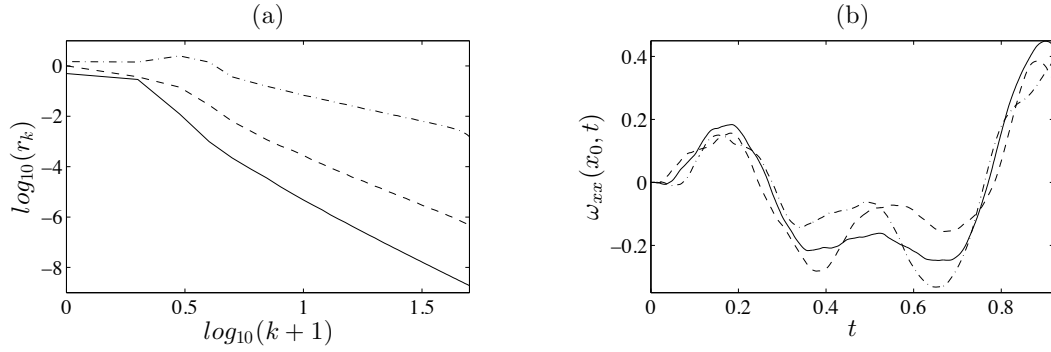


Figure 3.13: (a) The maximum amplitude of the principal coordinates and their derivatives, $r_k^{(0)}$ (solid line), $r_k^{(1)}$ (dashed line) and $r_k^{(2)}$ (dashed-dotted line), which are defined in the text, for the first 51 modes, $0 \leq k \leq 50$, in logarithmical scale. (b) The bending stress at the plate centre, $x_0 = 0.5$, (solid line) at $x_0 = 0.35$ (dashed line) and at $x_0 = 0.65$ (dashed-dotted line).

The maximum amplitude of $\ddot{a}_k(t)$ is large for the first two elastic modes $\psi_2(x)$, $\psi_3(x)$, but we found a decay rate of $O(k^{-2})$ for $r_k^{(2)}$ as k increases. The speed of convergence of $r_k^{(2)}$ especially guarantees a quick convergence of $(\ddot{\mathbf{a}}, \mathbf{F}^{(d)}(x))$ in (3.138) for increasing number of modes retained in the computations (see also appendix C). We found that the pressure $p(x, 0, t)$ is well approximated for $M = 8$.

The distribution of the bending stresses $\sigma'(s', t')$ in the plate and the maximum stress $\sigma'_{\max}(t')$ are important characteristics of the elastic plate impact problem. The dimensional stresses σ' are defined by $\sigma' = (\varepsilon h E / 2L) \omega_{xx}$. Figure 3.13(b) shows the time-evolutions of the bending stress at $x = 0.35$, $x = 0.5$ and $x = 0.65$ in non-dimensional form. The maximum absolute values of the bending stresses are reached shortly before the plate is completely wetted and is approximately 0.45, which corresponds to 79 N mm^{-2} . This is about a third of the yield stress of A36 steel of about 250 N mm^{-2} . Bending stresses are higher for smaller initial inclination angle and larger initial vertical velocity. Under certain circumstances the bending stresses may be higher than yield stress such that the steel plate deforms plastically or cracks during impact. The point on the plate, where the maximum bending stress occurs, can be quite far from the midpoint (see Figure 3.13(b)): our calculations revealed that the position, where the maximum bending stress occurs, is close to the contact point when $0.3 \leq d(t) \leq 0.7$. This is due to the high hydrodynamic loads acting on the plate close to the Wagner contact point.

3.3.4 Fluid structure interaction when the plate is fully wetted

In this subsection we investigate the plate behaviour and the hydrodynamic pressure after the plate becomes fully wetted at time $t = t_0$. In this stage, which we refer to as the penetration stage, we have no turnover region but we find a second splash at the right end of the plate. Hence, the pressure peak disappears. Almost the same model presented in subsection 3.3.1 can be used to investigate fluid-plate interaction for $t > t_0$. However, instead of using Wagner's condition, the position of the right contact point is fixed at the right edge of the plate. It can be shown that the final system is given by (3.130) where $d = 1$. The initial conditions for \mathbf{a} and $\dot{\mathbf{a}}$ are obtained by assuming continuity of these functions at

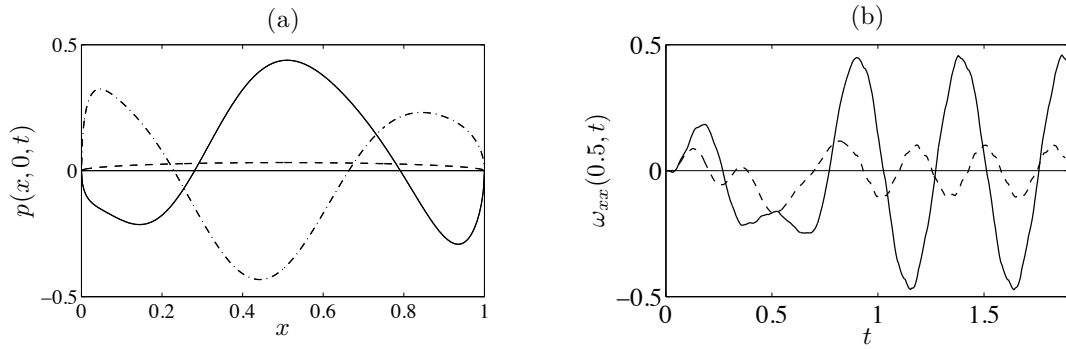


Figure 3.14: (a) Pressure distributions along the elastic plate at $t = 1.17$ (solid line) and at $t = 1.38$ (dashed-dotted line) and the almost constant pressure distribution along a rigid plate (dashed line). (b) The bending stress at the plate centre, $x_0 = 0.5$ (solid line). The dashed line is the bending stress for larger non-dimensional rigidity $\theta = 0.1377$.

the end of the Wagner stage. The pressure $p(x, 0, t)$ in this stage is given by (3.123), where $\dot{d} = 0$ removes the second term in (3.123) containing the inverse-square-root singularity so that we have square-root behaviours at both ends of the plate, $x = 0$ and $x = 1$. Since it is this term which mostly contributes to the hydrodynamic loads for $t < t_0$, the hydrodynamic loads are much smaller for $t > t_0$ than for $t < t_0$. As there is no jet leaving the fluid bulk, energy cannot leave the plate-fluid system for $t > t_0$. This justifies the fact that equation (3.130) has no damping term for $t > t_0$.

The first two components of (3.130) imply that there are no hydrodynamic forces driving the rigid plate motion. The plate accelerates vertically only due to the small non-dimensional gravity force $\mu\kappa$. To compute the problem in the penetration stage, we integrate equation (3.130), where $d = 1$, in time by a fourth order Runge-Kutta method and use the values $\mathbf{a}(t = t_0)$ and $\dot{\mathbf{a}}(t = t_0)$ from the previous stage as initial conditions. In the following, we show results for the pressure distribution along the plate and the bending stresses for $t > t_0$ with parameters $\mu = 0.080$, $\theta = 0.061$ and $\kappa = 0.38$, which were already used in section 3.3.3. Then the plate becomes fully wetted at time $t_0 = 0.916$.

Figure 3.14(a) shows the pressure distribution along an elastic plate for $t = 1.17$ and $t = 1.38$, when the plate is in the concave (plate has n-shape) and convex bending state. During concave bending negative pressure appears close to the ends of the plate, which may enable the ventilation of air in these low pressure zones. During the convex bending large negative pressure, even larger than for $t < t_0$, appear at the centre of the plate's surface. During the penetration stage, $t > t_0$, it may be possible that air bubbles accumulate under the plate, moving from the ends of the plate to its centre. The loads on a rigid plate are small compared to the ones on the elastic plate. Since the acceleration of a rigid plate is constant for $t > t_0$, also the pressure distribution is constant in time (see equation (3.123)).

Figure 3.14(b) shows the bending stresses at the centre of the plate for the impact and penetration stage. In particular, the bending stresses at $t > t_0$ are as large as the highest bending stresses for $t < t_0$. The bending stresses seem to oscillate periodically. Lower impact velocities decrease the bending stresses significantly, which is shown here for the example $V = 2\text{ms}^{-1}$ (instead of $V = 3\text{ms}^{-1}$), which changes the parameter θ to 0.1377.

3.3.5 Discussion

A fully coupled model of elastic plate impact onto a liquid free surface has been developed. Both rigid and elastic motions of the plate were determined simultaneously with the hydrodynamic pressure distribution, the shape of the free surface and the size of the wetted part of the plate. The structural part of the problem has been solved by the normal-mode method. In the present examples, the rigid body components of the plate's motion are very close to those of an equivalent rigid plate. However, the elastic plate experiences higher forces due to the higher velocity of the turnover region. The highest loads occur almost at the end of the impact, when the plate inclination angle is about a third of the initial inclination angle. We found large bending stresses of about a third of the yield stress of the plate material. Hydrodynamic pressures below atmospheric value were found in the contact region for the rigid-plate impact. It was shown that elastic vibrations of the plate lead to even lower pressures. We conclude that elasticity of the plate may promote cavitation of the fluid, and the detachment of the fluid from the solid surface during the early stage of impact. The plate impact model can be continued, when the plate becomes fully wetted. In this stage, the loads due to the plate vibration dominate and we find large negative pressures which are of the same order as in the impact stage.

The presented model deals only with a uniform distribution of mass and rigidity. A similar analysis is possible for non-homogeneous mass and rigidity distributions. In this case the parameters μ and θ in Euler's beam equation are functions of the longitudinal coordinate. The dry modes of a plate with non-uniform characteristics can be computed by using the solution of the spectral problem:

$$\psi_k^{(iv)} = \gamma_k \frac{\mu(x)}{\theta(x)} \psi_k \quad (0 \leq x \leq 1), \quad (3.141)$$

$$\psi_k'' = \psi_k''' = 0 \quad (s = 0 \text{ and } s = 1). \quad (3.142)$$

In general, the eigensolutions and the corresponding eigenvalues can be evaluated only numerically. Once the modes have been computed, the rest of the analysis is essentially the same as that presented in this section.

3.4 Conclusion

This chapter gave an introduction to Wagner theory. We showed the derivation of the linearised hydrodynamic model and used Wagner theory to solve the problem of an inclined plate impacting onto the water free surface at constant speed. For vertical impact of an inclined plate the present linearised hydrodynamic model leads to a singular free-surface elevation close to the sharp edge. An inner solution in this splash region which accounts for the nonlinear terms is needed. The inner solution in the turnover region was found by matching the steady Kelvin-Helmholtz flow with the global flow. We discussed the vertical impact of an elastic plate into water by using the normal-mode method.

The mixed boundary value problem (3.104) – (3.107) can be used for solving the impact problem for bodies of any shape where the deadrise angle of the body is small and for variable vertical velocity. In the next chapter we consider impact problems at high horizontal speed.

For impact problems at high speed the model in section 3.1 has to be modified. It is necessary to include a wake model behind the plate and to introduce a condition for the fluid detachment in the outer solution.

Chapter 4

Water entry of a rigid body at high horizontal speed

Slamming problems at high horizontal speed are characterised by high hydrodynamic loads, flow separation on the rear part of the body and a turnover region of the flow where a jet is thrown off (Faltinsen, 2005). Usually, much higher loads on the body are involved than for vertical slamming. Some experiments of body impact at horizontal speed have been reported. Smiley (1951) conducted experiments of a heavy rectangular steel plate landing on water at high speed for various angles of attack and impact velocities. It was shown that the hydrodynamic pressure acting on the plate is close to uniform in the transverse direction. The measured pressure drops to the ambient value just near the transverse edges of the plate. This observation supports our two-dimensional model which will be introduced in this chapter. Rosselini et al. (2005) conducted experiments on skipping where disks were shot onto the free surface with high horizontal velocity. They showed that the spin of a disk is mainly responsible for the exit of the body after initial impact. Without spin, the disk tilts during impact and dives into the water. Experiments about oblique impact of asymmetrical wedges were done by Judge et al. (2004). Depending on the inclination of the wedge and the entry velocity two different flow regimes were distinguished: Either the fluid overturns on both sides of the wetted area or, for sufficiently large horizontal speed, the fluid detaches smoothly from the vertex.

In this chapter we discuss the impact of bodies with small deadrise angle into water at high horizontal speed. In section 4.1, the linearised hydrodynamic problem for the impact of general-shaped bodies at high horizontal speed is derived and conditions at the ends of the contact region are introduced. We give general results for the position of the forward turnover region, for the hydrodynamic pressure acting on the body, for the wake flow, and the energies in the fluid bulk and in the jet. In section 4.2, we specify the shape of the body to be a plate which penetrates the fluid with constant horizontal and vertical velocity components and where the fluid separates from the trailing edge of the plate. In section 4.3, we present conditions to determine the position of the separation point along a smooth-shaped body. It will be shown that our proposed separation conditions are equivalent to the Brillouin-Villat criterion. The Brillouin-Villat condition will be used in section 4.4 for the free fall of a light plate at high horizontal speed. In particular it can be shown that the body exits the fluid shortly after impact if the horizontal velocity of the plate is large

enough. If not so, it is possible that the plate plans along the free surface after impact. In section 4.4, we will also discuss the behaviour of the plate during planing. Finally, we discuss the bounce of a blunt body at high horizontal speed in section 4.5, where we apply three different separation criteria. We will show that the body motion depends strongly on the separation criterion.

4.1 Impact of general-shaped bodies at high horizontal speed

In this section we discuss the impact of general shaped bodies with small deadrise angle at high horizontal speed. In particular, we introduce the relevant scalings and derive the leading-order MBVP governing the fluid flow in the small deadrise-angle regime. A general pressure formula and a formula for the position of the leading contact point are found. We further introduce Kutta's condition to determine the fluid flow in the wake region. Finally, the energy in the fluid bulk and the energy flux in the jet are identified in this section.

4.1.1 Non-dimensional and linearised hydrodynamic problem

We are concerned with the non-dimensionalisation of the problem of a flat body impact onto initially flat free surface, where the body has initial vertical component of velocity V and horizontal component U . In this chapter the body moves from left to the right. We assume that the deadrise angle of the body is of small order ε . The shape and motion of the body will be specified in sections 4.2, 4.4, 4.5 and 5.1. In general, the position of the bottom of such bodies is described by the equation $y' = \omega(x', t')$, where the Cartesian coordinate system $x'Oy'$ is such that the fluid initially covers the lower half plane $y' < 0$. The coordinate system is fixed such that the fluid in the far field is at rest. The body starts to penetrate the fluid at time $t' = 0$ at $x' = 0$ and $y' = 0$. For $V \gg \varepsilon U$ the fluid flow is dominated by the vertical motion of the body, so that we may use the scalings (3.2) – (3.5) and the linearised equations (3.15) – (3.18) for vertical slamming. However, if the initial horizontal speed is high such that

$$V/U = O(\varepsilon), \tag{4.1}$$

the contributions of the horizontal motion of the body to the fluid flow are significant. In this case we need to find a different non-dimensional form of the impact problem governed by (1.4) – (1.9). In this study, we assume that the horizontal speed of the body is constant, since the hydrodynamic loads acting on a body with small deadrise angle are almost vertical and the impact stage is of short time, such that the horizontal component of deceleration is negligible.

The characteristic lengthscale L of the body is the lengthscale of the problem. We are concerned with the initial stage of the body impact, whose duration is of order L/U . Hence, the non-dimensional time is 1, when the plate travels horizontally by L . In this initial stage of body impact, the vertical penetration of the body is small compared with L since we assume condition (4.1). Due to the small deadrise angle of the body the fluid disturbance due to the horizontal and vertical motion of the body is small, which gives a fluid speed of order εU . In summary, the scalings used for impact problems at high horizontal speed in

this chapter are given as follows:

$$x' = Lx, \quad y' = Ly, \quad t' = \frac{L}{U}t, \quad (4.2)$$

$$\eta' = \varepsilon L\eta, \quad \omega' = \varepsilon L\omega, \quad (4.3)$$

$$\varphi' = \varepsilon UL\varphi, \quad p' = \varepsilon \rho_F U^2 p. \quad (4.4)$$

where $\varphi'(x', y', t')$ is the velocity potential of the fluid flow, $p'(x', y', t')$ the pressure of the fluid and $y' = \eta'(x', t')$ describes the position of the free surface. Note that $\eta'(x', t')$ can be a multi-valued function of x' .

The fluid is in contact with the body along $D'_S(t')$ and the free surface part of the liquid boundary is along $D'_F(t')$. Then the governing equations of the fluid flow, the pressure distribution in the fluid and the free surface elevation due to the body impact, (1.4) – (1.9), are given in non-dimensional form by

$$\nabla^2 \varphi = 0 \quad ((x, y) \in \Omega), \quad (4.5)$$

$$\varphi_y = \omega_t + \varepsilon \omega_x \varphi_x \quad ((x, y) \in D_S), \quad (4.6)$$

$$\varphi_y = \eta_t + \varepsilon \eta_x \varphi_x \quad ((x, y) \in D_F), \quad (4.7)$$

$$p = -\varphi_t - \frac{\varepsilon}{2} (\varphi_x^2 + \varphi_y^2) - \frac{1}{\varepsilon \text{Fr}^2} y \quad ((x, y) \in D_S), \quad (4.8)$$

$$\varphi_t = -\frac{\varepsilon}{2} (\varphi_x^2 + \varphi_y^2) - \frac{1}{\varepsilon \text{Fr}^2} y \quad ((x, y) \in D_F), \quad (4.9)$$

$$\varphi = O((x^2 + y^2)^{-1/2}) \quad (x^2 + y^2 \rightarrow \infty), \quad (4.10)$$

where the Froude number is defined as $\text{Fr} = U/\sqrt{gL}$. The initial conditions of the system (4.5) – (4.10) are

$$\eta \equiv 0, \quad \varphi \equiv 0 \quad (t = 0). \quad (4.11)$$

Equations (4.5) – (4.10) differ from equations (3.6) – (3.10), resulting from the scaling for vertical impact problems, only in the hydrostatic terms in (4.8) and (4.9). While we had to assume large enough vertical velocity for vertical impact problems to neglect the hydrostatic pressure in (3.12) and (3.9), we have to assume for impact problems at horizontal speed that U is large enough, such that

$$\frac{1}{\varepsilon \text{Fr}^2} = O(1). \quad (4.12)$$

Here, apart from (4.1) there are no further conditions for the vertical velocity V .

During the early stage of the interaction the deformation of the liquid boundary is small compared with the length L of the body. This fact makes it possible to linearise the boundary conditions (4.6) – (4.9) and impose them on the original position of the liquid boundary, $y = 0$, in the leading order for small ε (see section 3.1). Together with the assumption (4.12) equations (4.5), (4.6), (4.9), (4.10) form a mixed boundary value problem in terms of the

velocity potential $\varphi(x, y, t)$:

$$\nabla^2 \varphi = 0 \quad (y < 0), \quad (4.13)$$

$$\varphi_y = \omega_t(x, t) \quad (y = 0, d_1 < x < d_2), \quad (4.14)$$

$$\varphi_t = 0 \quad (y = 0, x < d_1 \text{ and } x > d_2), \quad (4.15)$$

$$\varphi = O((x^2 + y^2)^{-1/2}) \quad (x^2 + y^2 \rightarrow \infty). \quad (4.16)$$

Within this model, the thin jet formed in the overturning region is not taken into consideration. Parameters of this jet can be determined after the flow in the main flow region has been obtained (see section 3.1.5). Equations (4.13) – (4.16) are written for impact problems, where the wetted part of the moving plate corresponds to one interval $d_1 \leq x \leq d_2$ on $y = 0$. Here, the point $x = d_1, y = 0$, corresponds to the rear contact point. The type of fluid flow to be found at this contact point depends on the specific problem. We will distinguish between a flow overturning at this contact point and fluid detaching from the body at this point. In case of fluid detachment the rear contact point may be fixed at the end of a sharp edge as it will be done for the problem discussed in section 4.2. A further condition is needed if the separation point $x = d_1(t)$ is allowed to move along a smooth-shaped bottom of a body. To determine such a point we will introduce a separation criterion in section 4.4. In all problems presented in this chapter the point $x = d_2, y = 0$ corresponds to the forward overturning region referred below as the Wagner contact point. The function $d_2(t)$ is unknown in advance and will be determined by Wagner's condition.

The pressure at the contact region is given by the linearised Bernoulli's equation and the free surface elevation is given by the linearised kinematic boundary condition (see equations (4.8) and (4.9)):

$$p = -\varphi_t \quad (y = 0, d_1 < x < d_2), \quad (4.17)$$

$$\varphi_y = \eta_t \quad (y = 0, x < d_1 \text{ and } x > d_2), \quad (4.18)$$

$$\eta \equiv 0 \quad (t = 0). \quad (4.19)$$

Note that equations (4.15) and (4.17) do not contain any hydrostatic terms since we assumed condition (4.12).

The linearisation and projection of the boundary conditions onto the x -axis is an admissible simplification which is also well-known to bring satisfactory results in the airfoil theory (see Newman (1977)). However, we have to be aware of the fact that the leading order problem (4.6) – (4.9) breaks down close to a turnover region, since $\varphi'_{x'}$ and $\varphi'_{y'}$ are of order U there and the slope of the free surface function, $\eta'_{x'}(x', t')$, is unbounded in the turnover region. In section 4.2, we will show for the oblique impact of an inclined plate that linearisation and projection of equations (4.7), (4.8), (4.9) are also not valid at the initial penetration point, since the free surface elevation $\eta(x, t)$, given by the time integration of equation (4.18), will be shown to be singular there.

4.1.2 The complex velocity and complex acceleration potential

In this subsection, we will present formulas for the horizontal velocity component of the flow along the body and the hydrodynamic pressure acting on the body. The flow is governed by

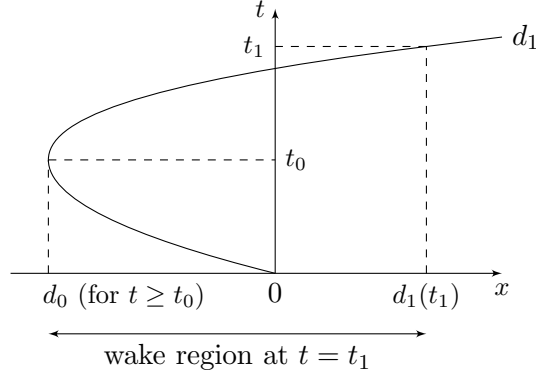


Figure 4.1: Illustration of d_0 and the wake region for a given function $d_1(t)$ at time $t = t_1$. Note that $d_0(t) = d_1(t)$ for $t \leq t_0$ with zero wake region.

the mixed boundary value problem (4.13) – (4.16). Differentiation of equation (4.15) with respect to x and integration in t implies for $x < d_1$ and $x > d_2$ that

$$\varphi_x(x, 0, t) = \int_{\mathcal{L}(x,t)} \varphi_{xt}(x, 0, \tau) d\tau, \quad \mathcal{L}(x, t) = \{\tau \in [0, t] : d_1(\tau) \leq x \leq d_2(\tau)\}. \quad (4.20)$$

The set $\mathcal{L}(x, t)$ consists of the time intervals, in which x belonged to the contact region at an earlier time than t . For monotonically decaying $d_1(t)$ and monotonically increasing $d_2(t)$ the set $\mathcal{L}(x, t)$ is empty for $x < d_1(t)$ and $x > d_2(t)$, so that $\varphi_x(x, 0, t) = 0$ there. The same observation has been made for the vertical impact of an inclined plate at constant speed in section 3.1. We assume that $\dot{d}_2(t) > 0$ in the examples presented in this thesis, so that $\mathcal{L}(x, t)$ is empty and, consequently, $\varphi_x(x, 0, t) = 0$ for $x > d_2$. In impact problems where the entering body has high horizontal speed, we cannot assume that $d_1(t)$ is monotonically decreasing in time. In fact, $\varphi_x(x, 0, t)$ need not to be zero for $d_0(t) \leq x \leq d_1(t)$, where

$$d_0(t) = \min_{0 < \tau < t} d_1(\tau). \quad (4.21)$$

The position of d_0 has been illustrated in Figure 4.1. We will call the region $d_0 < x < d_1$, $y = 0$ the wake region which corresponds in airfoil theory to the position of the vortex line behind the foil. In summary, we obtain from equation (4.20)

$$\varphi_x = \bar{\varphi}_x(x) \quad (y = 0, d_0 < x < d_1), \quad (4.22)$$

$$\varphi_x = 0 \quad (y = 0, x < d_0 \text{ and } x > d_2), \quad (4.23)$$

where the time-independent wake function $\bar{\varphi}_x(x)$ must be determined as part of the solution (see Figure 4.2). Hence, we have to impose a further condition to determine $\bar{\varphi}_x(x)$ (see section 4.1.4). Since $\bar{\varphi}_x(x)$ does not depend on time, it needs to be determined only once for any point in the wake region. Here we assume that the fluid velocity $\bar{\varphi}_x(x)$ is Hölder-continuous in the wake region $d_0 < x < d_1$, $y = 0$ but $\varphi_x(x, 0, t)$ need not to be continuous at $x = d_0$, as will be shown in section 4.2, so that the fluid velocity may be logarithmic-singular at $x = d_0$, $y = 0$ as discussed in section 2.3.

Now we solve the mixed boundary value problem (4.13), (4.14), (4.16), (4.22), (4.23) with the assumption that the kinetic energy in the fluid is finite. It can be shown as in section 3.1

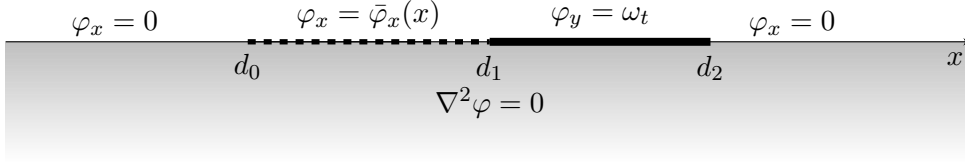


Figure 4.2: Mixed boundary value problem on the lower half plane for impact problems at high horizontal speed.

that the complex velocity $f_t(z) = \varphi_x(x, y, t) - i\varphi_y(x, y, t)$ may have square-root singularities at $z = d_1$ and $z = d_2$. As it was shown in subsection (3.1.3) the far-field condition (4.16) implies that $|f_t(z)| = O(z^{-2})$ for $|z| \rightarrow \infty$. We use formula (2.28) with $k_1 = 0$ and $k_2 = 0$ to obtain

$$\varphi_x(x, 0, t) = \frac{K(x, t)}{\pi\sqrt{(x-d_1)(d_2-x)}} \quad (d_1 < x < d_2), \quad (4.24)$$

where

$$K(x, t) = \int_{d_0}^{d_1} \frac{\sqrt{(d_1-\xi)(d_2-\xi)}}{\xi-x} \bar{\varphi}_x(\xi) d\xi + \int_{d_1}^{d_2} \frac{\sqrt{(\xi-d_1)(d_2-\xi)}}{\xi-x} \omega_t(\xi, t) d\xi. \quad (4.25)$$

Note that eigensolutions of the problem (4.13) – (4.16) with $\omega(x, t) \equiv 0$ are not included in (4.24), because their strong singularities lead to infinite energy in the fluid.

To determine the complex acceleration potential $F_{tt}(z) = \varphi_t + i\psi_t$, we specify the asymptotic behaviour of $\varphi_t(x, 0, t)$ at $x = d_1$ and $x = d_2$. First, we identify the behaviours of $\varphi_x(x, 0, t)$ close to the contact points:

$$\varphi_x(x, 0, t) = \frac{K(d_1, t)}{\pi\sqrt{d_2-d_1}}(x-d_1)^{-1/2} + O(1) \quad (x \rightarrow d_1^+), \quad (4.26)$$

$$\varphi_x(x, 0, t) = \frac{K(d_2, t)}{\pi\sqrt{d_2-d_1}}(d_2-x)^{-1/2} + O(1) \quad (x \rightarrow d_2^-). \quad (4.27)$$

We assume that the contact point $x = d_1(t)$ does not have a fixed x -position, but is moving in time. Here we do not specify if this point is moving in positive or negative direction. Since $\dot{d}_1 \neq 0$ and $\dot{d}_2 > 0$, differentiating of (4.26) and (4.27) with respect to time and integrating the resulting equations in x afterwards gives us the asymptotic behaviour of $\varphi_t(x, 0, t)$ at $x = d_1$ and $x = d_2$:

$$\varphi_t(x, 0, t) = -\frac{\dot{d}_1 K(d_1, t)}{\pi\sqrt{d_2-d_1}}(x-d_1)^{-1/2} + O(1) \quad (x \rightarrow d_1^+), \quad (4.28)$$

$$\varphi_t(x, 0, t) = -\frac{\dot{d}_2 K(d_2, t)}{\pi\sqrt{d_2-d_1}}(d_2-x)^{-1/2} + O(1) \quad (x \rightarrow d_2^-). \quad (4.29)$$

Now, we reformulate the mixed boundary value problem of the velocity potential, (4.13) –

(4.16), as the following problem in terms of $F_{tt}(z)$:

$$F_{tt}(z) \text{ analytic} \quad (y < 0), \quad (4.30)$$

$$\text{Im}(F_{tt}) = -\hat{\omega}_{tt} + C(t) \quad (y = 0, d_1 < x < d_2), \quad (4.31)$$

$$\text{Re}(F_{tt}) = 0 \quad (y = 0, x < d_1 \text{ and } x > d_2), \quad (4.32)$$

$$F_{tt}(z) = O(z^{-1}) \quad (|z| \rightarrow \infty), \quad (4.33)$$

where $\hat{\omega}_{tt}(x, t) = \int_{d_1}^x \omega_{tt}(\xi, t) d\xi$. Due to equations (4.28) and (4.29), $F_{tt}(z)$ may only have square-root singularities at d_1 and d_2 . Formula (2.25) with $k_1 = -1$ and $k_2 = -1$ gives us a particular solution $F_{tt}^*(z)$ of (4.30) – (4.32) where $F_{tt}^*(z) = O(1)$ as $|z| \rightarrow \infty$ and $F_{tt}^*(z) = O(1)$ as $z \rightarrow d_n$, $n = 1, 2$. To obtain $F_{tt}(z)$ we add the corresponding eigensolutions to $F_{tt}^*(z)$:

$$F_{tt}(z) = \frac{i}{\pi} T(z, t) \sqrt{(z - d_1)(z - d_2)} + B_1(t) \sqrt{\frac{z - d_2}{z - d_1}} - B_2(t) \sqrt{\frac{z - d_1}{z - d_2}}, \quad (4.34)$$

$$T(z, t) = \int_{d_1}^{d_2} \frac{\hat{\omega}_{tt}(\xi, t) - C(t)}{(\xi - z) \sqrt{(\xi - d_1)(d_2 - \xi)}} d\xi. \quad (4.35)$$

The functions $B_1(t)$, $B_2(t)$ and $C(t)$ are given by the asymptotic behaviour of the real part of $F_{tt}(z)$ at the contact points in (4.28) and (4.29), and by the far-field behaviour (4.33). We obtain

$$B_1(t) = \frac{\dot{d}_1 K(d_1, t)}{\pi(d_2 - d_1)}, \quad B_2(t) = \frac{\dot{d}_2 K(d_2, t)}{\pi(d_2 - d_1)}, \quad (4.36)$$

$$C(t) = \int_{d_1}^{d_2} \frac{\hat{\omega}_{tt}(\xi, t)}{\sqrt{(\xi - d_1)(d_2 - \xi)}} d\xi + B_1(t) - B_2(t). \quad (4.37)$$

where $K(x, t)$ was defined in (4.25). The real part of $F_{tt}(z)$ gives us together with the linearised Bernoulli's equation (4.17) a general formula for the hydrodynamic pressure along the contact region:

$$p(x, 0, t) = -\frac{1}{\pi} T(x, t) \sqrt{(x - d_1)(d_2 - x)} + B_1(t) \sqrt{\frac{d_2 - x}{x - d_1}} + B_2(t) \sqrt{\frac{x - d_1}{d_2 - x}}, \quad (4.38)$$

$$T(x, t) = \int_{d_1}^{d_2} \frac{\hat{\omega}_{tt}(\xi, t)}{(\xi - x) \sqrt{(\xi - d_1)(d_2 - \xi)}} d\xi. \quad (4.39)$$

Due to identity (2.34), the function $T(x, t)$ does not depend on $C(t)$ for $d_1 < \text{Re}(z) < d_2$ and $\text{Im}(z) \rightarrow 0$.

The intensity of the singularities in the pressure distribution depend on the velocities of the contact points, \dot{d}_1 and \dot{d}_2 . Even though we assumed $\dot{d}_1 \neq 0$, it can be shown that equation (4.38) also holds for $\dot{d}_1 = 0$, where we obtain $B_1(t) = 0$, so that the pressure singularity at the rear contact point is removed. We will show later, that the pressure singularity at $x = d_1$ also diminishes if the fluid separates from the body smoothly enough.

4.1.3 The complex displacement and Wagner's condition

Experiments (e.g. Judge et al., 2004) and numerical solutions (e.g. Faltinsen and Semenov, 2008) show that, for impact problems at horizontal speed, the free surface flow overturns at

the forward end of the contact region, where a thin jet is formed adjacent to the impacting plate and thrown forward (see Figure 4.3). As for vertical slamming problems, it can be shown for bodies of general shape with small deadrise angle ε , that the thickness of the spray jet and the size of the turnover region are proportional to ε^2 (see later in section 4.1.5). Hence, we can determine the position of the forward contact point, d_2 , by Wagner's condition in the linearised hydrodynamic problem (4.13) – (4.18):

$$\eta(d_2, t) = \omega(d_2, t). \quad (4.40)$$

Furthermore, we impose the following continuity condition similar to equation (4.40) at the rear contact point $x = d_1, y = 0$:

$$\eta(d_1, t) = \omega(d_1, t). \quad (4.41)$$

Condition (4.41) corresponds to Wagner's condition at the rear contact point if the flow overturns at $x = d_1, y = 0$, and $\dot{d}_1 < 0$. Condition (4.41) is used to determine d_1 . If $\dot{d}_1 > 0$, condition (4.41) corresponds to the continuous separation of the fluid at the rear contact point. In this case, condition (4.41) will determine a function characterising the wake region and d_1 has to be either prescribed or determined by an additional condition.

To employ both conditions (4.40) and (4.41), we need to know the free surface elevation $\eta(x, t)$. We reformulate the hydrodynamic problem (4.13) – (4.18) with respect to the displacement potential $\Phi(x, y, t)$ defined in (3.33). The mixed boundary value problem in terms of the displacement potential is given by:

$$\nabla^2 \Phi = 0 \quad (y < 0), \quad (4.42)$$

$$\Phi_y = \omega(x, t) \quad (y = 0, d_1 < x < d_2), \quad (4.43)$$

$$\Phi_x = 0 \quad (y = 0, x < d_0 \text{ and } x > d_2), \quad (4.44)$$

$$\Phi_x = t\bar{\varphi}_x(x) + A(x) \quad (y = 0, d_0 < x < d_1), \quad (4.45)$$

$$\Phi = O((x^2 + y^2)^{-1/2}) \quad (x^2 + y^2 \rightarrow \infty). \quad (4.46)$$

Equations (4.42), (4.44), (4.45) and (4.46) are obtained by integrating equations (4.13), (4.22), (4.23) and (4.16) in time (see also subsection 3.1.4). The function $A(x)$ in equation (4.45) is an undetermined term due to the time-integration. As for equation (4.43) we have to be aware that a fixed point $d_1(t) < x < d_2(t), y = 0$ may be behind the contact region, $x < d_1(\tau)$, or is in front of the contact point, $x > d_2(\tau)$, at time intervals $\tau \in (t_0, t_1), (t_2, t_3), \dots, (t_{n-1}, t_n)$, where $0 = t_0 < t_1 < \dots < t_n < t$. In particular, x belongs to the contact region $d_1(\tau) < x < d_2(\tau)$ at time intervals $\tau \in (t_1, t_2), \dots, (t_{n-2}, t_{n-1}), (t_n, t)$. Then we obtain together with equations (4.14), (4.18), conditions (4.40), (4.41) and initial condition $\eta(x, 0) \equiv 0$:

$$\begin{aligned} \Phi_y(x, 0, t) &= \int_{t_0}^{t_1} \varphi_y(x, 0, \tau) d\tau + \int_{t_1}^{t_2} \varphi_y(x, 0, \tau) d\tau + \dots + \int_{t_n}^t \varphi_y(x, 0, \tau) d\tau \\ &= \eta(x, t_1) - \omega(x, t_1) + \omega(x, t_2) - \eta(x, t_2) + \dots - \omega(x, t_n) + \omega(x, t) \\ &= \omega(x, t) \end{aligned} \quad (4.47)$$

A derivation similar to (4.47) using (4.14), (4.18), (4.40), (4.41) implies that

$$\eta(x, t) = \Phi_y(x, 0, t). \quad (4.48)$$

Equation (4.48) is used to determine the free surface elevation, where $\Phi_y(x, 0, t)$ is determined by the problem (4.42) – (4.46).

The boundary-value problem (4.42) – (4.46) for $\Phi(x, y, t)$ is similar to the problem (4.13) – (4.16). We seek the solution of the problem (4.42) – (4.46) where $\Phi_x(x, y, t)$ and $\Phi_y(x, y, t)$ are bounded at $x = d_1$ and $x = d_2$, $y = 0$, since the complex velocity $f_t(z)$ is square-root singular there and we assume that $\dot{d}_1 \neq 0$ and $\dot{d}_2 > 0$. We use equation (2.27) and (2.29) with $k_1 = 0$ and $k_2 = 0$ to obtain

$$\Phi_y(x, 0, t) = \pm \frac{E(x, t)}{\pi \sqrt{(x - d_1)(x - d_2)}} \quad (x < d_1 \text{ and } x > d_2), \quad (4.49)$$

where

$$E(x, t) = \int_{d_0}^{d_1} \frac{\sqrt{(d_1 - \xi)(d_2 - \xi)}}{\xi - x} \Phi_x(\xi, 0, t) d\xi + \int_{d_1}^{d_2} \frac{\sqrt{(\xi - d_1)(d_2 - \xi)}}{\xi - x} \omega(\xi, t) d\xi. \quad (4.50)$$

The plus sign in (4.49) applies for $x > d_2$ and the minus sign for $x < d_1$. Note that the first integral on the right-hand side of (4.50) is not a Cauchy principal value integral for $x < d_0$ or $x > d_2$. It follows from equation (4.48) that (4.49) gives the free-surface elevation for $x < d_1$ and $x > d_2$. The boundedness of $\Phi_y(x, 0, t)$ at $x = d_1$ and $x = d_2$ implies that $E(d_1, t) = 0$ and $E(d_2, t) = 0$. The formula (4.50) applied to $x = d_1$ and $x = d_2$ yields two integral equations

$$\int_{d_0}^{d_1} \sqrt{\frac{d_2 - \xi}{d_1 - \xi}} \Phi_x(\xi, 0, t) d\xi = \int_{d_1}^{d_2} \sqrt{\frac{d_2 - \xi}{\xi - d_1}} \omega(\xi, t) d\xi, \quad (4.51)$$

$$\int_{d_0}^{d_1} \sqrt{\frac{d_1 - \xi}{d_2 - \xi}} \Phi_x(\xi, 0, t) d\xi = - \int_{d_1}^{d_2} \sqrt{\frac{\xi - d_1}{d_2 - \xi}} \omega(\xi, t) d\xi. \quad (4.52)$$

Equation (4.52) determines the forward contact point d_2 . If $\dot{d}_1 > 0$, equation (4.51) is used to determine the function $A(x)$ in equation (4.45) in the wake region at $x = d_1$. In this case, $d_1(t)$ and $\bar{\varphi}_x(t)$ have to be either prescribed or determined by additional conditions. However, if $\dot{d}_1(t) < 0$ at time t , the functions $\bar{\varphi}_x(x)$ and $A(x)$ are already known and equation (4.51) determines the position of the rear contact point d_1 , instead. In this case, no additional equations are needed. Combining equations (4.51) and (4.52) we obtain

$$\int_{d_1}^{d_2} \frac{\omega(\xi, t)}{\sqrt{(d_2 - \xi)(\xi - d_1)}} d\xi = \int_{d_0}^{d_1} \frac{\Phi_x(\xi, 0, t)}{\sqrt{(d_1 - \xi)(d_2 - \xi)}} d\xi. \quad (4.53)$$

Without accounting for the wake, equation (4.53) was derived by Korobkin (1995) for vertical-impact problems.

To evaluate the hydrodynamic pressure acting on the plate, given by equation (4.38), we also need to find \dot{d}_2 . We obtain the following equation for \dot{d}_2 by differentiating (4.52) in time

and using equation (4.53):

$$\dot{d}_2 = 2 \frac{\int_{d_0}^{d_1} \sqrt{\frac{d_1-\xi}{d_2-\xi}} \varphi_x(\xi) d\xi + \int_{d_1}^{d_2} \sqrt{\frac{\xi-d_1}{d_2-\xi}} \omega_t(\xi, t) d\xi}{\int_{d_0}^{d_1} \frac{\sqrt{d_1-\xi}}{(d_2-\xi)^{3/2}} \Phi_x(\xi, 0, t) d\xi - 2 \int_{d_1}^{d_2} \sqrt{\frac{\xi-d_1}{d_2-\xi}} \omega_\xi(\xi, t) d\xi - \int_{d_1}^{d_2} \frac{\omega(\xi, t)}{\sqrt{(\xi-d_1)(d_2-\xi)}} d\xi}. \quad (4.54)$$

Since in many examples discussed in this thesis a direct calculation of d_2 from equation (4.52) is not possible, we will compute d_2 by solving the ordinary differential equation (4.54) in terms of d_2 numerically.

Combining equations (4.49) and (4.51) together removes the square-root singularity of $\Phi_y(x, 0, t)$ at $x = d_1$, so that we obtain together with equation (4.48) the following formula for the position of the free surface for $x \leq d_1$:

$$\eta(x, t) = \omega(d_1, t) - \sqrt{\frac{d_1-x}{d_2-x}} \left(\frac{1}{\pi} H_1(x, t) + \omega(d_1, t) \right) \quad (x \leq d_1), \quad (4.55)$$

$$H_1(x, t) = \int_{d_0}^{d_1} \sqrt{\frac{d_2-\xi}{d_1-\xi}} \frac{\Phi_x(\xi, 0, t)}{\xi-x} d\xi - \int_{d_1}^{d_2} \sqrt{\frac{d_2-\xi}{\xi-d_1}} \frac{\omega(\xi, t) - \omega(d_1, t)}{\xi-x} d\xi. \quad (4.56)$$

Note that for (4.55) and (4.56) we used the following identity, which can be derived from (2.34):

$$\int_{d_1}^{d_2} \sqrt{\frac{d_2-\xi}{\xi-d_1}} \frac{1}{\xi-x} d\xi = \pi \left(\sqrt{\frac{x-d_2}{x-d_1}} - 1 \right) \quad (x < d_1 \text{ and } x > d_2). \quad (4.57)$$

The integrals in $H_1(x, t)$ are bounded as $x \rightarrow d_1$. Similarly, we imply from (4.49) and (4.52) the formula for the fluid elevation in front of the contact region,

$$\eta(x, t) = \omega(d_2, t) - \sqrt{\frac{x-d_2}{x-d_1}} \left(\frac{1}{\pi} H_2(x, t) + \omega(d_2, t) \right) \quad (x \geq d_2), \quad (4.58)$$

$$H_2(x, t) = \int_{d_0}^{d_1} \sqrt{\frac{d_1-\xi}{d_2-\xi}} \frac{\Phi_x(\xi, 0, t)}{\xi-x} d\xi + \int_{d_1}^{d_2} \sqrt{\frac{\xi-d_1}{d_2-\xi}} \frac{\omega(\xi, t) - \omega(d_2, t)}{\xi-x} d\xi. \quad (4.59)$$

In particular, formulas (4.55) and (4.58) confirm the continuity of the fluid boundary at $x = d_1$ and $x = d_2$ imposed by conditions (4.40) and (4.41). The formulas (4.55) and (4.58) are suitable to compute the position of the free surface.

To obtain the asymptotical behaviour of the free surface at $x = d_1$ and $x = d_2$, we start with the vertical velocity $\varphi_y(x, 0, t)$ given by the mixed boundary value problem (4.13) – (4.16) where we use (2.27) and (2.29) with $k_1 = k_2 = 0$:

$$\varphi_y(x, 0, t) = \pm \frac{K(x, t)}{\pi \sqrt{(x-d_1)(x-d_2)}} \quad (x < d_1 \text{ and } x > d_2). \quad (4.60)$$

The function $K(x, t)$ is given by (4.25). The plus sign in (4.60) applies for $x > d_2$ and the minus sign for $x < d_1$. Integrating the asymptotic behaviour of $\varphi_y(x, 0, t)$ at $x = d_1$ and $x = d_2$ in time and accounting for the continuity of the fluid boundary at $x = d_1$ and $x = d_2$

lead to

$$\eta(x, t) = \omega(d_1, t) - \frac{2K(d_1, t)}{\pi \dot{d}_1 \sqrt{d_2 - d_1}} \sqrt{d_1 - x} + O(d_1 - x) \quad (x < d_1, x \rightarrow d_1), \quad (4.61)$$

$$\eta(x, t) = \omega(d_2, t) - \frac{2K(d_2, t)}{\pi \dot{d}_1 \sqrt{d_2 - d_1}} \sqrt{x - d_2} + O(x - d_2) \quad (x > d_2, x \rightarrow d_2). \quad (4.62)$$

If $K(d_1, t) \neq 0$ and $K(d_2, t) \neq 0$, we obtain the typical free surface-shape characterising the turnover region in the linearised hydrodynamic problem. However, in the case of fluid separation we expect that the fluid detaches tangentially.

If d_1 and $\omega(x, t)$ are prescribed and $\dot{d}_1 > 0$, then we have three unknown functions, namely $d_2(t)$, $\bar{\varphi}_x(x)$ and $A(x)$, but we have only derived two equations (4.51) and (4.52). In the next section we introduce Kutta's condition to obtain a third equation, which determines $\bar{\varphi}_x(x)$.

4.1.4 Kutta's condition

In this section we introduce Kutta's condition which characterises the fluid detachment at the separation point. In viscous fluid, thin boundary layers are generated along the body surface. Usually for high Reynolds-numbers these boundary layers are very thin and give only negligible contribution to the global fluid flow so that we can treat the fluid as inviscid. However, at sharp edges of the body, viscous effects play a significant role. While in potential theory the fluid flows around the sharp edge with infinite flow speed, experimental and numerical results show that the fluid separates from the body at the sharp edge (Batchelor, 1967). This phenomenon is also well known in air flow around thin wings where air along the wing surface detaches from the wing at the trailing edge.

Inviscid fluid flow problems around a wing requires a condition to incorporate flow separation at the trailing edge. Flow separation at edges can be enforced by the condition of finite flow speed at the sharp edge, corresponding to Kutta's condition (see e.g. Newman, 1977). This condition is also suitable for unsteady problems and has been successfully applied in many problems, e.g. two-fluid problems along a body with a sharp edge and separated flows past bluff bodies (see Crighton, 1985).

For impact problems at high speed discussed in this thesis we use Kutta's condition if the fluid separates at the rear contact point. In the linearised hydrodynamic problem the rear contact point corresponds to $x = d_1$, $y = 0$, so that Kutta's condition is given by

$$|\nabla\varphi(d_1, 0, t)| < \infty. \quad (4.63)$$

Note that it is already sufficient to assume that only one of the velocity components, either vertical or horizontal velocity component, is finite at the separation point. In general, condition (4.24) implies that the flow speed is singular at $x = d_1$, $y = 0$, so that condition (4.63) gives us the following equation:

$$K(d_1, t) = 0. \quad (4.64)$$

Equation (4.64) removes the inverse-square-root singularity of the hydrodynamic pressure in (4.38) at $x = d_1$. More precisely, the pressure decreases to the atmospheric value as the

square-root of the distance from the trailing edge. Equation (4.61) indicates that Kutta's condition smoothens the fluid surface shape at the separation point. This will be discussed further in section 4.3.

In the following, we show that the vertical fluid velocity is continuous at the fluid separation point due to (4.64). By using the definition (4.25) for $K(x, t)$, equation (4.64) can be written as a square-root singular Volterra integral equation of the first kind w.r.t. $\bar{\varphi}_x(x)$:

$$\int_{d_0}^{d_1} \sqrt{\frac{d_2-\xi}{d_1-\xi}} \bar{\varphi}_x(\xi) d\xi = \int_{d_1}^{d_2} \sqrt{\frac{d_2-\xi}{\xi-d_1}} \omega_t(\xi, t) d\xi. \quad (4.65)$$

Similar results from Kutta's condition in mixed boundary value problems can be found in the two-dimensional thin-airfoil theory (see Newman, 1977). This equation will be used later to determine $\bar{\varphi}_x(x)$. Similar to the vertical elevation of the fluid in the wake in equation (4.55), it can be shown that the vertical velocity of the fluid can be written as follows:

$$\varphi_y(x, 0, t) = \omega_t(d_1, t) - \sqrt{\frac{d_1-x}{d_2-x}} \left(\frac{1}{\pi} H_3(x, t) + \omega_t(d_1, t) \right) \quad (x \leq d_1), \quad (4.66)$$

$$H_3(x, t) = \int_{d_0}^{d_1} \sqrt{\frac{d_2-\xi}{d_1-\xi}} \frac{\bar{\varphi}_x(\xi)}{\xi-x} d\xi - \int_{d_1}^{d_2} \sqrt{\frac{d_2-\xi}{\xi-d_1}} \frac{\omega_t(\xi, t) - \omega_t(d_1, t)}{\xi-x} d\xi. \quad (4.67)$$

The integrals in $H_3(x, t)$ are bounded for x close to d_1 if the functions $\bar{\varphi}_x(\xi)$ and $\omega_t(x, t)$ are smooth enough in x . If so, the vertical velocity of the fluid $\varphi_y(x, 0, t)$ is continuous at $x = d_1$. This indicates that the fluid detachment from the body is tangential. A more detailed asymptotic analysis of $\varphi_y(x, 0, t)$ and $\Phi_y(x, 0, t)$ at $x = d_1$ will be presented in section 4.3.

4.1.5 Energy of the flow

The energy in the fluid bulk and the energy in the spray jet were calculated for the vertical impact of an inclined rigid plate in section 3.1.5. In this section, we identify these energies for the problem of body impact at high horizontal speed if Kutta's condition is satisfied at the rear contact point. We show that the total energy in this model is conserved for general body shape and general body motion.

During the early stage of impact the flow in the jet root can be approximated by the quasi-steady Kelvin-Helmholtz cavity flow as discussed in section 3.1.5. Here this cavity flow, given by equations (3.48) and (3.49), is obtained for the inner variables $\tilde{x} = (x - d_2)/\varepsilon^2$, $\tilde{y} = (y - \varepsilon\omega(d_2, t))/\varepsilon^2$ and the inner velocity potential $\tilde{\varphi}(\tilde{x}, \tilde{y}) = \varepsilon^{-1}\varphi(x, y)/\dot{d}_2 - \tilde{x}$. The solution of the cavity flow in the far-field is given by equation (3.48). We match this solution with the outer horizontal flow velocity given by (4.24) in the region $x = d_2 + O(\varepsilon)$ to obtain the non-dimensional thickness of the jet, δ :

$$\delta = \frac{\varepsilon^2 K^2(d_2, t)}{4\pi(d_2 - d_1) \dot{d}_2^2}, \quad (4.68)$$

where $K(x, t)$ is defined in (4.25). Equation (4.68) confirms that the thickness of the jet is proportional to ε^2 . The non-dimensional jet velocity in the reference frame moving with the turnover region is \dot{d}_2 , so the jet velocity in the global frame of reference xOy is $2\dot{d}_2$, hence

the energy flux into the jet in non-dimensional variables is

$$\frac{d}{dt} E_{\text{jet}}^{(f)} = \frac{1}{2} \left[2\dot{d}_2 \right]^2 \times \delta d_2 \times \frac{1}{\varepsilon^2} = \frac{\dot{d}_2 K^2(d_2, t)}{2\pi(d_2 - d_1)}, \quad (4.69)$$

where we scaled the energies by $\varepsilon^2 \rho_F U^2 L^2$. The rate of change of the kinetic energy of the fluid bulk (excluding that in the jet) can be written, using equations (4.14) and (4.17),

$$\begin{aligned} \frac{d}{dt} E_{\text{bulk}}^{(f)} &= \frac{1}{2} \frac{d}{dt} \int_{\{y \leq 0\}} (\varphi_x^2 + \varphi_y^2) dx dy = \frac{1}{2} \frac{d}{dt} \int_{d_0}^{d_2} \varphi \varphi_y \Big|_{y=0} dx \\ &= -\frac{1}{2} \int_{d_1}^{d_2} p \omega_t dx + \frac{1}{2} \int_{d_0}^{d_2} \varphi \varphi_{ty} \Big|_{y=0} dx. \end{aligned} \quad (4.70)$$

where $p = p(x, 0, t)$ in this subsection. With the help of equation (D.1) derived in appendix D and with the assumption that Kutta's condition is satisfied at $x = d_1$, we obtain

$$\frac{d}{dt} E_{\text{bulk}}^{(f)} = - \int_{d_1}^{d_2} p \omega_t dx - \frac{\dot{d}_2 K^2(d_2, t)}{2\pi(d_2 - d_1)}. \quad (4.71)$$

Equations (4.69) and (4.71) give

$$\frac{d}{dt} \left(E_{\text{bulk}}^{(f)} + E_{\text{jet}}^{(f)} \right) = - \int_{d_1}^{d_2} p \omega_t dx, \quad (4.72)$$

where the right-hand side is the time-derivative of the work done by the elastic plate on the fluid and $E_{\text{bulk}}^{(f)} + E_{\text{jet}}^{(f)}$ is the total kinetic energy of the flow both in the bulk and in the jet. This confirms that the energy in the fluid-plate system is also conserved in the linearised hydrodynamic model.

4.2 Oblique impact of a rigid plate at constant speed

We consider the unsteady water flow due to an inclined semi-infinite rigid plate which is obliquely moving onto a flat water surface with constant speed (see Figure 4.3). This problem is self-similar and was investigated for arbitrary angle of attack in Faltinsen and Semenov (2008). In this paper, numerical results were presented for the fully nonlinear problem for

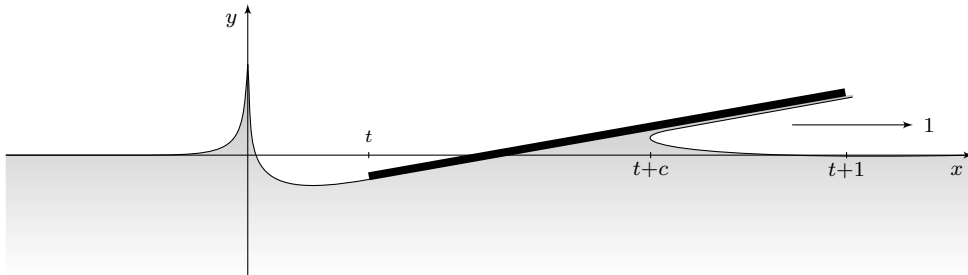


Figure 4.3: Impact of a semi-infinite plate onto deep water at time $t > 0$ as viewed in the frame of reference, where the fluid in the far-field is at rest. Note the splash region at the initial penetration point, the trailing edge at $x = t$, where the fluid detaches from the plate and the jet thrown forwards from the turnover region at $x = t + c$. The plate descends with constant non-dimensional vertical speed χ .

a wide range of angles of attack of such a plate. The problem of oblique plate impact for small angle of attack and horizontal speed much larger than its constant vertical speed can be solved using airfoil theory together with Wagner's condition at the forward contact point. Such a model was investigated in Wagner (1932), Sedov (1940) and Ulstein and Faltinsen (1996). Here, we reinvestigate this impact problem using the model introduced in section 4.1 and we will confirm the results in Sedov (1940) and Ulstein and Faltinsen (1996). We will arrive to the same analytical results as presented in Sedov (1940). Analytical results were not given in Wagner (1932) and Ulstein and Faltinsen (1996). It is worth to present the following derivation of the results, since it is much shorter and simpler than the one of Sedov (1940). Moreover, the results of the behaviour of the free surface elevation close to the initial penetration point and the energy in the jet are new. The results of the speed of the contact point and the velocity flow in the wake given in this section will be used later to start numerical calculations of more complicated plate impact problems as discussed for the free fall of rigid and elastic plates at high horizontal speed in sections 4.4, 5.1 and 5.2.

4.2.1 Mathematical formulation

Initially the liquid is at rest and occupies the lower half plane $y' < 0$. The rigid semi-infinite plate is inclined to the liquid free surface at a small angle ε and, initially, the trailing edge of the plate touches the free surface at a single point which is taken as the origin of the Cartesian coordinate system $x'Oy'$ described in subsection 4.1.1. At time $t' = 0$ the plate starts to penetrate the liquid vertically at constant velocity V , and to move horizontally at the constant speed U , where we assume that U is large compared to V (see equation (4.1)). The shape of the plate is given by the function $y' = (x' - Ut') \tan(\varepsilon) - Vt'$ for $x' \geq Ut'$. We choose a lengthscale L which is small enough such that the Froude number $Fr = U/\sqrt{gL}$ is small and the hydrostatic terms in equation (4.8) and (4.9) can be neglected in the leading order model.

We use the scalings given in equations (4.2) – (4.4). The non-dimensional position of the plate is given by $y = \varepsilon\omega(x, t)$ at leading order in ε where

$$\omega(x, t) = x - (1 + \chi)t \quad (x > t). \quad (4.73)$$

The parameter $\chi = V/(\varepsilon U)$ is the non-dimensional vertical velocity. In the linearised hydrodynamic model given by (4.13) – (4.19) the rear contact point $x = d_1$, $y = 0$, where here $d_1 = t$, corresponds to the trailing edge. At the trailing edge, we impose condition (4.41) and Kutta's condition (4.63). As to the forward contact point its horizontal speed \dot{d}_2 is assumed positive during the impact. Its position is given by Wagner's condition (4.40). Note that the solution of the problem (4.13) – (4.19), (4.40), (4.41) and (4.63) only depends on the non-dimensional vertical penetration velocity χ .

4.2.2 Solution of the problem

In the linearised hydrodynamic problem given by (4.13) – (4.19) in terms of the velocity potential and given by the problem (4.42) – (4.46) in terms of the displacement potential we have to find the position of the forward contact point $x = d_2(t)$, $y = 0$, and the two functions $\bar{\varphi}_x(x)$ and $A(x)$ in the wake region between the initial splash and the advancing

trailing edge, $0 \leq x \leq t$. It has been shown in section 4.1 that the three functions are determined by equations (4.51), (4.52) and (4.65) which are derived from the conditions (4.40), (4.41) and (4.63). In this problem equations (4.51), (4.52) and (4.65) have the form

$$\int_0^t \sqrt{\frac{t+c-\xi}{t-\xi}} \bar{\varphi}_x(\xi) d\xi = -\frac{\pi}{2}(1+\chi)c, \quad (4.74)$$

$$\int_0^t \sqrt{\frac{t+c-\xi}{t-\xi}} (t\bar{\varphi}_x(\xi) + A(\xi)) d\xi = \frac{\pi}{8}c(c-4\chi t), \quad (4.75)$$

$$\int_0^t \sqrt{\frac{t-\xi}{t+c-\xi}} (t\bar{\varphi}_x(\xi) + A(\xi)) d\xi = \frac{\pi}{8}c(-3c+4\chi t), \quad (4.76)$$

where $c(t) = d_2(t) - t$ is the length of the contact region. As mentioned before the flow resulting from rigid plate impact at constant speed is self-similar with φ/t depending on the variables x/t , y/t , and η/t , ω/t depending on x/t . As a result of this self-similarity, the speed of the turnover point \dot{c} is constant with $c(t) = \dot{c}^*t$, where the star stands for a constant value of the corresponding function. Since the function $\varphi_x(x, 0, t)$ depends on x/t and $\varphi_x(x, 0, t)$ is time-independent for $0 < x < t$, we find that $\bar{\varphi}_x(x) = \varphi_x^*$ is constant. Then it can be shown from (4.45) and the definition of the displacement potential, (3.33), that $A(x) = A^*x$. The self-similar representations of $\bar{\varphi}_x(x)$, $A(x)$ and $c(t)$ are used to evaluate the integrals in (4.74) – (4.76). Changing the variable of integration in (4.74) – (4.76) to $u = \xi/t$, we obtain a system of three algebraic equations with respect to three constants φ_x^* , A_* and \dot{c}^* . The solution of this system in parametric form is

$$\dot{c}^* = q^{-2}, \quad \varphi_x^* = -\frac{\pi}{4q} \frac{\chi - 1 + 2q^2(1 + 2\chi)}{(q^2 + 1)^{3/2}}, \quad A_* = -\varphi_x^* \frac{4q^2 + 1}{2q^2 + 2}, \quad (4.77)$$

where $q(\chi)$ depends on the downward velocity χ through the following equation

$$\operatorname{arsinh}(q) = q\sqrt{q^2 + 1} \frac{\chi + 3 - 2\chi q^2}{\chi - 1 + 2q^2(1 + 2\chi)}. \quad (4.78)$$

For $\chi > 0$ it can be shown that both the numerator and denominator in the fraction in equation (4.78) are positive. Hence, for any $\chi > 0$, equations in (4.77) show that the horizontal velocity φ_x^* in the wake is always negative, and A_* is always positive. In particular, $\varphi_x(x, 0, t)$ is not continuous at $x = 0$. The solution obtained in (4.77) will be used below to start the computations of the unsteady motions of either a rigid or an elastic plate, governed by either Newton's law or Euler's equation discussed in sections 4.4, 5.1 and 5.2.

For large χ we found the asymptotic behaviour of $q(\chi)$ from equation (4.78):

$$q(\chi) = \sqrt{3}\left(\frac{1}{2}\chi^{-1/2} - \frac{1}{20}\chi^{-3/2}\right) + O(\chi^{-5/2}) \quad (\chi \rightarrow \infty). \quad (4.79)$$

Equations in (4.77) gives us together with the asymptotics in (4.79) the asymptotic behaviour for \dot{c}^* , φ_x^* and A_* for large χ :

$$\dot{c}^* = \frac{4}{3}\chi + \frac{4}{15} + O(\chi^{-1}) \quad (\chi \rightarrow \infty), \quad (4.80)$$

$$\varphi_x^* = -\frac{\pi}{6}\sqrt{3}\left(\chi^{3/2} + \frac{39}{40}\chi^{1/2}\right) + O(\chi^{-1/2}) \quad (\chi \rightarrow \infty), \quad (4.81)$$

$$A_* = \frac{\pi}{12}\sqrt{3}\left(\chi^{3/2} + \frac{129}{40}\chi^{1/2}\right) + O(\chi^{-1/2}) \quad (\chi \rightarrow \infty). \quad (4.82)$$

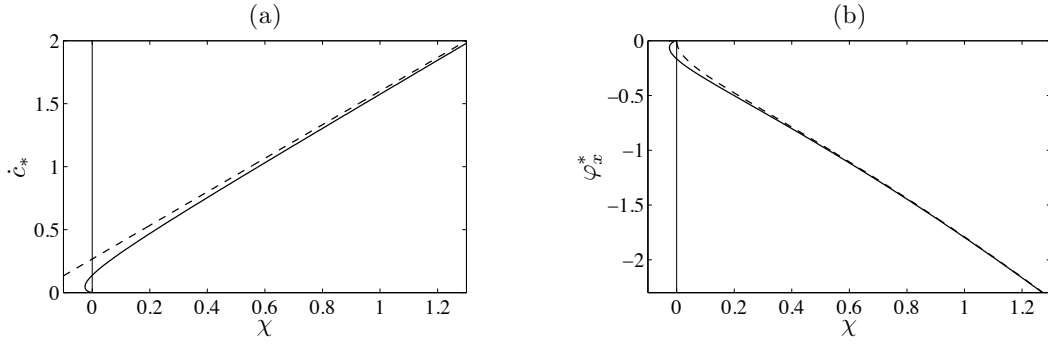


Figure 4.4: Results for a rigid plate that enters the water surface with constant vertical velocity χ . (a) The horizontal speed of the forward contact point, \dot{c}_* , and (b) the horizontal velocity of the fluid in the wake, φ_x^* , as functions of χ (solid lines). The dotted lines show the approximations given by equations (4.80) and (4.81).

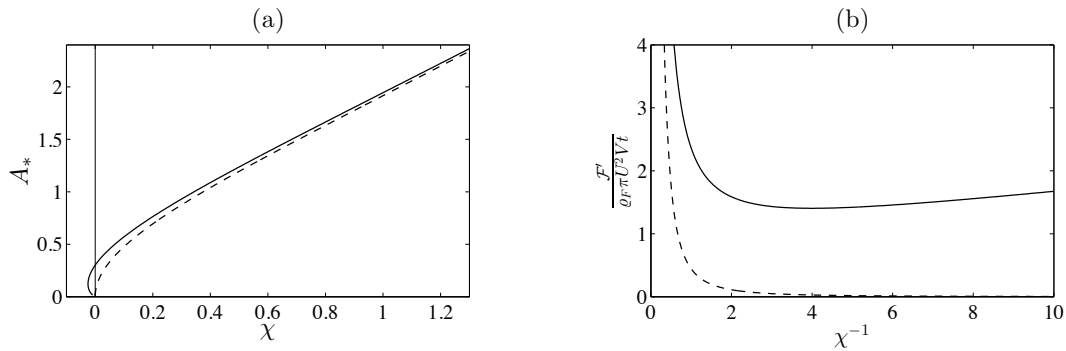


Figure 4.5: (a) A_* as a function of χ (solid line) and its approximation (dashed line) given by equations (4.82), (b) the vertical hydrodynamic force acting on the plate (rigid) which is compared with $\mathcal{F}'_{\text{vertical}} = \frac{4\pi}{9} V^3 \rho_F \varepsilon^{-2} t'$ (dashed line), which is the vertical hydrodynamic force for vertical impact of an inclined plate.

Figures 4.4(a), 4.4(b) and 4.5(a) show \dot{c}_* , φ_x^* and A_* as functions of χ , together with their asymptotes for large χ . The exact solutions already agree with their approximations very well for χ of order 1. Figures 4.4(a), 4.4(b) and 4.5(a) also show that nontrivial solutions exist for negative χ in the interval $-0.0251 < \chi \leq 0$. In this interval we find for each χ two possible solutions. These solutions may be not physical. Figure 4.4(a) also shows that the relative difference between the wetted length $\dot{c}_* t$ and the length of the plate below the equilibrium position of the fluid, χt , the so-called Karman wetted length, is larger for small χ . So the water pile-up is more important for smaller non-dimensional vertical speed. For large vertical speeds, when $\chi \rightarrow \infty$, we have $\dot{c}_*/\chi \rightarrow 4/3$ (see equation (4.80)) agreeing with the position of the contact point for the vertical impact of an inclined plate with zero horizontal speed, where we found $c'(t') = \frac{4}{3} V t' / \varepsilon$ (see section 3.1).

The pressure distribution along the wetted part of the plate, $t < x < t + \dot{c}_* t$, is given by (4.38), where now $B_1(t) = 0$ due to equation (4.74) and the first term in (4.38) is zero due

to equation (2.34), so that we obtain

$$p(x, 0, t) = p_*(\chi) \sqrt{\frac{x/t - 1}{1 + \dot{c}_* - x/t}}, \quad p_*(\chi) = 2\chi + 1 + \frac{\chi - 1}{2q^2(\chi)}. \quad (4.83)$$

It can be shown, that $p_*(\chi)$ is positive for all χ , so that the hydrodynamic pressure (4.83) is positive on the wetted part of the plate. The pressure is square-root singular at the turnover point $x = t + \dot{c}_*t$ and is zero at the trailing edge. The vertical component of the hydrodynamic force $F(t)$ acting on the plate is

$$\mathcal{F}(t) = \frac{\pi}{2} t p_*(\chi) \dot{c}_*. \quad (4.84)$$

The dimensional hydrodynamic force \mathcal{F}' is a linear function of time t' in this problem. The force is scaled in the same way as in Ulstein and Faltinsen (1996) and Sedov (1940). Our calculations yield

$$\frac{F'}{\rho_F U^2 V t' \pi} = \frac{\dot{c}_* p_*(\chi)}{2\chi}. \quad (4.85)$$

The non-dimensional force (4.85) is shown as a function of χ^{-1} in Figure 4.5(b) and it is identical to the results of Ulstein and Faltinsen (1996) and Sedov (1940). Furthermore, in Figure 4.5(b) the hydrodynamic force is compared with the one for vertical impact of an inclined plate (see first equation in (3.32)). It is shown that the loads are much larger when the plate enters the fluid with large horizontal speed corresponding to small χ . For $\chi \rightarrow \infty$, we obtain

$$\frac{\dot{c}_* p_*(\chi)}{2\chi} = \frac{4}{9} \chi^2 + \frac{16}{15} \chi + O(1) \quad (\chi \rightarrow \infty), \quad (4.86)$$

which is consistent with the hydrodynamic forces for vertical impact. As to the energy in the fluid bulk and the energy lost in the spray jet we obtain from equations (4.69) and (4.71):

$$E_{\text{bulk}}(t) = \frac{\pi p_*(\chi)(3 + \chi - 2\chi q^2)}{8q^2(1 + q^2)} t^2, \quad E_{\text{jet}}(t) = \frac{\pi p_*^2(\chi)}{4(1 + q^2)} t^2. \quad (4.87)$$

The total energy in the fluid is given by $E_{\text{total}}(t) = E_{\text{jet}}(t) + E_{\text{bulk}}(t)$. Figure 4.6(a) shows the total energy in the fluid at time $t = 1$ as a function of χ . For large χ this value increases quickly by $E_{\text{total}}(1) \sim \frac{4\pi}{9} \chi^4$. The portion of the energy lost in the jet, E_{jet} , relative to the total energy E_{total} is plotted in Figure 4.6(b). This figure shows that for small positive χ the energy lost in the jet can be up to 80% of the total energy in the fluid. For large χ the value $E_{\text{jet}}/E_{\text{total}}$ asymptotes to 0.5, which agrees with the equipartition of E_{jet} and E_{bulk} for vertical slamming.

The free surface elevation behind and in front of the body can be calculated by (4.55) and (4.58), where the horizontal displacement in the wake in equations (4.56) and (4.59) is given explicitly by $\Phi_x(x, 0, t) = t\varphi_x^* + A_*x$, so that we can find an analytical solution for the free surface elevation. However, here we only present the free surface elevation at the initial

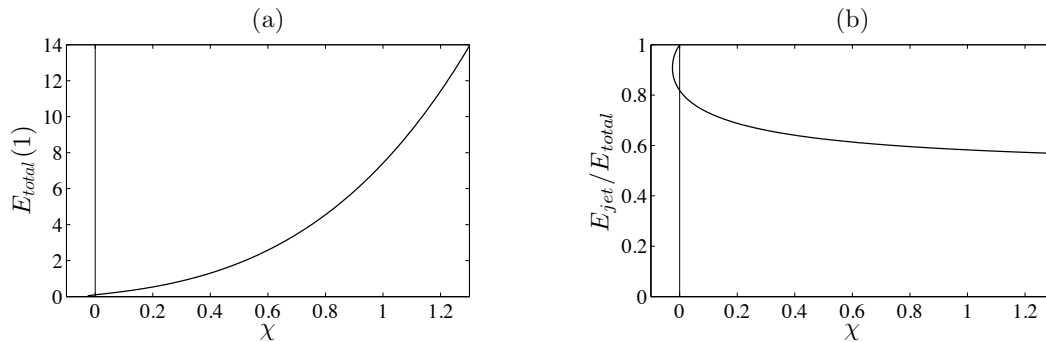


Figure 4.6: (a) The coefficient of the total energy $E_{\text{total}}(1)$ (see (4.87)) as a function of χ . (b) The ratio of the energy lost in the jet and the total energy in the fluid, $E_{\text{jet}}/E_{\text{total}}$.

penetration point which behaves as

$$\frac{\eta(x, t)}{t} = \frac{1}{\pi} \left(\varphi_x^* + A_* \frac{x}{t} \right) \log \left| \frac{x/t}{4(q^2 + 1)} \right| - (1 + \chi) + \frac{\varphi_x^*}{\pi} (1 - 2q^2) + O\left(\frac{x}{t}\right) \quad \left(\frac{x}{t} \rightarrow 0\right). \quad (4.88)$$

This logarithmic singularity represents the splash behind the plate developing in the region of the initial penetration point. Since the plate leaves the splash area quickly, this singularity is less pronounced than the inverse-square-root singularity of the free-surface elevation for the vertical impact of an inclined rigid plate as shown in section 3.1. Still, the presence of a singularity in $\eta(x, t)$ at $x = 0$ indicates the existence of an inner region. In this thesis, the local flow structure at the origin is not discussed.

4.2.3 Comparison with experiments and numerical solutions

We compared the horizontal speed of the contact point $x = \dot{c}_* t$ with the horizontal speed of the turnover regions in the numerical solutions of the fully nonlinear problem in Faltinsen and Semenov (2008) and Iafrati (2010). Unfortunately in Faltinsen and Semenov (2008) there is only one numerical solution available ($\varepsilon = 20^\circ$, $V/U = 0.36$), where the angle of attack ε is small and the horizontal speed of the plate is much faster than the vertical speed. Iafrati (2010) computed a numerical solution for $\varepsilon = 10^\circ$ and $V/U = 0.03$. Moreover, we compared our solution with the data given by the experiments in Smiley (1951), which were conducted for the oblique impact of a heavy steel plate with length 1.52m and width 0.30m for various angles of attack and various impact velocities (see Figure 4.7). In particular, Smiley (1951) presented results for the position of the maximum pressure, which we compare with the position of the contact point in our model. Note that in these results the speed of the maximum-pressure position, slightly decay in time, so that the experimental result do only roughly agree with a self-similar solution. This may come from the gravity acting on the fluid, the small deceleration of the plate during the impact and from three-dimensional effects, since the width of the plate is rather small compared to the length of the plate. The experimental data at the time shortly after the initial impact were chosen. We found a good agreement with the experimental data, where the analytical results overestimate results from the experiments slightly. Our analytical results for the position of the contact point agree

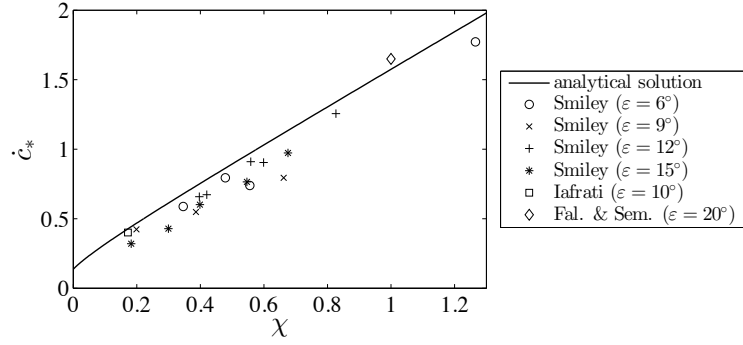


Figure 4.7: The self-similar solution of the position of the contact point, $x/t = \dot{c}_*$, in terms of χ (see also Figure 4.4), the position of the turnover region for one solution in Faltinsen and Semenov (2008, Figure 8d) and Iafrati (2010) and the position of the maximum fluid pressures in the experimental results of Smiley (1951).

very well with the two numerical results.

4.3 The Brillouin-type separation

In the problem in section 4.2, where the impact velocity of the plate was constant, we imposed fluid separation at the trailing edge. It is obvious that the fluid cannot detach earlier from the plate, since the pressure is above atmospheric on the entire contact region. However, if the vertical velocity of the plate is not constant with the plate decelerating quickly enough during the impact stage, as will be considered in section 4.4, the pressure may be below atmospheric on a part of the contact region. Then the fluid may separate from the plate in the low pressure zone. For blunt-shaped bodies, which will be discussed in section 4.5, we also have to account for fluid separation from the rear of the body. Difficulties arise in the modelling and the computation of such impact processes, because we must identify the location of both the spray root zone and the position where the water separates from the smooth body surface. Although we are aware of the roles of viscosity in separation processes, we aim to model flow separation in impact problems with large Reynolds numbers ($\sim 10^7$ or larger) as inviscid (see Sun and Faltinsen (2007)).

Here we are only concerned about flow separation at the rear contact point corresponding to $x = d_1(t)$, $y = 0$, where we assume that $\dot{d}_1 > 0$. Flow separation at the forward contact point, $x = d_2(t)$, $y = 0$, may be also possible but is not considered in this thesis. We model the position of the separation point and the horizontal fluid flow in the wake, $\bar{\varphi}_x(x)$, by the

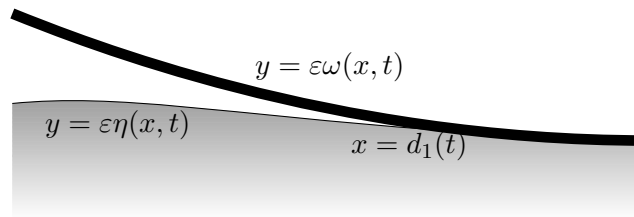


Figure 4.8: The fluid separates from the smooth body surface at $x = d_1(t)$.

following conditions:

$$|\nabla\varphi(x, 0, t)| < +\infty \quad (x = d_1), \quad (4.89)$$

$$\eta(x, t) = \omega(x, t) \quad (x = d_1), \quad (4.90)$$

$$\eta(x, t) \leq \omega(x, t) \quad (a < x < d_1), \quad (4.91)$$

$$p_x(x, 0, t) \geq 0 \quad (x > d_1, x \rightarrow d_1), \quad (4.92)$$

where the velocity potential $\varphi(x, y, t)$ is given by the mixed boundary value problem (4.13) – (4.16). Equation (4.89) is Kutta's condition that the fluid velocity at the separation point is finite. The fluid separates continuously from the body at the separation point in (4.90). Both conditions (4.89) and (4.90) have been considered before (see equations (4.41) and (4.63)). Equation (4.91) implies that the fluid free surface cannot intersect the plate surface behind the separation point (see Figure 4.8), where a is the rear end of the body. Equation (4.92) imposes that the pressure close to the rear contact point is not below atmospheric pressure. Note that condition (4.92) does not imply that the pressure inside the wetted region has to be above atmospheric pressure. It follows from (4.92) and from the behaviour of the pressure at the rear contact point given in (4.38) that:

$$L(d_1, t) \geq 0, \quad L(d_1, t) := \lim_{x \rightarrow d_1} \frac{p(x, 0, t)}{\sqrt{x - d_1}}, \quad (4.93)$$

Hence we can only have $p_x(d_1^+, 0, t) = 0$ and $p_x(d_1^+, 0, t) = \infty$, where d_1^+ is the right limit to d_1 .

In the following analysis we assume that the body-surface shape and motion, described by $y = \omega(x, t)$, are smooth enough, so that $\omega_{tt}(x, t)$ has Hölder index $\lambda > \frac{1}{2}$ as a function of x and is differentiable in t . To obtain the asymptotic behaviour of the free surface elevation and the hydrodynamic pressure as $x \rightarrow d_1$, we seek the complex acceleration $f_{tt}(z) = \varphi_{xt}(x, y, t) - i\varphi_{yt}(x, y, t)$ given by

$$f_{tt} \text{ analytic} \quad (y < 0), \quad (4.94)$$

$$\text{Im}(f_{tt}) = \omega_{tt} \quad (y = 0, d_1 < x < d_2), \quad (4.95)$$

$$\text{Re}(f_{tt}) = 0 \quad (y = 0, x > d_2 \text{ and } x < d_1), \quad (4.96)$$

$$f_{tt} = O(z^{-2}) \quad (|z| \rightarrow \infty). \quad (4.97)$$

Equation (4.95) and the far-field condition (4.97) are obtained by differentiating the boundary condition (4.14) and the far-field condition (4.16) in time. Equation (4.96) is the x -derivative of equation (4.15). To obtain a unique solution of the problem (4.94) – (4.97), we specify the behaviour of $\varphi_{xt}(x, 0, t)$ as $x \rightarrow d_1$ and as $x \rightarrow d_2$. The asymptotic behaviour of $\varphi_{xt}(x, 0, t)$, $x < d_2$ as $x \rightarrow d_2$ is given by the t -derivative of $\varphi_x(x, 0, t)$ in (4.27), so that we obtain:

$$\varphi_{xt}(x, 0, t) = -\frac{\dot{d}_2 K(d_2, t)}{2\pi\sqrt{d_2 - d_1}}(d_2 - x)^{-3/2} + O\left((d_2 - x)^{-1/2}\right) \quad (x \rightarrow d_2, x < d_2). \quad (4.98)$$

Since we assume Kutta's condition (4.89), the function $\varphi_x(x, 0, t)$ is non-singular at $x = d_1$ and, hence, we obtain

$$(x - d_1) \varphi_{xt}(x, 0, t) \rightarrow 0 \quad (x \rightarrow d_1, x > d_1), \quad (4.99)$$

The problem (4.94) – (4.97) is now uniquely determined by the asymptotic behaviours (4.98) and (4.99). We use formula (2.25) for $k_1 = -1$ and $k_2 = 1$ to obtain a particular solution of the problem (4.94) – (4.97). For the solution of the problem (4.94) – (4.97) we have to add the eigensolutions, which satisfy (4.98) and (4.99), to the particular solution. Hence, $f_{tt}(z)$ is given by

$$f_{tt}(z) = \frac{i}{\pi} \frac{(z - d_1)^{1/2}}{(z - d_2)^{3/2}} \int_{d_1}^{d_2} \frac{(d_2 - \xi)^{3/2}}{(\xi - d_1)^{1/2}} \frac{\omega_{tt}(\xi, t)}{\xi - z} d\xi + \frac{iD(t)}{(z - d_1)^{1/2}(z - d_2)^{3/2}}, \quad (4.100)$$

$$D(t) = \frac{1}{2\pi} \dot{d}_2 K(d_2, t) + \frac{1}{\pi} (d_2 - d_1) \int_{d_1}^{d_2} \sqrt{\frac{d_2 - \xi}{\xi - d_1}} \omega_{tt}(\xi, t) d\xi. \quad (4.101)$$

In particular, for $d_0 < x < d_1$, the imaginary part of $f_{tt}(x - i0)$ determines the vertical acceleration of the fluid in the wake region. Even though we assumed Kutta's condition, the acceleration of the fluid is singular at the separation point if $D(t) \neq 0$.

We analyse $\varphi_{yt}(x, 0, t)$ at a fixed point $x = d_1(t_0)$, which is the position of the separation point at time t_0 and belongs to the free surface in the wake for $t > t_0$. In the following, $\varphi_{yt}(x, 0, t)$ will be integrated twice in time for t close to t_0 where $t > t_0$. To do so, we assume that the functions $d_1(t)$, $d_2(t)$ and $D(t)$ are sufficiently smooth such that we can use the expansions

$$d_1(t) = d_1(t_0) + \dot{d}_1(t_0)(t - t_0) + O((t - t_0)^2) \quad (t \rightarrow t_0), \quad (4.102)$$

$$d_2(t) = d_2(t_0) + O(t - t_0) \quad (t \rightarrow t_0), \quad (4.103)$$

$$D(t) = D(t_0) + O(t - t_0) \quad (t \rightarrow t_0). \quad (4.104)$$

As to the first term on the right-hand side of equation (4.100) it can be approximated by $\omega_{tt}(d_1(t), t) + O((z - d_1)^{1/2})$ for $z \rightarrow d_1$, if $\omega_{tt}(z, t)$ is sufficiently smooth (see also equation (2.31)). The imaginary part of equation (4.100) together with (4.102) – (4.104) gives us for $t \rightarrow t_0$, $t > t_0$ and $y = 0$:

$$\varphi_{yt}(d_1(t_0), 0, t) = \frac{D(t_0)(t - t_0)^{-1/2}}{\dot{d}_1(t_0)^{1/2}(d_2(t_0) - d_1(t_0))^{3/2}} + \omega_{tt}(d_1(t_0), t_0) + O((t - t_0)^{1/2}). \quad (4.105)$$

We integrate equation (4.105) in time and use the body boundary condition (4.18):

$$\begin{aligned} \eta_t(d(t_0), t) &= \eta_t(d_1(t_0), t_0) + \frac{2D(t_0)(t - t_0)^{1/2}}{\dot{d}_1(t_0)^{1/2}(d_2(t_0) - d_1(t_0))^{3/2}} \\ &\quad + \omega_{tt}(d_1(t_0), t_0)(t - t_0) + O((t - t_0)^{3/2}). \end{aligned} \quad (4.106)$$

Note that we also used $\eta_t(d_1(t_0), t_0) = \omega_t(d_1(t_0), t_0)$, which was shown in equation (4.66). We integrate equation (4.106) once more and use the continuity of the fluid boundary at

$x = d_1(t_0)$ to obtain:

$$\begin{aligned} \eta(d_1(t_0), t) = & \omega(d_1(t_0), t_0) + \omega_t(d_1(t_0), t_0)(t - t_0) + \frac{\frac{4}{3}D(t_0)(t - t_0)^{3/2}}{\dot{d}_1(t_0)^{1/2}(d_2(t_0) - d_1(t_0))^{3/2}} \\ & + \frac{1}{2}\omega_{tt}(d_1(t_0), t_0)(t - t_0)^2 + O((t - t_0)^{5/2}) \quad (t \rightarrow t_0). \end{aligned} \quad (4.107)$$

In equation (4.107) we find the Taylor series of $\omega(d_1(t_0), t)$ about $t = t_0$. Since equation (4.107) is valid for any t_0 and the functions $d_1(t_0)$, $d_2(t_0)$, $D(t_0)$ are given by equations (4.102) – (4.104), we can write for $x < d_1$ close to the separation point

$$\eta(x, t) - \omega(x, t) = \frac{4D(t)(d_1(t) - x)^{3/2}}{3\dot{d}_1(t)^2(d_2(t) - d_1(t))^{3/2}} + O((d_1(t) - x)^{5/2}) \quad (x \rightarrow d_1(t)). \quad (4.108)$$

Equation (4.108) shows that the free-surface leaves the body tangentially. Note that we used Kutta's condition (4.89) to obtain equation (4.108). The value $D(t)$ in equation (4.108) is responsible, for whether or not the fluid intersects the body at the separation point. It follows from equations (4.91) and (4.108) that

$$D(t) \leq 0. \quad (4.109)$$

Note that the inequality (4.109) is independent of condition (4.92). To apply condition (4.92) we investigate the pressure behaviour at the detachment point d_1 . The pressure gradient along the contact region, $d_1 < x < d_2$ is given by the real part of $f_{tt}(x - i0)$ in (4.100) together with the linearised Bernoulli's equation (4.17). The asymptotic behaviour of $p_x(x, 0, t)$ at the separation point $x = d_1$ is

$$p_x(x, 0, t) = \frac{D(t)}{(d_2 - d_1)^{3/2}}(x - d_1)^{-1/2} + O\left((x - d_1)^{1/2}\right) \quad (x \rightarrow d_1), \quad (4.110)$$

where the coefficient $D(t)$ is given by (4.101). Since $p(d_1, 0, t) = 0$, integration of (4.110) in x provides

$$p(x, 0, t) = \frac{2D(t)}{(d_2 - d_1)^{3/2}}(x - d_1)^{1/2} + O\left((x - d_1)^{3/2}\right) \quad (x \rightarrow d_1). \quad (4.111)$$

The square-root behaviour of the pressure has already been confirmed in equation (4.38). If $D(t) < 0$, the pressure gradient is $-\infty$ in the vicinity of the detachment point d_1 , so that we obtain from equation (4.92):

$$D(t) \geq 0. \quad (4.112)$$

Note that inequality (4.112) does not guarantee, that the pressure is positive inside the wetted region. If we obtain negative-pressure zones inside the contact region $d_1 < x < d_2$, we may remove them by allowing the free surface to separate inside the contact region, so that cavities may develop.

Finally inequalities (4.109) and (4.112) give us together with (4.101) the equation

$$\frac{1}{2\pi}\dot{d}_2 K(d_2, t) + \frac{1}{\pi}(d_2 - d_1) \int_{d_1}^{d_2} \sqrt{\frac{d_2 - \xi}{\xi - d_1}} \omega_{tt}(\xi, t) d\xi = 0. \quad (4.113)$$

We will use equation (4.113) to determine the position of the separation point $d_1(t)$. Note that equation (4.113) can be only used if $\dot{d}_1(t) > 0$ and if $\omega_{tt}(x, t)$ is smooth enough in x and t . Equation (4.113) shows that $d_1(t)$ depends on the acceleration of the body. This indicates that $d_1(t)$ is sensitive to the motion of the body whereas a contact point modelled by Wagner's condition only depends on the position of the body surface shape as shown in equation (4.52). It follows from equations (4.110) and (4.113) that $p_x(x, 0, t)$ is continuous at $x = d_1$. Equation (4.111) implies that the following condition is equivalent to condition (4.113):

$$L(d_1, t) = 0, \quad (4.114)$$

where $L(d_1, t)$ is given in (4.93).

Equations (4.108) and (4.113) imply that the curvatures of the free and body surface are equal at the separation point $x = d_1$, which coincides with the Brillouin-Villat criterion (see e.g. Crighton, 1985). Hence, we will call equation (4.113) the Brillouin-Villat criterion. Equation (4.113) may not necessarily imply inequality (4.91). The higher order remainder term $O((d_1(t) - x)^{5/2})$ in equation (4.108) may be positive, so that the fluid free surface intersects the body surface at $x = d_1$ if $D(t) = 0$. However, numerical computations of the free-surface shape for many impact problems confirmed that the free surface behind the separation point is below the body surface, if condition (4.113) is satisfied. Since the Brillouin-Villat criterion does not allow negative pressure close to the separation point, this criterion cannot incorporate contact forces between fluid particles and the body surface, which have to be overcome for fluid detachment from the body. Viscosity of the fluid, intermolecular forces between fluid and body, and air flow may delay the separation of the fluid significantly.

4.4 Free fall of a rigid plate with high horizontal speed and ventilation

In section 4.2 we discussed the impact of a plate at constant velocity. If a sufficiently heavy plate impacts onto a fluid surface, the model in section 4.2 approximates closely the hydrodynamic loads. However, for the free fall of a light body we expect significantly different hydrodynamic loads compared with those predicted by the model with constant impact velocity, since the hydrodynamic pressure also depends on the body deceleration. For large horizontal speed of the body the hydrodynamic loads can be high enough for the plate to bounce out of the water without deep penetration of the body through the water surface as was shown in shallow water for plates by Hicks and Smith (2011) and for elliptic cylinders by Khabakhpasheva and Korobkin (2012). When the body decelerates vertically, the hydrodynamic pressure may drop below atmospheric pressure in the contact region, so that air can be sucked from the trailing edge under the plate and the fluid may separate from the body before the trailing edge. This phenomenon is known as ventilation. This section

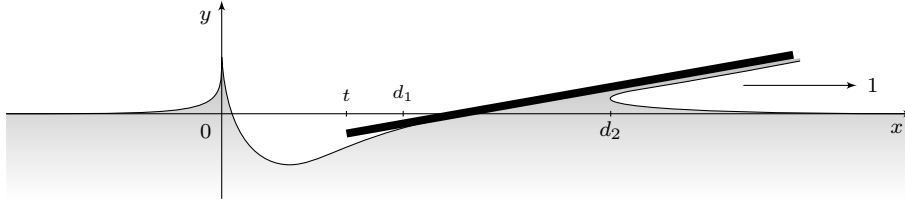


Figure 4.9: Plate impact onto deep water at time $t > 0$ as viewed in the global reference frame. Note the fluid separation from the plate at $x = d_1$ and the jet thrown forwards from the turnover point $x = d_2$. The rigid plate freely descends and has unit horizontal velocity component.

accounts for ventilation during the free fall of a rigid plate into water at high horizontal speed.

We first discuss the problem for very large Froude numbers, such that both gravity on the fluid and gravity on the plate can be neglected. It will be shown that with this assumption the plate exits the fluid after the initial impact stage for any small angle of attack of the plate and for any initial vertical velocity. Results show that ventilation only occurs if the initial vertical velocity component of the plate is large enough. In subsections 4.4.5 and 4.4.6, we analyse the plate motion during impact when gravity on the plate is accounted for. It will be shown for which initial impact velocities the plate does not exit the fluid. We also investigate the asymptotic behaviour of the the plate and of the contact point for large time.

4.4.1 Mathematical formulation

Initially, the liquid is at rest and occupies the lower half plane $y' < 0$. The rigid semi-infinite plate is inclined to the liquid free surface at a small angle ε , and touches the free surface at a single point, which is taken as the origin of the coordinate system $x'Oy'$ described in subsection 4.1.1. At time $t = 0$ the plate starts to penetrate the liquid vertically at the initial velocity V and to move horizontally at the constant sustained speed U , where $V/U = O(\varepsilon)$ (see Figure 4.9). The plate is not allowed to rotate. The shape of the body is given by $y' = (x' - Ut') \tan(\varepsilon) - h'(t')$ for $x' \geq Ut'$ where $h'(t')$ is the penetration depth of the plate which is unknown in advance. It will be determined by Newton's second law applied to the vertical motion of the plate where the plate mass is m . Consequently, the motion of the plate is coupled with the liquid flow and the hydrodynamic pressure.

In the problem of section 4.2, the plate impact at constant vertical velocity did not induce a length scale. However, in the coupled case, the mass m and the fluid density ρ_F induce the length-scale $L = \sqrt{m/\rho_F}$. Gravity can be neglected in the leading-order model for $Ut'/L = O(1)$ if the Froude-number $\text{Fr} = U/\sqrt{gL}$ is large enough, such that $1/\text{Fr}^2 = O(\varepsilon)$. Hence, the horizontal velocity of the plate is large and the plate is light. Below we use the scaling given in equations (4.2) – (4.4) and the scaling $h' = \varepsilon Lh$. The non-dimensional position of the plate at leading order for small ε is given by $y = \varepsilon\omega(x, t)$ where

$$\omega(x, t) = x - t - h(t) \quad (x > t). \quad (4.115)$$

In the linearised hydrodynamic model, the spatial interval $d_1 \leq x \leq d_2$ on $y = 0$ corresponds to the wetted part of the moving plate. The separation point $x = d_1, y = 0$ of the

fluid can move along the plate and is at or before the trailing edge $x = t$, so that $d_1 \geq t$. The point $x = d_2$, $y = 0$ is the Wagner contact point. The speed of the turnover region, \dot{d}_2 , is assumed positive during the early stage. The velocity potential $\varphi(x, 0, t)$ satisfies the mixed boundary-value problem (4.13) – (4.16).

Newton's second law is given in non-dimensional form, at leading order for small ε , by

$$\mathcal{F}(t) = -\ddot{h}, \quad \mathcal{F}(t) = \int_{d_1}^{d_2} p(x, 0, t) dx, \quad (4.116)$$

where $\mathcal{F}(t)$ is the non-dimensional vertical component of hydrodynamic force acting on the plate scaled by $\varepsilon \rho_F U^2 L$ and $p(x, y, t)$ is the non-dimensional hydrodynamic pressure given by equation (4.38). The initial conditions for equation (4.116) are $h(0) = 0$ and $\dot{h}(0) = -\chi$, where $\chi = V \varepsilon^{-1} U^{-1}$ is the non-dimensional initial vertical velocity of the plate. The equations in (4.116) are coupled with the fluid flow and they need to be determined together with the position of the contact region, $d_1 < x < d_2$.

The position of the forward contact point, $x = d_2$, is determined using Wagner's condition (4.40) together with equation (4.18) and (4.19). To take the early water detachment into account we determine $\bar{\varphi}_x(x)$ and $d_1(t)$ by conditions (4.89) – (4.92). Note that this system of conditions can only be used if $\dot{d}_1(t) > 0$. However, in our computation we could not find a parameter χ where \dot{d}_1 becomes zero. Hence, the case $\dot{d}_1(t) < 0$ is not considered here. Later in section (5.2), we will show that $\dot{d}_1(t)$ can become negative for an elastic plate. The time when $d_1 > t$ is referred to as the ventilation stage. The conditions (4.89) – (4.92) are satisfied not only in the ventilation stage, but also when $d_1 = t$, which is referred to as the separation stage. For $d_1 = t$, condition (4.91) has no meaning, so that in this stage we apply Kutta's condition as long as $L(t, t) > 0$ where $L(d_1, t)$ is defined in (4.93). Once $L(t, t) = 0$, the position of the separation point is determined by the condition $L(d_1, t) = 0$ (see equation (4.114)). The impact problem in this section consists of the fluid flow described by equations (4.13) – (4.16) together with the conditions (4.89) and (4.92), the structural part (4.116) and the kinematic part given by Wagner's condition at the forward contact point, equation (4.40), and equation (4.18), (4.19), (4.90) and (4.91). The solution of the problem only depends on the initial penetration velocity χ .

4.4.2 Solution of the coupled problem

First, we determine the vertical motion of the plate using the expressions in (4.116). Equation (4.38) gives us the hydrodynamic pressure on the wetted part of the plate, $d_1 < x < d_2$, $y = 0$:

$$p(x, 0, t) = \ddot{h} \sqrt{(x - d_1)(d_2 - x)} - \frac{\dot{d}_2 B(t)}{\pi(d_2 - d_1)} \sqrt{\frac{x - d_1}{d_2 - x}}, \quad (4.117)$$

$$B(t) = \int_0^{d_2} \sqrt{\frac{d_1 - \xi}{d_2 - \xi}} \bar{\varphi}_x(\xi) d\xi - \frac{\pi}{2} (d_2 - d_1) (1 + \dot{h}). \quad (4.118)$$

It can be shown that $B(t) < 0$ for $t \geq 0$ so that the pressure's square-root singularity at the trailing edge is positive. Equations (4.116) and (4.117) give us the vertical deceleration of

the plate:

$$\ddot{h} = \frac{\dot{d}_2 B(t)}{2(1 + \frac{\pi}{8}(d_2 - d_1)^2)}. \quad (4.119)$$

The term $1 + \frac{\pi}{8}(d_2 - d_1)^2$ in equation (4.119) consists of the non-dimensional mass of the plate, which is 1, and the added mass $\frac{\pi}{8}(d_2 - d_1)^2$, which increases the inertia of the plate due to the fluid attached.

Now, we can simplify the formula for the hydrodynamic pressure (4.117) by substituting equation (4.119) into (4.117). We obtain

$$p(x, 0, t) = -\frac{\dot{d}_2 B}{1 + \frac{\pi}{8}(d_2 - d_1)^2} \sqrt{\frac{x - d_1}{d_2 - x}} \left(\frac{1}{2}x - \frac{3}{8}d_2 - \frac{1}{8}d_1 + \frac{1}{\pi(d_2 - d_1)} \right). \quad (4.120)$$

It follows that the pressure $p(x, 0, t)$ in equation (4.120) has the same sign as the linear polynomial in x in the brackets. Hence, the pressure is positive on the entire contact region, if $d_2 - d_1 \leq \beta$ where $\beta = \sqrt{8/(3\pi)}$. If $d_2 - d_1 > \beta$, the pressure is negative for $d_1 < x < \frac{3}{8}d_2 + \frac{1}{8}d_1 - \frac{1}{\pi(d_2 - d_1)}$ and positive for $\frac{3}{8}d_2 + \frac{1}{8}d_1 - \frac{1}{\pi(d_2 - d_1)} < x < d_2$. In particular, a negative pressure zone cannot be captured inside the contact region. It will be shown later in section 4.5, 6.1 and 6.2, that zones of negative pressure can be well inside the contact region for the impact of parabolic-shaped bodies and rotating plates. Here the time interval $t_0 < t < t_1$ corresponds to the ventilation stage, where $d_2(t) - t > \beta$. In this stage, equations (4.90) – (4.92) imply the criterion of smooth decay of the pressure in (4.120) at the separation point, condition (4.114). Hence it follows that

$$d_1(t) = d_2(t) - \beta \quad (t_0 < t < t_1). \quad (4.121)$$

Equation (4.121) implies that the length of the contact region is constant in time for $t_0 < t < t_1$. The intervals $0 < t < t_0$ and $t > t_1$ correspond to the separation stage where $d_1(t) = t$. Note that $d_2(t) - t = \beta$ for $t = t_0$ and $t = t_1$.

Note that the separation stage and the ventilation stage also involve different behaviours of the complex displacement, complex velocity and complex acceleration at the separation point $x = d_1$, $y = 0$. In particular, the complex velocity $f_t(z) = \varphi_x - i\varphi_y$ is given by

$$\begin{aligned} f_t(z) = & \bar{\varphi}_x(d_1) - i\omega_t(d_1, t) + C_1(t)(z - d_1)^{1/2} + (\bar{\varphi}_{xx}(d_1) - i\omega_{tx}(d_1, t))(z - d_1) \\ & + C_2(t)(z - d_1)^{3/2} + O((z - d_1)^2) \quad (z \rightarrow d_1) \end{aligned} \quad (4.122)$$

where $C_1(t)$ is obtained from the behaviour of the pressure (4.120) at $x = d_1$. In the separation stage, $C_1(t)$ is positive and is given by

$$C_1(t) = \frac{\dot{d}_2 B(t)(1 - \frac{3\pi}{8}(d_2 - d_1))}{\pi(d_2 - d_1)^{3/2}(1 + \frac{\pi}{8}(d_2 - d_1)^2)}. \quad (4.123)$$

In the ventilation stage, it follows from equation (4.121) that $C_1(t) = 0$. Equation (4.122) confirms that the fluid-velocity behaviour at the separation point is smoother in the ventilation stage than in the separation stage. We also verified numerically that the function $\varphi_x(x)$ is differentiable at $x = t_0$ and $x = t_1$, such that we can exclude any square-root behaviour

at this point.

Kutta's condition (4.89) gives us the integral equation (4.65), which has the following form here:

$$\int_0^{d_1} \sqrt{\frac{d_2-\xi}{d_1-\xi}} \bar{\varphi}_x(\xi) d\xi = -\frac{\pi}{2}(d_2 - d_1)(1 + \dot{h}). \quad (4.124)$$

This equation will be used below to determine the wake function $\bar{\varphi}_x(x)$. In particular, the wake velocity $\bar{\varphi}_x(x)$ depends on the position of the forward contact point, $x = d_2$. To obtain $x = d_2$, we evaluate equations (4.51) and (4.52), which follow from Wagner's condition (4.40), condition (4.90) and the hydrodynamic problem (4.13) – (4.18). We obtain the following equations from equations (4.51), (4.52) and (4.115):

$$\int_0^{d_1} \sqrt{\frac{d_1-\xi}{d_2-\xi}} (t\bar{\varphi}_x(\xi) + A(\xi)) d\xi = -\frac{\pi}{8}(d_2 - d_1)(3d_2 + d_1 - 4t - 4h), \quad (4.125)$$

$$\int_0^{d_1} \sqrt{\frac{d_2-\xi}{d_1-\xi}} (t\bar{\varphi}_x(\xi) + A(\xi)) d\xi = \frac{\pi}{8}(d_2 - d_1)(3d_1 + d_2 - 4t - 4h). \quad (4.126)$$

Equation (4.126) is used to determine the unknown function $A(x)$. To decouple equation (4.126) from the function $\bar{\varphi}_x$, we subtract equation (4.124) multiplied by t , from (4.126):

$$\int_0^{d_1} \sqrt{\frac{d_2-\xi}{d_1-\xi}} A(\xi) d\xi = \frac{\pi}{8}(d_2 - d_1)(3d_1 + d_2 - 4h(t) - 4t\dot{h}(t)). \quad (4.127)$$

If the penetration depth $h(t)$ and the position of the separation point, $x = d_1$, are assumed given, then the system of integral equations (4.124), (4.127) and (4.125) determine the three unknown functions $\bar{\varphi}_x(x)$, $A(x)$ and $d_2(t)$.

We are able to find $h(t)$ by integrating Newton's second law (4.116) in time. By integrating (4.116) once and twice and using linearised Bernoulli's equation (4.17) we obtain

$$\int_0^{d_2} x\varphi_x(x, 0, t) dx = -\dot{h} + \chi, \quad \int_0^{d_2} x\Phi_x(x, 0, t) dx = -h + \chi t, \quad (4.128)$$

where we used $\varphi(x, 0, t) = \Phi(x, 0, t) = 0$ for $x = 0$ and $x = d_2$, $\dot{h}(0) = \chi$, and $h(0) = 0$. We use equation (2.41) for $u = \varphi_x$, $v = \varphi_y$ and $u = \Phi_x$, $v = \Phi_y$, respectively, with $r(x) = x$ to obtain together with equations in (4.128):

$$\dot{h} = \frac{1}{1 + \frac{\pi}{8}(d_2 - d_1)^2} \left(\chi - \frac{\pi}{8}(d_2 - d_1)^2 + \int_0^{d_1} \sqrt{(d_1 - \xi)(d_2 - \xi)} \bar{\varphi}_x(\xi) d\xi \right), \quad (4.129)$$

$$h = \frac{1}{1 + \frac{\pi}{8}(d_2 - d_1)^2} \left(\chi t + \frac{\pi}{16}(d_2 - d_1)^2(d_1 + d_2 - 2t) + \int_0^{d_1} \sqrt{(d_1 - \xi)(d_2 - \xi)} (t\bar{\varphi}_x(\xi) + A(\xi)) d\xi \right). \quad (4.130)$$

Substituting of equation (4.129) into (4.124) and equation (4.129) and (4.130) into (4.127)

give us integral equations in terms of the functions $\bar{\varphi}_x(x)$, $A(x)$, d_1 and d_2 :

$$\int_0^{d_1} \sqrt{\frac{d_2-\xi}{d_1-\xi}} \left(\frac{2}{\pi(d_2-d_1)} + \frac{3}{4}d_1 + \frac{1}{4}d_2 - \xi \right) \bar{\varphi}_x(\xi) d\xi = -(1+\chi) \quad (4.131)$$

$$\int_0^{d_1} \sqrt{\frac{d_2-\xi}{d_1-\xi}} \left(\frac{2}{\pi(d_2-d_1)} + \frac{3}{4}d_1 + \frac{1}{4}d_2 - \xi \right) A(\xi) d\xi = \frac{3}{4}d_1 + \frac{1}{4}d_2 - \frac{\pi}{32}(d_2-d_1)^3 \quad (4.132)$$

To obtain $\bar{\varphi}(x)$ and $A(x)$ we solve the two integral equations (4.131) and (4.132) numerically. To evaluate d_2 and t in terms of d_1 we find an ordinary differential equation in terms of d_2 by differentiating equation (4.125) in time:

$$\dot{d}_2 = \frac{2B}{\int_0^{d_1} \frac{\sqrt{d_1-\xi}}{(d_2-\xi)^{3/2}} (t\bar{\varphi}_x(x) + A(x)) d\xi + \frac{\pi}{2}(-3d_2 + d_1 + 2t + 2h)} \quad (4.133)$$

where the function $h(t)$ is given by equation (4.130) and $B(t)$ by equations (4.118) and (4.129). The initial condition of the ODE (4.133) is $d_2(0) = 0$. The functions $\dot{h}(t)$ in (4.129), $h(t)$ in (4.130) and $B(t)$ in (4.118) only weakly depend on the wake functions $\bar{\varphi}_x(x)$, $A(x)$ for x close to d_1 since the kernels in the integrals of these equations tend to zero as $x \rightarrow d_1$. This fact is used later to compute $h(t)$, $\dot{h}(t)$ and $B(t)$, also when $\bar{\varphi}_x(x)$, $A(x)$ are unknown for x close to d_1 .

4.4.3 Numerical implementation

Here we consider the numerical implementation in the separation stage $t < t_0$ and $t > t_1$. After the substitution of (4.118), (4.129) and (4.130) into equation (4.133), it forms an ODE

$$\dot{d}_2(t) = R(t, d_2; \bar{\varphi}_x(x)|_{x \in (0,t)}, A(x)|_{x \in (0,t)}) \quad (4.134)$$

with the initial condition $d_2(0) = 0$ for the time interval $0 < t < t_0$ and the initial condition $d_2(t_1^+) = d_2(t_1^-)$ for $t > t_1$. The functions $\bar{\varphi}_x(x)$ and $A(x)$ are given by the Volterra integral equations (4.131) and (4.132), which can be written as

$$\int_0^t \sqrt{\frac{d_2-\xi}{d_1-\xi}} K(t, d_2, \xi) \bar{\varphi}_x(\xi) d\xi = S_1(t), \quad (4.135)$$

$$\int_0^t \sqrt{\frac{d_2-\xi}{d_1-\xi}} K(t, d_2, \xi) A(\xi) d\xi = S_2(t), \quad (4.136)$$

where the functions K , S_1 and S_2 are explicitly known.

We use the discretisation $d_1^{(n)} = n\delta$ with constant step δ where $t_n = d_1^{(n)}$ in the separation stage. We use $d_2^{(n)}$ as the numerical value of $d_2(t_n)$ and we approximate $\bar{\varphi}_x(x)$ and $A(x)$ by constant values $\bar{\varphi}_x^{(n)}$ and $A^{(n)}$ in the intervals $(n-1)\delta < x < n\delta$.

For each time step the numerical solver consists of two stages. In the first stage we use

a modified Euler's method to integrate equation (4.134):

$$R_0^{(n-1)} = R(t_{n-1}, d_2^{(n-1)}; \bar{\varphi}_x^{(1)}, \dots, \bar{\varphi}_x^{(n-1)}; A^{(1)}, \dots, A^{(n-1)}), \quad (4.137)$$

$$\tilde{d}_2^{(n)} = d_2^{(n-1)} + \delta R_0^{(n-1)}, \quad (4.138)$$

$$R_1^{(n-1)} = R(t_n, \tilde{d}_2^{(n)}; \bar{\varphi}_x^{(1)}, \dots, \bar{\varphi}_x^{(n-1)}, \bar{\varphi}_x^{(n-1)}; A^{(1)}, \dots, A^{(n-1)}, A^{(n-1)}), \quad (4.139)$$

$$d_2^{(n)} = d_2^{(n-1)} + \frac{1}{2}\delta(R_0^{(n-1)} + R_1^{(n-1)}). \quad (4.140)$$

Note that we use $\bar{\varphi}_x^{(n-1)}$ and $A^{(n-1)}$ as the n -th input for $\bar{\varphi}_x(x)$ and $A(x)$ in (4.139), so that an error in $R_1^{(n-1)}$ of order $\delta^{5/2}$ is introduced (see equation (4.133)). After one integration step the wake region $0 < x < d_1^{(n)}$ is increased by one panel, in which the wake functions $\bar{\varphi}_x(x)$ and $A(x)$ are evaluated by integral equations (4.135) and (4.136) in the second stage. We solve the equations (4.135) and (4.136) by the following product-integration method (see Baker (1977)):

$$\bar{\varphi}_x^{(n)} = \frac{1}{\beta_{nn}} \left(S_1(t_n) - \sum_{m=1}^{n-1} \beta_{mn} \bar{\varphi}_x^{(m)} \right), \quad A^{(n)} = \frac{1}{\beta_{nn}} \left(S_2(t_n) - \sum_{m=1}^{n-1} \beta_{mn} A^{(m)} \right) \quad (4.141)$$

to obtain $\bar{\varphi}_x^{(n)}$ and $A^{(n)}$ where β_{mn} is defined by

$$\beta_{mn} = \int_{t_{m-1}}^{t_m} K(t_n, d_2^{(n)}, \xi) \sqrt{\frac{d_2^{(n)} - \xi}{t_n - \xi}} d\xi. \quad (4.142)$$

Since the kernel of the Volterra integral equations is square-root singular we have $\beta_{nn} = O(\sqrt{\delta})$ as the d_1 -step δ tends to zero. The method in (4.141) is also suitable for small steps δ , since the β_{nn} in (4.141) converge only slowly to zero as $\delta \rightarrow 0$.

Equations (4.137) – (4.141) are used starting from $n = 2$. At $d_1 = \delta$, $n = 1$, the unknown values are approximated by those for the oblique impact of a rigid plate with constant velocity in section 4.2 (see equations (4.77) and (4.78)). Numerical investigations show that $d_2(t)$ converges as $O(\delta^2)$ and $\bar{\varphi}_x(x)$ and $A(x)$ converge as $O(\delta)$ as $\delta \rightarrow 0$. These results agree with the theoretical estimations of the convergence speed for the modified Euler method and the product-integration method in their decoupled forms.

An analogue scheme is valid for the ventilation stage, $t_0 < t < t_1$. Here the size of the steps for d_1 is still constant, but the corresponding timesteps vary. We determine t in terms of d_1 by solving the ODE $dt/dd_1 = 1/\dot{d}_2$ (see equation (4.121)), where \dot{d}_2 is given by (4.134). An initial condition for t is obtained by assuming that t is continuous in terms of d_1 at $t = t_0$. Note that $d_2(t) = d_1(t) - \beta$ can be substituted into (4.131) – (4.133). In particular, we can use $\frac{2}{\pi(d_2 - d_1)} + \frac{3}{4}d_1 + \frac{1}{4}d_2 = d_2$ for the integral kernels in equations (4.131) and (4.132).

4.4.4 Numerical results

There is only one non-dimensional parameter in this problem of rigid impact at high horizontal speed, which is χ . In this subsection, we present some results for $\chi = 1.5$ and $\chi = 3$ and show some impact characteristics in terms of χ . Our computations terminate when $d_1(t) = d_2(t)$ corresponding to the exit of the plate from the fluid. We found that the plate exits the fluid for any χ . It is verified numerically for $\chi = 1.5$ and $\chi = 3$ that the relative

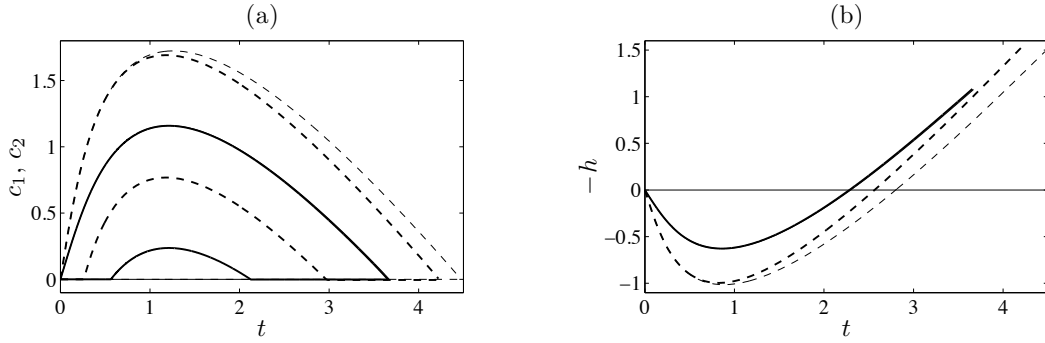


Figure 4.10: (a) Contact point motions $c_2 = d_2 - t$ and $c_1 = d_1 - t$ for $\chi = 1.5$ (solid lines) and $\chi = 3$ (dashed lines) each for the ventilated plate model in thick lines. The thin dashed line shows c_2 for the non-ventilated plate model for $\chi = 3$. (b) the function $-h$ as a function of t for the cases described in (a).

error of $\bar{\varphi}_x(x)$ is smaller than 1% during impact if we choose an integration step $\delta = 0.004$.

It can be shown numerically that ventilation does not occur for any $\chi < \chi_0$ and ventilation occurs for $\chi > \chi_0$, where we computed $\chi_0 \approx 1.02$. For $\chi > \chi_0$ we compare the results of the ventilated plate, where we allow the separation point to move along the plate, with the non-ventilated plate model, where we set $d_1 = t$ throughout the impact. Negative pressure contributes to the hydrodynamic loads on the non-ventilated plate.

Motions of the forward contact point and the separation point in the body's frame of reference, $c_2 = d_2 - t$ and $c_1 = d_1 - t$, are shown in Figure 4.10(a) for $\chi = 1.5$ and $\chi = 3$. Initially faster vertical motion increases the horizontal speed of the forward contact point, \dot{c}_2 , as already shown in section 4.2. The function c_2 decreases later, with the wetted length, $c_2 - c_1$, decreasing to zero, so that the plate exits the fluid completely. For all our computed examples, the forward contact point velocity, \dot{d}_2 , did not fall to zero, so that our model is valid until the body exits the fluid at $t = t_{\text{exit}}$. In the two examples we find ventilation starting at $t_0 = 0.56$ ($\chi = 1.5$) and $t_0 = 0.26$ ($\chi = 3$). During the ventilation stage, \dot{c}_2 changes sign and c_2 decreases until the separation point reaches the trailing edge which finishes the ventilation stage at $t_1 = 2.12$ ($\chi = 1.5$) and $t_1 = 2.98$ ($\chi = 3$). In general, c_2 exceeds $\beta = \sqrt{8/(3\pi)}$ in the time interval $t_0 < t < t_1$ if $\chi > \chi_0$, and c_2 is below β and the separation point stays at the trailing edge during the entire impact stage if $\chi < \chi_0$. If χ is much larger than χ_0 , we obtained notably larger values of c_2 for the non-ventilated plate than for the ventilated plate (see Figure 4.10(a)). On the other hand we find hardly any change in c_2 in both models, if χ is slightly larger than χ_0 .

Figure 4.10(b) shows the penetration depth of the plate, $h(t)$. Since no negative load is exerted on the rear part of the ventilated plate, this plate rises more quickly than the non-ventilated plate, and this is more significant when χ is much larger than χ_0 .

Figure 4.11(a) shows the pressure distribution in the body's frame of reference $s = x - t$ at time $t = 1$, which belongs to the ventilation stage for $\chi = 3$. The pressure distribution in the ventilated plate is close to that of the non-ventilated plate in the s -interval where the pressure is positive. However, for later times $t > 1$ the rigid motions of the ventilated and non-ventilated plates diverge, so that their pressure distributions also differ at the front wetted part of the plate. Note that $p_x(x, 0, t) = 0$ at the separation point $x = d_1$ for the

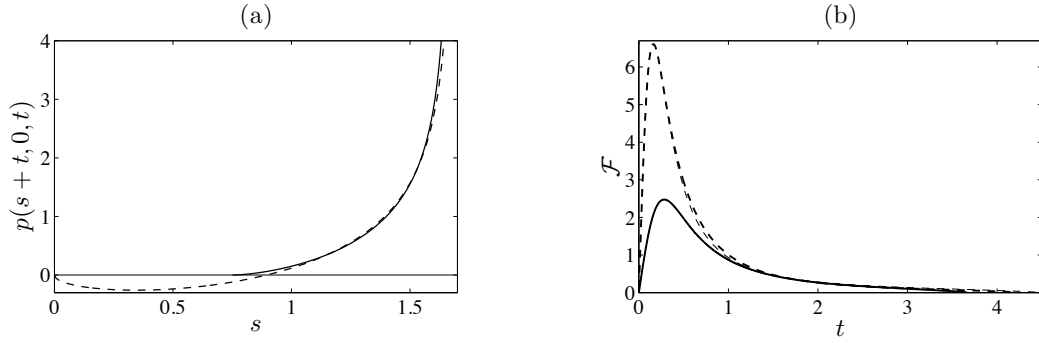


Figure 4.11: (a) Pressure distribution at time $t = 1$ for ventilated (solid line) and non-ventilated (dashed line) plate model for $\chi = 3$, (b) vertical hydrodynamic force $\mathcal{F}(t)$ for $\chi = 1.5$ (solid line) and $\chi = 3$ (dashed line) for ventilated (thick line) and non-ventilated (thin line) plate model. Note that for $\chi = 1.5$ the forces for both models are almost identical.

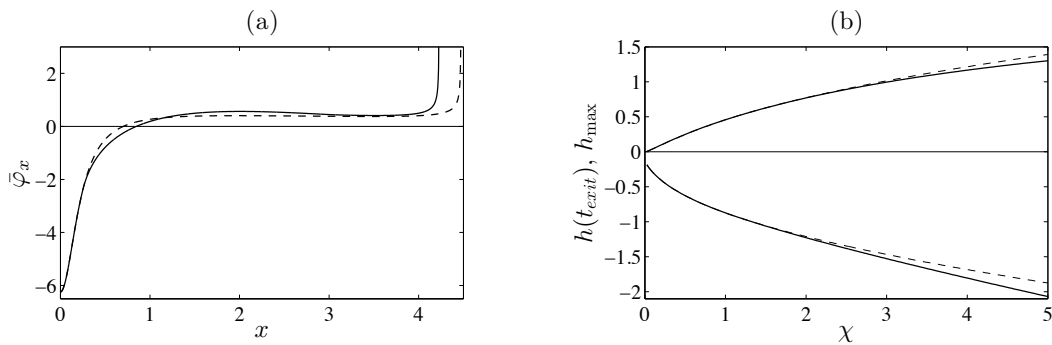


Figure 4.12: (a) Horizontal fluid velocity $\bar{\varphi}_x(x)$ shown for ventilated (solid line) and non-ventilated plate model (dashed line) for $\chi = 3$. Both functions have singularities at $x = t_{\text{exit}}$. (b) The maximum depth of the trailing edge, h_{max} , and the depth of the trailing edge at the instant of plate exit, $h(t_{\text{exit}})$, as functions of χ for ventilated (solid line) and non-ventilated plate model (dashed line). Note that $h_{\text{max}} > 0$ and $h(t_{\text{exit}}) < 0$.

ventilated plate when $t_0 < t < t_1$ (see equation (4.120)). The negative loads on the non-ventilated plate, due to the negative-pressure zone, are small in absolute value compared with the total loads.

Figure 4.11(b) shows the vertical hydrodynamic force on the plate as a function of time for $\chi = 1.5$ and $\chi = 3$. The force reaches its single maximum before the ventilation stage starts, and it decays to zero thereafter. Large differences in the force for the ventilated and non-ventilated plates were not detected. For $\chi = 1.5$ the differences are barely visible and for $\chi = 3$ the force on the ventilated plate is less than 10% larger than on the non-ventilated plate for $0 < t < 2$.

Figure 4.12(a) shows the horizontal fluid velocity in the wake for $\chi = 3$. The function $\bar{\varphi}_x(x)$ is negative in the initial penetration region and changes to slightly positive values for larger x . For $\bar{\varphi}_x(x)$, small differences are found between ventilated and non-ventilated plates. The function $\bar{\varphi}_x(x)$ becomes positive singular at the point where the trailing edge exits the fluid. The large positive values of $\bar{\varphi}_x(x)$ may come from the flow field in the contact region approaching the trailing edge.

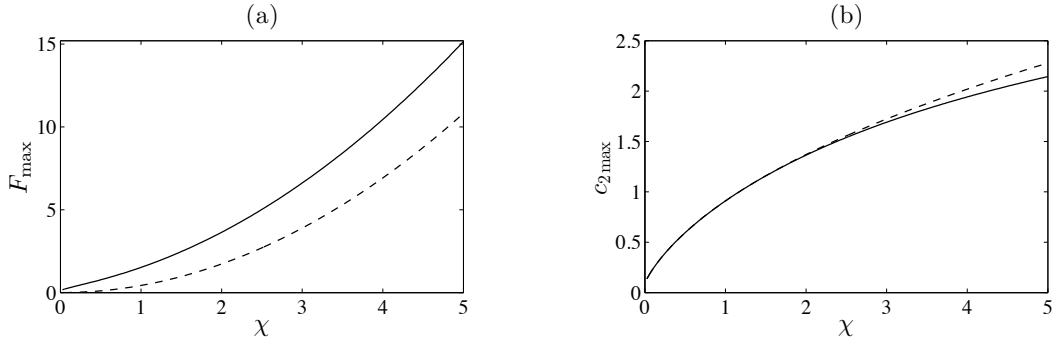


Figure 4.13: (a) Maximum vertical hydrodynamic force $\mathcal{F}_{\max} = \max_t \mathcal{F}(t)$ (solid line) and maximum force without horizontal speed $\mathcal{F}_{\max}^* = \frac{25}{324} \sqrt{10\pi} \chi^2$ (dashed line) as functions of χ , (b) $c_{2\max} = \max_t c_2(t)$ for ventilated (solid line) and non-ventilated (dashed line) plate.

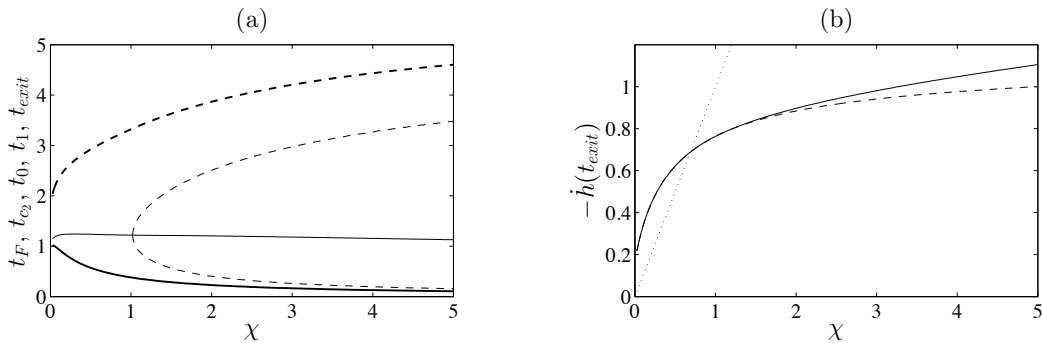


Figure 4.14: (a) Times t_F (thick solid line), t_{c_2} (thin solid line) when \mathcal{F}_{\max} , $c_{2\max}$ are reached; t_0 (thin dashed line), t_1 (thin dashed line) when ventilation starts, ends; t_{exit} (thick dashed line) when the plate exits the fluid. (b) The vertical velocity of the plate when it exits the fluid as a function of χ .

Figure 4.12(b) shows the maximum depth $h_{\max} = \max_t h(t)$ and the depth of the plate when it exits the fluid, $h(t_{\text{exit}})$, as functions of χ . Note that $h(t_{\text{exit}}) < 0$ for all $\chi > 0$, so that the plate exits the fluid when the trailing edge is above the x -axis. In absolute value, $|h(t_{\text{exit}})|$ increases, since larger χ means a later exit of the plate with the pile-up of the fluid in front of the contact point growing in time.

The maximum force $\mathcal{F}_{\max} = \max_t \mathcal{F}(t)$ is compared with the maximum force when the horizontal speed is zero, given by $\mathcal{F}_{\max}^* = \frac{25}{324} \sqrt{10\pi} \chi^2$ in Figure 4.13(a). The formula for \mathcal{F}_{\max}^* will be shown later in section 6.1. Note that the dimensional maximum force \mathcal{F}_{\max}' does not depend on U . The largest relative difference in \mathcal{F}_{\max} and \mathcal{F}_{\max}^* is for $\chi \rightarrow 0$ since $\mathcal{F}_{\max} \approx 0.15$ for $\chi = 0$, corresponding to very large horizontal velocity $U \gg V/\varepsilon$. For $\chi \rightarrow \infty$ the ratio $\mathcal{F}_{\max}/\mathcal{F}_{\max}^*$ tends to 1, indicating that this model is consistent with the Wagner model for vertical entry in section 6.1. Since the hydrodynamic force reaches its maximum before ventilation starts, \mathcal{F}_{\max} are equal for the ventilated and non-ventilated plates.

Figure 4.13(b) shows $c_{2\max} = \max_t c_2(t)$ as a function of χ . Note that $c_{2\max} \approx 0.12$ for $\chi = 0$ and $c_{2\max} = \beta$ for $\chi = \chi_0$. The value of $c_{2\max}$ for the ventilated plate differs only slightly from that for the non-ventilated plate for large χ , with $c_{2\max}$ slightly larger for the non-ventilated plate.

Figure 4.14(a) shows the time t_F when the force reaches its maximum, the time t_{c_2} when c_2 reaches its maximum, the times t_0 and t_1 between separation and ventilation stages and the time t_{exit} when the plate exits the fluid as functions of χ . This figure confirms that $t_F < t_0$ for $0 < \chi < 5$. We also could not find values $\chi > 5$ where $t_F > t_0$. Figure 4.14(a) also shows that t_{c_2} only slightly changes as χ increases. The value of t_{c_2} is inside the interval $(1.05, 1.25)$ for $0 < \chi < 5$. We find $t_0 = t_1 = t_{c_2}$ for $\chi = \chi_0$ and the size of the time interval $t_0 < t < t_1$ grows quickly as χ increases.

Figure 4.14(b) shows the vertical velocity component of the plate when exiting the fluid. For $\chi < 0.69$ the vertical velocity component at exit is faster than the one at entry. The increase of kinetic energy comes from the work on the plate to keep the horizontal speed of the plate constant. For $\chi = 5$ the coefficient of restitution $-\dot{h}(t_{\text{exit}})/\chi$ is only about 0.2.

The horizontal component $\mathcal{F}_x(t)$ of the hydrodynamic force acting on the plate can be estimated as the normal force component given by $\mathcal{F}(t) = -\ddot{h}(t)$ multiplied by the angle of attack. Hence the mean value of $\mathcal{F}_x(t)$ in time given by $\bar{\mathcal{F}}_x = \int_0^{t_{\text{exit}}} \mathcal{F}_x(t) dt / t_{\text{exit}}$ can be written together with the first equation in (4.116) as

$$\bar{\mathcal{F}}_x = \frac{\varepsilon}{t_{\text{exit}}}(\chi - \dot{h}(t_{\text{exit}})). \quad (4.143)$$

Now, we show that the viscous drag is small compared to $\bar{\mathcal{F}}_x$. In steady flow, the dimensional viscous force \mathcal{F}'_v is given by $\mathcal{F}'_v = \frac{1}{2}C_F \rho_F L^* U^2$. For viscous force acting on one side of a flat plate, which is placed parallel to a uniform flow at speed U , the friction coefficient C_F is about 0.003 (see Faltinsen, 2005, Table 2.1) and L^* is the length of the plate. This formula can give a rough estimate of the viscous drag in our unsteady problem, using the maximum possible length of the contact region, $L^* = L \min\{\beta, c_{2\text{max}}\}$. The non-dimensional viscous force is given by $\mathcal{F}_v = \frac{1}{2}\varepsilon^{-1}C_F L^*/L$. Then the ratio of viscous drag and mean horizontal hydrodynamic force can be estimated as $\mathcal{F}_v/\bar{\mathcal{F}}_x < 0.002\varepsilon^{-2}$ for any χ . Note that the mean viscous drag provided by Rayleigh's self-similar solution (see Acheson, 1990) for an infinite long plate moving suddenly with constant velocity, was found even smaller than the estimate based on steady flow. It follows that the mean inviscid force $\bar{\mathcal{F}}_x(t)$ is much greater than the mean viscous contribution for not too small plate inclinations ($\varepsilon > 3^\circ$). In order to keep the horizontal speed of the plate constant, the plate must do some work against this horizontal drag. Without such a work the plate would only slightly decelerate horizontally to a velocity U_{exit} with $U - U_{\text{exit}} = \varepsilon(V - \dot{h}'(t'_{\text{exit}}))$, so that the results shown here would not differ much from a plate, where also the horizontal speed is determined by Newton's second law.

4.4.5 Long time planing after impact with gravity

Though we assumed that $\text{Fr} \gg 1$, the gravitational force acting on the plate is significant if the Froude number is of order $1/\sqrt{\varepsilon}$. It will be shown that two classes of plate impacts are distinguished depending on the impact conditions: Either the plate exits the fluid soon after the initial impact or the plate planes along the free surface after impact without exiting the fluid. In this section we do not take ventilation into account so that we force $d_1 = t$.

With gravity included Newton's second law has the form

$$F(t) = -\ddot{h} + \kappa, \quad \kappa = \sqrt{m/\rho_F g} \varepsilon^{-1} U^{-2}. \quad (4.144)$$

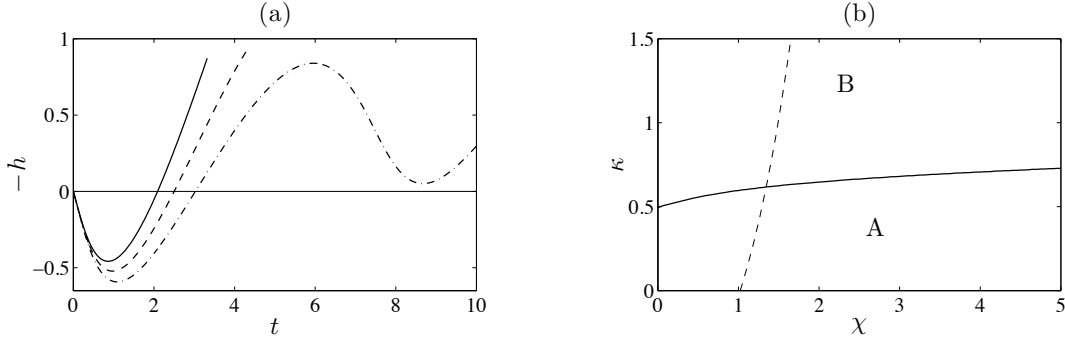


Figure 4.15: (a) Penetration depth as a function of time for $\chi = 1$ and $\kappa = 0$ (solid line), $\kappa = 0.3$ (dashed line), $\kappa = 0.6$ (dashed-dotted line). For $\kappa = 0$ the plate exits at $t = 3.3$ and for $\kappa = 0.3$ at $t = 4.4$. The plate does not exit for $\kappa = 0.6$. (b) Plane of parameters χ, κ with two scenarios of oblique impact of rigid plate divided by the solid line: (A) the plate exits the water, (B) the plate is in contact with the water ($c_2(t) > 0$) for $0 < t < 40$. Negative pressure appears for (χ, κ) right of the dashed line. Left of the dashed line the pressure is positive during the entire impact stage.

We can perform a similar analysis for non-zero gravity as in the previous section. In particular, equations (4.119), (4.129), (4.130), (4.131) and (4.132) are replaced by

$$\ddot{h} = \frac{\frac{1}{2}(1 + \dot{c})B + \kappa}{1 + \frac{\pi}{8}c^2}, \quad (4.145)$$

$$\dot{h} = \frac{1}{1 + \frac{\pi}{8}c^2} \left(\kappa t + \chi + \frac{\pi}{8}c^2 + \int_0^t \sqrt{(t - \xi)(t + c - \xi)} \bar{\varphi}_x(\xi) d\xi \right), \quad (4.146)$$

$$h = \frac{1}{1 + \frac{\pi}{8}c^2} \left(\frac{1}{2}\kappa t^2 + \chi t + \frac{\pi}{16}c^3 + \int_0^t \sqrt{(t - \xi)(t + c - \xi)} (t \bar{\varphi}_x(\xi) + A(\xi)) d\xi \right), \quad (4.147)$$

$$\int_0^t \left(\frac{2}{\pi c} + \frac{c}{4} + t - \xi \right) \sqrt{\frac{t+c-\xi}{t-\xi}} \varphi_x(\xi) d\xi = -(1 + \chi + \kappa t), \quad (4.148)$$

$$\int_0^t \left(\frac{2}{\pi c} + \frac{c}{4} + t - \xi \right) \sqrt{\frac{t+c-\xi}{t-\xi}} A(\xi) d\xi = \frac{c}{4} + t - \frac{\pi}{32}c^3 + \frac{1}{2}\kappa t^2, \quad (4.149)$$

where we define $c(t) = d_2(t) - t$ and $B(t)$ in equation (4.145) is defined in equation (4.118). Equations (4.117), (4.124), (4.125), (4.126) and (4.133) do not change, when the gravitational force on the plate is included.

Figure 4.15(a) shows the penetration depth of the trailing edge for impacts with parameters $\kappa = 0$, $\kappa = 0.3$ and $\kappa = 0.6$. The penetration depth significantly depends on κ and delays the exit of the plate. For large enough κ the ascending motion of the plate after entry is slowed down so much that the plate does not exit the fluid region, and planes along the water surface instead. Figure 4.15(b) shows the plane of parameters (χ, κ) , which is divided into two parts by the solid line. In region A the plate exits the fluid and in region B the wetted length c is positive for the time $0 < t < 40$ for which we computed the fluid-plate interaction. For all computed impact conditions corresponding to region A, the plate exits the fluid when the plate ascends for the first time. So, if the plate does not exit the fluid during its first ascent, the plate keeps on planing thereafter. Figure 4.15(b) shows also for which parameters (χ, κ) the pressure decreases below atmospheric pressure. For large χ a model accounting for ventilation may be necessary as shown in section 4.4.2.

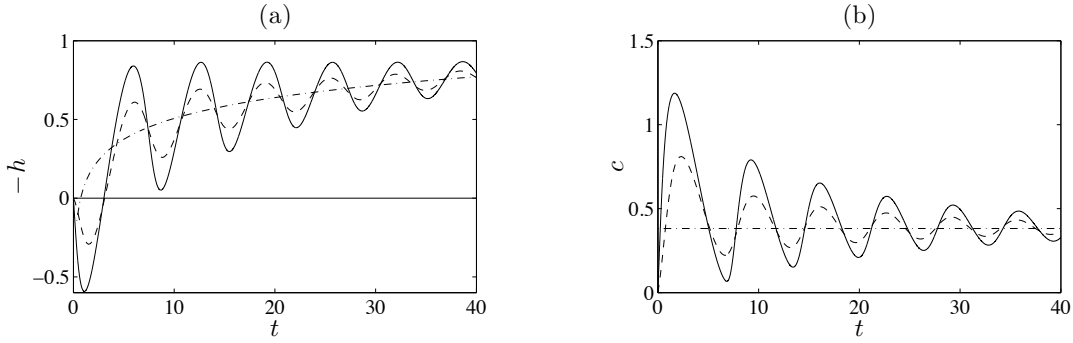


Figure 4.16: (a) Penetration depth for $\kappa = 0.6$ with initial vertical velocities $\chi = 1$ (solid line) and $\chi = 0.1$ (dashed line). Dashed-dotted line shows the asymptotic behaviour $h^*(t) = \frac{\kappa}{\pi}(2 - \log(\frac{2\pi}{\kappa}t))$ presented in equation (4.155). (b) Wetted length c as a function of time for conditions presented in (a). The function c converges to $c_0 = \frac{2}{\pi}\kappa$ as $t \rightarrow \infty$ (dashed-dotted line).

We now show some results of the long time planing of the plate for $\kappa = 0.6$. During planing, $h(t)$ oscillates, with the mean position increasing in time (see Figure 4.16(a)). This paradox behaviour of the plate in long time planing is consistent with steady planing without bouyancy investigated in Green (1936). Green showed that the free surface elevation behaves logarithmically in the far-field behind and in front of the plate. This behaviour is also known as Green's paradox. The behaviour of the free surface in the far-field can be corrected once gravity in the far-field is taken into account, as shown by Ting and Keller (1974). Also the corresponding linearised flow problem for a steadily planing plate with small angle of attack needs gravity to be included, because otherwise the velocity potential cannot be zero in the far field (see Oliver, 2002; Howison et al., 2004). However, the force of gravity on the fluid close to the plate may be negligible, as was assumed by Ting and Keller (1974). If the Froude number is large, then the influence of gravity on the fluid is only negligible in the impact stage when the duration of the fluid-plate interaction is of order L/U .

The length of the wetted interval, $c(t)$, oscillates in time around $c_0 = 0.38$ (see Figure 4.16(b)). In both functions, $h(t)$ and $c(t)$, the period of oscillation, T , is constant in time with $T \approx 6.6$. The amplitude of oscillation decays to zero for $\kappa = 0.6$ as $t \rightarrow \infty$. The asymptotic behaviour of $h(t)$ and $c(t)$ for large time will be investigated in the next subsection. In Figure 4.16(a) and (b) the asymptotics are already indicated by the dashed-dotted lines.

The initial vertical velocity of the plate determines the initial amplitude of the oscillation but does not influence the period of oscillation. But our computations showed that the period of oscillation, T , increases for growing κ . Also the rate of decay of the oscillation amplitude depends strongly on κ . The amplitude of oscillation is constant for $\kappa_0 \approx 0.55$. For $\kappa > \kappa_0$ the amplitude of oscillation is decreasing in time. For $\kappa = 0.8$ the decay is already so large, that the oscillation of $h(t)$ is only visible in the first three periods. For $\kappa < \kappa_0$ the amplitude of oscillation increases in time. Note that long time planing was only found for $\kappa > 0.51$ (see Figure 4.15(b)). Hence, we find the effect of negative damping only on a small interval $0.51 < \kappa < 0.55$ and for small χ . However, if the plate is guided by a prescribed $h(t)$ in the initial impact stage and later determined by Newton's second law, we may analyse the oscillations of the plate for $\kappa < 0.51$ without the plate exiting the fluid.

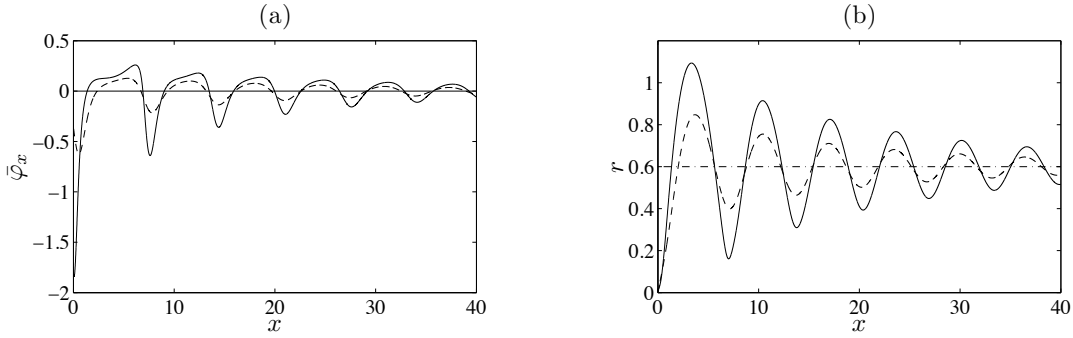


Figure 4.17: (a) $\bar{\varphi}_x(x)$ as a function of x for $\kappa = 0.6$ with initial vertical velocities $\chi = 1$ (solid line) and $\chi = 0.1$ (dashed line). (b) $r(x) = x\bar{\varphi}_x(x) + A(x)$ as a function of x for conditions presented in (a). The dashed-dotted line shows the constant function $r_0 = \kappa$.

We also found oscillations for $\bar{\varphi}_x(x)$ and $A(x)$ which are of the same period as the oscillations of $h(t)$ and $c(t)$. For our specific example ($\kappa = 0.6$) the oscillation amplitude for $A(x)$ grows in x . Hence, later for our analysis of the long-time behaviour we investigate the function $r(x) = x\bar{\varphi}_x(x) + A(x)$ instead of $A(x)$. Figure 4.17(b) shows that $r(x)$ decays in time. The behaviour of the function $\bar{\varphi}_x(x)$ is presented in Figure 4.17(a).

In the next subsection, we find the limits of the penetration depth, $h(t)$, of the wetted length, $c(t)$, and of the wake functions $\bar{\varphi}_x(t)$ and $r(t)$ as $t \rightarrow \infty$ from equations (4.117), (4.124), (4.125), (4.126), (4.145) – (4.149).

4.4.6 The plate and flow behaviour for large time

In this section we find c , $\bar{\varphi}_x(x)$ and $r(x)$, for steady planing, from the equations in subsections 4.4.2 and 4.4.5. Note that the buoyancy term in Bernoulli's equation is not included in this analysis.

We assume that the impact of a rigid plate with constant angle of attack leads to steady planing with the convergence of the wetted length $c(t) \rightarrow c_0$, the horizontal velocity in the fluid at the trailing edge $\bar{\varphi}_x(t) \rightarrow f_0$, the second wake function $r(t) \rightarrow r_0$ and the horizontal speed of the plate $\dot{h}(t) \rightarrow 0$ for large time t . We further assume that the convergence speed of $\bar{\varphi}_x(t)$ is quick enough: there exist an $\alpha > 0$ and a $C > 0$ so that $|\bar{\varphi}_x(t) - f_0| < Ct^{-\alpha}$ for all $t > 0$.

To find f_0 we divide equation (4.148) by t^2 , use the integral transformation $\xi = tu$ and consider the behaviour of the resulting integral equation as $t \rightarrow \infty$:

$$\int_0^1 (1-u)\bar{\varphi}_x(tu) du = O\left(\frac{1}{t}\right) \quad (t \rightarrow \infty). \quad (4.150)$$

Since the left-hand side of equation (4.150) tends to $\frac{1}{2}f_0$ as $t \rightarrow \infty$, we finally obtain $f_0 = 0$. To obtain r_0 we combine equations (4.126) and (4.146) so that

$$\int_0^t \sqrt{\frac{t+c-\xi}{t-\xi}} r(\xi) d\xi = \kappa t + \chi + \frac{\pi}{4}c^2 - \frac{\pi}{2}ch - \dot{h}\left(1 + \frac{\pi}{8}c^2\right). \quad (4.151)$$

The right-hand side behaves as κt , since h/t tends to zero because $\dot{h} \rightarrow 0$ as $t \rightarrow \infty$. It

follows that $r_0 = \kappa$. Combining equations (4.124) and (4.145) gives us

$$\int_0^t \frac{\varphi_x(\xi)}{\sqrt{(t-\xi)(t+c-\xi)}} d\xi = \frac{2}{1+\dot{c}} \left(\kappa - \left(1 + \frac{\pi}{8} c^2\right) \ddot{h} \right) + \pi c(1+\dot{h}) \xrightarrow{t \rightarrow \infty} \frac{2\kappa}{c_0} - \pi. \quad (4.152)$$

Since we assumed that $|\varphi_x(x)| < Cx^{-\alpha}$ for some $\alpha > 0$ for all $x > 0$, we obtain for $t > 4$

$$\left| \int_0^t \frac{\bar{\varphi}_x(\xi)}{\sqrt{(t+c-\xi)(t-\xi)}} d\xi \right| \leq 2Mt^{-1/2} + Ct^{-\alpha/2} \int_{\sqrt{t}}^t \frac{d\xi}{\sqrt{(t+c-\xi)(t-\xi)}}. \quad (4.153)$$

where $M = \max_{x>0} |\bar{\varphi}_x(x)|$. As the integral on the right-hand side increases only weakly as $O(\log t)$ as $t \rightarrow \infty$, the left-hand side of the inequality (4.153) tends to zero as $t \rightarrow \infty$. Finally, we obtain $c_0 = \frac{2}{\pi}\kappa$ from equation (4.152). The formula for c_0 agrees with the length of the wetted region of plate planing in heavy fluid which was presented in Dovgij et al. (2002). Subtracting equation (4.126) from (4.125) gives us together with equation (4.145)

$$h = \frac{1}{\pi} \left(-\frac{\pi}{2} c\dot{h} - \frac{2}{1+\dot{c}} \left(1 + \frac{\pi}{8} c^2\right) \ddot{h} + \frac{2\kappa}{1+\dot{c}} - \int_0^t \frac{r(\xi)}{\sqrt{(t-\xi)(t+c-\xi)}} d\xi \right). \quad (4.154)$$

With $r(x) \rightarrow \kappa$ as $x \rightarrow \infty$ we obtain from equation (4.154)

$$h(t) - \frac{\kappa}{\pi} \left(2 - \log\left(\frac{2\pi}{\kappa} t\right)\right) \rightarrow 0 \quad (t \rightarrow \infty). \quad (4.155)$$

Numerical results presented in Figure 4.16(a), 4.16(b), 4.17(a) and 4.17(b) agree with the derived asymptotic behaviour of $h(t)$, $c(t)$, $\bar{\varphi}_x(t)$, $r(t)$. Consequently, a quasi-steady solution exists where $c(t)$ and the two wake functions $\varphi_x(t)$ and $A(t)$ converge for large time, but the penetration depth of the plate, h , is unbounded for large time. Our asymptotic solution is consistent with Green's paradox.

4.4.7 Summary

We analysed the plate impact at high horizontal speed where the vertical motion is determined by Newton's second law. In cases, where the Froude number is large, gravity in the fluid can be neglected, since the time interval from entry to exit of the plate is short. We accounted for the separation point moving along the plate by using the Brillouin-Villat criterion. Gravity on the plate, with κ large enough keeps the plate in touch with the fluid. For large time we found quasi-steady planing of the plate with the plate's height increasing logarithmically with time.

4.5 Bouncing of a blunt body from a water surface at high horizontal speed

We consider the free fall of a blunt body onto a water free surface at high horizontal speed. Here the horizontal velocity component of the body is constant and the vertical velocity component is determined by Newton's second law. Initially, jets occur at the rear and front of the wetted area (see Figure 4.18(a)). This stage has been discussed in Howison et al. (2004) and Moore et al. (2012a) for constant vertical speed in two dimensions and in Miloh

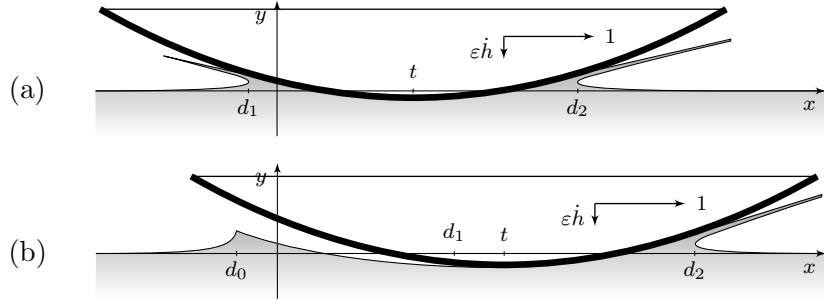


Figure 4.18: Blunt body impact onto deep water (a) $0 < t < t_0$, when a spray jet emerges at $x = d_1$ and (b) $t > t_0$, when the fluid separates smoothly from the body at $x = d_1$.

(1991) and Moore et al. (2012b) in three dimensions. In two dimensions, Moore et al. (2012a) showed that the position of the free-surface and the positions of the two contact points in the frame of reference with the body do not depend on the horizontal speed of the body. A similar result has been shown for small-time oblique entry of a blunt body in Korobkin (1988). A further characteristic of oblique impact of a blunt body is that the hydrodynamic pressure under the body falls below atmospheric pressure. Moore et al. (2012a) showed, that the negative-pressure zone reaches the rear contact point when the horizontal speed of the rear contact point becomes zero. In this section we will not only consider the initial stage, but also the subsequent stage, when the fluid separates from the body at the rear contact point.

It is common to use the Brillouin-Villat condition for laminar separation in high Reynolds-number flow. However, contact forces between the body surface and the fluid may delay the detachment of the fluid from the body. Moreover, in body-impact problems at high-speed, the fluid flow along the body may be turbulent, so that the fluid may detach far behind the separation point given by the Brillouin-Villat condition. We could not find practical separation criteria which account for such effects.

In this section we consider apart from the Brillouin-Villat criterion two further separation criteria: One criterion imposes that the fluid separates parallel to the body velocity. The other criterion imposes the separation point to be such that the kinetic energy in the fluid is minimised. In this section we mainly focus on the effects of the three different separation criteria on the body-water interaction. The work done in this section has been published in Reinhard et al. (2011).

4.5.1 Mathematical formulation

Initially the fluid is at rest and occupies the lower half plane $y' < 0$. The blunt body initially touches the free surface tangentially at a single point which is taken as the origin of the Cartesian coordinate system $x'Oy'$. Then the body starts to penetrate the liquid with initial vertical velocity component V and constant horizontal velocity component U where $\varepsilon = V/U$ is small. The shape of the body surface near its lowest point is approximated as parabolic, $y' = \frac{1}{2R}(x' - Ut')^2 - h'(t)$, where R is the radius of the curvature of the body surface at its lowest point. The function $h'(t')$ is the vertical displacement of the body at time t' and is determined by Newton's second law. We account for the gravitational force acting on the body. We assume that the Froude number $Fr = U/\sqrt{2\varepsilon gR}$ is large enough to neglect gravity

in the hydrodynamic model.

We take $L = 2\varepsilon R$ as the horizontal lengthscale of the problem. We use the scaling (4.2) – (4.4) and $h' = \varepsilon Lh$. The body position at time t is described in non-dimensional variables by the equation $y = \varepsilon\omega(x, t)$ where

$$\omega(x, t) = (x - t)^2 - h(t). \quad (4.156)$$

The velocity potential $\varphi(x, y, t)$ in the hydrodynamic model, linearised for small ε , satisfies the following equations:

$$\nabla^2\varphi = 0 \quad (y < 0), \quad (4.157)$$

$$\varphi_y = 2(t - x) - \dot{h}(t) \quad (y = 0, d_1 < x < d_2), \quad (4.158)$$

$$\varphi_x = 0 \quad (y = 0, x > d_2), \quad (4.159)$$

$$\varphi_x = \bar{\varphi}_x(x) \quad (y = 0, x < d_1), \quad (4.160)$$

$$\varphi = O((x^2 + y^2)^{-1/2}) \quad (x^2 + y^2 \rightarrow \infty). \quad (4.161)$$

The wetted part of the body corresponds to the interval $d_1 \leq x \leq d_2$, $y = 0$, where condition (4.159) implies that the speed of the forward contact point $x = d_2(t)$ is assumed positive. The rest of the x -axis corresponds to the free surface. We impose that the fluid boundary is continuous at $x = d_1$ and $x = d_2$ in the linearised hydrodynamic model:

$$\omega(d_1, t) = \eta(d_1, t), \quad \omega(d_2, t) = \eta(d_2, t) \quad (4.162)$$

where the free surface elevation is given by

$$\eta_t = \varphi_y \quad (y = 0, x < d_1 \text{ and } x > d_2), \quad (4.163)$$

$$\eta \equiv 0 \quad (t = 0). \quad (4.164)$$

As to the rear contact point, $x = d_1(t)$, initially its speed is unbounded, $\dot{d}_1(t) \rightarrow -\infty$ as $t \rightarrow 0$. Therefore, there is a time interval $0 < t < t_0$, during which $\dot{d}_1(t) < 0$ and the function $\bar{\varphi}_x(x)$ in equation (4.160) is zero. This stage is referred to as the Wagner stage. During the Wagner stage both points $x = d_1(t)$ and $x = d_2(t)$ model the forward and rear overturning region, where a spray jet is formed. Their positions are determined by (4.162). The end of the Wagner stage, $t = t_0$, is such that $\dot{d}_1(t_0) = 0$. We introduce $d_0 = d_1(t_0)$ as the final position of the rear contact point at the end of the Wagner stage.

In this model, the next stage $t > t_0$ of the impact is referred to as the separation stage. We expect that the fluid separates from the rear of the body with the formation of a wake on the free surface between $x = d_0$ and $x = d_1(t)$, $y = 0$ (see Figure 4.18(b)), where the function $\bar{\varphi}_x(x)$ has to be determined as part of the solution. The function $\bar{\varphi}_x(x)$ is zero for $x < d_0$. For $t > t_0$ we additionally impose Kutta's condition at the separation point:

$$|\nabla\varphi(d_1, 0, t)| < \infty. \quad (4.165)$$

If $d_1(t)$ and $h(t)$ are prescribed, conditions (4.162) and (4.165) determine together with (4.157) – (4.161) the position of the forward contact point $x = d_2(t)$ and the wake function

$\bar{\varphi}_x(x)$. A further condition is needed to determine the horizontal motion of the separation point $x = d_1(t)$ for $t > t_0$. We analyse the impact problem in terms of the following three separation conditions:

- (a) $p_x(x, 0, t) = 0 \quad (x = d_1^+)$,
- (b) $\omega_x(d_1, t) = \dot{h}$,
- (c) The position of the separation point, $x = d_1$, minimizes the increase of the total fluid kinetic energy $\frac{d}{dt}E_{\text{kin}}(t) = -\int p(x, 0, t)\omega_t(x, t) dx$ at each time $t > t_0$ compared with all possible separation conditions.

Condition (a) is the Brillouin-Villat condition (see also equation (4.114)). Condition (b) implies that the tangent vector on the body at the separation point is parallel to the body velocity vector, which was used for example in Miloh (1990). In high-Reynolds-number cavity flow past a body, experiments also show that the free surface separates close to the shoulder of the body in a steady fluid flow (see Batchelor, 1967). Hence, we call condition (b) the shoulder criterion. Since the fluid separation is tangential with Kutta's condition (4.165), the fluid velocity at the separation point is parallel to the velocity of the body. As to condition (c), the kinetic energy in the fluid is evaluated in the frame of reference where the fluid in the far-field is at rest. The function $d_1(t)$ may vary if another frame of reference is chosen. We call condition (c) the energy criterion.

The vertical motion of the body of mass m is governed by Newton's second law, which is in non-dimensional form by

$$\mathcal{F}(t) = \mu(-\ddot{h}(t) + \kappa), \quad \mathcal{F}(t) = \int_{d_1}^{d_2} p(x, 0, t) dx, \quad (4.166)$$

where $\mu = \frac{1}{4}mU^2\rho_F^{-1}V^{-2}R^{-2}$ and $\kappa = 2gRU^{-2}$. The initial conditions for equations in (4.166) are $h(0) = 0$ and $\dot{h}(0) = 1$.

The problem depends on the parameters μ and κ . We first consider the Wagner stage to obtain the initial values for $h(t)$ and $\dot{h}(t)$ in the separation stage.

4.5.2 Wagner stage

For $0 < t < t_0$ we analyse the problem with respect to the complex displacement potential $f(z) = \Phi_x(x, y, t) - i\Phi_y(x, y, t)$ (see equations (4.42) – (4.46)). The solution of the problem is given by

$$f(z) = -i \left((z - t)^2 - h - \sqrt{(z - d_1)(z - d_2)}(z - t) \right), \quad (4.167)$$

$$d_1 = -\sqrt{2h} + t, \quad d_2 = \sqrt{2h} + t, \quad (4.168)$$

where the contact point positions, $x = d_1$ and $x = d_2$, in (4.168) guarantee that $f(z)$ decays in the far-field as $O(z^{-2})$. Equations in (4.167) and (4.168) show that the free surface elevation given by $\eta(x, t) = -\text{Im}(f(x - i0))$ and the position of the contact points are symmetric about $x = t$. It will be shown that the velocity field and the distribution of the hydrodynamic pressure are not symmetric. In dimensional form, the free surface elevation $y' = \eta'(s' + Ut', t')$ and the contact point positions $c'_1 = d'_1 - Ut'$ and $c'_2 = d'_2 - Ut'$, in the

frame of reference moving with the body, $s'Oy'$, are independent of the horizontal velocity U for $0 < t' < t'_0$.

By integrating $f(z)$ in equation (4.167) w.r.t. z and by differentiating the result twice in time we obtain, together with the equations in (4.168), the complex acceleration $F_{tt}(z) = \varphi_t + i\psi_t$:

$$F_{tt}(z) = i \left[(\ddot{h} - 2)(z + t) + 2\dot{h} - (\ddot{h} - 1)\sqrt{(z - d_1)(z - d_2)} + \frac{(z - t + \dot{h})^2}{\sqrt{(z - d_2)(z - d_1)}} \right], \quad (4.169)$$

The hydrodynamic pressure is given by the real part of $F_{tt}(z)$ in (4.169) together with the linearised Bernoulli's equation (4.17):

$$p(x, 0, t) = (\ddot{h} - 1)\sqrt{(d_2 - x)(x - d_1)} + \frac{(x - t + \dot{h})^2}{\sqrt{(d_2 - x)(x - d_1)}}. \quad (4.170)$$

Equation (4.170) indicates that the pressure can be negative if the body decelerates rapidly enough and the vertical velocity is small enough. The vertical hydrodynamic force acting on the body, $\mathcal{F}(t)$, is given by

$$\mathcal{F}(t) = \pi(\ddot{h}h + \dot{h}^2). \quad (4.171)$$

It follows from equations in (4.166) and (4.171) that the vertical motion of the body is given by $-\mu\ddot{h} + \mu\kappa = \pi\ddot{h}h + \pi\dot{h}^2$. We integrate this equation twice in time to obtain

$$\frac{\pi}{2}h^2 - \mu h - \frac{1}{2}\mu\kappa t^2 - \mu t = 0. \quad (4.172)$$

In dimensional form, the hydrodynamic force in (4.171) and the evolution of the penetration depth in (4.172) do not depend on the horizontal velocity of the body in the Wagner stage $0 < t < t_0$. The separation stage starts at time t_0 when $\dot{d}_1(t_0) = 0$. The expressions in (4.168) and (4.172) imply that the penetration depth $h_0 = h(t_0)$ at the end of the Wagner stage is given by:

$$2\pi^2 h_0^3 - \pi\mu(4 + \kappa)h_0^2 + 2\mu^2(1 + \kappa)h_0 - \mu^2 = 0. \quad (4.173)$$

We find the solution of (4.173) numerically. The time t_0 and the two contact points $d_1(t_0)$ and $d_2(t_0)$, the speed of the forward contact point, $\dot{d}_2(t_0)$, the vertical velocity $\dot{h}(t_0)$ and vertical deceleration $\ddot{h}(t_0)$ are given in terms of h_0 using equations (4.168) and (4.172) and their time derivatives. In particular, the horizontal velocity of the forward contact point is given by $\dot{d}_2(t_0) = 2$. It can be shown, that the duration of the Wagner stage, t_0 , decreases to zero as $\mu \rightarrow 0$.

The pressure starts to be negative inside the contact region before the separation stage starts (see Figure 4.19). The fluid may cavitate in the low pressure zones. Cavities in the vertical impact of a blunt body have been considered by Korobkin (2003) and patch cavities in flow past a smooth body surface have been discussed by Howison et al. (1994). In this section the fluid stays in contact with the body surface along the entire contact region $d_1 < x < d_2$. In equation (4.170), the second term approaches zero as $x \rightarrow d_1$ and $t \rightarrow t_0$

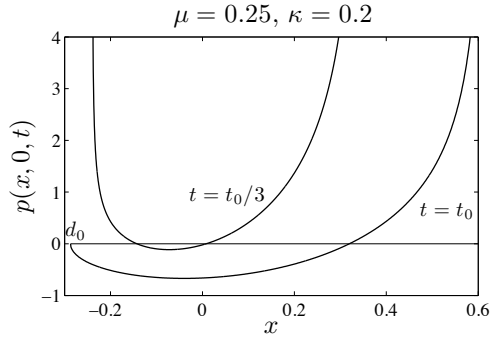


Figure 4.19: The pressure distribution $p(x, 0, t)$ along the contact region for the times $t = t_0/3$ and $t = t_0$, where for $\mu = 0.25$ and $\kappa = 0.2$ the end of the Wagner stage is at $t_0 = 0.165$

since $x - t_0 + \dot{h}(t_0) = x - d_1(t_0)$. Hence, the first term in (4.170), which is negative, starts to dominate for x close to d_1 . Consequently, at the end of the Wagner stage the negative-pressure zone is not trapped anymore between zones whose pressure exceeds atmospheric pressure. This confirms our model that the fluid starts to separate from the body at $t = t_0$.

There are three reasons why the Wagner approach described in this section cannot be used for $t > t_0$: Firstly, a Wagner contact point $x = d_1(t)$ has been shown to be unstable to disturbances for $\dot{d}_1(t) > 0$ (Howison et al., 1991; Howison et al., 2004). Secondly, the hydrodynamic pressure at a Wagner contact point is always positive singular at the rear contact point, also for $t > t_0$, which is unphysical at a fluid-separation point. Thirdly, the velocity potential is not necessarily zero for $d_0 < x < d_1(t)$, $y = 0$.

Before we start with the separation stage we consider the Wagner stage for constant vertical velocity. Results for constant vertical velocity are given by equations (4.167), (4.168) and (4.170) for $h(t) = t$. In this case, the Wagner stage ends at $t_0 = \frac{1}{2}$, where $d_1(t_0) = -\frac{1}{2}$. Consequently, the dimensional duration of the Wagner stage, t'_0 , decays to zero for increasing horizontal speed as U^{-2} . For $\frac{1}{4} < t < t_0$ the dimensional pressure is below atmospheric pressure in the interval

$$t - \frac{1}{2} (1 + \sqrt{4t - 1}) < x < t - \frac{1}{2} (1 - \sqrt{4t - 1}) . \quad (4.174)$$

In the next subsection we consider the separation stage, where the fluid separates from the rear contact point $x = d_1$. We assume that the penetration depth of the body, $h(t)$, and the vertical velocity component of the body, $\dot{h}(t)$, are continuous at $t = t_0$. Below d_1 and \ddot{h} are shown to be discontinuous at $t = t_0$. We superscript t_0 with a minus when we refer to values before the jump and with a plus after the jump.

4.5.3 Separation stage

The mixed boundary-value problems (4.157) – (4.161) and conditions (4.162) and (4.165) imply three integral equations (see equations (4.51), (4.52), (4.65)):

$$\int_{d_0}^{d_1} \sqrt{\frac{d_2-\xi}{d_1-\xi}} \bar{\varphi}_x(\xi) d\xi = \frac{\pi}{4}(d_2 - d_1)(4t - 3d_1 - d_2 - 2\dot{h}), \quad (4.175)$$

$$\int_{d_0}^{d_1} \sqrt{\frac{d_2-\xi}{d_1-\xi}} A(\xi) d\xi = \frac{\pi}{16}(d_2 - d_1) \left(d_2^2 + 2d_1d_2 + 5d_1^2 - 8t^2 - 8(h - \dot{h}t) \right), \quad (4.176)$$

$$\int_{d_0}^{d_1} \sqrt{\frac{d_1-\xi}{d_2-\xi}} \Phi_x(\xi, 0, t) d\xi = \frac{\pi}{16}(d_2 - d_1) (5d_2^2 + 2d_1d_2 + d_1^2 - 12td_2 - 4td_1 + 8t^2 - 8h). \quad (4.177)$$

where $\Phi_x(x, 0, t) = t\bar{\varphi}_x(x) + A(x)$. In particular, it can be shown that equations (4.175) – (4.177) are satisfied for $t = t_0^-$, where the integrals on the left-hand are zero, since $d_1(t_0^-) = d_0$. To obtain the wake functions $\bar{\varphi}_x(x)$ and $A(x)$ for $t > t_0$ we solve the equations (4.175) and (4.176) numerically.

The forward contact point $x = d_1$ is evaluated by the time-derivative of (4.177), which is given by

$$\dot{d}_2 = \frac{2B(t)}{\int_{d_0}^{d_1} \frac{\sqrt{d_1-\xi}}{(d_2-\xi)^{3/2}} \Phi_x(x, 0, t) d\xi - \frac{\pi}{8}(15d_2^2 - 6d_1d_2 - 24td_2 - d_1^2 + 8td_1 + 8t^2 - 8h)}, \quad (4.178)$$

$$B(t) = \int_{d_0}^{d_1} \sqrt{\frac{d_1-\xi}{d_2-\xi}} \bar{\varphi}_x(\xi) d\xi + \frac{\pi}{4}(d_2 - d_1)(4t - d_1 - 3d_2 - 2\dot{h}). \quad (4.179)$$

Since the rear contact point can jump at $t = t_0$ the wake region increases abruptly. A jump of the contact point also implies that the fluid surface at $d_0 < x < d_1(t_0^+)$ detaches from the body instantly in the present model. An inclusion of an air model in the region of detachment may give more insight into the physics of flow detachment. Air effects in the region of detachment may delay the fluid separation. Since the air speed is large during inflow of air into the gap between fluid and body, the air pressure acting on the fluid free surface decreases significantly. By including a local air model, the motion of the contact-point might become continuous at the time of switch between Wagner stage and separation stage. The air flow can be neglected again when the gap between fluid and body is large enough. We assume that $\bar{\varphi}_x(x) = \varphi_x(x, 0, t_0^-)$ and $A(x) = \Phi_x(x, 0, t_0^-) - t_0\varphi_x(x, 0, t_0^-)$ for $d_1^- < x < d_1(t_0^+)$. Then it can be shown that equations (4.175) – (4.177) at $t = t_0^+$ and $\dot{d}_2(t_0^+) = 2$ in (4.178) are satisfied for any choice of $d_1(t_0^+)$.

In the separation stage, the pressure is not singular at the rear contact point. It is given by equation (4.38):

$$p(x, 0, t) = -\frac{B(t)\dot{d}_2}{\pi(d_2 - d_1)} \sqrt{\frac{x-d_1}{d_2-x}} + (\ddot{h} - 2)\sqrt{(x - d_1)(d_2 - x)}. \quad (4.180)$$

We find numerically that the first term is positive and the second term is negative throughout the separation stage. Together with equations in (4.166) we obtain the vertical deceleration

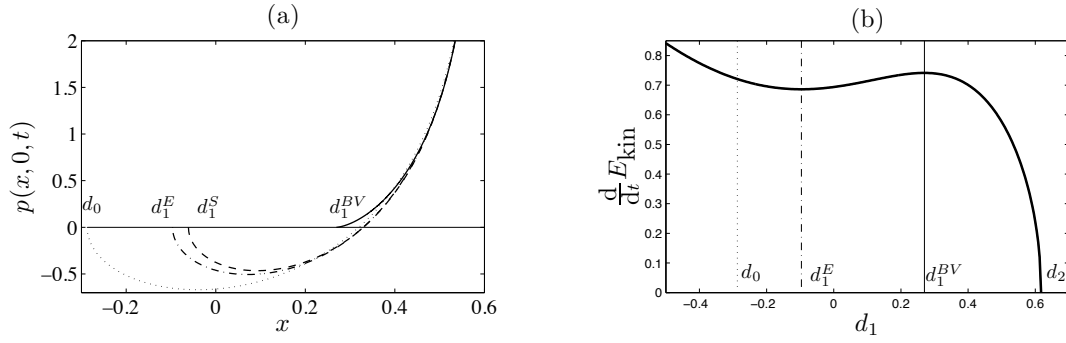


Figure 4.20: (a) The pressure distribution at time $t = t_0^-$ (dotted line) and at $t = t_0^+$ satisfying Brillouin-Villat criterion (solid line), $d_1 = d_1^{BV}$, satisfying shoulder criterion (dashed line), $d_1 = d_1^S$, satisfying energy criterion (dashed-dotted line), $d_1 = d_1^E$, (b) time derivative of kinetic energy in the fluid at time $t = t_0$ and the position of the separation points at $t = t_0^-$ and $t = t_0^+$ (legend see (a)).

of the body, \ddot{h} :

$$\ddot{h} = \frac{\frac{1}{2}\dot{d}_2 B + \frac{\pi}{4}(d_2 - d_1)^2 + \mu\kappa}{\mu + \frac{\pi}{8}(d_2 - d_1)^2}. \quad (4.181)$$

The initial conditions of the system of ordinary differential equations (4.178) and (4.181) are given by the values $h(t_0^-)$, $\dot{h}(t_0^-)$ and $d_2(t_0^-)$ at the end of the Wagner stage. The ODE system (4.178) and (4.181) is solved by a modified Euler's method. Since the pressure distribution changes abruptly at $t = t_0$ (see Figure 4.20(a)), \ddot{h} also jumps such that $|\ddot{h}(t_0^+)| > |\ddot{h}(t_0^-)|$.

As to the separation point $x = d_1(t)$, it will be evaluated by the conditions in (a), (b) and (c) (see subsection (4.5.1)), respectively. Now, we discuss the individual conditions:

Brillouin-Villat criterion: The Brillouin-Villat criterion is given by equation (4.113), which is here

$$(d_2 - d_1)(2 - \ddot{h}) + \dot{d}_2 B = 0. \quad (4.182)$$

Note that B given in (4.179) depends on d_1 . By substituting equations (4.178) and (4.181) into equation (4.182), equation (4.182) only depends on d_1 , d_2 , h , \dot{h} and φ_x . Equation (4.182) will be solved numerically by the secant method at the end of each integration step of equations (4.178) and (4.181).

Shoulder separation criterion: We obtain the following equation from the shoulder separation criterion (b):

$$d_1 = t - \frac{\dot{h}}{2}. \quad (4.183)$$

Equation (4.183) can be substituted into equations (4.175), (4.176), (4.178) and (4.181).

Energy criterion: Together with equations (4.156) and (4.180) the rate of change of the kinetic energy in condition (c) is given by

$$\frac{dE_{\text{kin}}}{dt} = \frac{\pi}{8}(d_2 - d_1) \left[\dot{d}_2 B(t)(4t - d_1 - 3d_2 - 2\dot{h}) + (d_2 - d_1)(2 + \ddot{h})(2t - d_1 - d_2 - \dot{h}) \right]. \quad (4.184)$$

To obtain the minimum of $\frac{d}{dt}E_{\text{kin}} = \frac{d}{dt}E_{\text{kin}}(t, d_1)$ we differentiate it with respect to d_1 for fixed t . The functions $h(t)$, $\dot{h}(t)$, $d_2(t)$ and $\dot{d}_2(t)$ are independent of the choice of the value d_1 . For $h(t)$, $\dot{h}(t)$, $d_2(t)$ this independence follows directly from equations (4.178) and (4.181), since their right-hand sides do not depend on \dot{d}_1 . The independence of \dot{d}_2 from d_1 can be shown by differentiating (4.178) in time. On the other hand \ddot{h} and B depend on d_1 and are determined by equations (4.179) and (4.181). The d_1 -derivative of $B(t) = B(t, d_1)$ and \ddot{h} are given by

$$\frac{dB}{dd_1} = \frac{B}{2(d_2 - d_1)}, \quad \frac{d\ddot{h}}{dd_1} = \frac{\pi}{4} \frac{(d_2 - d_1)(\ddot{h} - 2) - \dot{d}_2 B}{\mu + \frac{\pi}{8}(d_2 - d_1)^2}. \quad (4.185)$$

Condition (c) implies that the d_1 -derivative of $\frac{dE_{\text{kin}}}{dt}$ in equation (4.184) has to be zero. It follows after some calculations that either equation (4.182) or equation

$$\frac{\pi}{8}(d_2 - d_1)^3 + \mu(4t - 3d_1 - d_2 - 2\dot{h}) = 0 \quad (4.186)$$

has to be satisfied. Figure 4.20(b) shows $\frac{d}{dt}E_{\text{kin}}$ as a function of d_1 at time $t = t_0$. Equation (4.182) corresponds to a *local maximum* of $\frac{d}{dt}E_{\text{kin}}$. Since we cannot choose the separation point upstream of the point $x = d_1^{BV}$ (see Figure 4.20), we conclude equation (4.186) determines a *global minimum* of $\frac{d}{dt}E_{\text{kin}}$. Equation (4.186) will be solved numerically by the secant method and is incorporated into the system (4.175), (4.176), (4.178) and (4.181).

For all three separation criteria the point $x = d_1$ jumps at $t = t_0$ such that $d_1(t_0^+) > d_0$. The widest jump corresponds to the Brillouin-Villat criterion, the lowest jump corresponds to the energy criterion.

4.5.4 Local behaviour of the complex velocity in the separation stage

In this subsection, we discuss the behaviour of the complex velocity $f_t(z) = \varphi_x - i\varphi_y$, $z = x + iy$ at the points $z = d_0$, $z = d_1(t_0^+)$ and $z = d_1(t)$. At $t = t_0$ we find from the mixed boundary value problem (4.157) – (4.161) at $t = t_0^-$ and the assumption $\bar{\varphi}_x(x) = \varphi_x(x, 0, t_0^-)$ for $d_0 < x < d_1(t_0^+)$ that

$$\bar{\varphi}_x(x) = \sqrt{\frac{x - d_0}{d_2(t_0) - x}}(2x + d_0 - 3t_0) \quad (d_0 < x < d_1(t_0^+)). \quad (4.187)$$

In particular, the horizontal fluid velocity is continuous at $x = d_0$. In section 4.2, we showed for the problem of a plate impacting the fluid obliquely that the horizontal fluid velocity is discontinuous at the rear end of the wake region, involving an unbounded vertical flow velocity (see equation (4.88)). This is different in the present problem where, for $t > t_0$, the

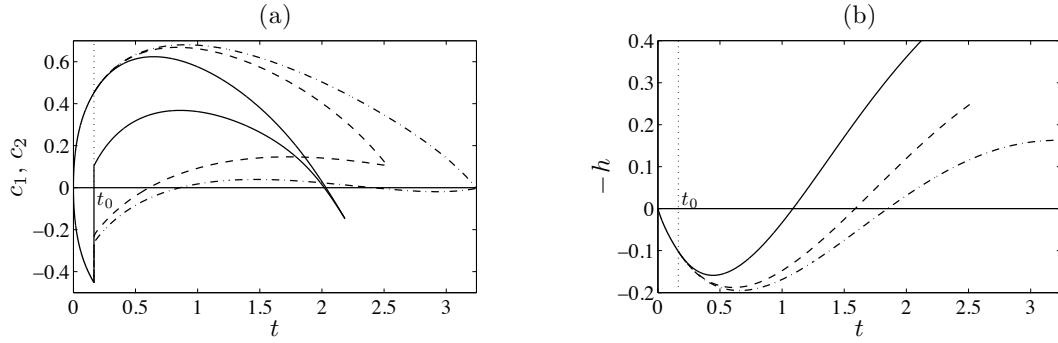


Figure 4.21: (a) The contact points c_1 and c_2 for $\mu = 0.25$ and $\kappa = 0.2$, where the Brillouin-Villat criterion (solid), shoulder criterion (dashed) and energy criterion (dashed-dotted) are satisfied. (b) The penetration depth h for all three separation criteria (legend see (a)).

complex velocity close to $z = d_0$ is given by

$$f_t(z) = -i\varphi_y(d_0, 0, t) - \frac{3(d_0 - t_0)}{\sqrt{2t_0}}(z - d_0)^{1/2} + O(z - d_0) \quad (z \rightarrow d_0). \quad (4.188)$$

The vertical fluid velocity at $x = d_0$, $y = 0$ is given by $\varphi_y(d_0, 0, t_0) = 2(t_0 - d_0) - \dot{h}(t_0)$ at the beginning of separation, $t = t_0$, and can be computed by equation (4.66) for $t > t_0$. By integrating $f_t(z)$ in (4.188) in time, we find that free surface-elevation has a square-root behaviour coming from the fluid pile-up in the Wagner stage. The behaviour of $f_t(z)$ at $z = d_1(t_0^+)$ is more difficult to determine. We verified only numerically that

$$\bar{\varphi}_x(x) = \bar{\varphi}_x(d_1(t_0^+)) + C(x - d_1(t_0^+))^{1/2} + O(x - d_1(t_0^+)) \quad (x \rightarrow d_1(t_0^+), x > d_1(t_0^+)) \quad (4.189)$$

where the real-valued constant C is positive if using the shoulder or energy criterion, and $C = 0$ if using the Brillouin-Villat criterion. Hence, we obtain for $t > t_0$

$$f_t(z) = \bar{\varphi}_x(d_1(t_0^+)) - i\varphi_y(d_1(t_0^+), 0, t) - C(z - d_1(t_0^+))^{1/2} + O(z - d_1(t_0^+)) \quad (z \rightarrow d_1(t_0^+)). \quad (4.190)$$

The behaviour of the complex velocity at the separation point $x = d_1(t)$, $y = 0$ for $t > t_0$ is given by

$$f_t(z) = \bar{\varphi}_x(d_1) - i\omega_t(d_1, t) + C_1(t)(z - d_1)^{1/2} + (\bar{\varphi}_{xx}(d_1) - i\omega_{tx}(d_1, t))(z - d_1) + C_2(t)(z - d_1)^{3/2} + O((z - d_1)^2) \quad (z \rightarrow d_1) \quad (4.191)$$

where $C_1(t)$ is positive if using the shoulder or energy criterion, and $C_1(t) = 0$ if using the Brillouin-Villat criterion.

4.5.5 Numerical results

Numerical results are presented in Figures 4.21 – 4.24 for $\mu = 0.25$ and $\kappa = 0.2$, corresponding to a body with curvature $R = 1\text{m}$, mass $m = 10\text{kg}$, horizontal velocity $U = 10\text{m s}^{-1}$, initial vertical velocity $V = 1\text{m s}^{-1}$, where the body is exposed to gravitational force with

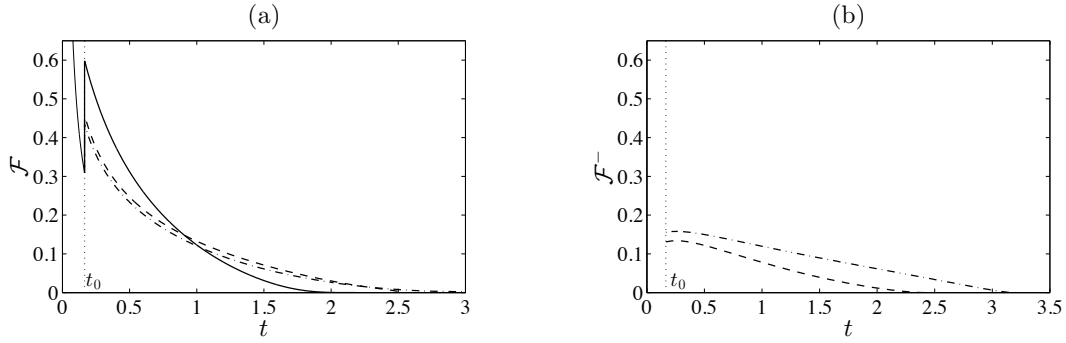


Figure 4.22: (a) The vertical hydrodynamic force in dependence of time for $\mu = 0.25$ and $\kappa = 0.2$, where the Brillouin-Villat criterion (solid), shoulder criterion (dashed) and energy criterion (dashed-dotted) are satisfied, (b) The negative hydrodynamic force \mathcal{F}^- (legend see (a)).

gravitational acceleration of $g = 9.81\text{m s}^{-2}$. In Figure 4.21(a) the evolution of the contact points in the frame of reference with the body, $c_1 = d_1 - t$ and $c_2 = d_2 - t$, during the Wagner stage is illustrated for $0 < t < t_0 = 0.165$. When $t = t_0$ the rear contact point c_1 jumps beyond the lowest point of the body if the Brillouin-Villat criterion is applied. In this case the hydrodynamic loads are highest compared with the shoulder and energy criterion, and the body is quickly forced out of the fluid (see Figures 4.21(b) and 4.22(a)). The energy criterion provides the smallest jump of c_1 at $t = t_0$ and the largest delay in the exit of the body from the fluid.

Figure 4.22(a) shows the hydrodynamic force acting on the body. Note that the initial force in the Wagner stage is $\mathcal{F}(0) = \pi$, which decays in the Wagner stage to $\mathcal{F}(t_0^-) = 0.31$ and jumps to one of the three force values at $t = t_0$ corresponding to the three separation criteria. The hydrodynamic force corresponding to the Brillouin-Villat criterion is larger at $t = t_0$ than for the two other criteria, but the force decays more quickly in the separation stage since the body exits the fluid more rapidly than for the two other separation criteria. The evolution of the vertical hydrodynamic force is quite similar to the shoulder and energy criteria. We define the negative part of the hydrodynamic force as

$$\mathcal{F}^-(t) = \left| \int_{\{x:p(x,0,t)<0\}} p(x,0,t) dx \right|. \quad (4.192)$$

For the Brillouin-Villat criterion negative pressure zones do not exist, so $\mathcal{F}^-(t) \equiv 0$. Figure 4.22(b) shows that $\mathcal{F}^-(t)$ is largest if we apply the energy criterion. The differences in the negative forces for the different separation criteria is mainly responsible for the different outcomes of the plate motion (see Figure 4.21(b)).

Figure 4.23 shows the time series of the position of the body and the free surface elevation in the separation stage, where we applied the energy criterion. The positions of the free surface have been computed using equations (4.55) and (4.58). In the zone $d_1(t_0^-) < x < d_1(t_0^+)$ a splash develops. The last frame of the series shows the body at the exit, where the body is completely detached from the fluid.

Figure 4.24 compares the coefficient of restitution, $|\dot{h}(t_{\text{exit}})/\dot{h}(0)|$, for $\kappa = 0$ for the three separation criteria as a function of the non-dimensional mass μ . For increasing μ the body

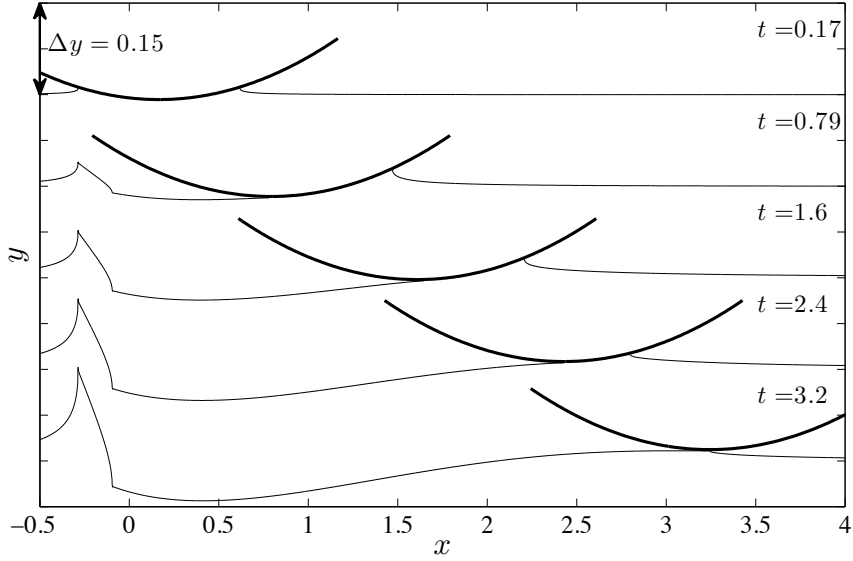


Figure 4.23: Body positions and free surface elevations for $\mu = 0.25$ and $\kappa = 0.2$ at times $t = 0.17$, $t = 0.79$, $t = 1.6$, $t = 2.4$, and $t = 3.2$, where we applied the energy separation criterion. The peak of the splash is at $x = 0.29$ and the bottom of the splash at $x = 0.10$. Note that the y -axis is stretched.

can keep a larger part of its initial kinetic energy after the exit of the body. The suction forces are responsible for a smaller restitution for shoulder and energy criterion compared to the Brillouin-Villat criterion.

4.5.6 Discussion

A coupled model of blunt body impact onto the free surface at high horizontal speed has been developed. The model consisted of a first stage with two turnover regions at the edges of the contact regions and a second stage where the fluid separates at the rear contact point. The negative pressure is released at the moment when the separation stage starts. In the

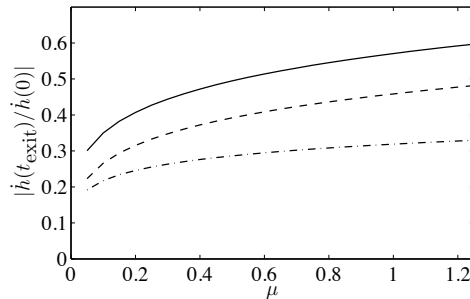


Figure 4.24: The coefficient of restitution $|\dot{h}(t_{\text{exit}})/\dot{h}(0)|$ for $\kappa = 0$ for the Brillouin-Villat criterion (solid line), the shoulder criterion (dashed line) and the energy criterion (dash-dotted line).

separation stage, the position of the contact point was modelled by three separation criteria, where the choice of the criterion is significant for the outcome of the fluid-body interaction. Experiments on blunt body impact at high speed may be very helpful to choose the right separation condition.

We focused on the effects of the different separation criteria on the body-water interaction and wanted to keep the body shape and dynamics as simple as possible. A pitch degree of freedom might be introduced. If the body's surface shape is an ellipsoid, the rotation of the body may influence the hydrodynamic loads significantly, as illustrated by the analysis of Khabakhpasheva and Korobkin (2012). A modified model may be used for stone skimming. In stone skimming the spin of the stone is important for the body dynamics and can be taken into account by a restoring force for the pitch motion. The spin itself has only negligible influence on the water flow.

4.6 Conclusion

This chapter introduced the theory of body impact at high horizontal speed for the linearised hydrodynamic problem. A general form of the pressure distribution has been found by considering the complex acceleration potential. The position of the forward contact point has been determined by Wagner's condition. The type of fluid flow at the rear contact point and the position of the contact point depends on the specific shape of the body and the motion of the body. In the first case study, where we considered the impact of a plate onto the water surface at constant speed, the fluid separates at the trailing edge. We imposed Kutta's condition at the separation point to obtain tangential flow separation. The free-surface elevation is logarithmic singular at the initial penetration point. In a second study, we determined the vertical motion of the plate by Newton's second law. If the plate is light enough it strongly decelerates in vertical direction. In this case, the hydrodynamic pressures at the rear part of the plate is below atmospheric pressure. We applied the Brillouin-Villat separation criterion and we showed that the contact region stays constant if the fluid separates ahead of the trailing edge. Finally, we discussed the impact of a blunt body onto the water surface. In this problem a negative pressure zone develops inside the contact region and expands to the rear contact point. We showed that the choice of the separation criterion influences significantly the motion of the body.

Chapter 5

Free fall of elastic plates at high horizontal speed

In this chapter we analyse the interactions that occur when an elastic plate falls onto a water free surface at high horizontal speed (see Figure 5.1). As we already have seen for the impact of rigid plates at high horizontal speed in sections 4.2 and 4.4, the hydrodynamic loads are high for small angles of attack, so that the flexibility of elastic plates may play a significant role in such interactions. We have shown for the problem of vertical impact of an elastic plate in section 3.3 that owing to the elastic deformation of the plate, the loads acting on the plate can differ significantly from those for a rigid plate. Hydroelastic effects due to slamming at high horizontal speed can be observed for high-speed vessels and should be accounted for during the design process. Ulstein (1995) investigated the fluid interaction with a flexible stern seal bag on surface-effect ships. The dynamic change in air cushion volume in the bag caused by waves leads to the cobblestone effect even in mild sea states where the bag alternately jumps out of and re-enters the water. Also the aircraft and spacecraft industries are interested in the hydroelastic effects (see Seddon and Moatamedi, 2006), in both the regular landing of aircraft and spacecraft onto water and for the safe landing during emergencies. The slamming loads in all of these problems may cause unwanted structural responses.

We will model the elasticity of the plate by Euler's beam equation, as was done in section 3.3. A mathematical model of the interactions of a flexible body and the water free surface at high horizontal speed were analysed by Ulstein (1995). To couple the structural part with the hydrodynamic part, he approximated the vertical motion. In the present chapter we consider the same linearised hydrodynamic problem, but overcome the difficulties in the coupling by using our explicit form of the hydrodynamic pressure in the contact region in equation (4.38). Furthermore, our formulation of the impact problem in terms of the displacement potential simplifies the determination of the size of the contact region.

In this chapter we are also concerned with the global characteristics of elastic plate impact. The decomposition of the energy and time evolutions of energy components are shown for two cases. It will be shown for these cases that more than 75% of the total energy of the fluid-plate system is carried away with the spray jet and only a minor part is kept as kinetic energy in the bulk of the flow domain.

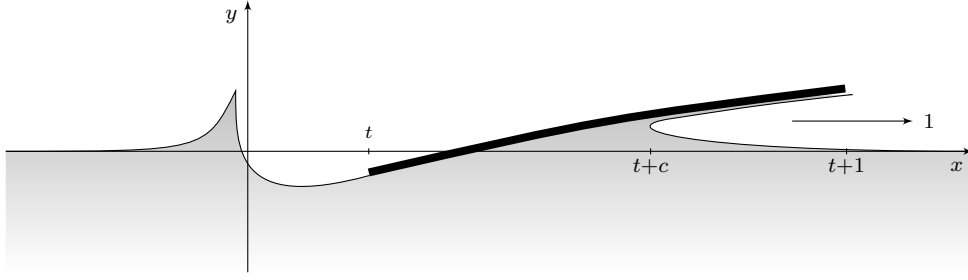


Figure 5.1: Impact of an elastic plate onto deep water at time $t > 0$ after the initial touch-down of the trailing edge. The plate freely descends and has unit horizontal velocity component.

5.1 Separation of the fluid at the trailing edge

In this section the fluid is assumed to be attached to the plate from the turnover region to the trailing edge, so that the separation point is fixed at the trailing edge and any suction forces of the fluid contribute to the dynamics of the plate. It will be shown that a sub-atmospheric pressure zone occurs on the rear side of the plate attached to the trailing edge, which arises due to the rotation of the plate. Elastic vibrations of the plate lead to even lower pressures. The fluid may detach from the body well before the trailing edge. In section 5.2 we will account for fluid separation along the elastic plate surface by determining the position of the mobile separation point by the Brillouin-Villat criterion.

Preliminary results were presented in Reinhard et al. (2011). The analysis done in this section has been published in Reinhard et al. (2013).

5.1.1 Mathematical formulation

Initially, the liquid is at rest and occupies the lower half plane $y' < 0$. The elastic plate is initially undeformed, inclined to the liquid free surface at a small angle ε , and touches the free surface at a single point which is taken as the origin of the Cartesian coordinate system $x'Oy'$. The plate material has density ρ_S , Young's modulus E and Poisson's ratio ν . The plate is of length L and small thickness h , such that $h/L \ll 1$. At time $t = 0$ the plate starts to penetrate the liquid vertically at the initial velocity V , and to move horizontally at the constant sustained speed U , where $V/U = O(\varepsilon)$. The initial angular velocity is zero. While the horizontal speed of the plate is constant, the vertical motion of the plate is free and will be determined by Euler's beam equation (see equation (3.64)). We are concerned with the initial stage of the plate impact, whose duration is of order L/U . We use the scaling given in (4.2) – (4.4).

The position of the plate at time t is described, in the non-dimensional variables, by the equation $y = \alpha\omega(x, t)$, which includes both the rigid body motions of the plate and its elastic deflection. The function $\omega(x, t)$ is unknown in advance and must be determined together with the liquid flow and the hydrodynamic pressure. In the coordinate system of the plate, the shape of the plate is described by the equations

$$y = \alpha\zeta(s, t), \quad s = x - t \quad (0 \leq s \leq 1), \quad (5.1)$$

such that $\zeta(s, t) = \omega(s + t, t)$. We model the plate motions, both rigid and elastic, with

Euler's beam equation subject to free-free boundary conditions (see equations (3.64) and (3.66)), which in non-dimensional form are given by

$$\mu \frac{\partial^2 \zeta}{\partial t^2} + \theta \frac{\partial^4 \zeta}{\partial x^4} = p(s+t, 0, t) - \mu \kappa \quad (0 < s < 1), \quad (5.2)$$

$$\frac{\partial^2 \zeta}{\partial x^2} = \frac{\partial^3 \zeta}{\partial x^3} = 0 \quad (s = 0 \text{ and } s = 1). \quad (5.3)$$

The non-dimensional parameters are given by $\mu = \rho_S h \rho_F^{-1} L^{-1}$, $\theta = D \rho_F^{-1} L^{-3} U^{-2}$, $\kappa = g L \alpha^{-1} U^{-2}$, where $D = E h^3 / (12(1 - \nu^2))$ is the flexural rigidity of the plate. Note that equation (5.2) is written in the moving coordinate system sOy . In the global coordinate system xOy , the moving plate corresponds to the interval $y = 0$, $t < x < t + 1$. The initial conditions for equations (5.2) and (5.3) are

$$\zeta(s, 0) = s, \quad \zeta_t(s, 0) = -\chi, \quad (5.4)$$

where $\chi = V/(\alpha U)$ is the non-dimensional initial vertical velocity of the plate. The rigid body motions of the plate and its elastic deflection will be evaluated in subsection 5.1.2 by the normal-mode method.

The scheme of the flow produced by the plate impact is shown in Figure 5.1. In the linearised hydrodynamic model the interval $t \leq x \leq t + c(t)$ on $y = 0$ corresponds to the wetted part of the moving plate. The point $x = t$, $y = 0$ corresponds to the trailing edge of the plate, and the point $x = t + c(t)$, $y = 0$ is the Wagner contact point. The speed $1 + \dot{c}(t)$ is assumed positive during the early stage. The velocity potential $\varphi(x, y, t)$ satisfies the following equations:

$$\nabla^2 \varphi = 0 \quad (y < 0), \quad (5.5)$$

$$\varphi_y = \omega_t(x, t) \quad (y = 0, t < x < t + c), \quad (5.6)$$

$$\varphi_x = 0 \quad (y = 0, x < 0 \text{ and } x > t + c), \quad (5.7)$$

$$\varphi_x = \bar{\varphi}_x(x) \quad (y = 0, 0 < x < t), \quad (5.8)$$

$$\varphi = O((x^2 + y^2)^{-1/2}) \quad (x^2 + y^2 \rightarrow \infty). \quad (5.9)$$

The wake function $\bar{\varphi}_x(x)$ must be determined as part of the solution. The length of the wetted part of the plate, $c(t)$, is determined by using Wagner's condition at $x = t + c$:

$$\eta(t + c, t) = \omega(t + c, t), \quad (5.10)$$

where the shape of the free surface is given by equations (4.18) and (4.19). The wake function $\bar{\varphi}_x(x)$ in (5.8) is obtained with the help of Kutta's condition at the trailing edge together with the condition of continuous separation of the free surface from the trailing edge, at $x = t$:

$$|\nabla \varphi(t, 0, t)| < +\infty, \quad (5.11)$$

$$\eta(t, t) = \omega(t, t). \quad (5.12)$$

The solution of the coupled problem (5.2) – (5.12) depends on four parameters χ , μ , θ and κ . Our analysis will treat both rigid and elastic motions of the plate, and the associated

hydrodynamic loads. The flow, the pressure distribution, the motions of the plate and its elastic deflection have to be determined simultaneously with the size of the contact region and the shape of the free surface.

5.1.2 Solution of the coupled problem

The function $\zeta(s, t)$ in (5.1) is presented as a linear superposition of normal modes $\psi_k(s)$:

$$\zeta(s, t) = \sum_{k=0}^{\infty} a_k(t) \psi_k(s) \quad (0 \leq s \leq 1) \quad (5.13)$$

with the principal coordinates $a_k(t)$ to be determined. The normal modes $\psi_k(s)$ are defined to be the dry modes of a free-free elastic plate. Properties and explicit forms of these modes were given in section 3.2.

Wagner's condition (5.10), the continuity condition (5.12) and the hydrodynamic problem (5.5) – (5.9) gives an equation for the position of the forward contact point $x = t + c(t)$ (see equation (4.54)):

$$\frac{dc}{dt} = \frac{2B(t)}{\int_0^t \frac{\sqrt{t-\xi}}{(t+c-\xi)^{3/2}} \Phi_x(\xi, 0, t) d\xi - \left(a_k, \frac{1}{c} \left[\Gamma_c^{(1)}(\psi_k) + \Gamma_c^{(2)}(\psi_k) \right] + 2\Gamma_c^{(1)}(\psi'_k) \right)} - 1, \quad (5.14)$$

$$B(t) = \int_0^t \sqrt{\frac{t-\xi}{t+c-\xi}} \bar{\varphi}_x(\xi) d\xi - \left(a_k, \Gamma_c^{(1)}(\psi'_k) \right) + \left(\dot{a}_k, \Gamma_c^{(1)}(\psi_k) \right), \quad (5.15)$$

where the terms in brackets in (5.14) are inner products, $(a_k, b_k) = \sum_{k=0}^{\infty} a_k b_k$. The functions ψ'_k are defined as the s -derivatives of ψ_k . The functionals $\Gamma_c^{(1)}$ and $\Gamma_c^{(2)}$ are defined as

$$\Gamma_c^{(1)}(f) = \int_0^c \sqrt{\frac{u}{c-u}} f(u) du, \quad \Gamma_c^{(2)}(f) = \int_0^c \sqrt{\frac{c-u}{u}} f(u) du. \quad (5.16)$$

Wagner's condition (5.10), Kutta's condition (5.11), the continuity condition (5.12) and the hydrodynamic problem (5.5) – (5.9) give us two integral equations for the wake functions $\bar{\varphi}_x(x)$ and $A(x)$ (see equations (4.51) and (4.65)):

$$\int_0^t \sqrt{\frac{t+c-\xi}{t-\xi}} \bar{\varphi}_x(\xi) d\xi = \left(\dot{a}_k, \Gamma_c^{(2)}(\psi_k) \right) - \left(a_k, \Gamma_c^{(2)}(\psi'_k) \right), \quad (5.17)$$

$$\int_0^t \sqrt{\frac{t+c-\xi}{t-\xi}} A(\xi) d\xi = \left(a_k - t\dot{a}_k, \Gamma_c^{(2)}(\psi_k) \right) + t \left(a_k, \Gamma_c^{(2)}(\psi'_k) \right). \quad (5.18)$$

If the motion of the elastic plate given by $(a_k(t))$ is prescribed, then the system of equations (5.14), (5.17) and (5.18) serves to compute the three unknown functions $\bar{\varphi}_x(x)$, $A(x)$ and $c(t)$.

The hydrodynamic pressure, the flow in the wake, and the motion of the turnover point $x = t + c(t)$ are coupled with the motions of the plate. We substitute (5.13) in (5.2) and project the result onto each individual mode $\psi_k(s)$ with the help of the orthonormality relation (3.79). We obtain a system of ordinary differential equations for the principal coor-

dinates $a_k(t)$:

$$\mu \ddot{a}_k + \theta \lambda_k^4 a_k = \int_0^c p(s+t, 0, t) \psi_k(s) ds - \mu \kappa \delta_{0k} \quad (k = 0, 1, 2, \dots). \quad (5.19)$$

Here $\delta_{kl} = 1$ for $k = l$ and $\delta_{kl} = 0$ for $k \neq l$. An explicit formula for the hydrodynamic pressure $p(x, 0, t)$ in (5.19) is given in (4.38) where $B_1(t) = 0$ due to Kutta's condition and $\omega(x, t)$ is given by (5.13). Then equations (5.19) are written in matrix-vector form as

$$M(c) \ddot{\mathbf{a}} = D(c, \dot{c}) \dot{\mathbf{a}} + S(c, \dot{c}) \mathbf{a} + \mathbf{d}(c, \dot{c}) \int_0^t \sqrt{\frac{t-\xi}{t+c-\xi}} \bar{\varphi}_x(\xi) d\xi - \mu \kappa \mathbf{e}_0, \quad (5.20)$$

where $\mathbf{a}(t) = (a_0(t), a_1(t), a_2(t), \dots)^T$ and $\mathbf{e}_0 = (1, 0, 0, \dots)^T$. The elements of the matrices $M(c)$, $D(c, \dot{c})$, $S(c, \dot{c})$, and the vector $\mathbf{d}(c, \dot{c})$ are

$$M_{kl}(c) = \Lambda_c(\Psi_l, \psi_k) + \mu \delta_{kl}, \quad (5.21)$$

$$D_{kl}(c, \dot{c}) = 2\Lambda_c(\psi_l, \psi_k) - \frac{1+\dot{c}}{\pi c} \Gamma_c^{(1)}(\psi_k) \Gamma_c^{(1)}(\psi_l), \quad (5.22)$$

$$S_{kl}(c, \dot{c}) = -\Lambda_c(\psi_l', \psi_k) - \theta \lambda_k^4 \delta_{kl} + \frac{1+\dot{c}}{\pi c} \Gamma_c^{(1)}(\psi_k) \Gamma_c^{(1)}(\psi_l'), \quad (5.23)$$

$$d_k(c, \dot{c}) = -\frac{1+\dot{c}}{\pi c} \Gamma_c^{(1)}(\psi_k), \quad (5.24)$$

where k and l are non-negative integers and $\Psi_k(s) = \int_0^s \psi_k(u) du$. The functionals $\Gamma_c^{(1)}$ and $\Gamma_c^{(2)}$ are defined in (5.16) and the functional Λ_c is defined by

$$\Lambda_c(f_1, f_2) = \frac{1}{\pi} \int_0^c \int_0^c \sqrt{\frac{v(c-v)}{u(c-u)}} \frac{f_1(u) f_2(v)}{u-v} du dv. \quad (5.25)$$

It can be shown that $\Lambda_c(\Psi_l, \psi_k) = \Lambda_c(\Psi_k, \psi_l)$, which implies that the matrix M defined in (5.21) is symmetric. A proof for this symmetry and analytical forms of the matrices and the vector in (5.21) – (5.24) in terms of c are presented in appendix B. The initial conditions for the system of ordinary differential equations (5.14) and (5.20) are

$$\mathbf{a}(0) = (\frac{1}{2}, \frac{1}{6}\sqrt{3}, 0, 0, \dots)^T, \quad \dot{\mathbf{a}}(0) = (-\chi, 0, 0, 0, \dots)^T, \quad c(0) = 0. \quad (5.26)$$

The functions $\bar{\varphi}_x(x)$ and $A(x)$, which are needed to calculate the integrals in (5.14) and (5.20), are obtained by solving the integral equations (5.17) and (5.18).

5.1.3 An account of work and energy

In this section we identify the energies contributing to the fluid plate system. We already showed in section 4.1.5, that the energy in the fluid generated by the impact of the plate is distributed in the kinetic energy of flow in the jet and in the liquid bulk (see equation (4.72)), where their time-derivatives are given in (4.69) and (4.71).

We only need to consider the energy in the plate and the work that must be done on the fluid to keep the horizontal velocity component of the plate constant. To account for the energy in the plate we multiply Euler's beam equation (5.2) with $\zeta_t(x, t)$ and integrate the

terms from $x = t$ to $x = t + c$. Hence, we obtain

$$\frac{d}{dt} \left(E_{\text{kin}}^{(p)} + E_{\text{bend}}^{(p)} + E_{\text{grav}}^{(p)} \right) = \int_0^c p \zeta_t dx, \quad (5.27)$$

where the kinetic energy, the elastic potential energy and the gravitational potential energy of the plate are

$$E_{\text{kin}}^{(p)} = \frac{\mu}{2} \int_0^1 \zeta_t^2 ds, \quad E_{\text{bend}}^{(p)} = \frac{\theta}{2} \int_0^1 \zeta_{ss}^2 ds, \quad E_{\text{grav}}^{(p)} = \mu\kappa \int_0^1 \zeta ds, \quad (5.28)$$

respectively. Now, to keep the horizontal velocity component of the plate constant, the plate does work $W(t)$ on the fluid. The time derivative of this work in non-dimensional variables is given by

$$\frac{d}{dt} W = \int_t^{t+c} p \omega_x dx. \quad (5.29)$$

By combining equations (4.72), (5.27) and (5.29) we find

$$\frac{d}{dt} \left(E_{\text{kin}}^{(p)} + E_{\text{bend}}^{(p)} + E_{\text{grav}}^{(p)} + E_{\text{bulk}}^{(f)} + E_{\text{jet}}^{(f)} - W \right) = 0. \quad (5.30)$$

Equation (5.30) implies that the total energy of the plate-liquid system including the jet energy is constant. The components of the total energy can be of different magnitude. It is valuable to investigate where the energy supplied to the plate-liquid system goes. It will be shown in the next subsection that the main part of this energy leaves the flow region with the jet.

For numerical implementation the kinetic energy, the elastic potential energy and the gravitational potential energy of the plate in (5.28) can be written as

$$E_{\text{kin}}^{(p)} = \frac{\mu}{2} \sum_{k=0}^{\infty} \dot{a}_k^2(t), \quad E_{\text{bend}}^{(p)} = \frac{\theta}{2} \sum_{k=0}^{\infty} \lambda_k^4 a_k^2(t), \quad E_{\text{grav}}^{(p)} = \mu\kappa a_0(t). \quad (5.31)$$

The time-derivative of the work $W(t)$ in (5.29) can be calculated as

$$\frac{d}{dt} W = -\frac{1+\dot{c}}{\pi c} B(t) \left(a_k, \Gamma_c^{(2)}(\psi'_k) \right) \quad (5.32)$$

$$- \sum_{k,l=0}^{\infty} \left[\Lambda_c(\Psi_l, \psi'_k) \ddot{a}_l(t) - 2\Lambda_c(\psi_l, \psi'_k) \dot{a}_l(t) + \Lambda_c(\psi'_l, \psi'_k) a_l(t) \right] a_k(t). \quad (5.33)$$

where $B(t)$ is given by (5.15). As to the kinetic energy in the fluid bulk, its time derivative given by (4.71) can be written as

$$\frac{d}{dt} E_{\text{bulk}}^{(f)} = \frac{d}{dt} W - \frac{d}{dt} E_{\text{jet}}^{(f)} + \int_t^{t+c} p(x, 0, t) \zeta_t(x, t) dx, \quad (5.34)$$

$$\int_t^{t+c} p(x, 0, t) \zeta_t(x, t) dx = -\frac{1+\dot{c}}{\pi c} B(t) \left(\dot{a}_k, \Gamma_c^{(2)}(\psi_k) \right) \quad (5.35)$$

$$- \sum_{k,l=0}^{\infty} \left[\Lambda_c(\Psi_l, \psi_k) \ddot{a}_l(t) - 2\Lambda_c(\psi_l, \psi_k) \dot{a}_l(t) + \Lambda_c(\psi'_l, \psi_k) a_l(t) \right] \dot{a}_k(t). \quad (5.36)$$

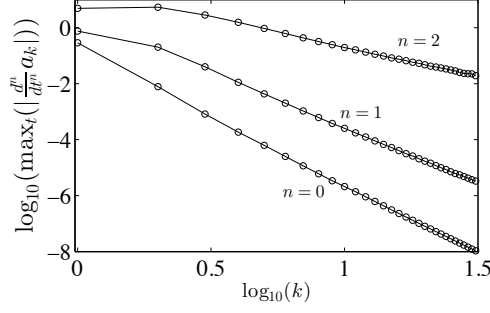


Figure 5.2: The maximum amplitude of the principle coordinates, $\max_t |a_k(t)|$ and their first, $\max_t |\dot{a}_k(t)|$, and second, $\max_t |\ddot{a}_k(t)|$, derivatives for $0 \leq k \leq 32$ in logarithmical scale.

where the energy flux $\frac{d}{dt} E_{\text{jet}}^{(f)}$ is given by (4.69). Note that $\Lambda_c(\Psi_l, \psi_k)$, $\Lambda_c(\psi_l, \psi_k)$ and $\Lambda_c(\psi_l', \psi_k)$ are already computed in (5.21) – (5.23).

5.1.4 The hydrodynamic loads on the plate

Equation (5.19) for $k = 0$ and $k = 1$ provides the following formula for the hydrodynamic force $\mathcal{F}(t) = \int_0^c p(s+t, 0, t) ds$ acting on the plate and the moment $\mathcal{M}(t) = \int_0^c sp(s+t, 0, t) ds$ about the trailing edge in terms of the principal coordinates of the rigid modes a_0 and a_1 :

$$\mathcal{F}(t) = \mu (\ddot{a}_0(t) + \kappa), \quad \mathcal{M}(t) = \frac{\mu}{2} \left(\frac{1}{\sqrt{3}} \ddot{a}_1(t) + \ddot{a}_0(t) + \kappa \right). \quad (5.37)$$

The hydrodynamic pressure is given by (4.38) where $B_1(t) = 0$ and \dot{c} is given by (5.14). As to the functions $B_2(t)$ and $T(s+t, t)$ in equation (4.38), they are given by (4.36) and (4.35). Using equation (5.13) they can be written as

$$B_2(t) = -\frac{1 + \dot{c}}{\pi c} B(t), \quad (5.38)$$

$$T(s+t, t) = \left(a_k, F_k^{(1)}(s) \right) - 2 \left(\dot{a}_k, F_k^{(2)}(s) \right) + \left(\ddot{a}_k, F_k^{(3)}(s) \right) \quad (0 < s < c). \quad (5.39)$$

where the elements of the vectors $F_k^{(i)}(s)$ are defined as:

$$F_k^{(1)}(s) = \int_0^c \frac{\psi_k'(u)}{(u-s)\sqrt{u(c-u)}} du, \quad (5.40)$$

$$F_k^{(2)}(s) = \int_0^c \frac{\psi_k(u)}{(u-s)\sqrt{u(c-u)}} du, \quad (5.41)$$

$$F_k^{(3)}(s) = \int_0^c \frac{\Psi_k(u)}{(u-s)\sqrt{u(c-u)}} du. \quad (5.42)$$

Note that these functions depend on the size of the contact region but not on the impact conditions. This implies that these functions can be pre-computed for $0 \leq c \leq 1$. We found analytical forms for $F_k^{(i)}(s)$ in terms of c which are presented in appendix C. As to the convergence of $(a_k, F_k^{(1)}(s))$, $(\dot{a}_k, F_k^{(2)}(s))$ and $(\ddot{a}_k, F_k^{(3)}(s))$, it can be shown that $F_k^{(i)}(s)$ behaves as $O(k^{2-i})$ for large k for fixed x and fixed c . In particular, $F_k^{(1)}$ diverges for growing k . However, Figure 5.2 shows for the impact problem with parameters $\mu = 0.18$,

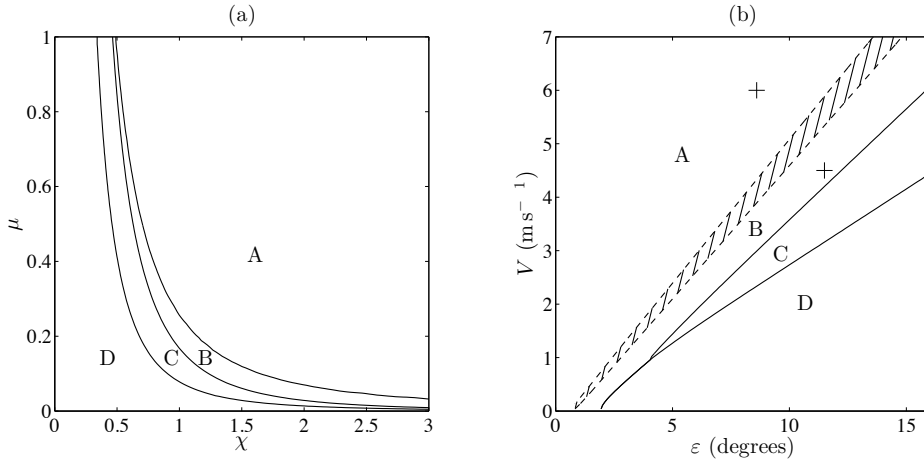


Figure 5.3: Plane of the parameters χ , μ for the rigid plate impact without gravity (a) and plane of the initial vertical speed V and initial inclination angle ε for the elastic steel plate impact with gravity (b). There are four scenarios of oblique impact of the free plate: (A) the plate is completely wetted at the end of the calculations; (B) air cavity is trapped close to the leading edge of the plate; (C) wake regions appear on both sides of the wetted area of the plate; (D) the plate exits the water before being completely wetted. Classes (A), (B) and (C) are also found to occur in the shaded region of Figure 5.3(b). The points marked by + correspond to Cases 1 and 2 described in the main text.

$\theta = 0.36$, $\chi = 1.67$, $\kappa = 0.273$ that $\max_t |a_k(t)| \approx O(k^{-4.7})$, $\max_t |\dot{a}_k(t)| \approx O(k^{-3.8})$ and $\max_t |\ddot{a}_k(t)| \approx O(k^{-1.9})$. Hence, the products $a_k(t)F_k^{(1)}(s)$, $\dot{a}_k(t)F_k^{(2)}(s)$ and $\ddot{a}_k(t)F_k^{(3)}(s)$ converge quickly to zero for increasing k .

5.1.5 Numerical results

For numerical implementation we use the time discretisation $t_n = n\Delta t$ with constant timestep Δt . We approximate $\bar{\varphi}_x(x)$ and $A(x)$ by constant values $\bar{\varphi}_x^{(n)}$ and $A^{(n)}$ in the intervals $x \in (t_{n-1}, t_n)$ for $n = 1, \dots, N$. The number of modes is limited in computations by setting $a_k = 0$ for $k \geq M$. Only the first M equations $k = 0, \dots, M-1$ in (5.20) are retained. Then equations (5.14), (5.20), (5.17) and (5.18) are solved by a numerical scheme analogue to the one described in subsection 4.4.3. In this scheme the time step Δt has to be much smaller than T_{M-1} , which is the period of the highest mode retained in our computations. Equation (3.93) shows that the period of the eigenoscillations quickly decreases as $T_k = O(k^{-2})$ as k increases.

There are many physical parameters in the problem of elastic plate impact. We are concerned with conditions when the elasticity of the plate matters and the structural behaviour of the plate is strongly coupled with the flow generated by the impact. We found that the time of interaction between a light plate and the fluid in oblique impact is very short, so that the elasticity of the plate is barely noticed. At the end of the short interaction stage for a light plate, the plate leaves the water by bouncing back up. The hydroelastic effect is much more pronounced for relatively heavy thick plates, when the interaction stage is longer.

There are two non-dimensional parameters, χ and μ , which govern the rigid plate impact, when the gravity force is neglected compared to the hydrodynamic force acting on the plate.

Depending on the values of these parameters four scenarios of the plate interaction with water were revealed as shown in Figure 5.3(a). The corresponding sketches of the flow configurations are shown in Figure 5.4. To determine the regions corresponding to the different outcomes of the plate impact, the calculations were performed for χ from 0.3 to 3 with step 0.03, and for μ from 0.01 to 1 with step 0.01. We computed a walk along the dividing curves, where we determined the next point with a fixed distance from the previous point by the bisection method.

For impact conditions from region A, the plate is completely wetted at the end of the impact, with the speed of the Wagner contact point, $1 + \dot{c}(t)$, being positive from the beginning to the end of the impact stage. The computation terminates when c becomes 1. In region B, the leading edge of the rigid plate enters the liquid free surface before the Wagner contact point arrives at the leading edge. This is also the time when our computation terminates. Despite the high forward speed, the subsequent scenario is similar to the so-called blockage phenomenon discussed in Korobkin and Khabakhpasheva (2006) for an elastic plate entering the water vertically. In particular, an air cavity is captured under the plate. Due to the horizontal speed of the plate, the leading edge of the plate will be submerged by fluid in the subsequent stage. We also have to consider the impact of the forward jet onto the free surface. This phenomenon already occurs shortly before the leading edge collides with the free surface. Since the jet is of high speed, the fluid free surface may be significantly disturbed which makes the modelling of the leading-edge impact and the subsequent cavity stage more difficult. Here, we do not further investigate these flow regimes. In region C, the speed of the Wagner contact point in the global coordinate system, $1 + \dot{c}$, becomes zero well before the plate is completely wetted and we stop the computation at that timestep. Here, the velocity of the forward jet decays to zero and the jet detaches from the fluid bulk. In the subsequent stage, the free surface at the forward contact point starts to separate from the plate. A wake region can be introduced to replace the Wagner contact point at the time instant when $\dot{c} = -1$. This subsequent stage is not further discussed in this thesis. The impact conditions from region D provide an exit of the plate from the liquid. In this class, the wetted length of the plate increases initially but shrinks later on, with $c(t)$ decreasing to zero while $1 + \dot{c}(t)$ remains positive from the beginning to the end of the interaction process.

Apart from the scenarios A, B, C and D, no other types were distinguished in our exploration of the (χ, μ) -plane in Figure 5.3(a). In particular, we could not find impact conditions which lead to steady planing of the free plate. The impact problems belonging to classes A and D are covered by the model presented in this section. Regions B and C are narrow and it was discovered that in these classes the height of the left edge, $h(t) = \varepsilon a_0(t)$, becomes positive and the inclination angle, $\alpha(t) = 2\varepsilon\sqrt{3}a_1(t)$, becomes negative before the present model becomes invalid. In these flow regimes, we require non-trivial extensions of the present impact model to accommodate the discussed phenomena of flow separation, bubble entrapment and jet impact. Note that a jet impact close to the plate may also occur outside of class B if the plate is flexible and the jet separates from the plate at a point x_0 where $\omega_x(x_0, t) < 0$.

In our calculations detailed in this section the plate length L is 2.4 m with plate thickness $h = 54$ mm. The plate is made of steel with density $\rho_S = 7850 \text{ kg m}^{-3}$ and flexural rigidity $D = 2860 \text{ kNm}$. The horizontal component of the plate velocity was fixed as $U = 24 \text{ m s}^{-1}$.

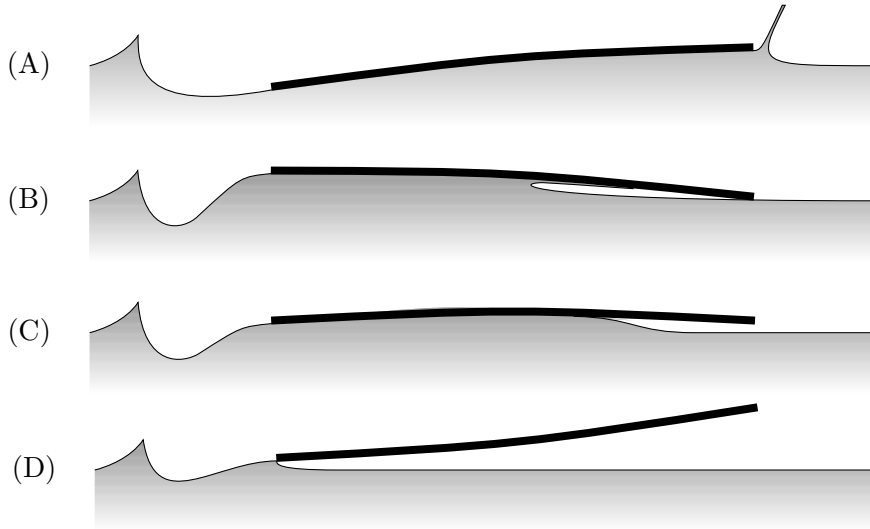


Figure 5.4: Sketches of the four flow configurations at the end of computations for an elastic plate within the present model. Classes A, B, C, D are described in the main text and in the caption for Figures 5.3(a) and (b).

The gravity acceleration g is 9.81ms^{-2} in the calculations. The mass of the plate per unit width is rather high, 1017.36kg m^{-1} , which guarantees that the interaction time is long enough for the elastic effects to be well pronounced. The values above specify the parameters $\mu = 0.18$ and $\theta = 0.36$. Although the plate is very thick, the rigidity parameter θ is rather small due to the large horizontal speed of the plate. The hydrodynamic forces acting on the plate were found to be large and strongly dependent on the plate flexibility. The only parameters which have not been fixed yet are the vertical component of the initial velocity of the plate, V , and the initial angle of attack ε .

In Figure 5.3(b) the distinguished regions A, B, C and D are shown in the (ε, V) plane with the parameters μ , κ , θ and the horizontal velocity U specified above. In contrast to Figure 5.3(a) the plate is elastic and gravity is taken into account in the equations of the plate motions. We first consider the flow regimes where the mean inclination angle of the plate, defined by $\alpha(t) = 2\varepsilon\sqrt{3}a_1(t)$, becomes zero. Then our computations stops shortly after the time when $\alpha(t) = 0$ and we mainly arrive at the fluid regimes B or C. The deflections of the elastic plate with free ends are of highest amplitude at the end points of the plate. If the contact point comes close to the leading edge at the instant when the current mean inclination angle of the plate is negative, then the class of the impact strongly depends on the current deflection of the leading edge of the plate. This makes the boundary between regions A and B less certain. We identified a region, shaded in Figure 5.3(b), in which we found examples of classes A, B and even C. The boundaries between B, C and between C, D are still sharp for a flexible plate. The regions A – D for the rigid plate have almost the same boundaries as in Figure 5.3(b), except for the shaded area, which becomes narrower as the plate rigidity increases, and it becomes sharp when the plate is rigid. Values of ε and V which lead to steady planing of the elastic plate were not detected.

Two cases were selected to illustrate the elastic plate motions with initial conditions from region A (Case 1, $\varepsilon = 8.6^\circ$, $V = 6\text{m s}^{-1}$) and region B (Case 2, $\varepsilon = 11.5^\circ$, $V = 4.5\text{m s}^{-1}$) in Figure 5.3(b) which corresponds to the parameters $\mu = 0.18$, $\theta = 0.36$, $\chi = 1.67$, $\kappa = 0.27$ and $\mu = 0.18$, $\theta = 0.36$, $\chi = 0.94$, $\kappa = 0.20$. Calculations were performed with five elastic

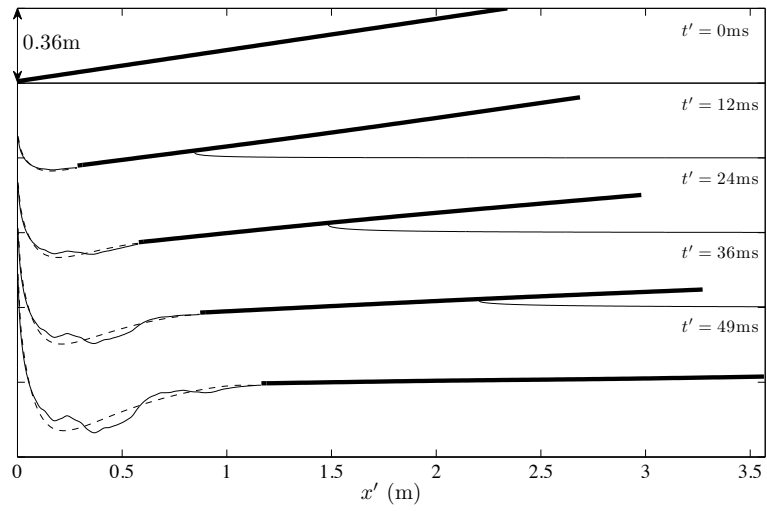


Figure 5.5: Elastic plate position (thick line), free-surface elevation (thin solid line), and the free-surface elevation for a corresponding rigid plate (thin dashed line) for Case 1. The vertical scale is the same as the horizontal scale.

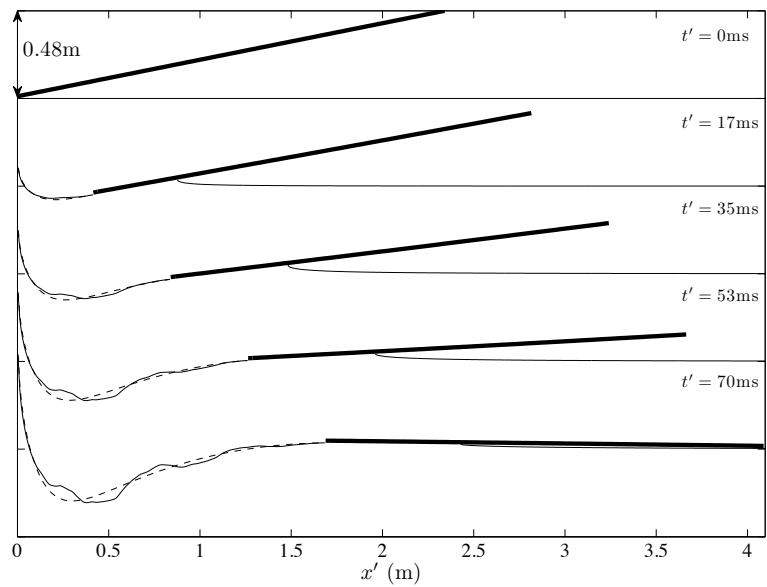


Figure 5.6: Elastic plate position (thick line), free surface elevation (thin solid line), and the free-surface elevation for a corresponding rigid plate (thin dashed line) for Case 2. The vertical scale is the same as the horizontal scale.

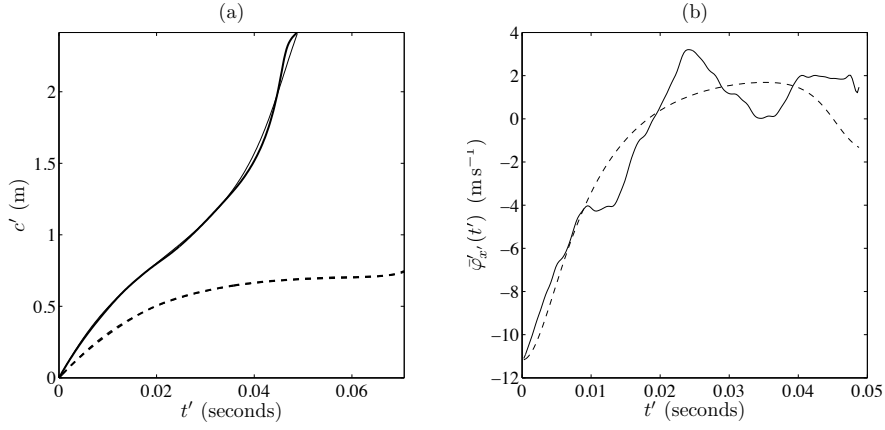


Figure 5.7: (a) Contact point motions in Case 1 (solid lines) and Case 2 (overlapping dashed lines) for elastic (thick lines) and rigid (thin line) plate, (b) horizontal fluid velocity $\bar{\varphi}'_{x'}(t')$ at the trailing edge in Case 1 shown for elastic (solid line) and rigid (dashed line) plate.

modes ($M = 7$) and an integration time step $\Delta t = 5 \times 10^{-4}$. The non-dimensional period of the fifth elastic mode is 0.01, which is 20 times larger than Δt . It was verified numerically that the relative error of the solution with five elastic modes is smaller than 1% for Case 1. The numerical solutions were compared with those for rigid plates.

The positions of the plate and the free surface at several times are shown in Figures 5.5 and 5.6 for Case 1 and Case 2, respectively. The rigid-plate solutions for the free surface are shown with dashed lines. The free surface elevations have been computed with the help of equations (4.55) and (4.58). Note that the positions of the plate and the free-surface elevations in front of the moving plate are weakly dependent on the plate elasticity. However, the free surface shape in the wake behind the plate is smooth for the rigid plate but visibly reproduces the vibrations of the elastic plate. For the initial conditions from region B (Figure 5.6) the leading edge of the plate collides with the free surface when less than a third of the plate is wetted ($c' = 0.75\text{m}$ at $t' = 70\text{ms}$). A thin air bubble is captured under the plate at this instant. Figure 5.5 and 5.6 also show the logarithmic-singular free surface elevation at $x = 0$, which we found in section 4.2 (see equation (4.88)).

Motions of the contact points for elastic and rigid plates in Cases 1 and 2 are shown in Figure 5.7(a). The initial inclination angle ε is smaller in Case 1, which leads to faster motion of the contact point than in Case 2. The motion of the contact point for the elastic plate only differs weakly from that of a rigid plate. A similar result was shown for the vertical impact of an elastic plate in section 3.3. The contact point speed, \dot{c} , is more sensitive to the plate bending in Case 1. Elasticity of the plate temporarily increases the speed of the contact point and, correspondingly, increases the hydrodynamic loads. Note that the speed of the contact point in Case 2 is rather low.

The horizontal component of velocity at the trailing edge, $\bar{\varphi}'_{x'}(t')$, is plotted as a function of time in Figure 5.7(b) for Case 1. This velocity is rather different for elastic and rigid plates, with corresponding differences in the free surface elevation (see Figure 5.5). At the beginning the horizontal flow velocity is negative, but then changes to positive values, which continue to be much smaller than the horizontal plate velocity.

Figure 5.8 shows the vertical hydrodynamic forces acting on rigid and elastic plates in

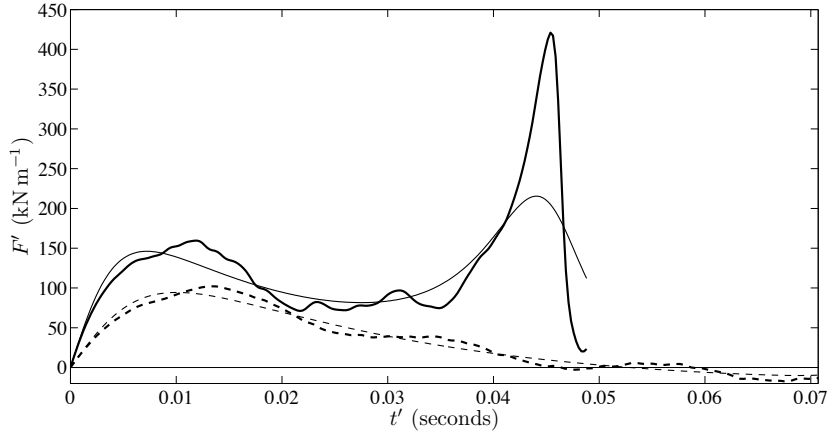


Figure 5.8: Vertical force evolution for elastic plate (thick solid line) and rigid plate (thin solid line) for Case 1 and for elastic plate (thick dashed line) and rigid plate (thin dashed line) for Case 2.

Cases 1 and 2. The forces on elastic and rigid plates in Case 1 are different in amplitude but similar in behaviour. As for the vertical impact of an elastic plate in section 3.3 we find two local maxima for the rigid plate in Case 1. Note that the maximum hydrodynamic force for the elastic plate is 415kNm^{-1} , which is double the corresponding force for the rigid plate. This amplification in the maximum force is explained by bending of the elastic plate towards the liquid and, as a result, a higher speed of the contact point. Just after the second peak the force drops sharply to zero, with the plate being completely wetted at the end of the computations. For Case 2, the difference between the forces acting on rigid and elastic plates is also well pronounced. The force has a single maximum, which is smaller than in Case 1. At the end of our calculations, the forces become negative in Case 2, which indicates that the hydrodynamic pressure in the wetted area takes negative values.

Figure 5.9(a) shows the pressure distributions for Case 1 at those times when the vertical force (see Figure 5.8) reaches its second maximum ($t'(45\text{ms}) \approx 2.1\text{m}$ for rigid and elastic plate) and when the plate is fully wetted ($t'(49\text{ms}) \approx 2.4\text{m}$ for the rigid and elastic plate). Corresponding curves for Case 2 are shown in Figure 5.9(b) for $t' = 34\text{ms}$ and $t' = 45\text{ms}$. In Case 1, the pressure in the wetted area oscillates for the elastic plate but is rather uniform for the rigid plate. The negative pressures are more pronounced for elastic plates in both cases. The fluid may cavitate in the zones of negative pressures, and this is more likely for elastic plates than for rigid ones.

Figure 5.10 shows how the total energy of the plate-liquid system is partitioned into the kinetic energy of the plate $E_{\text{kin}}^{(p)}(t)$, elastic potential energy of the plate $E_{\text{bend}}^{(p)}(t)$, gravitational potential energy of the plate $E_{\text{grav}}^{(p)}(t)$, kinetic energy of the flow in the main region $E_{\text{bulk}}^{(f)}(t)$, kinetic energy in the spray jet $E_{\text{jet}}(t)$ and the work $W(t)$ done by the plate on the fluid to keep the horizontal velocity constant. Note that $E_{\text{kin}}^{(p)}(t)$ includes the energies of vertical motion and rotation of the plate, as well as the energy of the elastic deflection. In both Cases, the work $W(t)$ is an important component in the energy balance. Figures 5.10(a) and 5.10(b) indicate that the energy supplied to the system mainly goes to the jet. In Case 1 the kinetic energy of the plate almost decays to zero, whereas in Case 2 the plate keeps a

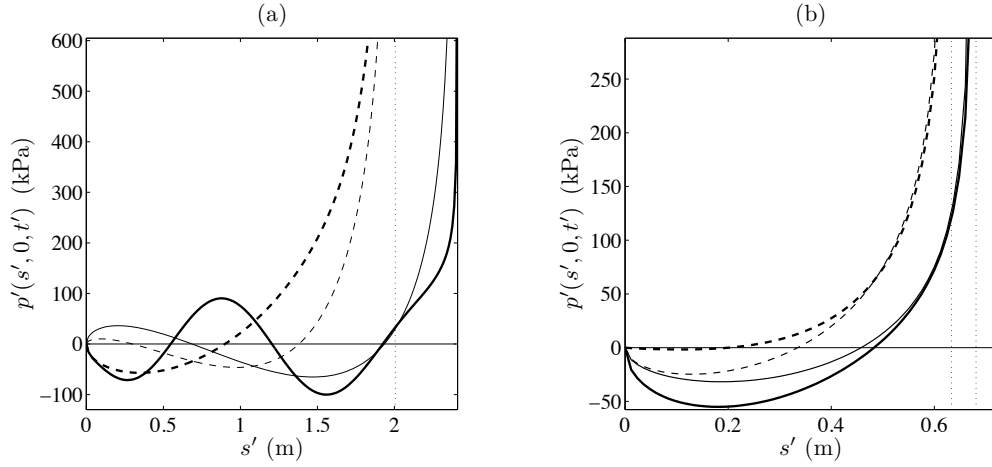


Figure 5.9: (a) Pressure distribution along the plate at $t' = 45\text{ms}$ (dashed line) and $t' = 49\text{ms}$ (solid line) for rigid (thin line) and elastic plate impact (thick line) in Case 1, (b) pressure distribution at $t' = 34\text{ms}$ (dashed line) and $t' = 45\text{ms}$ (solid line) for rigid (thin lines) and elastic plate impact (thick line) in Case 2.

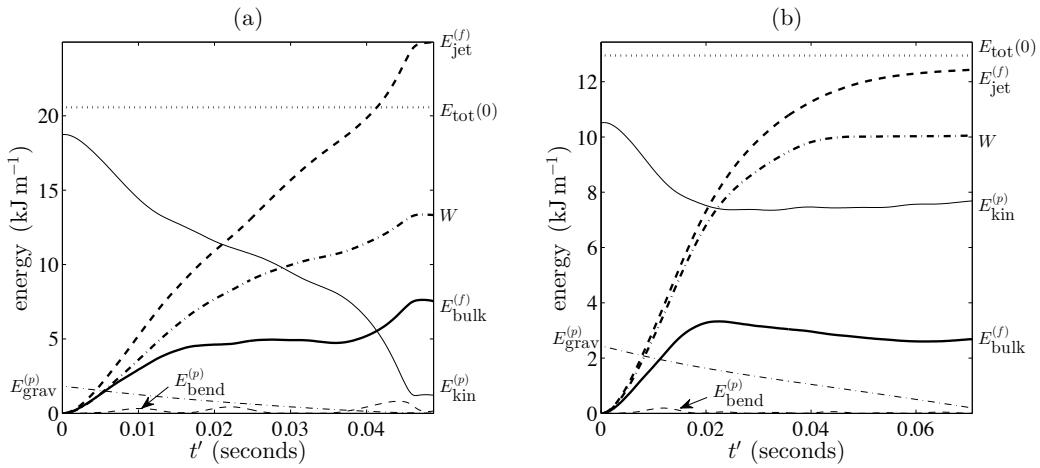


Figure 5.10: Thin lines describe $E_{\text{kin}}^{(p)}$ (solid), $E_{\text{bend}}^{(p)}$ (dashed), $E_{\text{grav}}^{(p)}$ (dash-dotted) and thick lines describe $E_{\text{bulk}}^{(f)}$ (solid), $E_{\text{jet}}^{(f)}$ (dashed), W (dash-dotted) for (a) Case 1 and (b) Case 2.

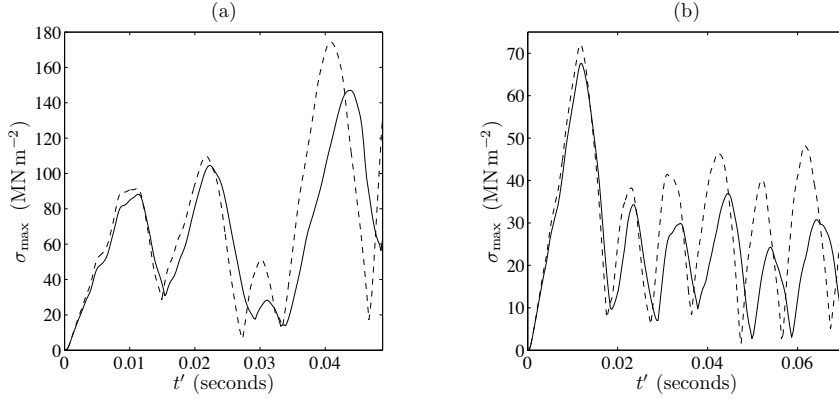


Figure 5.11: Maximum bending stress for the coupled problem (solid line) and for the uncoupled problem (dashed line) as functions of time, (a) for Case 1 and (b) for Case 2.

large part of its initial energy due to its rotation. A minor part is transferred into the kinetic energy of the bulk water flow. The contribution of the plate-bending energy to the energy balance is negligible. The energies presented in Figures 5.10(a) and (b) are much lower than the kinetic energy of the plate due to its horizontal motion, $E_{\text{kin}}^{(\text{hor})} = 318 \text{ kJ m}^{-1}$. The latter energy is independent of time t . If the horizontal motion is free and determined by Newton's second law, then $E_{\text{kin}}^{(\text{hor})}$ will be reduced by W , which is less than 15 kJ m^{-1} in both Cases. This implies that the plate will only slightly decelerate in the horizontal direction and the results of the presented analysis will not change significantly.

The distribution of the bending stresses $\sigma'(s', t')$ in the plate and the maximum stress $\sigma'_{\text{max}}(t')$ are important characteristics of the elastic plate impact problem. The dimensional stresses σ' are defined by $\sigma' = (E\varepsilon h/2L)\zeta_{ss}$, where $\zeta(s, t)$ is the non-dimensional deflection of the plate during the impact. The maximum stress is calculated at each time instant t' as

$$\sigma_{\text{max}}(t') = \max_{0 < s' < L} |\sigma'(s', t')|.$$

Figure 5.11 shows the time-evolutions of maximum bending stresses for Cases 1 and 2. Dashed lines in this Figure correspond to maximum stress estimated by the uncoupled problem of plate impact. In the uncoupled problem we apply the pressure, determined in the problem of the rigid plate impact, to the elastic plate. There is no elastic interaction between the plate and the fluid. However, the rigid motions of the plate are determined together with the fluid flow. In both Cases the bending stresses, calculated by the coupled and uncoupled approaches, are in good agreement at the beginning, but later differ strongly. For Case 1 the maximum bending stress is comparable with the yield stress which is about 250 MN m^{-2} for A36 steel, at the end of the impact stage. In Case 2, see Figure 5.11(b), the spatial maximum stress reaches its global maximum when the plate bends for the first time. Due to low hydrodynamic forces later, the maximum bending stress decays thereafter. It is possible that the stresses will increase again when the leading edge of the plate collides with the water free surface.

5.2 Fluid separation from the plate surface

In the last section, it was shown that the pressure in front of the trailing edge can be below atmospheric pressure, which may lead to separation of the liquid surface from the solid surface of the plate. Free-surface separation from the plate near the trailing edge can matter, since, in this case, negative loads cannot appear under the rear part of the plate. Here we introduce a mobile separation point on the plate whose position is determined by the Brillouin-Villat criterion. However, we are aware that there may be other separation criteria as discussed in section 4.5, which may give more plausible results and, in particular, allow pressures to be below atmospheric value in the rear part of the contact region.

The mathematical formulation of the problem is similar to the one for the problem in section 5.1. It will be shown that the motion of the separation point is sensitive to the vibration of the plate. As suction forces are absent in this model, the rigid motion differs notably from that with the separation point fixed to the trailing edge. The work done in this section has been published in Reinhard et al. (2012b).

5.2.1 Structural problem

As in section 5.1 we expand the plate deflection $\zeta(s, t)$ defined in (5.1) in terms of the dry normal modes $\psi_k(s)$ given by (3.77) and (3.78) (see equation (5.13)). Here, Euler's beam equation (5.2) in terms of the principal coordinates $a_k(t)$ is similar to the equations (5.19) and has the form

$$\mu \ddot{a}_k + \theta \lambda_k^4 a_k = \int_{d_1}^{d_2} p(x, 0, t) \psi_k(x - t) ds - \mu \kappa \delta_{0k} \quad (k = 0, 1, 2, \dots) \quad (5.43)$$

where $x = d_1$, $y = 0$, and $x = d_2$, $y = 0$, correspond to the rear and front contact points. The parameters in (5.43) are given by $\mu = \rho_S h \rho_F^{-1} L^{-1}$, $\theta = D \rho_F^{-1} L^{-3} U^{-2}$, $\kappa = g L \varepsilon^{-1} U^{-2}$. The integral (5.43) contains the hydrodynamic pressure given in (4.38), where we use (5.13) for the shape of the elastic plate. Then equation (5.43) can be written in the matrix form

$$M(d_1, d_2) \ddot{\mathbf{a}} = D(d_1, d_2, \dot{d}_1, \dot{d}_2) \dot{\mathbf{a}} + S(d_1, d_2, \dot{d}_1, \dot{d}_2) \mathbf{a} + \mathbf{b}(d_1, d_2, \dot{d}_1, \dot{d}_2; \bar{\varphi}_x(x)), \quad (5.44)$$

where $\mathbf{a}(t) = (a_0(t), a_1(t), a_2(t), \dots)^T$ is the vector with the principal coordinates of $\zeta(s, t)$. The matrices M , D and S and the vector \mathbf{b} are explicitly given by

$$M_{kl} = \Gamma(\Psi_l, \psi_k) + \mu \delta_{kl}, \quad (5.45)$$

$$D_{kl} = 2\Gamma(\psi_l, \psi_k) + \frac{1}{\pi(d_2 - d_1)} \left(\dot{d}_1 \Gamma^{(2)}(\psi_k) \Gamma^{(2)}(\psi_l) - \dot{d}_2 \Gamma^{(1)}(\psi_k) \Gamma^{(1)}(\psi_l) \right), \quad (5.46)$$

$$S_{kl} = -\Gamma(\psi'_l, \psi_k) - \theta \lambda_k^4 \delta_{kl} - \frac{1}{\pi(d_2 - d_1)} \left(\dot{d}_1 \Gamma^{(2)}(\psi_k) \Gamma^{(2)}(\psi'_l) - \dot{d}_2 \Gamma^{(1)}(\psi_k) \Gamma^{(1)}(\psi'_l) \right), \quad (5.47)$$

$$b_k = \frac{1}{\pi(d_2 - d_1)} \left(\dot{d}_1 \Gamma^{(2)}(\psi_k) \int_0^{d_1} \sqrt{\frac{d_2 - \xi}{d_1 - \xi}} \varphi_x(\xi) d\xi + \dot{d}_2 \Gamma^{(1)}(\psi_k) \int_0^{d_1} \sqrt{\frac{d_1 - \xi}{d_2 - \xi}} \varphi_x(\xi) d\xi \right) - \mu \kappa \delta_{0k}, \quad (5.48)$$

where $\Psi_k(s) = \int_0^s \psi_k(u) du$. The functionals Λ , $\Gamma^{(1)}$ and $\Gamma^{(2)}$ are defined by

$$\Lambda(f_1, f_2) = \frac{1}{\pi} \int_{c_1}^{c_2} \int_{c_1}^{c_2} \sqrt{\frac{(v-c_1)(c_2-v)}{(u-c_1)(c_2-u)}} \frac{f_1(u)f_2(v)}{u-v} dudv, \quad (5.49)$$

$$\Gamma^{(1)}(f) = \int_{c_1}^{c_2} \sqrt{\frac{u-c_1}{c_2-u}} f(u) du, \quad \Gamma^{(2)}(f) = \int_{c_1}^{c_2} \sqrt{\frac{c_2-u}{u-c_1}} f(u) du. \quad (5.50)$$

where $c_1(t) = d_1(t) - t$ and $c_2(t) = d_2(t) - t$. It is shown in appendix B that $\Lambda(\Psi_l, \psi_k) = \Lambda(\Psi_k, \psi_l)$. Hence, the matrix M defined in (5.45) is symmetric. Analytical expressions of the matrices and the vector in (5.45) – (5.48) can be found similarly as for equation (5.21) – (5.24). Setting $d_1 = t$ in (5.44) – (5.48) and using equation (5.17) gives us equations (5.20) – (5.24). However, here we need the general form in (5.44) – (5.48) to accommodate all possible fluid flow regimes at the rear contact point, as will be shown in the next subsection.

5.2.2 Hydrodynamic problem

The forward contact point, $x = d_2(t)$, is determined by equation (4.54), which can be written as

$$\dot{d}_2(t) = T_{\text{Wag1}}(d_1, d_2, \mathbf{a}, \dot{\mathbf{a}}; \bar{\varphi}_x(x), A(x)), \quad (5.51)$$

where T_{Wag1} is an explicitly known function.

The position of the rear contact point $x = d_1(t)$ is determined as follows: As we have seen in section 5.1 the pressure along the body is initially positive, so that the rear contact point stays at the trailing edge as long the pressure is positive. This is referred to as the *Kutta regime*, where we use the same model as in section 5.1. As soon as

$$L(t) = 0, \quad L(t) := \lim_{x \rightarrow t} \frac{p(x, 0, t)}{\sqrt{x-t}}, \quad (5.52)$$

the rear contact point is ahead of the trailing edge, $d_1(t) > t$, and its position is determined by the Brillouin-Villat criterion given in equation (4.113). This type of flow is referred to as the *Brillouin regime*. Note that the Brillouin-Villat criterion can only be used if the velocity of the rear contact point is positive, $\dot{d}_1(t) > 0$. Our computations of rigid-plate fall at high horizontal speed only detected the case $\dot{d}_1(t) > 0$. However, we found for elastic plates, that $\dot{d}_1(t)$ can become negative. When $\dot{d}_1(t) < 0$, we impose Wagner's condition at the rear contact point. We call this type of flow the *Wagner regime*. We discuss the three regimes starting with the Wagner regime.

Wagner regime: In the Wagner regime the horizontal velocity of the rear contact point is negative, $\dot{d}_1(t) < 0$, where $d_1(t) > t$. In this regime we have to find the functions $d_1(t)$, $d_2(t)$ and $\mathbf{a}(t)$. The position of the rear contact point is determined by Wagner's condition which is given by equation (4.51). By using equation (4.53) with $d_0 = 0$, we find that the

time derivative of equation (4.51) implies

$$\dot{d}_1 = -\frac{\int_0^{d_1} \sqrt{\frac{d_2-\xi}{d_1-\xi}} \bar{\varphi}_x(\xi) d\xi - R_2(d_1, d_2, \mathbf{a}, \dot{\mathbf{a}})}{\int_0^{d_1} \sqrt{\frac{d_2-\xi}{d_1-\xi}} (t\bar{\varphi}_{xx}(\xi) + A_x(\xi)) d\xi - R_1(t, d_1, d_2, \mathbf{a}, \bar{\varphi}_x(0))}, \quad (5.53)$$

where R_1 and R_2 are explicitly known functions. The wake functions $\bar{\varphi}_x(x)$, $\bar{\varphi}_{xx}(x)$, $A_x(x)$ are known for $0 < x < d_1$ since the wake region $0 < x < d_1$ shrinks. They are determined in the Brillouin regime and the Kutta regime, respectively (see below). In the Wagner regime the functions $d_1(t)$, $d_2(t)$ and $\mathbf{a}(t)$ are solved by the ODE system (5.44), (5.51) and (5.53). The Wagner regime ends either when \dot{d}_1 increases to zero, where we switch to the Brillouin regime. Note that we have not found any initial configurations where the position of the rear contact point $x = d_1$ reaches the left edge $x = t$, because the Wagner regimes are only of short time with the speed of the rear contact point being low. However, if there is a case where $x = d_1$, we switch to the Kutta regime. It will be shown later that the transition from Wagner to Kutta regime is complicated.

Brillouin regime: The Brillouin regime is defined to be at the times when $\dot{d}_1(t) > 0$ and $d_1(t) > t$. In this regime we have to determine the functions $d_1(t)$, $d_2(t)$, \mathbf{a} , $\bar{\varphi}_x(x)$, $A(x)$, $\bar{\varphi}_{xx}(x)$ and $A_x(x)$.

The functions $d_1(t)$ and $\mathbf{a}(t)$ are obtained by the system of ODEs (5.44) and (5.51), where D , S and \mathbf{b} in (5.44) do not depend \dot{d}_1 since Kutta's condition is satisfied. As to the position of the rear contact point, $x = d_1$, it is determined by equation (4.113), where we define the right-hand side of (4.113) by R_3 , so that equation in (4.113) can be written together with equation (5.13) as

$$R_3(d_1, d_2, \dot{d}_2, \mathbf{a}, \dot{\mathbf{a}}, \ddot{\mathbf{a}}; \bar{\varphi}_x(x)) = 0. \quad (5.54)$$

The functions $\ddot{\mathbf{a}}(t)$ and $\dot{d}_2(t)$ in equation (5.54) are obtained by equations (5.44) and (5.51). We need to find $\bar{\varphi}_x(x)$, $\bar{\varphi}_{xx}(x)$, $A(x)$, $A_x(x)$. The functions $\bar{\varphi}_x(x)$ and $A(x)$ are given by (4.51) and (4.65), which can be written as

$$\int_0^{d_1} \sqrt{\frac{d_2-\xi}{d_1-\xi}} \bar{\varphi}_x(\xi) d\xi = R_2(d_1, d_2, \mathbf{a}, \dot{\mathbf{a}}), \quad (5.55)$$

$$\int_0^{d_1} \sqrt{\frac{d_2-\xi}{d_1-\xi}} A(\xi) d\xi = R_4(t, d_1, d_2, \mathbf{a}, \dot{\mathbf{a}}), \quad (5.56)$$

where R_4 is an explicitly known function. We differentiate equations (4.51) and (4.65) in time to obtain the following integral equations for $\bar{\varphi}_{xx}(x)$ and $A_x(x)$:

$$\int_0^{d_1} \sqrt{\frac{d_2-\xi}{d_1-\xi}} \bar{\varphi}_{xx}(\xi) d\xi = R_5(d_1, d_2, \mathbf{a}, \dot{\mathbf{a}}; \bar{\varphi}_x) + \frac{1}{d_1} R_3, \quad (5.57)$$

$$\int_0^{d_1} \sqrt{\frac{d_2-\xi}{d_1-\xi}} A_x(\xi) d\xi = R_1 - tR_5 - \frac{t}{d_1} R_3, \quad (5.58)$$

where R_5 is an explicitly known function. Note that R_3 in equations (5.57) and (5.58) is zero in the Brillouin regime, as equation (5.54) is satisfied. The Brillouin regime ends either if $\dot{d}_1(t) = 0$, where we switch to the Wagner regime, or if $d_1(t) = t$, where we switch to the

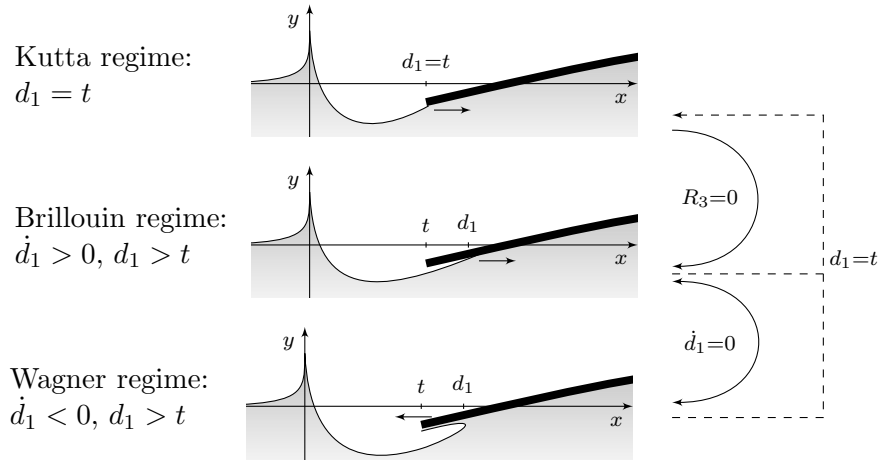


Figure 5.12: The three flow regimes at the rear contact point and the conditions when to switch to a different flow regime. The arrows in the sketches show the direction of the motion of the rear contact point in the frame of reference where the fluid in the far-field is at rest.

Kutta regime.

Kutta regime: In the Kutta regime we set $d_1(t) = t$, and we have to determine the functions $d_2(t)$, $\mathbf{a}(t)$, $\bar{\varphi}_x(x)$, $\bar{\varphi}_{xx}(x)$, $A(x)$, $A_x(x)$. As in the Brillouin regime we solve the ODE system (5.44) and (5.51). The wake functions $\bar{\varphi}_x(x)$ and $A(x)$ are described by the integral equations (5.55) and (5.56). As to the integral equations of (5.57) and (5.58), they are also valid in the Kutta regime, where we set $\dot{d}_1 = 1$. Note that $\bar{\varphi}_{xx}(x)$ and $A_x(x)$ depend on $\ddot{\mathbf{a}}$ and \dot{d}_2 , which are given by equations (5.44) and (5.51). We force the contact point to stay at the trailing edge as long as the pressure close to the trailing edge is positive, which is equivalent to $R_3(t) \leq 0$. As soon as $R_3(t) = 0$ we switch to the Brillouin regime.

5.2.3 Implementation and the switch between the flow regimes

We investigate numerically the interaction between the plate and the fluid free surface by setting $a_k = 0$ for $k \geq M$ and taking only the first M components $k = 0, \dots, M - 1$ of (5.44) into account. To integrate (5.44), (5.51) and (5.53) we use a modified Euler's method. If we are in the Brillouin or Kutta regime, the system of ODEs (5.44), (5.51) and (5.53) is coupled with the integral equations in (5.55) – (5.58). In these regimes we used a numerical scheme similar to the one described in subsection 4.4.3. Accurate results for $\bar{\varphi}_x(x)$, $A(x)$, $\bar{\varphi}_{xx}(x)$, $A_x(x)$ are necessary to evaluate equation (5.53) in the Wagner regime, so that we approximated the functions $\bar{\varphi}_x(x)$, $A(x)$, $\bar{\varphi}_{xx}(x)$, $A_x(x)$ by linear splines instead of approximating them by piecewise constant functions. In the Brillouin regime we find $d_1(t)$ from equation (5.54) by a secant method.

Initial values $\dot{d}_2(0)$, $\bar{\varphi}_x(0)$, $A(0)$ and $A_x(0)$ are taken from the self-similar results (4.77) of the oblique impact of a rigid plate with constant velocity in section 4.2. For $\bar{\varphi}_{xx}(0)$, we have to account for the presence of gravity on the plate, so that it is given by

$$\bar{\varphi}_{xx}(0) = -\frac{4\kappa}{4 + \dot{c}(0)} A_x(0), \quad (5.59)$$

where $A_x(0)$ is obtained from (4.77).

An overview of the different regimes and the conditions for the switch of the regimes is shown in Figure 5.12. A similar transition from the Kutta regime to the Brillouin regime and back has been discussed for the free fall of a rigid plate at high horizontal speed in section 4.4. Since $R_3(t) = 0$ at the end of the Kutta regime and we solve $R_3(t) = 0$ after the switch in the Brillouin regime, $d_1(t)$ does not jump at the moment of the switch. We also did not find any difficulties for the switch from the Brillouin regime to the Kutta regime. The behaviour of the complex velocity in the transition of these two regimes has been described in subsection 4.4.2 (see equation (4.122)).

Now we discuss the two switches between the Brillouin regime and the Wagner regime. The switch from the Wagner regime to the Brillouin regime is similar to the transition from the Wagner stage to the separation stage discussed in the bounce of a blunt body at high horizontal speed in section 4.5. At the moment of switch, $t = t_{WB}$, the jet at the rear contact point vanishes and the fluid detaches instantly from the rear part of the contact region where the hydrodynamic pressure is negative. Hence, the rear contact point jumps at $t = t_{WB}$ (see Figures 5.13(a) and (b)). Since $\dot{d}_1(t_{WB}^-) = 0$, equation (5.53) implies that equation (5.55) is satisfied for $t = t_{WB}^-$ and we only experience a square-root behaviour of $\bar{\varphi}_x(x)$ at $x = d_1(t_0^-)$. A small singularity appears for $A(x)$ at $x = d_1(t_0^-)$, which comes from small numerical inaccuracies. If we choose a sufficiently small time step this singularity disappears. We verified numerically that the functions $\bar{\varphi}_x(x)$ and $A(x)$ are differentiable at $x = d_1(t_0^+)$. A more detailed discussion of the flow behaviour in the transition from the Wagner regime to the Brillouin regime is given in subsection 4.5.4. Difficulties arise at times $t = t_{BW}$ when we switch from the Brillouin regime to the Wagner regime. Before the start of the Wagner regime, $\dot{d}_1(t)$ is approaching zero, while $\bar{\varphi}_x(x)$ and $A(x)$ become singular at $x = d_1(t_{BW})$. At $t = t_{BW}$ the numerator and the denominator of the fraction in equation (5.53) are zero, since the equations (5.55), (5.57) and (5.58) are satisfied at $t = t_{BW}^-$. To avoid the evaluation of equation (5.53) we directly solve the following equation derived from Wagner's condition at the rear contact point to determine $d_1(t)$ (see equation (4.52)):

$$\int_0^{d_1} \sqrt{\frac{d_2 - \xi}{d_1 - \xi}} (t\bar{\varphi}_x(\xi) + A(\xi)) d\xi - tR_2 - R_4 = 0. \quad (5.60)$$

Equation (5.60) is solved by the bisection method for the first few timesteps after $t = t_{BW}$. We experienced a small jump of $d_1(t)$ at time $t = t_{BW}$ due to numerical inaccuracies. The value $d_1(t_{BW}^+)$ converges slowly to $d_1(t_{BW}^-)$ for smaller time steps, so that a jump is not visible anymore for very small timesteps. Hence, it is advantageous to sharply reduce the time step shortly before the switch. As soon as the denominator of the fraction in equation (5.53) is distant enough from zero, we determine $d_1(t)$ by equation (5.53). In the transition from the Brillouin regime to the Wagner regime, the complex velocity $\varphi_x - i\varphi_y$ becomes square-root singular at $x = d_1$, $y = 0$. The intensity of this singularity is zero at $t = t_{BW}$ and is continuously increasing in time for $t > t_{BW}$.

Finally, we discuss the switch from the Wagner regime to the Kutta regime. We have mentioned before that we did not find any initial configuration where the rear contact point reaches the rear end of the plate in the Wagner regime, since the Wagner regimes are only of short time with the speed of the rear contact point being low. However, for prescribed motion of the plate, $d_1 = t$ can certainly happen in the Wagner regime. In the switch from

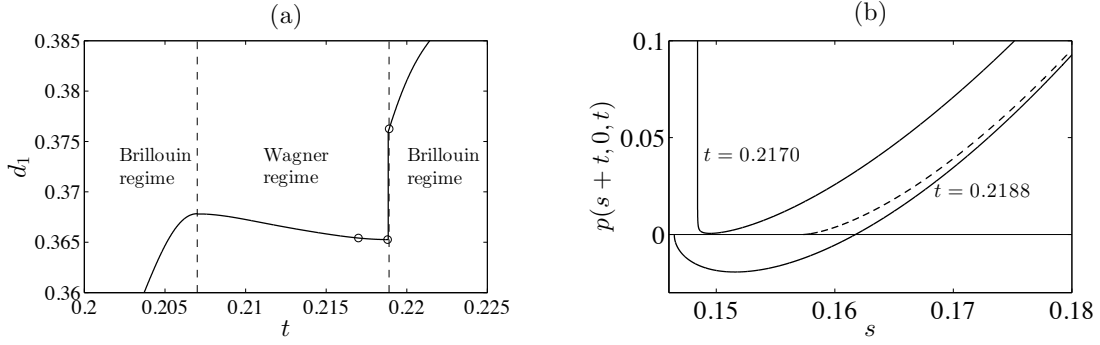


Figure 5.13: (a) The motion of the contact point for $0.2 < t < 0.225$ for the parameters $\mu = 0.16$, $\theta = 0.24$, $\chi = 1.7$ and $\kappa = 0.28$ where the first 8 elastic modes are retained. The small circles on the curve show the times when the local hydrodynamic pressure $p(x, 0, t)$ close to the rear contact point is plotted in (b). The dashed curve in (b) is the local pressure after the jump of d_1 .

the Wagner regime to the Kutta regime we would experience inverse-square-root singularities of the wake functions $\bar{\varphi}_x(x)$ and $A(x)$, because equations (5.55) and (5.56) are not satisfied at $t = t_{WK}^-$. Equations (5.55) and (5.56) are satisfied for $t = t_{WK}^+$ only if

$$\bar{\varphi}_x(x) \sim C_1(x - d_1(t_{WK}))^{-1/2}, \quad A(x) \sim C_2(x - d_1(t_{WK}))^{-1/2} \quad (x \rightarrow d_1(t_{WK})^+), \quad (5.61)$$

where the constants C_1 and C_2 are given by

$$C_1 = \frac{1}{\pi \sqrt{d_2(t_{WK}) - d_1(t_{WK})}} \left(R_2(t_{WK}) - \int_0^{d_1(t_{WK})} \sqrt{\frac{d_2(t_{WK}) - \xi}{d_1(t_{WK}) - \xi}} \bar{\varphi}_x(\xi) d\xi \right), \quad (5.62)$$

$$C_2 = \frac{1}{\pi \sqrt{d_2(t_{WK}) - d_1(t_{WK})}} \left(R_4(t_{WK}) - \int_0^{d_1(t_{WK})} \sqrt{\frac{d_2(t_{WK}) - \xi}{d_1(t_{WK}) - \xi}} A(\xi) d\xi \right), \quad (5.63)$$

It follows that $\bar{\varphi}_{xx}(x)$ and $A_x(x)$ are not integrable, which is needed to derive equations (5.57), (5.58) and (5.53). New equations need to be derived to account for the singular behaviour (5.61). Such an analysis has not been done and is not necessary, since we have not detected such a transition so far.

5.2.4 Numerical results

Numerical results are presented in Figures 5.14 – 5.19 for $\mu = 0.16$, $\theta = 0.24$ and $\chi = 1.7$. These parameters correspond to the impact of a steel plate onto water, where the plate length is $L = 2.5\text{m}$, the plate thickness is $h = 0.05\text{m}$, material density is $\rho_S = 8000\text{ kg m}^{-3}$, the flexural rigidity is $D = 2300\text{ kN m}$, the initial plate inclination is $\varepsilon = 8^\circ$, the horizontal velocity component is $U = 25\text{ m s}^{-1}$, the initial vertical velocity is $V = 6\text{ m s}^{-1}$ and the gravitational acceleration is $g = 9.81\text{ m s}^{-2}$. As discussed in section 5.1, the computation has to be stopped when the mean inclination angle $\alpha(t) = 2\sqrt{3}a_1(t)$ becomes negative, because either the plate gets fully wetted or the free surface touches the dry part of the plate ahead of the wetted part. We compare the results of the elastic plate, where we use 8 elastic modes ($M = 10$), with the rigid plate impact ($M = 2$). The computations for $M = 10$ were performed with variable non-dimensional time step ranging between 8.8×10^{-5} and

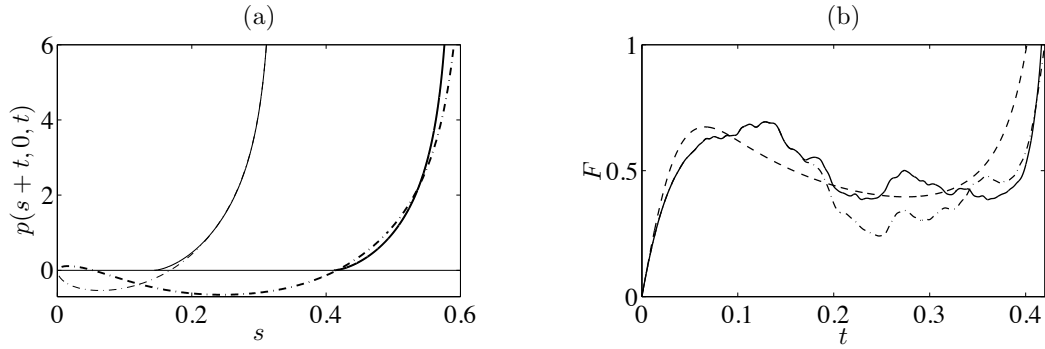


Figure 5.14: (a) Pressure distribution at times $t = 0.20$ (thin lines) and $t = 0.39$ (thick lines) for ventilated elastic (solid lines) and non-ventilated elastic (dashed-dotted lines) plate, (b) vertical hydrodynamic force for ventilated elastic (solid line), ventilated rigid (dashed line) and non-ventilated elastic (dashed-dotted line) plate.

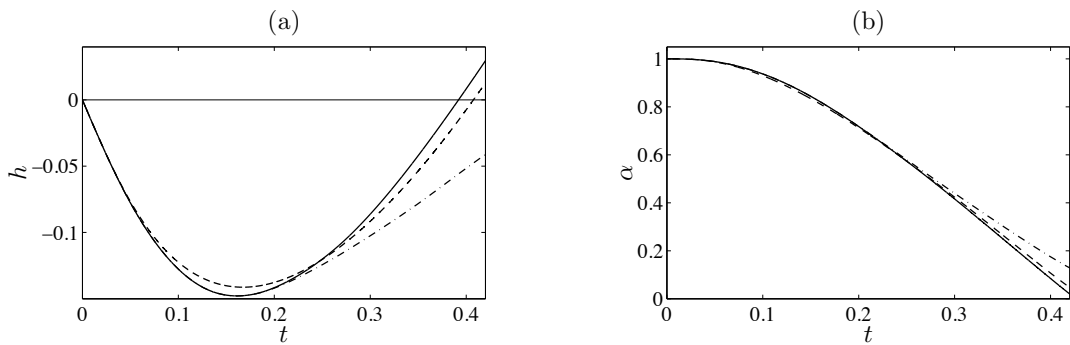


Figure 5.15: (a) The rigid motion of the plate through the mean penetration depth of the trailing edge, $h(t) = a_0(t) - \sqrt{3}a_1(t)$, and (b) the instantaneous angle of attack $\alpha(t) = 2\sqrt{3}a_1(t)$, for ventilated rigid (dashed line), ventilated elastic (solid line) and non-ventilated elastic (dashed-dotted line) plate.

8.8×10^{-4} , where we choose smaller timesteps when $\dot{d}_1(t)$ is close to zero. To see the effects of the fluid separation before the trailing edge (which is referred to as the ventilated plate), we also show the results for a non-ventilated plate where we enforce $d_1(t) = t$ as presented in section 5.1.

The pressure distribution in Figure 5.14(a) of the ventilated plate is close to that of the non-ventilated plate in the interval where the pressure is positive. Note that in the Brillouin regime the pressure distribution along the ventilated plate passes smoothly to zero pressure at $x = d_1(t)$. However, for later times the rigid motions of the ventilated and non-ventilated plate diverge, so that their pressure distributions differ at the front wetted part of the plate. In the Wagner regime, the pressure has an inverse-square root singularity at the rear contact point, the coefficient of which has a factor \dot{d}_1 (see equations (4.36) and (4.38)). The function \dot{d}_1 is usually close to zero in this regime, and so the pressure singularity at $x = d_1$ is barely pronounced. Figure 5.14(b) shows differences in the force as a function of time between the rigid and elastic plates. Since no negative pressure zones contribute to the total hydrodynamic loads of a ventilated plate, higher loads can be seen for the ventilated elastic plate as soon as $d_1(t) > t$. Large hydrodynamic loads occur here for $t > 0.4$, when

the angle of attack is very small and the downward motion of the leading edge is still quick.

Figure 5.15(a) and Figure 5.15(b) indicate the rigid body motion of the plate through the penetration depth of the left edge, and the inclination of the plate, respectively. Since no negative load is exerted on the rear part of the ventilated plate, the trailing edge is rising more quickly and the angle of attack is decaying to zero more quickly than for the non-ventilated plate.

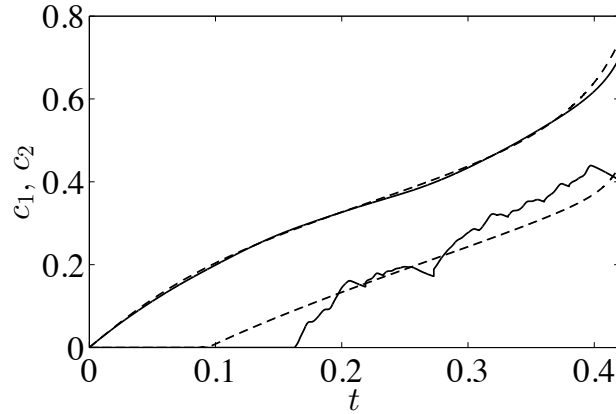


Figure 5.16: The positions of the contact points c_1 and c_2 as functions of time for rigid (dashed line) and elastic (solid line) plate with ventilation.

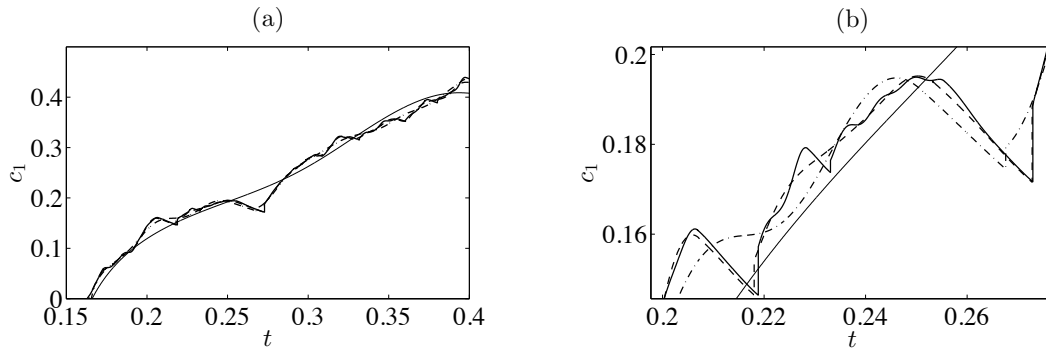


Figure 5.17: (a) The function $c_1(t)$ for 1 (thin solid line), 3 (dash-dotted line), 5 (dashed line) and 7 (thick solid line) elastic modes retained in the calculations. (b) A magnification of figure (a) in the time interval $0.20 \leq t \leq 0.27$

Figure 5.16 shows the positions of the contact points in the coordinate system moving with the plate, $c_1(t) = d_1(t) - t$ and $c_2(t) = d_2(t) - t$, as functions of time. Since the rigidity of the plate is high, the motion of the leading contact point $s = c_2(t)$ for the ventilated elastic plate only differs weakly from that of a ventilated rigid plate. The position of the separation point, $s = c_1(t)$, stays at the trailing edge $s = 0$ before starting to move forward along the plate at time t_0 . For the rigid plate the separation point departs from the trailing edge earlier ($t_0^{(r)} = 0.09$) than for the elastic plate ($t_0^{(e)} = 0.16$), since the bending of the plate delays the occurrence negative hydrodynamic forces on the rear part of the plate. Due to the rotation of the plate the coordinate $c_1(t)$ is increasing quickly for $t > t_0^{(r)}$ and $t > t_0^{(e)}$, respectively. The length of the wetted region does not exceed one-third of the length of the

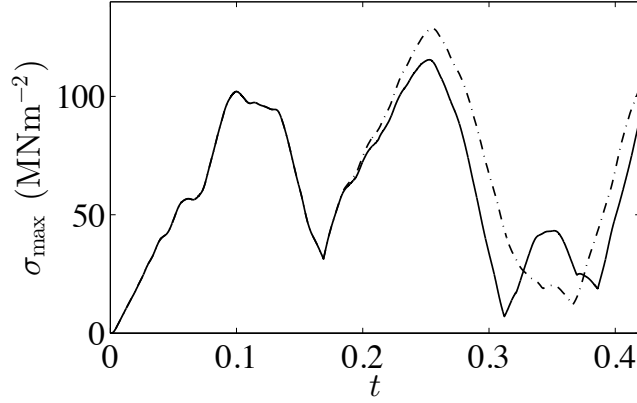


Figure 5.18: Maximum bending stress $\sigma_{\max}(t) = \max_s |\sigma(s, t)|$ for the ventilated elastic plate (solid line) and non-ventilated elastic plate (dashed-dotted line).

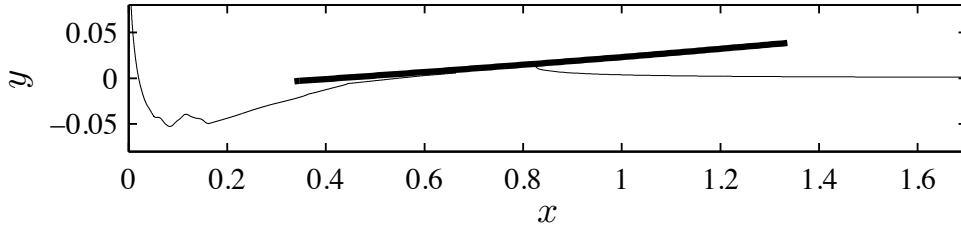


Figure 5.19: Free surface elevation $y = \varepsilon\eta(x, t)$ for $x < d_1$ and $x > d_2$ and the position of the plate $y = \varepsilon\omega(x, t)$ when $t = 0.37$.

plate. The vibrations of the elastic plate lead to oscillations of $c_1(t)$ such that $\dot{d}_1(t) < 0$, occasionally, where we switch to the Wagner regime. For $M = 10$ the computation changes from the Brillouin regime to the Wagner regime and back nine times between $t_0^{(e)}$ and 0.42. The number of switches increase, if more elastic modes are retained in the computations. We verified for up to 9 elastic modes retained in the calculations ($M = 11$) that the function c_1 converges. In Figures (5.17)(a) and (b) the function $c_1(t)$ is shown for 1, 3, 5 and 7 elastic modes. The convergence is visible from this figure.

Figure 5.18 presents the maximum bending stress of the plate $\sigma_{\max}(t) = \max_s |\sigma(s, t)|$ where $\sigma = \varepsilon E h \zeta_{ss} / (2L)$. The bending stress for a non-ventilated elastic plate is higher than for a ventilated plate. In particular, large bending stresses are observed close to the forward contact point of the plate $s = c_2(t)$, since the pressure is highest there.

Figure 5.19 shows the free surface elevation in the wake region and in front of the plate. We need to know the free surface shape to verify that the free surface does not contact the plate behind the separation point. Figure 5.19 indicates that, indeed, the free surface is below the plate. Figure 5.19 also shows the logarithmically-singular free surface elevation at $x = 0$. The plate bending is barely visible to the naked eye.

5.3 Discussion

In this chapter we presented two models for the fall of an elastic plate at high horizontal speed. In the first model we forced the rear contact point to stay at the trailing edge. We identified four different classes of plate motions depending on the impact conditions. We presented specific results for a rather thick steel plate. In this case the rigid body components of the plate's motion are very close to those of an equivalent rigid plate. However, the elastic plate experiences higher forces due to higher velocity of the turnover region. The highest loads occur at the end of the impact when the plate inclination approaches zero. The maximum bending stress in the plate was found to be close to the yield stress of the plate material. We showed that the bending stresses are overestimated if the problem is solved by a decoupled approach. Hydrodynamic pressures below atmospheric value were found in the contact region for the rigid-plate impact. It was shown that elastic vibrations of the plate lead to even lower pressures. Furthermore, it was confirmed that the shape of the free surface, hydrodynamic pressure and the flow are sensitive to such vibrations. We studied the evolutions of different energy components of the fluid-plate system. It was shown that the largest part of the plate energy was transferred into the kinetic energy in the jet and only a minor part was in the fluid bulk.

In the second model the rear contact point was able to move along the plate. The second model is more complicated since the flow regime at the rear contact point changes many times, if the plate is elastic. Difficulties in modelling the rear contact point when $\dot{d}_1(t)$ reaches zero have been overcome by introducing the Wagner regime. The motion of the rear contact point is very sensitive to the plate vibration, so that we found strong oscillations in the rear contact point. We obtained lower bending stresses in the second model than in the first model.

The initial angular speed of the plate was zero in both models presented. A non-zero angular speed can be included simply by changing the initial condition $\dot{\mathbf{a}}(0)$ in (5.26). The analysis presented in this chapter can be used for further impact problems. For example, the elastic plate can be considered as the bottom of a bigger structure landing on the water surface at high horizontal speed. In such problems realistic end conditions for the plate must be decided upon. Such a configuration makes it possible to consider more flexible plates than those treated in this chapter.

Chapter 6

Free-fall problems with flow separation

In this chapter we discuss vertical free-fall problems of a rigid plate and a rigid blunt body onto an initially flat free water surface accounting for fluid separation from the body surface. Fluid separation may occur due to vertical deceleration and rotation of the body which often involve a drop of the hydrodynamic pressure below atmospheric. In section 6.1 we analyse the free fall of a rigid plate onto the water surface, where our model involves the separation of the fluid from the lower edge of the plate, corresponding to air ventilation under the plate. In section 6.2 we discuss the free fall of a blunt body accounting for the development of cavities at the bottom of the body. The method used to analyse these problems is similar to the technique used for impact problems of bodies at high horizontal speed introduced in chapter 4.

6.1 Free vertical fall of a rigid plate with flow separation

In this section we consider the free fall of an inclined rigid plate onto a liquid surface initially at rest. This model is for general mass distribution of the plate. As we have seen in section 3.3 for the fall of an elastic plate, the plate starts to decelerate vertically and rotate so that the inclination angle decreases during the impact stage. If fluid separation is not included in the hydrodynamic model, the hydrodynamic pressure falls below atmospheric pressure on the underside of the plate either close to the impacting edge or well inside the contact region. Negative pressure zones may promote vapour cavities or air bubbles to appear under the body (Type I) or the air ventilates under the rear part of the body (Type II) (see Figure 6.1). In this section we only account for ventilation for impact problems of Type II. In the case of a wedge or blunt body impact it is unlikely that air from outside the impact region is ventilated into the low pressure zones, since these zones are enclosed by high-pressure turnover regions. The situation is different for the impact of an inclined plate: Since a turnover region at the left edge of the plate (see Figure 6.1) does not exist, air can be sucked under the plate from the initial splash region.

The type of separation depends on the mass distributions along the plate and the initial impact speed of the plate. First we identify for the impact problem without fluid separation the conditions, under which the hydrodynamic pressure first starts to drop below atmospheric

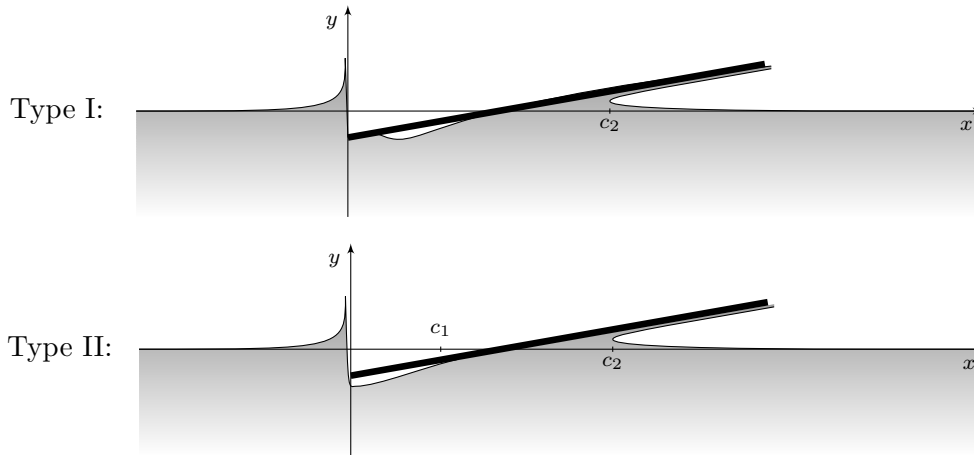


Figure 6.1: Vertical free fall of a plate onto deep water after the initial Wagner stage. Type I: The fluid separates from the plate well inside the interval $0 < x < c_2$. Type II: Ventilation occurs on the left side of the plate. The fluid is detached from the body along an interval $0 < x < c_1$. Note for both, Type I and II, the splash region is close to the initial penetration point $x = 0$ and the jet is thrown forwards from the turnover region $x = c_2$.

pressure at the left edge of the body. For the identified impact conditions we derive a model which accounts for the detachment of the fluid from the plate starting at the left edge (see Figure 6.1, Type II). The plate will be in contact with the fluid between the turnover point and a second point where the free surface separates as soon as the fluid detachment occurs. The position of the separation point is determined by the Brillouin-Villat criterion (see section 4.3). Although the coupling between the plate motion, the hydrodynamic pressure, the fluid flow and the motions of the contact points is complicated, we will obtain semi-analytical solutions of the modified model reducing the problem to two Volterra integral equations.

We show that the region on the plate surface, where the fluid detaches from the plate, is larger the more distant the centre of mass of the plate is from the trailing edge and the smaller the inertia of moment (about the centre of mass) of the plate is. Since negative pressure is not present in the modified model the plate rotates slightly quicker than in the model without account for separation. We will also compare our results with those of a plate which is not allowed to rotate.

6.1.1 Mathematical formulation

Initially, the fluid occupies the lower half-plane, $y' < 0$, and is at rest. The left edge of the inclined semi-infinite plate touches the free surface at a single point, which is taken as the origin. The initial inclination angle ε between the plate and the undisturbed free water surface is small. Then at $t' = 0$ the plate starts to penetrate the liquid with initial vertical speed V and without initial rotation. The position of the plate is described by its vertical displacement from the undisturbed free surface, $y' = x' \tan(\alpha'(t')) - h'(t')$. The position of the plate is written in terms of the penetration depth of the left edge of the plate, $h'(t')$, and the inclination angle $\alpha'(t')$ between the undisturbed free water surface and the plate. The plate is free in vertical motion and free to rotate. The functions $h'(t')$ and $\alpha'(t')$ are

determined by Newton's second law where the forcing term is given by the hydrodynamic pressure acting on the plate.

The plate has mass m , where the distance of the centre of mass of the plate from the trailing edge is D_c . The moment of inertia of the plate about the centre of mass is J . We choose $L = \sqrt{m/\rho_F}$ as the lengthscale of the problem, as in section 4.4. We assume that the initial vertical velocity is large enough that the Froude number $V^2/(gL) \gg \varepsilon$, so that we can neglect gravity as the external force acting on the plate and in the hydrodynamic model.

The body motions are governed by Newton's second law

$$m \frac{d^2 y'_0}{dt'^2} = \mathcal{F}'_y(t'), \quad J \frac{d^2 \alpha'}{dt'^2} = \mathcal{M}'(t'), \quad (6.1)$$

where $\mathcal{F}'_y(t')$ is the vertical component of the hydrodynamic force acting on the plate surface in the contact region and $\mathcal{M}'(t')$ is the moment of the hydrodynamic force about the centre of mass. The function $y'_0(t')$ is the height of the centre of mass of the plate above the equilibrium position of the free surface.

We use the scaling in (4.2) – (4.4) and $h' = \varepsilon L h$, $\alpha' = \varepsilon \alpha$. In particular, the body position at time t is described in non-dimensional variables by the following equation at the leading order as $\varepsilon \rightarrow 0$:

$$y = \varepsilon \omega(x, t), \quad \omega(x, t) = \alpha x - h \quad (x \geq 0). \quad (6.2)$$

The boundary conditions can be linearised and imposed on the initial position of the liquid boundary, $y = 0$. The wetted part of the plate corresponds to the interval $c_1 \leq x \leq c_2$, $y = 0$. The rest of the x -axis corresponds to the free surface, where the hydrodynamic pressure is zero. The hydrodynamic pressure is given by Bernoulli's equation (3.24). The velocity potential φ satisfies the following equations:

$$\nabla^2 \varphi = 0 \quad (y < 0), \quad (6.3)$$

$$\varphi_y = \dot{\alpha} x - \dot{h} \quad (y = 0, c_1 < x < c_2), \quad (6.4)$$

$$\varphi_x = 0 \quad (y = 0, x < 0 \text{ and } x > c_2), \quad (6.5)$$

$$\varphi_x = \bar{\varphi}_x(x) \quad (y = 0, 0 < x < c_1), \quad (6.6)$$

$$\varphi = O((x^2 + y^2)^{-1/2}) \quad (x^2 + y^2 \rightarrow \infty). \quad (6.7)$$

where the wake function $\bar{\varphi}_x(x)$ must be determined as part of the solution. The point $x = c_2(t)$ models the forward overturning region, where a spray jet is formed. Condition (6.5) implies that the speed of the contact point is assumed positive. The position of this point is given by Wagner's condition together with the kinematic boundary condition:

$$\eta(c_2, t) = \alpha c_2 - h \quad (c_2 \geq 0), \quad (6.8)$$

$$\eta_t = \varphi_y \quad (y = 0, c_1 \leq x \leq c_2), \quad (6.9)$$

$$\eta \equiv 0 \quad (t = 0). \quad (6.10)$$

As to the rear contact point we focus on impact conditions corresponding to Type II (see Figure 6.1). The pressure distribution at the start of impact is approximately given by the

pressure distribution for plate impact at constant vertical velocity (see equations (3.31)), which indicates that there is a time interval $0 < t < t_0$, during which the pressure is positive close to the sharp left edge:

$$L(0, t) > 0, \quad L(c_1, t) := \lim_{x \rightarrow c_1} \frac{p(x, 0, t)}{\sqrt{x - c_1}}. \quad (6.11)$$

This time interval is referred to as the Wagner stage. During the Wagner stage the rear contact point, $x = c_1(t)$, stays at $x = 0$, corresponding to the sharp left edge of the plate. The Wagner stage stops at $t = t_0$, when $L(0, t) = 0$. The time interval $t > t_0$ is referred to as the separation stage. The model of the separation stage accounts for the fluid separation from the rear part of the plate with the formation of a wake on the free surface between $x = 0$ and $x = c_1(t)$. We determine the motion of the rear contact point by the Brillouin-Villat criterion if $\dot{c}_1(t) > 0$ (see section 4.3):

$$L(c_1, t) = 0. \quad (6.12)$$

We stop our calculations as soon as $\dot{c}_1(t) = 0$. For $t > t_0$ we assume that the fluid elevation at $x = c_1$ equals the corresponding plate elevation:

$$\omega(c_1, t) = \eta(c_1, t). \quad (6.13)$$

As seen from section 3.1, condition (6.13) will not hold at $x = 0$ in the Wagner stage $0 < t < t_0$, where the free surface elevation is square-root singular. Finally, in the separation stage we assume Kutta's condition

$$|\nabla\varphi(c_1, 0, t)| < +\infty, \quad (6.14)$$

as outlined in subsection 4.1.4 to determine the vertical velocity component of the fluid in the wake region $0 < x < c_1$, $y = 0$.

To determine the position of the right contact point and the free surface we work with the displacement potential $\Phi(x, y, t)$ which satisfies the following mixed boundary value problem (see equations (4.42) – (4.46)) obtained from (6.3) – (6.8) and the kinematic boundary condition (6.9):

$$\nabla^2\Phi = 0 \quad (y < 0), \quad (6.15)$$

$$\Phi_y = \alpha x - h \quad (y = 0, c_1 < x < c_2), \quad (6.16)$$

$$\Phi_x = 0 \quad (y = 0, x < 0 \text{ and } x > c_2), \quad (6.17)$$

$$\Phi_x = t\bar{\varphi}_x + A \quad (y = 0, 0 < x < c_1), \quad (6.18)$$

$$\Phi = O((x^2 + y^2)^{-1/2}) \quad (x^2 + y^2 \rightarrow \infty). \quad (6.19)$$

Equation (6.18) characterises the wake formation with unknown wake functions $\bar{\varphi}_x(x)$, $A(x)$ and is applied only when $t > t_0$. The conditions (6.13) and (6.14), together with the condition that the kinetic energy in the fluid is finite, guarantee that the mixed boundary value problems (6.3) – (6.7) and (6.15) – (6.19) have unique solutions for given $x = c_1(t)$, $\alpha(t)$ and $h(t)$.

The functions $\alpha(t)$ and $h(t)$ are given by equations in (6.1). The non-dimensional form of equations in (6.1) at leading order are given by:

$$\mathcal{F}(t) = b\ddot{\alpha} - \dot{h}, \quad \mathcal{M}(t) = \theta\ddot{\alpha}, \quad (6.20)$$

where $b = D_c \sqrt{\rho_F/m}$ and $\theta = J \rho_F/m^2$ are the non-dimensional coordinate of centre of mass and the non-dimensional moment of inertia. In the case of a finite plate of length L^* with constant density we obtain $b = \frac{1}{2}\ell$ and $\theta = \frac{1}{12}\ell^2$ where $\ell = L^* \sqrt{\rho_F/m}$. The initial conditions for equations in (6.20) are

$$h(0) = 0, \quad \dot{h}(0) = 1, \quad \alpha(0) = 1, \quad \dot{\alpha}(0) = 0. \quad (6.21)$$

In (6.20) the non-dimensional vertical hydrodynamic force and the non-dimensional moment about the centre of mass at leading order as $\varepsilon \rightarrow 0$ are given by

$$\mathcal{F}(t) = \int_{c_1}^{c_2} p(s, 0, t) ds, \quad \mathcal{M}(t) = \int_{c_1}^{c_2} (s - b)p(s, 0, t) ds, \quad (6.22)$$

in terms of the hydrodynamic pressure $p(x, y, t)$ in the contact region $c_1 < x < c_2$, $y = 0$.

6.1.2 Wagner stage

In this subsection we find analytical solutions for the motion of the plate, the hydrodynamic pressure, the positions of the right contact point and the free surface elevation during the Wagner stage, $0 < t < t_0$. We also identify the values of the parameters b and θ for which the hydrodynamic pressure becomes negative at the left edge of the plate (Type II) and becomes negative inside the contact region (Type I) (see also Figure 3.2). Note that in the Wagner stage we have $c_1 = 0$ and we set $c := c_2$.

We analyse the impact problem by using the complex displacement $f = \Phi_x - i\Phi_y$, which is analytic in the lower half plane $y < 0$. The function $f(z)$ decays as z^{-2} in the far-field and behaves as $|f(z)| = O(|z|^{-1/2})$ when $z \rightarrow 0$ and is bounded at $z = c$. The solution of the problem (6.15) – (6.19) is given by (see equation (2.14))

$$f(z) = i \left(-\alpha z + h + \sqrt{\frac{z-c}{z}} (\alpha z + \frac{1}{2}\alpha c - h) \right), \quad (6.23)$$

$$h = \frac{3}{4}\alpha c. \quad (6.24)$$

Equation (6.24) guarantees that $f(z)$ in (6.23) decays as z^{-2} in the far field. From the complex displacement in equation (6.23) and the time integrated kinematic boundary condition (3.34) we find that the free surface elevation is given by

$$\eta(x, t) = \alpha x - h - \sqrt{\frac{x-c}{x}} (\alpha x - \frac{1}{2}\alpha c - h) \quad (x < 0 \text{ and } x > c). \quad (6.25)$$

The free-surface elevation has the typical square-root singularity at $x = 0$ as was already shown in section 3.1. The displacement potential and velocity potential in the contact region $0 < x < c$, $y = 0$, are obtained from equation (6.23) subject to the conditions at the left

edge $\varphi(0, 0, t) = \Phi(0, 0, t) = 0$:

$$\Phi(x, 0, t) = -\frac{\alpha}{2}\sqrt{x}(c-x)^{3/2} \quad (0 < x < c), \quad (6.26)$$

$$\varphi(x, 0, t) = \left(\frac{1}{2}\dot{\alpha}x + \frac{1}{4}\dot{\alpha}c - \dot{h}\right)\sqrt{x(c-x)} \quad (0 < x < c). \quad (6.27)$$

Both formulas (6.26) and (6.27) are needed later to find explicit solutions for h , α , \dot{h} and $\dot{\alpha}$. The time-derivative of (6.27) and Bernoulli's equation (3.24) together with the time-derivative of equation (6.24) show that the hydrodynamic pressure on the plate is given by

$$p(x, 0, t) = \frac{3}{8}\alpha c^2 \sqrt{\frac{x}{c-x}} + \left(\ddot{h} - \frac{1}{4}\ddot{\alpha}(2x+c)\right)\sqrt{x(c-x)} \quad (0 \leq x < c). \quad (6.28)$$

Substituting (6.28) in the force and momentum formulas (6.22), we find:

$$\mathcal{F}(t) = \pi c \left(\frac{3}{16}\alpha \dot{c}^2 + \frac{1}{8}c\ddot{h} - \frac{1}{16}c^2\ddot{\alpha} \right), \quad (6.29)$$

$$\mathcal{M}(t) = \pi c^2 \left(\frac{9}{64}\alpha \dot{c}^2 + \frac{1}{16}c\ddot{h} - \frac{9}{256}c^2\ddot{\alpha} \right) - b\mathcal{F}(t). \quad (6.30)$$

Formulas (6.25), (6.28), (6.29) and (6.30) are written in terms of the functions $c(t)$, $h(t)$ and $\alpha(t)$. For these three unknown functions we have three equations (6.20) and (6.24). Equations (6.29) and (6.30) give:

$$\left(1 + \frac{\pi}{8}c^2\right)\ddot{h} - \left(b + \frac{\pi}{16}c^3\right)\ddot{\alpha} = -\frac{3\pi}{16}\alpha c \dot{c}^2, \quad (6.31)$$

$$\left(b + \frac{\pi}{16}c^3\right)\ddot{h} - \left(\theta + b^2 + \frac{9\pi}{256}c^4\right)\ddot{\alpha} = -\frac{9\pi}{64}\alpha c^2 \dot{c}^2. \quad (6.32)$$

The coefficients of the system (6.31) and (6.32) form the inertia matrix $M(c)$, which consists of the non-dimensional structural mass matrix M_p of the dry plate and the added mass matrix $M_a(c)$. The matrices M_p and M_a are given by

$$M_p = \begin{pmatrix} 1 & -b \\ b & -\theta - b^2 \end{pmatrix}, \quad M_a(c) = \pi c^2 \begin{pmatrix} 1/8 & -c/16 \\ c/16 & -9c^2/256 \end{pmatrix}. \quad (6.33)$$

The system of ordinary differential equations consisting of the equations (6.31), (6.32) and equation (6.24) can already be solved numerically. However, analytical solutions are obtained by exploiting the fact that the right-hand sides of equations in (6.20) have simple time-integrals. Using the linearised Bernoulli's equation (3.24) we integrate the equations in (6.20) in time and use the fact that $\varphi(0, 0, t) = 0$ and $\varphi(c, 0, t) = 0$ to obtain the equations

$$\int_0^c \varphi(s, 0, t) ds = (\dot{h} - 1) - b\dot{\alpha}, \quad \int_0^c s\varphi(s, 0, t) ds = b(\dot{h} - 1) - (\theta + b^2)\dot{\alpha}. \quad (6.34)$$

Substituting expression (6.27) into equations (6.34) gives us a system in terms of \dot{h} and $\dot{\alpha}$:

$$M(c) \begin{pmatrix} \dot{h} \\ \dot{\alpha} \end{pmatrix} = \begin{pmatrix} 1 \\ b \end{pmatrix}, \quad (6.35)$$

where $M(c) = M_p + M_a(c)$ and M_p and $M_a(c)$ are given in (6.33). We integrate equations

in (6.34) once again to obtain the expressions:

$$\int_0^c \Phi(s, 0, t) ds = h - t - b(\alpha - 1), \quad \int_0^c s\Phi(s, 0, t) ds = b(h - t) - (\theta + b^2)(\alpha - 1), \quad (6.36)$$

which can be coupled with (6.26). The resulting equations can be written as:

$$M(c) \begin{pmatrix} h \\ \alpha \end{pmatrix} = \begin{pmatrix} t - b \\ bt - \theta - b^2 \end{pmatrix}, \quad (6.37)$$

which do not depend on the time-derivatives of the unknown functions c, h, α . Equations (6.24) and (6.37) contain the variables t, h and α which can be viewed as functions of c . Equations (6.24), (6.35) and (6.37) provide

$$t = \frac{\frac{\pi}{32}c^3(\theta + b^2) - \frac{3\pi}{256}c^4b + \frac{3}{4}c\theta}{\theta + \frac{\pi}{32}c^3b - \frac{3\pi}{256}c^4}, \quad \alpha = \frac{\theta}{\theta + \frac{\pi}{32}c^3b - \frac{3\pi}{256}c^4}, \quad (6.38)$$

$$\dot{h} = \frac{1}{\det M} \left(-\theta + \frac{\pi}{16}c^3b - \frac{9\pi}{256}c^4 \right), \quad \dot{\alpha} = \frac{1}{\det M} \left(\frac{\pi}{8}c^2b - \frac{\pi}{16}c^3 \right), \quad (6.39)$$

$$\dot{c} = -\frac{4}{3\theta \det M} \left(\theta + \frac{\pi}{32}c^3b - \frac{3\pi}{256}c^4 \right)^2, \quad (6.40)$$

$$\det M = -\theta - \frac{\pi}{8}(\theta + b^2)c^2 + \frac{\pi}{8}bc^3 - \frac{9\pi}{256}c^4 - \frac{\pi^2}{2048}c^6. \quad (6.41)$$

It can be shown that $\det M$ in (6.41) is negative for $c \geq 0$. Since $\det M$ is negative for $t \geq 0$ and $\theta + \frac{\pi}{32}c^3b - \frac{3\pi}{256}c^4 = 0$ only if $t = \infty$ (see first equation in (6.38)), it follows from (6.40) that $\dot{c} > 0$ for $t \geq 0$. This is consistent with our assumptions.

The formula for α in (6.38) implies that the inclination angle initially decreases in time down to its minimum value $\alpha_{\min} = \theta/(\theta + \frac{\pi}{16}b^4)$, where the contact point is $c = 2b$, and that α increases when $c > 2b$. If the mass is uniformly distributed along a finite plate, the angular velocity is zero when the plate becomes fully wetted. A similar result can also be shown if a gravity force is applied to the plate. In particular, the inclination angle cannot be negative for the vertical impact problem, in contrast to the problem where the plate impacts the water at high horizontal speed, as shown in section 5.1.

The vertical acceleration \ddot{h} and the angular acceleration $\ddot{\alpha}$ are obtained from (6.31) and (6.32):

$$\ddot{h} = \frac{3\pi}{16}\alpha\dot{c}^2 \frac{\theta + b^2 - \frac{3}{4}bc - \frac{3\pi}{256}c^4}{\det M}, \quad \ddot{\alpha} = \frac{3\pi}{16}c\dot{c}^2 \frac{b - \frac{3}{4}c - \frac{\pi}{32}c^3}{\det M}, \quad (6.42)$$

where \dot{c} is given by (6.40). Hence, we find the pressure distribution, force and momentum from (6.28), (6.29) and (6.30). With the help of (6.40) and (6.42), equation (6.29) gives us the vertical hydrodynamic force as a function of c :

$$F(t) = -\frac{\pi c}{3} \frac{(\theta + \frac{\pi}{32}c^3b - \frac{3\pi}{256}c^4)^4}{\theta(\det M)^3}. \quad (6.43)$$

Note that the force is positive for any $c \geq 0$. Similarly, we find the hydrodynamic pressure given by (6.28):

$$p(x, 0, t) = -\frac{2}{3} \frac{(\theta + \frac{\pi}{32}c^3b - \frac{3\pi}{256}c^4)^3}{\theta(\det M)^3} \sqrt{\frac{x}{c-x}} q(x), \quad q(x) = a_0 + a_1x + a_2x^2, \quad (6.44)$$

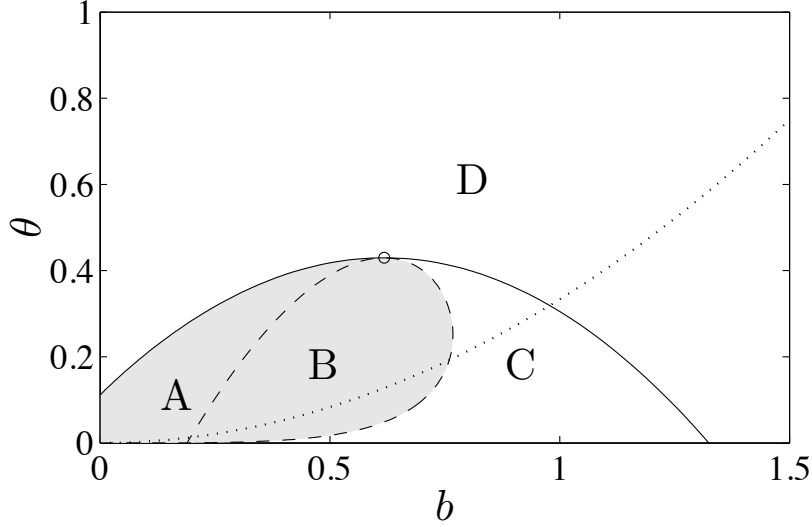


Figure 6.2: Plane of the parameters b and θ for the vertical plate impact showing four classes of solution bounded by the solid and dashed curve: (A) negative pressure zone appears inside the wetted area and expands to the left edge later, (B) negative pressure zone appears inside the wetted area and disappears without reaching the left edge, (C) negative pressure zone starts at the left edge, expands, then shrinks and disappears finally at the left edge, (D) negative pressure zone starts at the left edge, expands and moves into the wetted region, and is then closed from the left. The grey-shaded region (classes A and B) corresponds to impact of Type II, the remaining part to impact of Type I. The four classes are divided by the two curves at which $a_0 = 0$, $da_0/dc = 0$ (dashed line) and $a_0 = 0$, $a_1 = 0$ (solid line). The dashed and solid line meet tangentially at the point marked by \circ . The dotted line shows the possible values for a plate with uniform mass distribution.

where the coefficients $a_1(c)$, $a_2(c)$, $a_3(c)$ of the polynomial $q(x)$ are defined by

$$a_0(c) = \theta - \frac{3\pi}{8}(\theta + b^2)c^2 + \frac{3\pi}{8}bc^3 - \frac{15\pi}{256}c^4 + \frac{5\pi^2}{2048}c^6, \quad (6.45)$$

$$a_1(c) = \frac{\pi}{8}c(4\theta + 4b^2 - 2bc - \frac{3}{4}c^2 - \frac{5\pi}{64}c^4), \quad a_2(c) = \frac{\pi}{4}c(-b + \frac{3}{4}c + \frac{\pi}{32}c^3). \quad (6.46)$$

Equation (6.44) shows that the polynomial $q(x)$ has the same sign as $p(x, 0, t)$. Note that initially, when $c = 0$, the polynomial $q(x)$ is a positive constant. The negative pressure zone can start either at the left end of the plate, which corresponds to Type II (see Figure 6.1), or somewhere inside the wetted region, $0 < x < c$, which corresponds to Type I.

The parameter plane (b, θ) can be divided into four regions, as shown in Figure 6.2. To determine the regions corresponding to the four different scenarios of negative-pressure development during the plate impact, the calculations were performed for b from 0.01 to 1.5 with step 0.01 and for θ from 0.01 to 1 with step 0.01. For the plates from region A, negative pressure zones appear inside the wetted area (Type I). The negative pressure zone is growing, such that the left end of the negative pressure zone reaches the left edge of the plate. In region B, the negative pressure zone also starts inside the wetted interval (Type I) but stays inside the wetted area with its left boundary in $x > 0$. In regions C and D, negative pressure first appears at the left edge (Type II). For plates from region D, the negative pressure zone is moving inside the wetted region later so that the negative pressure zone gets trapped

between positive pressure at the forward contact point and at the left edge. In region C , the negative pressure zone does not get trapped. Hence, we subdivided each type of impact, Type I and II, into two classes C, D and A, B , respectively.

The precise dividing curves have been calculated analytically. Negative pressure appears first at the left edge at the time instant when the coefficients of the polynomial $q(x)$ in (6.44) satisfy $a_0 = 0$, $a_1 > 0$ and $da_0/dc < 0$. To obtain the boundary in the (b, θ) -plane of the zone corresponding to Type II, we determine the curve at which $a_0 = 0$ and $da_0/dc = 0$, shown as the solid line in Figure 6.2. The dashed line corresponds to the values b and θ for which $a_0 = 0$ and $a_1 = 0$. These two curves divide the (b, θ) -plane into the four regions A, B, C, D. Figure 6.2 shows that for a plate of length L^* with uniformly distributed mass for $0 < x' < L^*$, all four cases are possible (see dotted line), depending on the value of $L^* \sqrt{\rho_F/m}$. In Figure 6.2 the two boundaries, given by the solid and dashed line, meet tangentially at the point $b = \sqrt{6/(5\pi)}$, $\theta = 27/(20\pi)$. This point corresponds to the case when the pressure at the left end of the plate has the behaviour $p(x, 0, t) = O(x^{5/2})$ as $x \rightarrow 0$ when $c = \sqrt{24/(5\pi)}$ and becomes negative inside the wetted region thereafter.

Apart from the four classes no other cases were distinguished in our calculations. In particular, we could not find impact conditions that do not lead to negative pressure zones. However, if the mass of the plate and the moment of inertia are large, the negative pressure zone appears at sufficiently large times t .

Impact problems of Type I require the calculation of three contact points, two of which determine the spatial boundaries of the cavity. The beginning of the cavity stage, $t = t_0$, is given by $a_1^2(t_0) = 4a_0(t_0)a_2(t_0)$, when the hydrodynamic pressure becomes zero inside the contact region. This case is not discussed further in this thesis. We consider a simpler problem with cavitation in section 6.2. The separation stage for Type II impact starts at $t = t_0$ where $a_0(t_0) = 0$. The problem during the separation stage, $t \geq t_0$, is solved in the next subsection.

6.1.3 Separation stage

This subsection concerns with the free-fall of the plate onto the water free surface during the separation stage $t > t_0$ for impact problems of Type II. Since our model includes a wake region $0 < x < c_1$, $y = 0$, the problem is complicated and it was not possible to find analytical results. However, we can reduce our problem to two Volterra integral equations of the first kind and one algebraic equation, which are suitable for numerical analysis. The method for the solution of problems in which a body impacts the fluid free surface at high horizontal speed, described in chapter 4, can also be used in the present problem. In particular, the Brillouin-Villat condition implies (see equation (4.113))

$$-4\ddot{h} + (3c_1 + c_2)\ddot{\alpha} = \frac{4\dot{c}_2 B}{\pi(c_2 - c_1)^2}, \quad (6.47)$$

$$B(t) = \frac{\pi}{2}(c_2 - c_1)\dot{h} - \frac{\pi}{8}(c_2 - c_1)(3c_2 + c_1)\dot{\alpha} - \int_0^{c_1} \sqrt{\frac{c_1 - \xi}{c_2 - \xi}} \varphi_x(\xi) d\xi. \quad (6.48)$$

Equation (6.47) helps us to determine the pressure distribution along the contact region. By combining (6.47) and (4.38), we obtain

$$p(x, 0, t) = \frac{1}{4} \frac{(x - c_1)^{3/2}}{\sqrt{c_2 - x}} (2\ddot{\alpha}x + 3\ddot{\alpha}c_1 - \ddot{\alpha}c_2 - 4\ddot{h}) \quad (c_1 < x < c_2). \quad (6.49)$$

Note that the pressure (6.49) depends explicitly only on c_1 , c_2 , $\ddot{\alpha}$ and \ddot{h} . However, we substituted the Brillouin-Villat condition (4.113) into (6.49). This means that the contact point c_1 depends on the rotational velocity $\dot{\alpha}$ and the vertical velocity \dot{h} , so that $p(x, 0, t)$ depends implicitly on $\dot{\alpha}$ and \dot{h} .

We formulate the hydrodynamic force and moment and couple them with the structural part given in equations (6.20). We obtain the vertical hydrodynamic force $F(t)$ and the moment about the left edge, $M(t)$, from (6.49):

$$\mathcal{F}(t) = \frac{\pi}{16} (c_2 - c_1)^2 (\ddot{\alpha}c_2 + 5\ddot{\alpha}c_1 - 6\ddot{h}), \quad (6.50)$$

$$\mathcal{M}(t) = \frac{\pi}{4} (c_2 - c_1)^2 \left(\frac{3}{64} \ddot{\alpha} (5c_2^2 + 22c_1c_2 + 5c_1^2) - \frac{1}{4} \ddot{h} (5c_2 + c_1) \right) - b\mathcal{F}(t). \quad (6.51)$$

By substituting (6.50) and (6.51) in Newton's second law equations (6.20), we find

$$\left[1 - \frac{3\pi}{8} (c_2 - c_1)^2 \right] \ddot{h} + \left[-b + \frac{\pi}{16} (c_2 - c_1)^2 (c_2 + 5c_1) \right] \ddot{\alpha} = 0, \quad (6.52)$$

$$\left[b - \frac{\pi}{16} (c_2 - c_1)^2 (5c_2 + c_1) \right] \ddot{h} + \left[-\theta - b^2 + \frac{3\pi}{256} (c_2 - c_1)^2 (5c_2^2 + 22c_1c_2 + 5c_1^2) \right] \ddot{\alpha} = 0. \quad (6.53)$$

This linear system has a non-trivial solution only if its determinant is equal to zero:

$$\theta - (c_2 - c_1)^2 \left[\frac{3\pi}{256} (5c_2^2 + 22c_1c_2 + 5c_1^2) + \frac{3\pi}{8} (\theta + b^2) - \frac{3\pi}{8} b (c_1 + c_2) \right] + \frac{5\pi^2}{2048} (c_2 - c_1)^6 = 0. \quad (6.54)$$

This equation provides the coordinate c_1 of the separation point as a function of c_2 . This function is plotted in Figure 6.3 for three sets of parameters (b, θ) . We compare these curves with the ones arising from the zeros of the pressure in (6.44) in the model without account for separation. For $b = 1$, $\theta = \frac{1}{3}$ and $b = \frac{4}{3}$, $\theta = \frac{2}{9}$, the separation point is below the zero of the pressure for the model without account for separation. For $b = 2$, $\theta = \frac{1}{2}$ the separation point is also initially below the zero of the pressure, but becomes larger than the zero of the pressure for $c_2 > 1.3$. Figure 6.3 also shows that the function c_1 can have a maximum, so that $\dot{c}_1 < 0$ after the maximum, which is not accounted for in this model. However, the present model could be modified to accommodate the change of direction of the separation point as shown in section 5.2.

Next, we find h and α . We use the time-integrated versions of Newton's second law, presented in (6.34) and (6.36). Integrating the left-hand sides of equations in (6.34) and (6.36) by parts and using formula (2.41), for $u = \varphi_x$, $v = -\varphi_y$ and $u = \Phi_x$, $v = -\Phi_y$ where

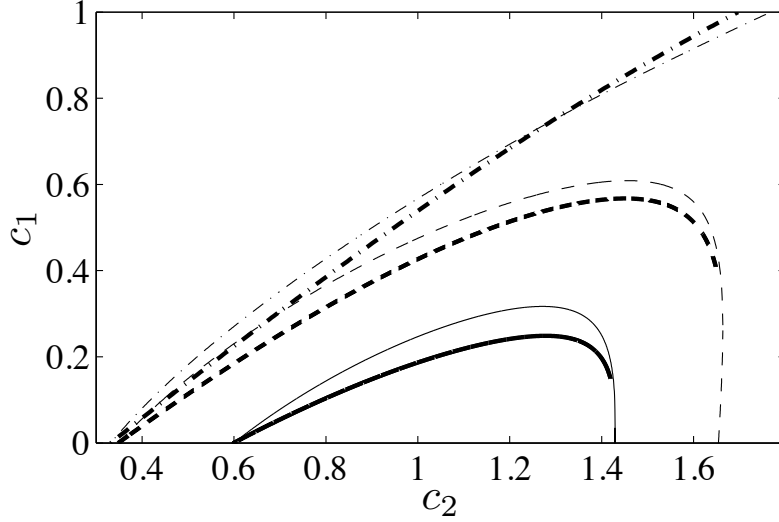


Figure 6.3: Graphs of c_1 as a function of c_2 for $b = 1$, $\theta = \frac{1}{3}$ (solid line), $b = \frac{4}{3}$, $\theta = \frac{2}{9}$ (dashed line), and $b = 2$, $\theta = \frac{1}{2}$ (dashed-dotted line), all in thick lines. Thin lines show the zero of the pressure as a function of c_2 in the model without account for separation for the same sets of the parameters.

$r(x) = x$ and $r(x) = \frac{1}{2}x^2 - c_1x$ we obtain

$$M^{(s)}(c_1, c_2) \begin{pmatrix} \dot{h} \\ \dot{\alpha} \end{pmatrix} = \mathbf{v}(\bar{\varphi}_x) + \begin{pmatrix} 1 \\ b \end{pmatrix}, \quad (6.55)$$

$$M^{(s)}(c_1, c_2) \begin{pmatrix} d_h \\ d_\alpha \end{pmatrix} = \mathbf{v}(A) - \begin{pmatrix} b \\ \theta + b^2 \end{pmatrix}, \quad (6.56)$$

where the functions d_h , d_α are given by

$$d_h = h - t\dot{h}, \quad d_\alpha = \alpha - t\dot{\alpha}. \quad (6.57)$$

and the functions $\bar{\varphi}_x(x)$ and $A(x)$ arise as unknowns in the mixed boundary-value problems (6.3) – (6.7) and (6.15) – (6.19), respectively. The functional $\mathbf{v}(f)$ is defined by

$$\mathbf{v}(f) = \begin{pmatrix} \int_0^{c_1} \sqrt{(c_1 - \xi)(c_2 - \xi)} f(\xi) d\xi \\ \int_0^{c_1} \left(\frac{1}{4}(c_1 + c_2) + \frac{1}{2}\xi \right) \sqrt{(c_2 - \xi)(c_1 - \xi)} f(\xi) d\xi \end{pmatrix}. \quad (6.58)$$

The values $\mathbf{v}(\bar{\varphi}_x)$ and $\mathbf{v}(A)$ in equations (6.55) and (6.56) describe the influence of the wake in $0 < x < c_1$, $y = 0$ on the motion of the plate. The added mass matrix in the separation stage, $M^{(s)}$, is defined by $M^{(s)} = M_p + M_a^{(s)}$, where the structural mass matrix M_p is given in (6.33) and the added mass matrix, $M_a^{(s)}$, is given by

$$M_a^{(s)}(c_1, c_2) = \pi(c_2 - c_1)^2 \begin{pmatrix} 1/8 & -(c_1 + c_2)/16 \\ (c_1 + c_2)/16 & -(9c_1^2 + 14c_1c_2 + 9c_2^2)/256 \end{pmatrix}. \quad (6.59)$$

Note that for $c_1 = 0$ the added mass matrix in the separation stage, $M_a^{(s)}$, coincides with

the added mass matrix for the non-ventilated plate, M_a , defined in (6.33).

Equations (6.55) and (6.56) can be regarded as two linear equation systems in \dot{h} , $\dot{\alpha}$ and d_h , d_α , respectively, which depend on c_1 , where c_2 is a function of c_1 via (6.54), and $\bar{\varphi}_x(x)$, $A(x)$ are assumed to be known. In fact, the functions $\bar{\varphi}_x(x)$ and $A(x)$ are determined by the conditions (6.13) and (6.14). Conditions (6.13) and (6.14) imply (see equations (4.65) and (4.51)):

$$\int_0^{c_1} \sqrt{\frac{c_2-\xi}{c_1-\xi}} \bar{\varphi}_x(\xi) d\xi = \frac{\pi}{8}(c_2 - c_1)(3\dot{\alpha}c_1 + \dot{\alpha}c_2 - 4\dot{h}), \quad (6.60)$$

$$\int_0^{c_1} \sqrt{\frac{c_2-\xi}{c_1-\xi}} A(\xi) d\xi = -\frac{\pi}{2}(c_2 - c_1)d_h + \frac{\pi}{8}(c_2 - c_1)(3c_1 + c_2)d_\alpha. \quad (6.61)$$

Consequently, we have two independent systems to solve: We find \dot{h} , $\dot{\alpha}$ and $\bar{\varphi}_x$ in terms of c_1 from equations (6.55) and (6.60), while d_h , d_α and A are found from equations (6.56) and (6.61) with c_2 given by equation (6.54). The right-hand sides of the linear systems (6.55) and (6.56) depend weakly on the functions $\bar{\varphi}_x(x)$ and $A(x)$ for x close to d_1 . To evaluate the functions d_h , d_α , \dot{h} , $\dot{\alpha}$ in terms of t , we need to find a relation between c_1 and t : We use the problem (6.15) – (6.19) to obtain (see equation (4.52))

$$t = -\frac{1}{B} \left(\frac{\pi}{2}(c_2 - c_1)d_h - \frac{\pi}{8}(c_2 - c_1)(3c_2 + c_1)d_\alpha - \int_0^{c_1} \sqrt{\frac{c_1-\xi}{c_2-\xi}} A(\xi) d\xi \right), \quad (6.62)$$

where $B = B(c_1, c_2; \bar{\varphi}_x)$ is given by equation (6.48). Since we know t , d_h , d_α , \dot{h} , $\dot{\alpha}$ in terms of c_1 , equations in (6.57) establish relations between h and t as well as α and t .

To evaluate the pressure distribution along the plate by equation (6.49), the vertical force in equation (6.50) and the moment in equation (6.51), we need to know $\ddot{\alpha}$ and \ddot{h} . To avoid numerical differentiation, we solve the system of equations (6.47), (6.52) with known right-hand sides for \ddot{h} and $\ddot{\alpha}$. The horizontal velocity of the forward contact point, \dot{c}_2 , in equation (6.47) is given by the time derivative of (6.62):

$$\dot{c}_2 = -\frac{2B}{\int_0^{c_1} \frac{\sqrt{c_1-\xi}}{(c_2-\xi)^{3/2}} (t\bar{\varphi}_x(x) + A(x)) d\xi + \frac{\pi}{2}(\alpha c_1 - 3\alpha c_2 + 2h)} \quad (6.63)$$

By using the obtained values of \ddot{h} and $\ddot{\alpha}$ we calculate the force and pressure distribution by formulas (6.28) and (6.50).

6.1.4 Vertical impact without rotation

Before we show some numerical results we consider the impact of a plate which is not allowed to rotate. A solution of this problem is obtained from the results of the previous section by increasing the moment of inertia of the plate: $\theta \rightarrow \infty$. Note that the same solution can be obtained by solving this specific free-fall problem of a plate with constant inclination. Since the response in vertical translation of the plate depends on the total mass but not on the mass distribution, the results from letting $\theta \rightarrow \infty$ must be independent of b . We obtain from equations (6.24) and (6.38):

$$t = \frac{\pi}{32}c^3 + \frac{3}{4}c, \quad \alpha = 1, \quad h = \frac{3}{4}c. \quad (6.64)$$

where we set $c_2 = c$ in the Wagner stage. In contrast to the previous section, the first equation in (6.64) shows that the contact point position, $x = c(t)$, increases to infinity as $t \rightarrow \infty$. The functions \dot{h} , \ddot{h} and c are given by equations (6.39), (6.42) and (6.64):

$$\dot{h} = \frac{1}{1 + \frac{\pi}{8}c^2}, \quad \ddot{h} = -\frac{\pi c}{3} \frac{1}{(1 + \frac{\pi}{8}c^2)^3}. \quad (6.65)$$

The vertical hydrodynamic force on the plate is $\mathcal{F}(t) = -\ddot{h}$ and from (6.44) the pressure is given by

$$p(x, 0, t) = \frac{2 - \frac{3\pi}{4}c^2 + \pi cx}{3(1 + \frac{\pi}{8}c^2)^3} \sqrt{\frac{x}{c-x}}. \quad (6.66)$$

For a non-ventilated plate, negative pressure arises on the underside of the plate, starting at $x = 0$, when $c = \sqrt{8/(3\pi)}$. The first formula in (6.64) implies that $t_0 = \frac{5}{3}\sqrt{2/(3\pi)}$. At this instant we find from (6.65) that $\dot{h}(t_0) = 3/4$ and $\dot{c}(t_0) = 1$.

Simplifications are also obtained in the separation stage. We obtain from equation (6.54) a relation between c_1 and c_2 for $t > t_0$:

$$c_2 - c_1 = \beta, \quad \beta := \sqrt{8/(3\pi)}. \quad (6.67)$$

Hence the length of the region in contact with the fluid is constant. We obtained the same results for the free fall of a plate at high horizontal speed in section 4.4. Note that for $c_1 = 0$, when the separation stage starts, the position of the forward contact point agrees with $c(t_0) = \beta$ at the end of the Wagner stage. Due to equation (6.67) it is helpful to introduce the following scaling:

$$c_1 = \beta r, \quad c_2 = \beta c_2^*, \quad t = \beta t^*, \quad h = \beta h^*, \quad \dot{h} = \dot{h}^*, \quad (6.68)$$

$$d_h = \beta d_h^*, \quad \bar{\varphi}_x(x) = \varphi_x^*(r)/\beta^2, \quad A(x) = A^*(r)/\beta. \quad (6.69)$$

In particular, we obtain from equation (6.67) that $c_2^* = 1 + r$. A plate with infinite moment of inertia cannot rotate, so that $\dot{\alpha} = 0$ and $\alpha = 1$. This is confirmed by the second component in each of (6.55) and (6.56). The first component in each of (6.55) and (6.56) provide

$$\dot{h}^*(r) = \frac{3}{4} \left(\int_0^r \sqrt{(r-u)(1+r-u)} \varphi_x^*(u) du + 1 \right), \quad (6.70)$$

$$d_h^*(r) = \frac{3}{4} \left(\int_0^r \sqrt{(r-u)(1+r-u)} A^*(u) du + \frac{1}{16}(2r+1) \right). \quad (6.71)$$

We eliminate \dot{h}^* and d_h^* by combining equations (6.70) with (6.60) and combining (6.71) with (6.61), so that we obtain the two following convolution type integral equations:

$$\int_0^r \frac{(1+r-u)^{3/2}}{\sqrt{r-u}} \varphi_x^*(u) du = -1, \quad \int_0^r \frac{(1+r-u)^{3/2}}{\sqrt{r-u}} A^*(u) du = r + \frac{1}{6}. \quad (6.72)$$

Substituting $d_\alpha = 1$, $\dot{\alpha} = 0$ and equations (6.70) and (6.71) into (6.62) to eliminate \dot{h} and

d_h gives us

$$t^* = \frac{\frac{5}{6} + r - \int_0^r \frac{(r-u)^{3/2}}{\sqrt{1+r-u}} A^*(u) \, du}{1 + \int_0^r \frac{(r-u)^{3/2}}{\sqrt{1+r-u}} \varphi_x^*(u) \, du}. \quad (6.73)$$

The integral equations in (6.72) can be solved by the Laplace transform. Here we define the Laplace transform of an integrable function $f : \mathbb{R}^+ \rightarrow \mathbb{R}$ by $\mathcal{L}(f)(s) = \int_0^\infty e^{-sr} f(r) \, dr$, where the argument of the transformed function, s , is complex. We evaluate the Laplace transforms with the help of the following relations (see Woods (1961), p. 370):

$$\frac{(1+r)^{3/2}}{\sqrt{r}} = \frac{1}{2} \frac{1}{\sqrt{r(r+1)}} + \sqrt{r(r+1)} + \frac{d}{dr} \sqrt{r(r+1)}, \quad (6.74)$$

$$\mathcal{L}\left((r(r+1))^{\nu-1/2}\right) = \frac{\Gamma(\nu + \frac{1}{2}) e^{\frac{s}{2}} K_\nu(\frac{s}{2})}{\sqrt{\pi} s^\nu}, \quad (6.75)$$

where K_ν is the modified Bessel function of the second kind. After transforming the integral equations in (6.72) we find

$$\mathcal{L}(\varphi_x^*)(s) = -\frac{2e^{-s/2}}{sK_0(s/2) + (1+s)K_1(s/2)}, \quad (6.76)$$

$$\mathcal{L}(A^*)(s) = \left(\frac{1}{s} + \frac{1}{6}\right) \frac{2e^{-s/2}}{sK_0(s/2) + (1+s)K_1(s/2)}. \quad (6.77)$$

Unfortunately, we could not find analytical forms for $\varphi_x^*(u)$ and $A^*(u)$. However equations (6.76) and (6.77) can be inverted numerically.

We found the asymptotic behaviour of $\varphi_x^*(r)$ and $A^*(r)$ as $r \rightarrow 0$ by expressing $\sqrt{r}\varphi_x^*(r)$ and $\sqrt{r}A^*(r)$ in the integral equations in (6.72) as Taylor series about zero:

$$\varphi_x^*(r) = \frac{1}{\pi} \left(-r^{-\frac{1}{2}} + \frac{3}{2}r^{\frac{1}{2}} - \frac{3}{8}r^{\frac{3}{2}} - \frac{1}{16}r^{\frac{5}{2}} + \frac{279}{4480}r^{\frac{7}{2}} \right) + O\left(r^{\frac{9}{2}}\right), \quad (6.78)$$

$$A^*(r) = \frac{1}{\pi} \left(\frac{1}{6}r^{-\frac{1}{2}} + \frac{7}{4}r^{\frac{1}{2}} - \frac{15}{16}r^{\frac{3}{2}} + \frac{77}{480}r^{\frac{5}{2}} + \frac{67}{8960}r^{\frac{7}{2}} \right) + O\left(r^{\frac{9}{2}}\right). \quad (6.79)$$

Hence, the horizontal velocity in the fluid, $\bar{\varphi}_x(x)$, is square-root singular at $x = 0$, which agrees with the horizontal velocity $\varphi_x(x, 0, t_0)$ at the end of the Wagner stage. Together with the expansions (6.78) and (6.79) we find an expansion of t^* in terms of r from equation (6.73):

$$t^*(r) = \frac{5}{6} + r + \frac{1}{4}r^2 + \frac{1}{12}r^3 + O(r^5) \quad (r \rightarrow 0). \quad (6.80)$$

Equation (6.80) shows that the horizontal velocity of the separation point and the forward contact point starts with velocity $\dot{c}_1 = 1$ in the separation stage, which is equal to the velocity of the forward contact point at the end of the Wagner stage.

Substituting (6.78) back into equation (6.70) and substituting (6.79) into (6.71) we obtain expansions for \dot{h}^* and h^* about $r = 0$:

$$\dot{h}^* = \frac{3}{4} - \frac{3}{8}r + \frac{3}{64}r^3 - \frac{3}{128}r^4 + O(r^5) \quad (r \rightarrow 0), \quad (6.81)$$

$$h^* = \frac{3}{4} + \frac{3}{4}r - \frac{3}{256}r^4 + O(r^6) \quad (r \rightarrow 0). \quad (6.82)$$

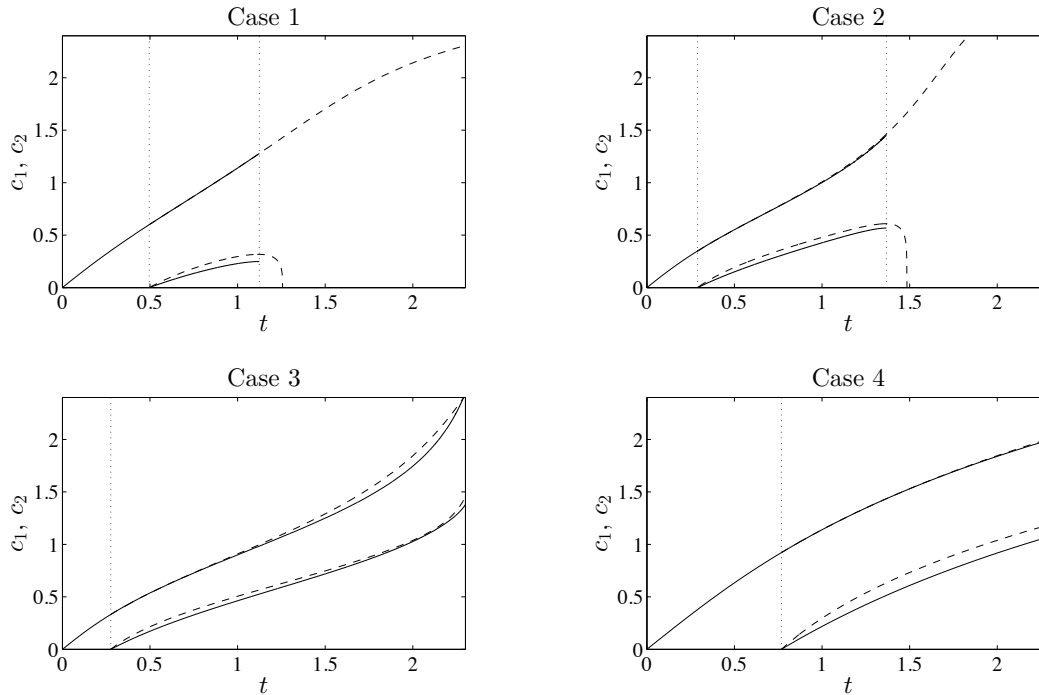


Figure 6.4: Motion of the forward contact point and the separation point (solid lines) for Cases 1, 2, 3 and 4. Motion of the forward contact point and the zero in the pressure for a non-ventilated plate are drawn in dashed lines.

Equation (6.82) shows that h^* in (6.82) is well approximated by $h^* = \frac{3}{4}(1 + r)$, which is the solution of the penetration depth in the model without account for separation (see third equation in (6.64)).

For impact of a plate with constant inclination angle onto the water free surface we found three different methods to find the motion of the contact points and the motion of the plate. In the first method, equations (6.70) – (6.73) can be solved numerically by introducing piecewise constant functions as approximations of $\varphi_x^*(x)$ and $A^*(x)$. The second approach is to invert equations (6.76) and (6.77) and to substitute the solution into equations (6.70), (6.71) and (6.73). The third solution method is an expansion in terms of the position of the rear contact point given by equations (6.78) – (6.82).

6.1.5 Numerical results

In this subsection we present some results for the impact of a plate onto the free surface. For the impact of a plate which is free to rotate there are two physical parameters, which are b and θ . We show results for the plate configurations used above (see caption of Figure 6.3): For Case 1 we let $b = 1$, $\theta = \frac{1}{3}$; for Case 2, $b = \frac{4}{3}$, $\theta = \frac{2}{9}$; and for Case 3 we choose the parameters $b = 2$, $\theta = \frac{1}{2}$. Results for a plate which is not able to rotate ($\theta \rightarrow \infty$) is shown as Case 4. Results for the separation stage are compared with a non-ventilated plate where the rear contact point is forced to stay at the left edge: $c_1 = 0$. For the non-ventilated plate we apply formulas in subsection 6.1.2 for time $t > t_0$.

In the separation stage, $x = c_1(t)$ increases until the time t_1 when $\dot{c}_1(t_1) = 0$ for Cases 1 and 2. Since we expect $c_1(t)$ to decrease for $t > t_1$, we had to stop computations at $t = t_1$

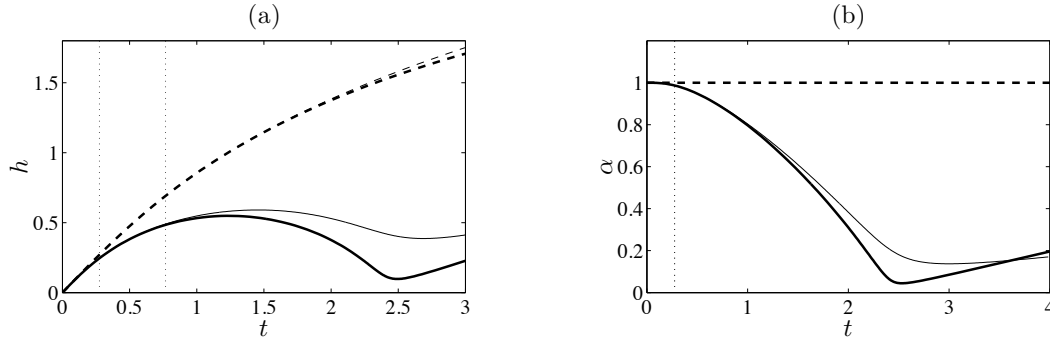


Figure 6.5: (a) Penetration depth for Case 3 (solid line) and Case 4 (dashed line) for the ventilated plate (thick line) and non-ventilated plate (thin line), (b) inclination angle with lines described in (a).

for Cases 1 and 2. However, it is possible to model the motion of the rear turnover point for $t > t_1$ as shown in section 5.2. This modelling has not been done here and we stop the calculations at $t = t_1$ for Cases 1 and 2. Our computations for Cases 3 and 4 show that $\dot{c}_1(t)$ does not become zero for $0 < t < 4$.

Figure 6.4 compares $c_1(t)$ as a function of time with the zero of the pressure for the impact of a non-ventilated plate, c_1^* , given by $q(c_1^*) = 0$ where q is defined in (6.44). The value of c_1^* increases more quickly than c_1 , as we already have seen in Figure 6.3. However, c_1 and c_1^* share similar trends, so that for Cases 1 and 2 we expect a quick decay of $c_1(t)$ for $t > t_1$, since c_1^* decreases quickly for $t > t_1$. It may be possible that an air bubble is captured under a ventilated plate, if the rear edge or any part of the plate contacts the fluid behind the rear contact point before c_1 reaches 0. For Cases 3 and 4 the separation point increases quickly so that a large part of the plate surface is dry behind the contact region.

The forward contact point follows closely the motion of the contact point of a non-ventilated plate, c_2^* . Only in Case 3 do the functions c_2 and c_2^* differ notably for t larger than 1. When the inclination angle becomes small, the forward contact point moves rapidly from left to right. In particular, in Case 3 the horizontal speed of the forward contact point is very high for $2.2 < t < 2.4$ resulting in a large hydrodynamic pressure close to the forward contact point.

All further plots are shown for Cases 3 and 4 only. Figures 6.5(a) and (b) show the plate motion through the penetration depth of the left edge, $h(t)$, and the inclination angle, $\alpha(t)$, respectively. Since no negative load is exerted on the rear part of the ventilated plate, the left edge rises more quickly and the inclination angle decreases more quickly than for a non-ventilated plate. The penetration depth and the inclination angle for ventilated and non-ventilated plates deviate very slowly at the beginning of the separation stage, but deviate significantly for larger times. For the inclination angle a minimum is visible for Case 3, which is much smaller for the ventilated plate than for the non-ventilated plate.

Figure 6.6 shows the vertical hydrodynamic forces acting on the plate for Case 3 and 4. In Case 3 the force has two local maxima. The first maximum is due to the initial increase of the wetted area, which leads to the deceleration of the vertical motion and a decrease in the inclination angle of the plate. By the time of the second maximum, which is much larger than the first local maximum, the angle is rather small but the vertical speed of the

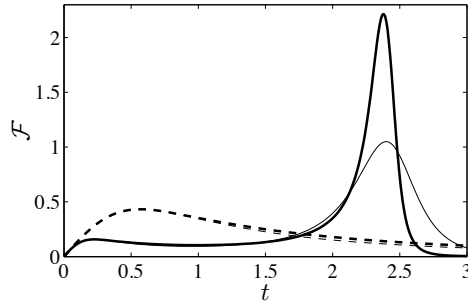


Figure 6.6: Vertical force for Case 3 (solid line) and Case 4 (dashed line) for the ventilated plate (thick line) and non-ventilated plate (thin line).

leading edge of the plate is large. This forces the contact point to move faster forwards, increasing the hydrodynamic force acting on the plate. Just after the second peak the force drops sharply to zero. The vertical forces on the plate for the ventilated and non-ventilated plate are significantly different. The maximum hydrodynamic force for the ventilated plate is more than double the corresponding one for the non-ventilated plate. In Case 4 the force has only one maximum. A second maximum is missing in Case 4 because the inclination angle is fixed. In Case 4 the force of the ventilated and non-ventilated plate hardly differ.

6.2 Free vertical fall of a blunt body with cavitation

In this section we consider the free fall of a symmetric light blunt body onto a flat free surface of deep fluid. The free fall of a blunt body has been analysed in Oliver (2002) within the Wagner theory. Due to the large hydrodynamic loads a light blunt body decelerates quickly and hydrodynamic pressures far below atmospheric occur in the contact region. As shown in Oliver (2002) the low pressures lie well inside the contact region, so that a cavity may develop under the body. This chapter discusses the case where cavities develop as soon as the pressure drops below atmospheric pressure. In classical cavitation, cavities occur not before the hydrodynamic pressure drops below the vapour pressure of water, which is 23hPa at 20° Celsius. This is close to absolute zero pressure. However, cavities may develop at about atmospheric pressure if air is ventilated under the body or air bubbles, already present in the fluid, accumulate in the low pressure zones.

In order to take cavities into account, one needs to modify the boundary condition on the wetted part of the body. The account of a cavity in blunt body impact has been studied in Korobkin (2003) for general entry motion. Korobkin (2003) presented asymptotic results of the problem for times when the cavity is small compared to the length of the contact region. The analysis is complicated because both the position of the free surface in the cavity region and the four contact points are unknown.

The analysis given in this chapter for the free-fall of a blunt body provides results not only a short time after the formation of the cavity but also for times when the length of the cavity region becomes large. We will compare the models where a cavity is accounted for with the classical impact results without a cavity. In particular, it will be shown that the length of the negative pressure zone in the latter model is significantly larger than the size of

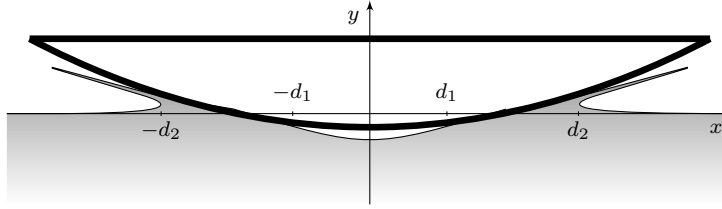


Figure 6.7: Blunt body impact onto deep water at time $t > t_0$ when a cavity develops at the bottom of the body. The spatial position of the cavity is $-d_1 < x < d_1$.

the cavity in the model with fluid separation. We also show that the cavity is thin compared to the horizontal length of the cavity.

6.2.1 Mathematical formulation

Initially the liquid is at rest and occupies the lower half plane $y' < 0$. The blunt body initially touches the free surface tangentially at a single point which is taken as the origin of the coordinate system. Then the body starts to penetrate the liquid vertically with initial speed V . The shape of the body surface near its lowest point is approximated as parabolic, with $y' = x'^2/(2R) - h'(t')$, where R is the radius of curvature of the body surface at its lowest point and $h'(t')$ is the penetration depth of the body at time t' . The function $h'(t')$ is determined by Newton's second law. We choose $L = \sqrt{m/\rho_F}$ as the lengthscale of the problem. We assume that the mass m of the body is small enough so that $\varepsilon = L/(2R)$ is small and the Froude number V/\sqrt{gL} is large enough to neglect gravity in the hydrodynamic model and in Newton's second law. Below we use the scaling given by equations (3.2) – (3.5) and the scaling $h' = \varepsilon Lh$. The non-dimensional position of the body at time t is given by

$$y = \varepsilon\omega(x, t), \quad \omega(x, t) = x^2 - h(t). \quad (6.83)$$

It follows from the symmetric shape of the body and the symmetric geometry of the initial hydrodynamic configuration, that the generated flow is also symmetric.

Figure 6.7 shows the blunt body as it penetrates the fluid free surface. In the linearised hydrodynamic model, we distinguish between two stages during the impact. In the first stage, which we define as the Wagner stage, the wetted part of the body corresponds to the interval $|x| < d_2$, $y = 0$, where the pressure along the contact region is positive. The second stage starts at the time instant $t = t_0$ when the pressure has first decreased to zero at $x = 0$. In this second stage, which we call the cavitation stage, the fluid is wetted in $d_1 < |x| < d_2$. The interval $|x| < d_1$, $y = 0$ corresponds to the region where the fluid is detached from the body and a cavity develops. Note that for $|x| < d_1$ the position of the body surface given by (6.83) and the position of the free surface $y = \varepsilon\eta(x, t)$ define the boundary of the cavity between the fluid and body.

To omit repetitions we define the set $\mathcal{R}(t)$, which defines the x -values of the region where the fluid is in contact with the body in the linearised hydrodynamic problem:

$$\mathcal{R}(t) = \begin{cases} \{x : |x| < d_2(t)\}, & (0 < t < t_0) \\ \{x : d_1(t) < |x| < d_2(t)\}. & (t > t_0) \end{cases} \quad (6.84)$$

The region $|x| > d_2$, $y = 0$, corresponds to the free surface outside the impact region. The hydrodynamic pressure is given in terms of the velocity potential $\varphi(x, y, t)$ (see equation (3.24)), where $\varphi(x, y, t)$ satisfies the following equations:

$$\nabla^2 \varphi = 0 \quad (y < 0), \quad (6.85)$$

$$\varphi_y = -\dot{h} \quad (y = 0, x \in \mathcal{R}(t)), \quad (6.86)$$

$$\varphi_t = 0 \quad (y = 0, x \in \mathcal{R}^c(t)), \quad (6.87)$$

$$\varphi = O((x^2 + y^2)^{-1/2}) \quad (x^2 + y^2 \rightarrow \infty), \quad (6.88)$$

where \mathcal{R}^c is the complement of the set \mathcal{R} . The points $x = -d_2$, $y = 0$ and $x = d_2$, $y = 0$ correspond to the overturning regions. We assume that the horizontal velocity of the contact point at $x = d_2(t)$ is positive so that equation (6.87) implies that $\varphi(x, 0, t) = 0$ for $|x| > d_2$. The positions of $x = -d_2(t)$ and $x = d_2(t)$ are determined by using Wagner's condition and the linearised kinematic boundary condition,

$$\eta(x, t) = \omega(x, t) \quad (x = -d_2 \text{ and } x = d_2), \quad (6.89)$$

$$\eta_t = \varphi_y \quad (y = 0, x \in \mathcal{R}^c(t)), \quad (6.90)$$

$$\eta \equiv 0 \quad (t = 0). \quad (6.91)$$

In the cavitation stage, $t > t_0$, equation (6.87) implies $\varphi_x(x, 0, t) = \bar{\varphi}_x(x)$ for $|x| < d_1$, where the function $\bar{\varphi}_x(x)$ has to be determined as part of the solution in the cavity region $|x| < d_1$. If $\dot{d}_1(t) > 0$, the functions $d_1(t)$ and $\bar{\varphi}_x(x)$ are determined by the following conditions:

$$\eta(x, t) = \omega(x, t) \quad (|x| = d_1), \quad (6.92)$$

$$|\nabla \varphi(x, 0, t)| < +\infty \quad (|x| = d_1), \quad (6.93)$$

$$p_x(x, 0, t) = 0 \quad (|x| \rightarrow d_1 + 0). \quad (6.94)$$

Our computations only detected the case $\dot{d}_1 > 0$, so that we do not have to consider the case $\dot{d}_1 < 0$.

The vertical motion of the body is governed by Newton's second law, which is in non-dimensional form and in leading order for small ε (see also equation (4.116)):

$$\mathcal{F}(t) = -\ddot{h}(t), \quad \mathcal{F}(t) = \int_{\mathcal{R}(t)} p(x, 0, t) dx. \quad (6.95)$$

The equations in (6.95) are subject to the initial conditions $h(0) = 0$ and $\dot{h}(0) = 0$. We also assume that the functions $h(t)$ and $\dot{h}(t)$ are continuous at $t = t_0$.

The solution of the problem (6.85) – (6.88) is not dependent on any parameter. Our analysis will be focused on the motion of the body and the contact points, the hydrodynamic loads and the shape of the cavity region. We start with the Wagner stage $0 < t < t_0$ to obtain the initial conditions for the cavitation stage.

6.2.2 Wagner stage

First we consider the solution of the problem in the Wagner stage $0 < t < t_0$, which has been discussed in Oliver (2002). The complex displacement $f(z) = \Phi_x - i\Phi_y$ is determined

by the time-integrated problem of (6.85) – (6.88) (see also (3.124) – (3.127)). Its solution is given by

$$f(z) = -i \left(z^2 - h - z\sqrt{z^2 - d_2^2} \right), \quad (6.96)$$

$$d_2 = \sqrt{2h}. \quad (6.97)$$

Equation (6.97) has to be satisfied to guarantee that the complex displacement satisfies the far-field condition $f(z) = O(z^{-2})$ as $z \rightarrow \infty$. By integrating $f(z)$ in equation (6.96) with respect to z and by differentiating the result twice in time we obtain the complex acceleration $F_{tt}(z) = \varphi_t + i\psi_t(z)$:

$$F_{tt}(z) = i \left[\ddot{h} \left(z - \sqrt{z^2 - d_2^2} \right) + \frac{\dot{h}^2}{\sqrt{z^2 - d_2^2}} \right]. \quad (6.98)$$

In particular, the hydrodynamic pressure is given by the real part of $F_{tt}(z)$ together with the linearised Bernoulli equation (3.24):

$$p(x, 0, t) = \ddot{h}\sqrt{d^2 - x^2} + \frac{\dot{h}^2}{\sqrt{d_2^2 - x^2}}. \quad (6.99)$$

The first term on the right-hand side of equation (6.99) indicates that the pressure can be negative if the body decelerates quickly enough and the vertical velocity of the body is small enough. Equations in (6.95) and equation (6.99) imply that $\pi(\ddot{h}h + \dot{h}^2) = -\ddot{h}$, which can be integrated twice in time together with the initial conditions $h(0) = 0$ and $\dot{h}(0) = 1$. Hence,

$$\frac{\pi}{2}h^2 + h - t = 0. \quad (6.100)$$

Equations (6.97), (6.99) and (6.100) determine the start of the cavitation stage $t = t_0$, when $p(0, 0, t_0) = 0$, together with the values h , d_2 and their derivatives at this time:

$$t_0 = \frac{3}{2\pi}, \quad d_2(t_0) = \sqrt{\frac{2}{\pi}}, \quad \dot{d}_2(t_0) = \frac{1}{2}\sqrt{\frac{\pi}{2}}, \quad (6.101)$$

$$h(t_0) = \frac{1}{\pi}, \quad \dot{h}(t_0) = \frac{1}{2}, \quad \ddot{h}(t_0) = -\frac{\pi}{8}. \quad (6.102)$$

Note that the hydrodynamic pressure becomes negative when the body mass is equal to the added mass, which is in nondimensional form πh . The pressure starts to become negative at $x = 0$, so that the cavity will develop from the bottom point of the body surface. Note that the vertical hydrodynamic force at the end of the Wagner stage given by $\mathcal{F}(t_0) = \frac{\pi}{8}$ is only one-eighth of the initial force $\mathcal{F}(0) = \pi$. In the next subsection we consider the impact problem in the cavitation stage.

6.2.3 Cavitation stage

To solve the problem in the cavitation stage we analyse the complex acceleration $f_{tt}(z) = \varphi_{xt}(x, y, t) - i\varphi_{yt}(x, y, t)$, the complex velocity $f_t(z) = \varphi_x(x, y, t) - i\varphi_y(x, y, t)$ given by (6.85) – (6.88) and the complex displacement $f(z) = \Phi_x(x, y, t) - i\Phi_y(x, y, t)$. We start with the boundary problem in terms of the complex acceleration $f_{tt}(z)$ resulting from the problem

(6.85) – (6.88):

$$f_{tt} \text{ analytic} \quad (y < 0), \quad (6.103)$$

$$\text{Im}(f_{tt}) = \ddot{h} \quad (y = 0, d_1 < |x| < d_2), \quad (6.104)$$

$$\text{Re}(f_{tt}) = 0 \quad (y = 0, |x| > d_2 \text{ and } |x| < d_1), \quad (6.105)$$

$$f_{tt} = O(z^{-2}) \quad (|z| \rightarrow \infty). \quad (6.106)$$

Note that the function $\bar{\varphi}_x(x)$ does not appear in the problem (6.103) – (6.106). The boundary problem (6.103) – (6.106) does not recover the problem (6.85) – (6.88) completely: Problem (6.103) – (6.106) is satisfied for any pressure in the cavity $-d_1 < x < d_1$ which is constant in x . Furthermore, the problem (6.85) – (6.88) is independent of the initial vertical velocity of the body. Since we know that $d_2(t)$ is determined by Wagner's condition (6.89) and the conditions (6.92) – (6.94) are satisfied at the inner contact points, we obtain the asymptotic behaviours of $f_{tt}(z)$ at $z = -d_2, -d_1, d_1, d_2$:

$$f_{tt}(z) = O((z + d_1)^{1/2}) \quad (z \rightarrow -d_1), \quad (6.107)$$

$$f_{tt}(z) = O((z - d_1)^{1/2}) \quad (z \rightarrow d_1), \quad (6.108)$$

$$f_{tt}(z) = O((z + d_2)^{-3/2}) \quad (z \rightarrow -d_2), \quad (6.109)$$

$$f_{tt}(z) = O((z - d_2)^{-3/2}) \quad (z \rightarrow d_2). \quad (6.110)$$

A solution of the problem (6.103) – (6.110) can be derived similarly as in chapter 2, where we consider the homogeneous problem for $f_{tt}^*(z) = f_{tt}(z) - i\ddot{h}$ and replace the characteristic function in (2.5) by $g(z) = (z^2 - d_1^2)^{-1/2}(z^2 - d_2^2)^{3/2}$. Then the solution of the problem (6.103) – (6.110) is given by

$$f_{tt}(z) = i\ddot{h} \left(1 - \frac{\sqrt{z^2 - d_1^2}}{(z^2 - d_2^2)^{3/2}} (z^2 + \mathcal{A}(t)) \right), \quad (6.111)$$

where $\mathcal{A}(t)$ is an unknown function of time. In particular, $f_{tt}(z)$ in (6.111) satisfies the far-field condition (6.106), so that

$$f_{tt}(z) \sim ia_{-2}z^{-2} \quad (|z| \rightarrow \infty), \quad (6.112)$$

$$a_{-2} = \ddot{h} \left(-\frac{3}{2}d_2^2 + \frac{1}{2}d_1^2 - \mathcal{A} \right). \quad (6.113)$$

To find $\mathcal{A}(t)$ we specify a_{-2} . It follows from Cauchy's integral theorem that $\text{Re}(\int_{C_\delta} F_{tt}(z) dz) = 0$, where $F_{tt}(z) = \varphi_t + i\psi_t$ is the complex acceleration potential and the contour of integration, C_δ , is defined in Figure 6.8. Since $F_{tt}(z) = -a_{-2}z^{-1}$ as $|z| \rightarrow \infty$, $F_{tt}(z) = O((z + d_2)^{-1/2})$ as $z \rightarrow -d_2$ and $F_{tt}(z) = O((z - d_2)^{-1/2})$ as $z \rightarrow d_2$, we obtain for $\delta \rightarrow 0$ the equation

$$\int_{-\infty}^{\infty} \text{Re}(F_{tt}(x - i0)) dx = \pi a_{-2}. \quad (6.114)$$

Using the linearised Bernoulli equation (3.24) and the equations in (6.95), we deduce that $a_{-2}(t)$ is given by:

$$a_{-2}(t) = \frac{1}{\pi} \ddot{h}(t), \quad (6.115)$$

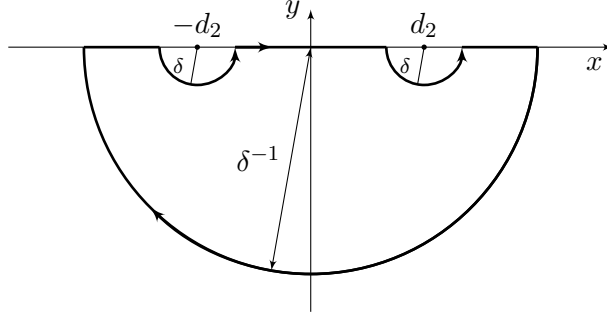


Figure 6.8: The contour C_δ .

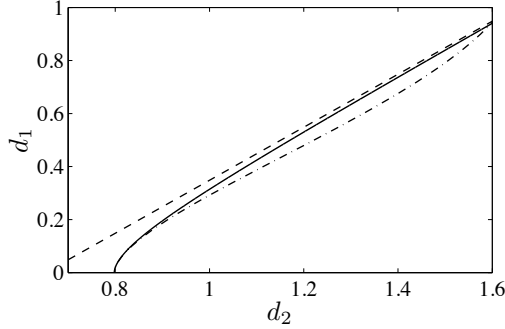


Figure 6.9: Plot of d_1 as a function of d_2 (solid line) and the asymptotic behaviour at $d_1 = 0$ given by $d_2 = \sqrt{2/\pi} - \sqrt{\pi/2}d_1^2(\log(\sqrt{\pi/32}d_1) + \frac{1}{2})$ (dashed-dotted line) (see equation (6.118)) and for $d_1 \rightarrow \infty$ given by $d_1 = d_2 - 2/\sqrt{3\pi}$ (dashed line).

so that we obtain from equation (6.113):

$$\mathcal{A}(t) = -\frac{1}{\pi} + \frac{1}{2}d_1^2 - \frac{3}{2}d_2^2. \quad (6.116)$$

The function \ddot{h} appears as a factor in (6.113) and (6.115), so that $\mathcal{A}(t)$ does not depend on \ddot{h} . Note that $\ddot{h} \neq 0$ since the body still decelerates in the cavitation stage due to the positive hydrodynamic loads.

Equation (6.105) and the linearised Bernoulli's equation induce a pressure distribution along the cavity region $|x| < d_1$ which is constant in x , but not necessary zero. Equation (6.87) and the far-field condition $\varphi_t(0, y, t) = O(y^{-1})$ as $y \rightarrow -\infty$ imply that $\int_{-\infty}^0 \varphi_{yt}(0, y, t) dy = 0$. It follows from the last integral, where φ_{yt} is given by the imaginary part of $f_{tt}(z)$ in (6.111), that d_1 and d_2 can be written in the following parametric form with parameter q :

$$d_1 = \left[\pi \left(\frac{2 - q^2}{2 - 2q^2} - \frac{K(q)}{E(q)} \right) \right]^{-1/2}, \quad d_2 = \frac{d_1}{\sqrt{1 - q^2}} \quad (0 \leq q < 1), \quad (6.117)$$

where K and E are the complete elliptic integrals of the first and second kind. The value $q = 1$ corresponds to the start of the ventilation stage, where the following asymptotic

behaviour of d_2 in terms of d_1 is obtained from equations in (6.117):

$$d_2 = \sqrt{\frac{2}{\pi}} - \sqrt{\frac{\pi}{2}} d_1^2 \left(\log \left(\sqrt{\frac{\pi}{32}} d_1 \right) + \frac{1}{2} \right) + O(d_1^4 \log^2(d_1)) \quad (d_1 \rightarrow 0). \quad (6.118)$$

For large d_2 , which corresponds to $q = 0$, we obtain from (6.117) that the size of the region in contact with the fluid for $x > 0$ is $\lim_{q \rightarrow 1} d_2 - d_1 = 2/\sqrt{3\pi}$. Figure 6.9 shows d_1 as a function of d_2 and the asymptotic behaviours of these functions at $d_2 = \sqrt{\frac{2}{\pi}}$ ($q = 1$) and as $d_2 \rightarrow \infty$ ($q = 0$).

The equations in (6.117) give us a relation between d_1 and d_2 . However, we have three unknown functions $d_1(t)$, $d_2(t)$ and $h(t)$ in time to be determined. We find further equations when we solve the hydrodynamic problem in terms of the complex velocity $f_t(z) = \varphi_x - i\varphi_y$, given by equations (6.85) – (6.88). In particular, equation (6.87) gives us $\varphi_x(x, 0, t) = 0$ for $|x| > d_2$ and $\varphi_x(x, 0, t) = \bar{\varphi}_x(x)$ for $|x| < d_1$, where the function $\bar{\varphi}_x(x)$ arising from the integration of equation (6.87) has to be determined as part of the solution in the cavity-region $|x| < d_1$, $y = 0$. Since the flow is symmetric with respect to $x = 0$, we obtain $\bar{\varphi}_x(-x) = -\bar{\varphi}_x(x)$. The problem (6.85) – (6.88) can be reformulated as a Dirichlet problem if we consider the function $(f_t(z) - i\dot{h})g_1(z)$ where $g_1(z) = (z^2 - d_1^2)^{1/2}(z^2 - d_2^2)^{1/2}$. Then the complex velocity is given by

$$f_t(z) = i \left(\dot{h} + \frac{\mathcal{K}(z, t) + \mathcal{J}(t) - \dot{h}z^2}{\sqrt{(z^2 - d_1^2)(z^2 - d_2^2)}} \right), \quad (6.119)$$

$$\mathcal{K}(z, t) = -\frac{1}{\pi} \int_0^{d_1^2} \frac{\sqrt{(d_1^2 - u)(d_2^2 - u)}}{u - z^2} \bar{\varphi}_x(\sqrt{u}) \, du. \quad (6.120)$$

In equation (6.120) we used that $\bar{\varphi}_x(x)$ is anti-symmetric. We determine $\mathcal{J} = \mathcal{J}(t)$ by the specific far-field behaviour $f_t(z) \sim \frac{i}{\pi}(\dot{h} - 1)z^{-2}$ as $z \rightarrow \infty$ obtained from (6.112) and (6.115). It follows that, $\mathcal{J}(t)$ in equation (6.119) is given by

$$\mathcal{J}(t) = \frac{1}{2}(d_1^2 + d_2^2)\dot{h} + \frac{1}{\pi}(\dot{h} - 1). \quad (6.121)$$

Equations (6.107) and (6.108) imply that $f_t(z)$ is not singular at $z = d_1$, so that we obtain the integral equation:

$$\int_0^{d_1^2} \sqrt{\frac{d_2^2 - u}{d_1^2 - u}} \bar{\varphi}_x(\sqrt{u}) \, du = - \left[\frac{\pi}{2}(d_2^2 - d_1^2) + 1 \right] \dot{h} + 1. \quad (6.122)$$

Note the similarity of conditions (6.122) and (4.65). Equation (6.122) will be used later to determine the wake function $\bar{\varphi}_x$. Comparing the asymptotic behaviour of $f_t(z)$ in (6.111) and $f_{tt}(z)$ in (6.119) at $z = d_2$ gives us

$$\ddot{h} = \frac{d_2 \dot{d}_2 B(t)}{(d_2^2 - d_1^2) \left(\frac{\pi}{2}(d_2^2 - d_1^2) + 1 \right)}, \quad (6.123)$$

$$B(t) = \int_0^{d_1^2} \sqrt{\frac{d_1^2 - u}{d_2^2 - u}} \bar{\varphi}_x(\sqrt{u}) \, du - \left(\frac{\pi}{2}(d_2^2 - d_1^2) - 1 \right) \dot{h} - 1. \quad (6.124)$$

Equation (6.123) has similarities with the Brillouin-Villat criterion (see e.g. equation (4.119)). This equation will be used to determine $\ddot{h}(t)$.

We have used the vertical speed of the body, but not the shape of the body. The calculations above in this subsection are also valid for the free fall of general-shaped symmetric bodies, $\omega(x, t) = S(x) - h(t)$ where $S(-x) = -S(x)$. We have three equations (6.117), (6.122) and (6.123) for four unknowns $\bar{\varphi}_x(x)$, $d_1(t)$, $d_2(t)$ and $h(t)$. We obtain a complete set of equations when we also analyse the impact problem in terms of the complex displacement $f(z) = \Phi_x(x, y, t) - i\Phi_y(x, y, t)$. Integrating equations (6.85) – (6.88) in time, using the initial conditions and Wagner's conditions (6.89) we derive the following mixed boundary value problem

$$\nabla^2 \Phi = 0 \quad (y < 0), \quad (6.125)$$

$$\Phi_y = x^2 - h \quad (y = 0, d_1 < |x| < d_2), \quad (6.126)$$

$$\Phi_x = 0 \quad (y = 0, |x| > d_2), \quad (6.127)$$

$$\Phi_x = t\bar{\varphi}_x(x) + A(x) \quad (y = 0, |x| < d_1), \quad (6.128)$$

$$\Phi = O((x^2 + y^2)^{-1/2}) \quad (x^2 + y^2 \rightarrow \infty), \quad (6.129)$$

where $A(x)$ is an undetermined term due to the time-integration. Since $\Phi_x(x, 0, t)$ and $\bar{\varphi}_x(x)$ are anti-symmetric with respect to the origin, $A(x)$ is also anti-symmetric. The condition of continuous separation (6.92) together with (6.126) and the kinematic boundary condition $\eta_t = \varphi_y$ gives us the free surface elevation $\eta = \Phi_y$ for $|x| > d_2$ and $|x| < d_1$. Since $f_t(z)$ has only square-root singularities at the points $z = -d_2$ and $z = d_2$ and we assume that these points are moving ($\dot{d}_1 > 0$), we seek the solution $\Phi(x, y, t)$ of the problem (6.125) – (6.129) which is continuous together with its first derivatives Φ_x and Φ_y in the flow region $y \leq 0$.

The boundary value problem (6.125) – (6.129) for $\Phi(x, y, t)$ is similar to the problem (6.85) – (6.88) for $\varphi(x, y, t)$. By using the same techniques, we find the elevation of the free surface in the form

$$f(z) = i \left(-z^2 + h + \frac{\mathcal{E}(z, t) + z^4 - (h + \frac{1}{2}(d_1^2 + d_2^2))z^2 + \mathcal{C}(t)}{\sqrt{(z^2 - d_1^2)(z^2 - d_2^2)}} \right), \quad (6.130)$$

$$\mathcal{E}(z, t) = -\frac{1}{\pi} \int_0^{d_1^2} \frac{\sqrt{(d_1^2 - u^2)(d_2^2 - u^2)}}{u - z^2} (t\bar{\varphi}_x(\sqrt{u}) + A(\sqrt{u})) du, \quad (6.131)$$

$$\mathcal{C}(t) = \left(\frac{1}{2}d_1^2 + \frac{1}{2}d_2^2 + \frac{1}{\pi}\right) h - \frac{1}{8}(d_2^2 - d_1^2)^2 - \frac{t}{\pi}, \quad (6.132)$$

where equation (6.132) follows from the far-field behaviour $f(z) = \frac{1}{\pi}(h - t)z^{-2} + O(z^{-3})$ (see equations (6.112) and (6.115)). Since $f(z)$ is not singular at $z = d_1$ and $z = d_2$ it follows that the numerator in the fraction of equation (6.130) has to be zero at $z = d_1$ and $z = d_2$. Hence, we obtain the integral equations

$$\int_0^{d_1^2} \sqrt{\frac{d_1^2 - u}{d_2^2 - u}} (t\bar{\varphi}_x(\sqrt{u}) + A(\sqrt{u})) du = -\frac{\pi}{8}(d_2^2 - d_1^2)(3d_2^2 + d_1^2 - 4h) - h + t, \quad (6.133)$$

$$\int_0^{d_1^2} \sqrt{\frac{d_2^2 - u}{d_1^2 - u}} (t\bar{\varphi}_x(\sqrt{u}) + A(\sqrt{u})) du = \frac{\pi}{8}(d_2^2 - d_1^2)(3d_1^2 + d_2^2 - 4h) - h + t. \quad (6.134)$$

Equation (6.133) is used to determine the positions of the outer contact points $x = -d_2$, $x = d_2$, $y = 0$. Subtracting the other equation (6.134) from (6.122) multiplied by t yields an

integral equation for $A(x)$:

$$\int_0^{d_1^2} \sqrt{\frac{d_2^2 - u}{d_1^2 - u}} A(\sqrt{u}) du = - \left[\frac{\pi}{8}(d_2^2 - d_1^2) + 1 \right] (h - th) + \frac{\pi}{8}(d_2^2 - d_1^2)(3d_1^2 + d_2^2). \quad (6.135)$$

To obtain $\bar{\varphi}_x(x)$ and $A(x)$ we solve numerically the two integral equations (6.122) and (6.135).

The functions $d_1(t)$ and $d_2(t)$ are obtained from the t -derivatives of (6.117) and (6.133), which are given by:

$$\dot{d}_1 = 2 \frac{\dot{d}_2 d_2^2 (2d_1^2 - d_2^2) E(q)^2 - 2d_1^4 E(q) K(q) + d_1^4 K(q)^2}{d_2 (2d_2^2 - d_1^2) E(q)^2 - 2d_2^2 E(q) K(q) + d_1^2 K(q)^2}, \quad q = \sqrt{1 - \left(\frac{d_1}{d_2}\right)^2}, \quad (6.136)$$

$$\dot{d}_2 = \frac{1}{d_2} \frac{B(t)}{\int_0^{d_1^2} \frac{\sqrt{d_1^2 - u}}{(d_2^2 - u)^{3/2}} (t\bar{\varphi}_x(\sqrt{u}) + A(\sqrt{u})) du + \frac{\pi}{2}(-3d_2^2 + d_1^2 + 2h)}. \quad (6.137)$$

Note that the system of ordinary differential equations (6.123), (6.137) and (6.136) for h , d_1 and d_2 only weakly depends on the wake functions $\bar{\varphi}_x(x)$ and $A(x)$ for x close to d_1 . Hence, we can evaluate (6.123), (6.137) and (6.136) together with the integral equations (6.122) and (6.135) by a similar numerical scheme as it was presented in subsection 4.4.3. Equations (6.123) and (6.136) depend on \dot{d}_2 , which can be substituted by equation (6.137). The initial conditions of this system (6.123), (6.137) and (6.136) is (see equations in (6.101) and (6.102)):

$$d_1(t_0) = 0, \quad d_2(t_0) = \sqrt{\frac{2}{\pi}}, \quad h(t_0) = \frac{1}{\pi}, \quad \dot{h}(t_0) = \frac{1}{2} \quad (t_0 = \frac{3}{2\pi}). \quad (6.138)$$

We solve the final system of equations with a constant time step Δt with the time discretisation $t_n = t_0 + n\Delta t$. The functions $\bar{\varphi}_x(x)$ and $A(x)$ are approximated by constant values in $d_1(t_n) < x < d_1(t_{n+1})$.

We compare our numerical results with the following expansions obtained by equations (6.117), (6.122), (6.123), (6.133) and (6.135):

$$d_2(t) = \sqrt{\frac{2}{\pi}} + \frac{1}{2}(t - t_0)\sqrt{\frac{\pi}{2}} + O((t - t_0)^2) \quad (t \rightarrow t_0), \quad (6.139)$$

$$h(t) = \frac{1}{\pi} + \frac{1}{2}(t - t_0) - \frac{\pi}{16}(t - t_0)^2 + O((t - t_0)^3) \quad (t \rightarrow t_0), \quad (6.140)$$

$$t(d_1) = t_0 - 2d_1^2 \left(\log \left(\sqrt{\frac{\pi}{32}} d_1 \right) + \frac{1}{2} \right) + O(d_1^4 \log(d_1)^2) \quad (d_1 \rightarrow 0), \quad (6.141)$$

$$\bar{\varphi}_x(x) = \frac{1}{4}\sqrt{2\pi}x + O(x^2) \quad (x \rightarrow 0), \quad (6.142)$$

$$A(x) = \frac{5}{8}\sqrt{\frac{2}{\pi}}x + O(x^2) \quad (x \rightarrow 0). \quad (6.143)$$

Equations (6.139) and (6.140), together with the equations in (6.101) and (6.102), imply that the functions $\dot{d}_2(t)$ and $\ddot{h}(t)$ are continuous at $t = t_0$.

The pressure $p(x, 0, t)$ along the contact region will be determined by integration of $p_x(x, 0, t)$ w.r.t. x . The function $p_x(x, 0, t)$ is obtained from the real part of $f_{tt}(z)$ in equation (6.111) and the linearised Bernoulli's equation:

$$p_x(x, 0, t) = -\ddot{h} \frac{\sqrt{x^2 - d_1^2}}{(d_2 - x^2)^{3/2}} (x^2 - \frac{3}{2}d_2^2 + \frac{1}{2}d_1^2 - \frac{1}{\pi}), \quad (6.144)$$

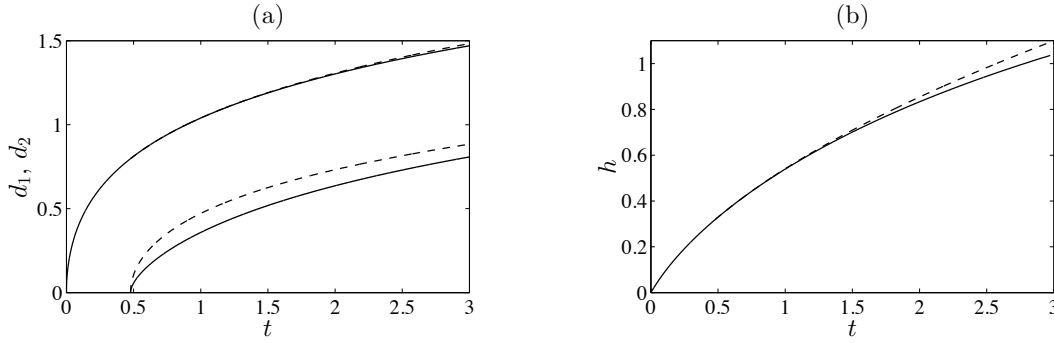


Figure 6.10: (a) The contact points $d_1(t)$ and $d_2(t)$ as functions of time (solid line) and the position of the zero of the pressure for the model without cavity (dashed line). (b) The penetration depth $h(t)$ as a function of time for the models with cavity (solid line) and without cavity (dashed line).

where \ddot{h} is determined by equation (6.123). The thickness of the cavity at $x = 0$ is defined as $\delta(t) = \omega(0, t) - \eta(0, t)$ and the volume of the cavity is defined as $V(t) = \int_{-d_1}^{d_1} (\omega(x, t) - \eta(x, t)) dx$. The function $\eta_{tt}(x, t)$ is given by the imaginary part of $f_{tt}(z)$ in equation (6.111), so that the second time-derivative of $\delta(t)$ and $V(t)$ are given by

$$\ddot{\delta}(t) = \ddot{h} \frac{d_1}{d_2^3} \left(-\frac{1}{\pi} + \frac{1}{2}d_1^2 - \frac{3}{2}d_2^2 \right), \quad (6.145)$$

$$\ddot{V}(t) = \frac{\ddot{h}}{d_2} \left[\left(\frac{2}{\pi} - d_2^2 - d_1^2 \right) E \left(\frac{d_1}{d_2} \right) + \left(-\frac{2}{\pi} + d_2^2 - d_1^2 \right) K \left(\frac{d_1}{d_2} \right) \right]. \quad (6.146)$$

We numerically integrate equations (6.145) and (6.146) twice in time to obtain $\delta(t)$ and $V(t)$. The asymptotic behaviour of $\delta(t)$ and $V(t)$ at the beginning of the cavitation stage as $d_1 \rightarrow 0$ is given by

$$\delta(t) = \frac{2\sqrt{2}\pi^{3/2}}{15} d_1^5 \left[\log^2 \left(\sqrt{\frac{\pi}{32}} d_1 \right) + \frac{19}{15} \log \left(\sqrt{\frac{\pi}{32}} d_1 \right) + \frac{31}{75} \right] + O(d_1^7 \log^3(d_1)), \quad (6.147)$$

$$V(t) = \frac{\sqrt{2}\pi^{5/2}}{24} d_1^6 \left[\log^2 \left(\sqrt{\frac{\pi}{32}} d_1 \right) + \frac{17}{12} \log \left(\sqrt{\frac{\pi}{32}} d_1 \right) + \frac{37}{72} \right] + O(d_1^7 \log^3(d_1)). \quad (6.148)$$

The asymptotic behaviours of $\delta(t)$ and $V(t)$ will be compared with the numerical results.

6.2.4 Numerical results

Computations only need to be done once since the problem given by (6.123), (6.136), (6.137), (6.122) and (6.135) does not depend on any parameter. We compare our results with the ones in which a cavity is not accounted for, which was presented in section 6.2.2.

Figure 6.10(a) shows the motion of the inner and outer contact points d_1 and d_2 . The motion of d_1 is compared with the position $x = d_1^*(t)$ at which the hydrodynamic pressure on the non-cavitated body is zero, i.e. $p^*(d_1^*, 0, t) = 0$. The pressure distribution p^* is given by (6.99). Figure 6.10(a) shows that d_1^* increases more rapidly than d_1 . Note that there is hardly any difference in the motions of the Wagner contact points. As already observed in previous sections, the motions of the Wagner contact points is insensitive to the flow in other parts of the fluid region.

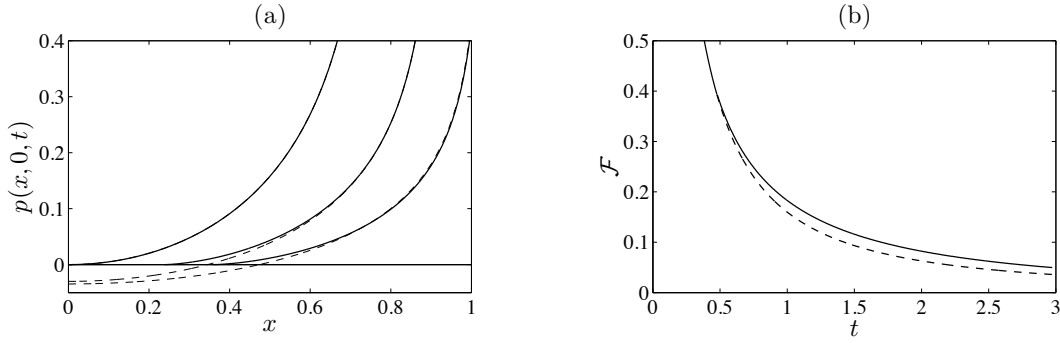


Figure 6.11: (a) The hydrodynamic pressure $p(x, 0, t)$ on the positive part of the contact region, $0 < x < d_1$, for $t = t_0$, $t = 0.74$ and $t = 1.0$. The solid line is the pressure for the blunt body impact with cavity and dashed line for the model where a cavity is not accounted for. (b) The vertical hydrodynamic force \mathcal{F} acting on the body as a function of time (solid line). The dashed line is the vertical force for the model without cavity. Note that Figure 6.11(b) does not show the hydrodynamic force in the Wagner stage $0 < t < t_0$.

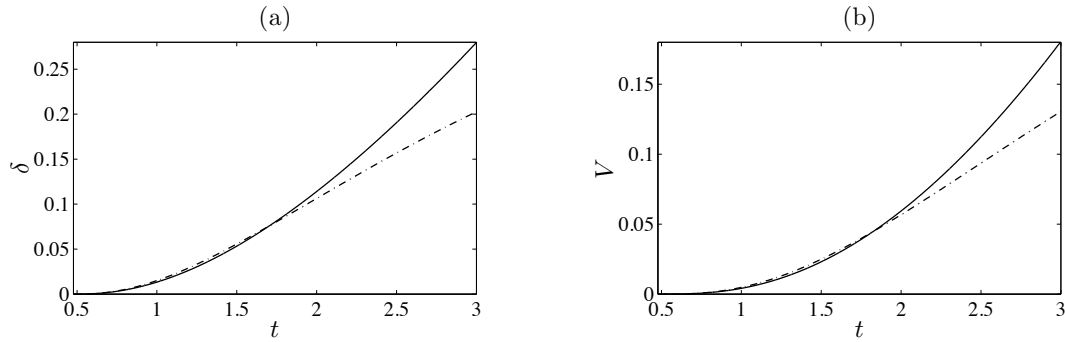


Figure 6.12: (a) The thickness of the cavity at $x = 0$ (solid line). The dashed line shows the asymptotic behaviour of $\delta(t)$ at $t = t_0$ (see equation (6.147)). (b) The volume of the cavity, $V(t)$, as a function of time (solid line). The dashed line shows the asymptotic behaviour of $V(t)$ at $t = t_0$ (see equation (6.148)).

Figure 6.10(b) shows that the difference in the penetration depths of the models is rather small. This is due to the small difference in the hydrodynamic loads of the models in the cavitation stage (see Figure 6.11(b)).

Time series of the pressure distributions of both models are presented in Figure 6.11(a). At $t = t_0$ these pressure distributions are identical. Apart from the region close to $x = d_1$, the differences between the pressures are small. In particular, the pressure distributions are very similar for x close to d_2 . In Figure 6.11(b) the hydrodynamic force is up to 30% smaller for the impact model where a cavity is accounted for $t_0 < t < 3$, however the absolute difference between the forces is small compared to the initial force $\mathcal{F}(0) = \pi$. This is due to the rapid decay of the forces during the Wagner stage.

Figure 6.12(a) shows the thickness $\delta(t)$ of the cavity. The thickness of the cavity grows slowly and is much smaller than the length of the cavity, $2d_1$. Hence, the volume of the cavity is very small (see Figure 6.12(b)).

Figure 6.13 shows a time series of the development of the cavity. The free-surface in the cavity region is obtained by the imaginary part of $f(x - i0)$ in equation (6.130). In particular,

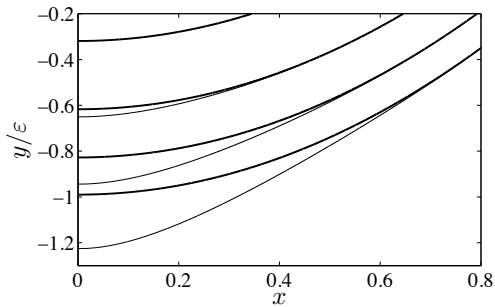


Figure 6.13: (a) The position of the body (thick line) and the shape of the cavity (thin line) for the times $t = 0.48, 1.23, 1.98, 2.73$.

we checked that the thickness of the cavity at $x = 0$ agrees with the explicit calculations of the thickness given by equation (6.145). Note the smooth transition from the cavity surface to the body surface at $x = d_1$.

6.3 Discussion

This chapter considered two vertical impact problems where fluid separation is accounted for as soon as the hydrodynamic pressure dropped below atmospheric pressure. In the first model we discussed the free fall of a rigid plate onto a fluid surface. We identified the parameters corresponding to fluid detachment inside the contact region (Type I) and the one starting at the left edge of the contact region (Type II). In this model we only accounted for the detachment of the fluid corresponding to Type II and our model was restricted to the case where the rear contact point moves from left to right. We had to stop calculations when the horizontal speed of the rear contact point became zero. An analysis of the subsequent stage may be of interest since high hydrodynamic forces can act on the plate close to this contact point. Furthermore an air-bubble may be trapped under the plate. On the other hand it has been shown that the fluid can detach from a large part of the contact region. An account for fluid separation increases the plate rotation, which can lead to much larger peaks in the vertical hydrodynamic forces on the plate.

In the second model we considered the free fall of a blunt body onto the free surface. The model includes a cavity region that grows from the centre of the bottom of the body. We compared the model with the one in which a cavity region is not included. The motion of the body and the hydrodynamic loads of the models with and without cavity agree well at the beginning and start to differ for large non-dimensional time. The expansion of the negative pressure zone in the model without cavity is significantly quicker than the expansion of the cavity region in the model with cavity. Consequently, the size of the negative-pressure zone is not suitable as a practical estimation of the length of the cavity. The shape of the free surface in the cavity region showed that the cavity thickness is much smaller than its horizontal extension. This model only considered cavity pressures which are equal to the atmospheric pressure. The presented model may be modified to account for any constant cavity pressure.

In general for both models, the motions of the Wagner contact points do not significantly

change if fluid detachment is not accounted for. However, we showed that the negative pressure zones in the model without fluid detachment give only a rough estimation of the location at which the fluid detaches from the fluid. Both models neglect gravity force on the body, so that the model presented in this section is only valid for very large Froude numbers. In cases where the Froude number is not sufficiently large, a gravity term has to be included in Newton's second law (6.20), which makes the calculations in the cavitation stage far more complicated than presented here.

Chapter 7

Conclusions and further work

7.1 Conclusions

We developed and analysed a number of novel fluid impact models for bodies, with small deadrise angle, impacting on a water surface within the framework of Wagner theory. We included the elasticity of the body using Euler's beam equation, a fixed horizontal speed of the body, fluid separation from the edge and along the smooth surface of the body. We accounted for a wake region behind the contact region.

In chapter 3, we analysed the vertical impact of a rigid and an elastic plate. For the rigid plate we found analytical solutions for the size of the contact region, the fluid velocity and the free-surface elevation. The solution involved a singularity of the fluid velocity and of the vertical free-surface elevation at the initial penetration point, where nonlinearity in the hydrodynamics is important. However, we believe that this singularity has only a minor effect on the global fluid flow. We found the equipartition of energy in the jet and in the fluid bulk. We established a fully coupled model of an elastic plate falling onto the water surface. We showed that the inclusion of elasticity changes significantly the hydrodynamic loads on the plate, and can increase the maximum hydrodynamic forces. Hydrodynamic pressures below atmospheric were already found for the rigid-plate impact, but it was shown that elastic vibrations of the plate lead to even lower pressures. We conclude that the elasticity of the plate may promote cavitation of the fluid and its detachment from the solid surface during the early stage of impact. The vibrations of the body remain large after the plate is completely wetted.

In chapter 4, we analysed the impact of rigid bodies onto the water surface at high horizontal speed. We showed that, for the oblique impact of a rigid plate at high horizontal speed, the forces on the plate are much larger than without horizontal speed. The part of the energy in the jet can be up to four times larger than the energy in the rest of the fluid. At the initial penetration point the vertical free-surface elevation is logarithmically singular. This singularity is weaker than for vertical impact. If the plate falls freely onto the water surface the plate exits the fluid and the duration of impact is of order $U\sqrt{m/\rho_F}$ if $V/(\varepsilon U) = O(1)$. If the vertical speed is large enough ($V > \varepsilon U$), the pressure below the rear part of the plate can be below atmospheric and the fluid may detach from the plate before the trailing edge. We modelled this early detachment with the Brillouin-Villat criterion, and showed that due to the missing negative pressure the plate can exit the fluid slightly earlier. Furthermore, a

coupled model of blunt body impact onto the free surface at high horizontal speed has been developed. The model consisted of a first stage with two turnover regions at the edges of the contact regions and a second stage where the fluid separates at the rear contact point. The negative pressure is released at the moment when the separation stage starts. In the separation stage, the position of the contact point was modelled by three separation criteria, where the choice of the criterion is significant for the outcome of the fluid-body interaction.

Fully coupled models of elastic plate impact with high horizontal speed have been discussed in chapter 5. In the first model the fluid separates at the trailing edge. We distinguished four different regimes of plate motions. In an example of a thick plate the forces on the plate can be so high that the resulting bending stresses were found to be close to the yield stress of the plate material. Also here we found hydrodynamic pressures in the contact region below the atmospheric value. It was shown that the shape of the free surface in the wake region is sensitive to the plate's vibrations. We studied the evolutions of different energy components of the fluid-plate system. It was shown in two cases that more than 75% of the total energy of the fluid-plate system is carried away with the spray jet and only a minor part is kept as kinetic energy in the bulk of the flow domain. In the second model the separation point on the plate was determined by the Brillouin-Villat criterion. Difficulties in modelling the rear contact point have been overcome by introducing Wagner's condition at this point when the wake region shrinks. We conclude that the rear contact point is sensitive to the plate vibrations. An early fluid detachment decreases the bending stress on the plate.

In chapter 6, we presented two models for the free fall of light bodies where we account for the separation of the fluid from the body. In the first study where a plate of general mass distribution falls freely onto the water surface, we showed that the fluid may separate either inside the contact region or at the edge of the contact region. Accounting for fluid separation only changes slightly the motion of the plate. However, this can have large effects on the hydrodynamic loads when the inclination angle reaches its minimum. In the model of the vertical impact of a light blunt body, the fluid separates inside the contact region. In particular, we showed that the expansion of the cavity between the body and fluid surface is significantly smaller than the expansion of the negative pressure zone in the model without cavitation.

7.2 Future work

This topic is far from being complete. Some problems considered in this thesis need further discussion. For example, in section 3.1 and 4.2, the flow behaviour at the initial penetration point due to the impact of a plate with a sharp edge has to be analysed with account for nonlinear terms in the hydrodynamic model. Differences in the splash development for a plate impacting with and without horizontal speed might be of interest. In sections 4.4 and 4.5, a further discussion is needed for the flow behaviour at the contact region shortly before the body exits the fluid. In chapter 5, a new model for plate impact at horizontal speed is required when the leading edge of the plate collides with the free-surface and when the horizontal velocity of the forward contact point becomes zero. In sections 4.5 and 6.1, we did not account for cavitation when the pressure becomes negative inside the contact region. To find a solution for the cavity is more difficult in these unsymmetric problems

than in the one discussed in section 6.2, which is symmetric. In section 6.1, we had to stop computations when the horizontal speed of the separation point reaches zero. As in section 5.2 we could continue the calculations by introducing Wagner's condition at this point. A detailed analysis of the flow at this point during the switch of the flow regimes may be of interest.

Further models can be suggested, whose analysis shall be straightforward with the tools provided in this thesis. For example, the impact of an elastic plate attached to a bigger structure into water at high horizontal speed is similar to the analysis in chapter 5. The problem of a vertical impact of an elastic shell onto a flat free surface, where fluid detachment is accounted for, may show bigger cavities than for a rigid blunt body presented in section 6.2. The model for an elastic cylindrical shell given by Ionina and Korobkin (1999) may be suitable to tackle the structural part of the problem. Furthermore, it is necessary to find solutions for the problem of vertical blunt body impact for any cavity pressure. With such a modified model we can account for cavitation developing at the vapour pressure.

In section 4.4, we showed that a plate ascends during planing logarithmically in time. This abnormality may be removed by taking far-field gravity into account. We believe that a linearised hydrodynamic model in the near field is valid, but such a model has to be properly matched with the correct far-field behaviour of the fluid flow.

In theory it is common to use the Brillouin-Villat criterion to determine the position of fluid separation. However, the fluid separates much more downstream from such a point in nature, especially, if the flow is turbulent. Using boundary layer theory requires advanced models, which can only be solved numerically with large computational expense. A practical separation condition approximating the separation point in reality would significantly simplify research in impact problems at high speed. Experimental results on unsteady flow separation at high speed may be very helpful to choose the right separation condition.

Further experiments and numerical solutions of plate impact at high horizontal speed are needed to assess our asymptotic model. Within the Wagner theory hydrodynamic forces on a wedge are overestimated. Several modified models, for example the modified Logvinovich model in Korobkin (2004), are available for vertical impact to correct the error in the asymptotic model. Similar modifications may be done for body impact at horizontal speed.

Appendix A

The norm of the eigenmodes

The elastic eigenmodes of a dry Euler beam are given by

$$\psi(r, x) := a_1 \cosh(rx) + a_2 \sinh(rx) + a_3 \cos(rx) + a_4 \sin(rx), \quad (\text{A.1})$$

where the constants a_1, a_2, a_3, a_4 and r depend on the conditions at the beam's ends $x = 0$ and $x = 1$. Here we give a general formula for $\int_0^1 \psi(r, x)^2 dx$ in terms of the values of $\psi(r, 0)$, $\frac{\partial}{\partial x}\psi(r, 0)$, $\frac{\partial^2}{\partial x^2}\psi(r, 0)$, $\psi(r, 1)$, $\frac{\partial}{\partial x}\psi(r, 1)$ and $\frac{\partial^2}{\partial x^2}\psi(r, 1)$. In particular, we find the norm of $\psi_k(x)$, $k \geq 2$, in equation (3.77), when we set $a_1 = a_3 = 1$, $a_2 = a_4 = \gamma_k$, $r = \lambda_k$ where λ_k and γ_k are given by equations (3.76) and (3.78).

The function $\psi(r, x)$ in (A.1) satisfies the following two relations:

$$\frac{\partial^4}{\partial x^4}\psi(r, x) = r^4\psi(r, x), \quad (\text{A.2})$$

$$r \frac{\partial}{\partial r}\psi(r, x) = x \frac{\partial}{\partial x}\psi(r, x), \quad (\text{A.3})$$

for any real r and x . In the following, we will only use the two conditions (A.2) and (A.3) to find a formula for $\int_0^1 \psi(r, x)^2 dx$. We obtain the following identity by using equation (A.2) and by integrating by parts twice:

$$\begin{aligned} r^4 \int_0^1 \psi(r, x)\psi(r_0, x) dx &= \left[\frac{\partial^3}{\partial x^3}\psi(r, x)\psi(r_0, x) - \frac{\partial^2}{\partial x^2}\psi(r, x)\frac{\partial}{\partial x}\psi(r_0, x) \right]_{x=0}^{x=1} \\ &\quad + \int_0^1 \frac{\partial^2}{\partial x^2}\psi(r, x)\frac{\partial^2}{\partial x^2}\psi(r_0, x) dx \end{aligned} \quad (\text{A.4})$$

where we define $[f(x)]_{x=a}^{x=b} = f(b) - f(a)$. We obtain a similar identity if we replace r^4 on the left-hand side of (A.4) by r_0^4 . By subtracting the second identity from the first we obtain

$$\begin{aligned} (r^4 - r_0^4) \int_0^1 \psi(r, x)\psi(r_0, x) dx &= \left[\frac{\partial^3}{\partial x^3}(\psi(r, x) - \psi(r_0, x))\psi(r_0, x) - (\psi(r, x) - \psi(r_0, x))\frac{\partial^3}{\partial x^3}\psi(r_0, x) \right. \\ &\quad \left. + \frac{\partial}{\partial x}(\psi(r, x) - \psi(r_0, x))\frac{\partial^2}{\partial x^2}\psi(r_0, x) - \frac{\partial^2}{\partial x^2}(\psi(r, x) - \psi(r_0, x))\frac{\partial}{\partial x}\psi(r_0, x) \right]_{x=0}^{x=1}. \end{aligned} \quad (\text{A.5})$$

Now, the right-hand side of identity (A.5) is free of integrals. We divide the identity (A.5) by $r^4 - r_0^4$, let $r \rightarrow r_0$ and use the relations (A.2) and (A.3) to obtain the following identity

for any $r_0 \neq 0$:

$$\begin{aligned} \int_0^1 \psi(r_0, x)^2 dx &= \frac{1}{4r_0^4} \left(r_0^4 \psi(r_0, 1)^2 - 2 \frac{\partial}{\partial x} \psi(r_0, 1) \frac{\partial^3}{\partial x^3} \psi(r_0, 1) + \left(\frac{\partial^2}{\partial x^2} \psi(r_0, 1) \right)^2 \right. \\ &\quad + 3 \frac{\partial^3}{\partial x^3} \psi(r_0, 1) \psi(r_0, 1) - \frac{\partial^2}{\partial x^2} \psi(r_0, 1) \frac{\partial}{\partial x} \psi(r_0, 1) \\ &\quad \left. - 3 \frac{\partial^3}{\partial x^3} \psi(r_0, 0) \psi(r_0, 0) + \frac{\partial^2}{\partial x^2} \psi(r_0, 0) \frac{\partial}{\partial x} \psi(r_0, 0) \right). \end{aligned} \quad (\text{A.6})$$

This identity (A.6) can be used for $\psi(r, x)$ in (A.1) for any a_1, a_2, a_3, a_4 and r . For example, we obtain from (A.6) for $a_1 = a_2 = a_3 = 0, a_4 = 1, r = \pi k$, where k is an integer, the well-known identity $\int_0^1 \sin(\pi k x)^2 dx = \frac{1}{2}$.

The dry normal modes of an Euler beam with free-free ends, $\psi_k(x)$, $k \geq 2$, are given by equation (3.77) and satisfy the boundary conditions $\frac{\partial^2}{\partial x^2} \psi_k(x) = \frac{\partial^3}{\partial x^3} \psi_k(x) = 0$ at $x = 0$ and $x = 1$ (see conditions (3.72)), so that we obtain the following formula for the norm of the normal modes ψ_k :

$$\left(\int_0^1 \psi_k(x)^2 dx \right)^{1/2} = \frac{1}{2} |\psi_k(1)|. \quad (\text{A.7})$$

Equations (3.91) and (3.92) show that $|\psi_k(1)| = 2$, so that equation (A.7) implies that the modes ψ_k in (3.91) and (3.92) are normed.

Appendix B

Coefficients in the final equations for impact problems of elastic plates

In this appendix we find analytical expressions for

$$\Lambda(f, g) := \frac{1}{\pi} \int_0^c \int_0^c \frac{\sqrt{\xi(c-\xi)}}{\sqrt{x(c-x)}} \frac{g(\xi)f(x)}{\xi-x} dx d\xi, \quad (\text{B.1})$$

$$\Gamma^{(1)}(f) = \int_0^c \sqrt{\frac{u}{c-u}} f(u) du, \quad \Gamma^{(2)}(f) = \int_0^c \sqrt{\frac{c-u}{u}} f(u) du, \quad (\text{B.2})$$

where the functions f and g are either normal modes ψ_k given in (3.74) and (3.77) or their derivatives or indefinite integrals. Hence f and g in the arguments of Λ , $\Gamma^{(1)}$ and $\Gamma^{(2)}$ can be polynomials or a linear combination of trigonometrical and hyperbolic functions of the forms

$$p(x) = B_0 + B_1x + B_2x^2, \quad q(x) = A_0 + A_1x, \quad (\text{B.3})$$

$$\psi(\lambda, \mathbf{a}; x) = a_1 \cosh(\lambda x) + a_2 \sinh(\lambda x) + a_3 \cos(\lambda x) + a_4(\lambda x), \quad (\text{B.4})$$

where $\lambda \geq 0$ are the corresponding eigenvalues. Expressions of the form (B.1) and (B.2) are given in equations (3.131), (3.132), (5.16) and (5.25).

In subsection B.1 we show that Λ satisfies the following symmetry condition for any smooth functions $v(x)$ and $w(x)$:

$$\Lambda(w, v_x) = \Lambda(v, w_x). \quad (\text{B.5})$$

If f and g are functions of the form (B.4), they can be represented as a linear combination of exponential functions e^{rx} where we choose $r = \lambda, -\lambda, i\lambda, -i\lambda$. Hence, it is sufficient to find $\Lambda(e^{sx}, e^{r\xi})$ for complex constants r and s . An analytical form of $\Lambda(e^{sx}, e^{r\xi})$ will be derived in section B.2. In section B.3 we will present the specific values of $\Lambda(\psi(\mu, \mathbf{b}; \cdot), \psi(\lambda, \mathbf{a}; \cdot))$, $\Lambda(p, \psi(\lambda, \mathbf{a}; \cdot))$, $\Lambda(\psi(\lambda, \mathbf{a}; \cdot), q)$ and $\Lambda(p, q)$. The dot signifies that $\psi(\lambda, \mathbf{a}; \cdot)$ appears in the arguments of Λ as functions in terms of x . Finally, in section B.4 we give results for the values of $\Gamma^{(1)}(q)$, $\Gamma^{(2)}(q)$, $\Gamma^{(1)}(\psi(\lambda, \mathbf{a}; \cdot))$ and $\Gamma^{(2)}(\psi(\lambda, \mathbf{a}; \cdot))$.

B.1 The symmetry of $\Lambda(v, w_x)$

To show the symmetry relation (B.5) we assume that the x -derivatives of the $w(x)$ and $v(x)$ are Hölder-continuous in $0 \leq x \leq c$. We define the auxiliary complex function $f(z)$, $z = x + iy$ on the lower half plane as the solution of the following mixed boundary value problem:

$$f(z) \text{ analytic} \quad (y < 0), \quad (\text{B.6})$$

$$\text{Im } f(x - i0) = v(x) \quad (0 < x < c), \quad (\text{B.7})$$

$$\text{Re } f(x - i0) = 0 \quad (x < 0 \text{ and } x > c), \quad (\text{B.8})$$

$$f(z) = O(z^{-1}) \quad (|z| \rightarrow \infty), \quad (\text{B.9})$$

$$f(z) = O(1) \quad (|z| \rightarrow 0), \quad (\text{B.10})$$

$$f(z) = O(1) \quad (|z| \rightarrow c). \quad (\text{B.11})$$

The solution of the problem (B.6) –(B.11) is given by equation (2.25) with $k_1 = k_2 = -1$:

$$f(z) = -\frac{i}{\pi} \sqrt{z(c-z)} \int_0^c \frac{v(\xi)}{\sqrt{\xi(c-\xi)}(\xi-z)} d\xi \quad (y < 0). \quad (\text{B.12})$$

It was shown in section 2.4 that $f(z)$ is continuous at $z = d_1$ and $z = d_2$ since $v(x)$ is differentiable. Hence, equation (B.8) implies $\text{Re}(f(x - i0)) = 0$ at $x = 0$ and $x = c$. It follows from (B.1) and (B.12) that $\Lambda(w_x, v) = \int_0^c w_x(x) \text{Re}(f(x - i0)) dx$. Integrating $\Lambda(w_x, v)$ by parts gives us

$$\Lambda(w_x, v) = - \int_0^c w(x) \text{Re}(f_z(x - i0)) dx, \quad (\text{B.13})$$

where $f_z(z)$ is the complex derivative of $f(z)$. We reformulate the problem (B.6) – (B.11) in terms of $f_z(z)$:

$$f_z(z) \text{ analytic} \quad (y < 0), \quad (\text{B.14})$$

$$\text{Im } f_z(x - i0) = v_x(x) \quad (0 < x < c), \quad (\text{B.15})$$

$$\text{Re } f_z(x - i0) = 0 \quad (x < 0 \text{ and } x > c), \quad (\text{B.16})$$

$$f_z(z) = O(z^{-2}) \quad (|z| \rightarrow \infty), \quad (\text{B.17})$$

$$f_z(z) = O(z^{-1/2}) \quad (|z| \rightarrow 0), \quad (\text{B.18})$$

$$f_z(z) = O((z - c)^{-1/2}) \quad (|z| \rightarrow c). \quad (\text{B.19})$$

The solution of the problem (B.14) – (B.19) is given by formula (2.25) with $k_1 = 0$ and $k_2 = 0$:

$$\text{Re}(f_z(x - i0)) = -\frac{1}{\sqrt{x(c-x)}} \int_0^c \frac{\sqrt{\xi(c-\xi)}}{\xi-x} v_x(\xi) d\xi \quad (0 < x < c). \quad (\text{B.20})$$

Substituting $\text{Re}(f_z(x - i0))$ in (B.20) into equation (B.13) and an interchange of the integrals proves equation (B.5).

B.2 An analytical expression for $\Lambda(e^{sx}, e^{r\xi})$

In this section we derive a formula for $\Lambda(e^{sx}, e^{r\xi})$ where Λ is given by (B.1). Since

$$\Lambda(e^{sx}, e^{r\xi}) = \frac{c}{2} e^{c(r+s)/2} \Lambda^*(e^{sx}, e^{r\xi}), \quad (\text{B.21})$$

where

$$\Lambda^*(f, g) := \frac{1}{\pi} \int_{-1}^1 \int_{-1}^1 \frac{\sqrt{1-\xi^2} g(\xi) f(x)}{\sqrt{1-x^2} x-\xi} d\xi dx. \quad (\text{B.22})$$

We only have to find an analytical expression for $\Lambda^*(e^{sx}, e^{r\xi})$.

An expansion of e^{sx} in terms of the Chebyshev polynomials of the first kind, T_n , is given by $e^{sx} = \sum_{n=0}^{\infty} f_n T_n(x)$ where the coefficients f_n are obtained by

$$f_n = \frac{2}{\pi} \int_{-1}^1 \frac{e^{sx} T_n(x)}{\sqrt{1-x^2}} dx = \frac{2}{\pi} \int_0^\pi e^{s \cos(u)} \cos(nu) du = 2I_n(s). \quad (\text{B.23})$$

In (B.23) we used the relation $T_n(\cos \theta) = \cos(n\theta)$ for the Chebyshev polynomials and the integral representation for the modified Bessel functions of the first kind, I_n . With the help of Gradshteyn and Ryzhik (1994, item 7.344) we have

$$\int_{-1}^1 \frac{T_n(x)}{(x-\xi)\sqrt{1-x^2}} dx = \pi U_{n-1}(\xi), \quad (\text{B.24})$$

where $U_n(x)$ are the Bessel functions of the second kind. Hence, with the expansion of e^{sx} and with equation (B.23) we conclude that

$$\Lambda^*(e^{sx}, e^{r\xi}) = \sum_{n=1}^{\infty} f_n \int_{-1}^1 e^{r\xi} U_{n-1}(\xi) \sqrt{1-\xi^2} d\xi = \pi \sum_{n=1}^{\infty} I_n(s) (I_{n-1}(r) - I_{n+1}(r)), \quad (\text{B.25})$$

where we used $U_n(\cos \theta) = \sin((n+1)\theta)/\sin \theta$. To rewrite the right-hand side of equation (B.25) we employ the following recursion formula from Abramowitz and Stegun (1965, item 9.6.26):

$$I_{n-1}(z) - I_{n+1}(z) = \frac{2n}{z} I_n(z). \quad (\text{B.26})$$

We use the identity (B.26) twice with $z = s$ and $z = r$, and then divide the relations to obtain

$$\frac{r}{s} I_n(s) (I_{n-1}(r) - I_{n+1}(r)) = I_n(r) (I_{n-1}(s) - I_{n+1}(s)). \quad (\text{B.27})$$

Finally it follows from equation (B.27) that

$$(1 + \frac{r}{s}) \sum_{n=1}^{\infty} I_n(s) (I_{n-1}(r) - I_{n+1}(r)) = I_1(s) I_0(r) + I_0(s) I_1(r). \quad (\text{B.28})$$

For $s \neq -r$, the identity (B.28) gives us together with equation (B.25) the following formula

for $\Lambda^*(e^{sx}, e^{r\xi})$:

$$\Lambda^*(e^{sx}, e^{r\xi}) = \begin{cases} \frac{\pi s}{r+s} [I_0(r)I_1(s) + I_0(s)I_1(r)] , & (s \neq -r) \\ -\pi^2 (rI_1^2(r) - rI_0^2(r) + I_0(r)I_1(r)) . & (s = -r) \end{cases} \quad (\text{B.29})$$

By substituting equation (B.29) into (B.21), an explicit formula for $\Lambda(e^{sx}, e^{r\xi})$ is obtained.

B.3 Expressions for $\Lambda(f, g)$ for specific f and g

This subsection presents the specific expressions for $\Lambda(\psi(\mu, \mathbf{b}, \cdot), \psi(\lambda, \mathbf{a}, \cdot))$, $\Lambda(p, \psi(\lambda, \mathbf{a}, \cdot))$, $\Lambda(\psi(\lambda, \mathbf{a}, \cdot), q)$ and $\Lambda(p, q)$. To write the results in a compact form, we define the following for $k = 0, 1$ in terms of λ and \mathbf{a} :

$$I_k^+(\lambda, \mathbf{a}) = I_k(\frac{c}{2}\lambda)(a_1 \cosh(\frac{c}{2}\lambda) + a_2 \sinh(\frac{c}{2}\lambda)) , \quad (\text{B.30})$$

$$I_k^-(\lambda, \mathbf{a}) = I_k(\frac{c}{2}\lambda)(a_1 \sinh(\frac{c}{2}\lambda) + a_2 \cosh(\frac{c}{2}\lambda)) , \quad (\text{B.31})$$

$$J_k^+(\lambda, \mathbf{a}) = J_k(\frac{c}{2}\lambda)(a_3 \cos(\frac{c}{2}\lambda) + a_4 \sin(\frac{c}{2}\lambda)) , \quad (\text{B.32})$$

$$J_k^-(\lambda, \mathbf{a}) = J_k(\frac{c}{2}\lambda)(-a_3 \sin(\frac{c}{2}\lambda) + a_4 \cos(\frac{c}{2}\lambda)) . \quad (\text{B.33})$$

It follows from (B.29) that $\Lambda(\psi(\mu, \mathbf{b}, \cdot), \psi(\lambda, \mathbf{a}, \cdot))$ has the following explicit form

$$\Lambda(\psi(\mu, \mathbf{b}, \cdot), \psi(\lambda, \mathbf{a}, \cdot)) = \frac{\pi cs}{2} \left(\frac{\alpha(\lambda, \mu, \mathbf{a}, \mathbf{b})}{\lambda^2 - \mu^2} + \frac{\beta(\lambda, \mu, \mathbf{a}, \mathbf{b})}{\lambda^2 + \mu^2} \right) , \quad (\text{B.34})$$

where

$$\begin{aligned} \alpha(\lambda, \mu, \mathbf{a}, \mathbf{b}) = & \\ & r[I_1^+(\lambda, \mathbf{a})I_0^-(\mu, \mathbf{b}) + I_0^-(\lambda, \mathbf{a})I_1^+(\mu, \mathbf{b}) + J_1^+(\lambda, \mathbf{a})J_0^-(\mu, \mathbf{b}) + J_0^-(\lambda, \mathbf{a})J_1^+(\mu, \mathbf{b})] \\ & -s[I_1^-(\lambda, \mathbf{a})I_0^+(\mu, \mathbf{b}) + I_0^+(\lambda, \mathbf{a})I_1^-(\mu, \mathbf{b}) + J_1^-(\lambda, \mathbf{a})J_0^+(\mu, \mathbf{b}) + J_0^+(\lambda, \mathbf{a})J_1^-(\mu, \mathbf{b})] \end{aligned} \quad (\text{B.35})$$

and

$$\begin{aligned} \beta(\lambda, \mu, \mathbf{a}, \mathbf{b}) = & \\ & r[I_1^+(\lambda, \mathbf{a})J_0^-(\mu, \mathbf{b}) - I_0^-(\lambda, \mathbf{a})J_1^+(\mu, \mathbf{b}) + J_1^+(\lambda, \mathbf{a})I_0^-(\mu, \mathbf{b}) - J_0^-(\lambda, \mathbf{a})I_1^+(\mu, \mathbf{b})] \\ & +s[I_1^-(\lambda, \mathbf{a})J_0^+(\mu, \mathbf{b}) + I_0^+(\lambda, \mathbf{a})J_1^-(\mu, \mathbf{b}) + J_1^-(\lambda, \mathbf{a})I_0^+(\mu, \mathbf{b}) + J_0^+(\lambda, \mathbf{a})I_1^-(\mu, \mathbf{b})] . \end{aligned} \quad (\text{B.36})$$

For $\mu = \lambda$ we consider the limit of $\lambda \rightarrow \mu$ in (B.34), where the limit of $\alpha(\lambda, \mu, \mathbf{a}, \mathbf{b})/(\lambda^2 - \mu^2)$ as $\lambda \rightarrow \mu$ is given by

$$\begin{aligned} \lim_{\lambda \rightarrow \mu} \frac{\alpha(\lambda, \mu, \mathbf{a}, \mathbf{b})}{\lambda^2 - \mu^2} = & \\ & \frac{cs}{2(r+s)} [I_1^-(\mu, \mathbf{a})I_1^+(\mu, \mathbf{b}) - I_0^-(\mu, \mathbf{a})I_0^+(\mu, \mathbf{b}) + I_1^+(\mu, \mathbf{a})I_1^-(\mu, \mathbf{b}) - I_0^+(\mu, \mathbf{a})I_0^-(\mu, \mathbf{b}) \\ & - J_1^-(\mu, \mathbf{a})J_1^+(\mu, \mathbf{b}) - J_0^-(\mu, \mathbf{a})J_0^+(\mu, \mathbf{b}) + J_1^+(\mu, \mathbf{a})J_1^-(\mu, \mathbf{b}) + J_0^+(\mu, \mathbf{a})J_0^-(\mu, \mathbf{b})] \\ & + \frac{2}{r+s} [I_0^-(\mu, \mathbf{a})I_1^+(\mu, \mathbf{b}) + J_0^-(\mu, \mathbf{a})J_1^+(\mu, \mathbf{b})] . \end{aligned} \quad (\text{B.37})$$

For polynomials $p(x) = B_0 + B_1x + B_2x^2$ and $q(x) = A_0 + A_1x$ we obtain the analytical expressions:

$$\begin{aligned} \Lambda(p, \psi(\lambda, \mathbf{a}, \cdot)) &= B_1 \frac{\pi c}{2\lambda} (I_1^+(\lambda, \mathbf{a}) + J_1^+(\lambda, \mathbf{a})) + B_2 \frac{\pi c}{\lambda} \left[\frac{1}{\lambda} (-I_1^-(\lambda, \mathbf{a}) + J_1^-(\lambda, \mathbf{a})) \right. \\ &\quad \left. + \frac{c}{4} (2I_1^+(\lambda, \mathbf{a}) + 2J_1^+(\lambda, \mathbf{a}) + I_0^-(\lambda, \mathbf{a}) - J_0^-(\lambda, \mathbf{a})) \right], \end{aligned} \quad (\text{B.38})$$

$$\begin{aligned} \Lambda(\psi(\lambda, \mathbf{a}, \cdot), q) &= A_0 \frac{\pi c}{2} (I_1^-(\lambda, \mathbf{a}) + J_1^-(\lambda, \mathbf{a})) + A_1 \frac{\pi c}{2} \left[-\frac{1}{\lambda} (I_1^+(\lambda, \mathbf{a}) + J_1^+(\lambda, \mathbf{a})) \right. \\ &\quad \left. + \frac{c}{4} (2I_1^-(\lambda, \mathbf{a}) + 2J_1^-(\lambda, \mathbf{a}) + I_0^+(\lambda, \mathbf{a}) - J_0^+(\lambda, \mathbf{a})) \right] \end{aligned} \quad (\text{B.39})$$

and

$$\Lambda(p, q) = \frac{\pi c^2}{8} (A_0 B_1 + \frac{c}{2} A_1 B_1 + c A_0 B_2 + \frac{9}{16} c^2 A_1 B_2). \quad (\text{B.40})$$

In the next section we evaluate $\Gamma^{(1)}(f)$ and $\Gamma^{(2)}(f)$ for $f = q$ and $f = \psi(\lambda, \mathbf{a}, \cdot)$.

B.4 Expressions for $\Gamma^{(1)}(f)$ and $\Gamma^{(2)}(f)$ for specific f

Results for $\Gamma^{(1)}(q)$ and $\Gamma^{(2)}(q)$, where $\Gamma^{(i)}$ is defined in (B.2) and $q(x) = A_0 + A_1x$, are given by

$$\Gamma^{(1)}(q) = \frac{\pi}{2} c A_0 + \frac{3\pi}{8} c^2 A_1, \quad (\text{B.41})$$

$$\Gamma^{(2)}(q) = \frac{\pi}{2} c A_0 + \frac{\pi}{8} c^2 A_1. \quad (\text{B.42})$$

We found the following equations by using the integral representations of the modified Bessel functions I_0 and I_1 :

$$\Gamma_c^{(1)}(e^{rx}) = \frac{\pi c}{2} (I_0(\frac{cr}{2}) + I_1(\frac{cr}{2})) e^{cr/2}, \quad (\text{B.43})$$

$$\Gamma_c^{(2)}(e^{rx}) = \frac{\pi c}{2} (I_0(\frac{cr}{2}) - I_1(\frac{cr}{2})) e^{cr/2}. \quad (\text{B.44})$$

By using the identities (B.43) and (B.44) we obtain

$$\Gamma^{(1)}(\psi(\lambda, \mathbf{a}, \cdot)) = \frac{\pi c}{2} (I_0^+(\lambda, \mathbf{a}) + I_1^-(\lambda, \mathbf{a}) + J_0^+(\lambda, \mathbf{a}) + J_1^-(\lambda, \mathbf{a})), \quad (\text{B.45})$$

$$\Gamma^{(2)}(\psi(\lambda, \mathbf{a}, \cdot)) = \frac{\pi c}{2} (I_0^+(\lambda, \mathbf{a}) - I_1^-(\lambda, \mathbf{a}) + J_0^+(\lambda, \mathbf{a}) - J_1^-(\lambda, \mathbf{a})), \quad (\text{B.46})$$

where I_k^+ , I_k^- , J_k^+ and J_k^- are defined by equations (B.30) – (B.33).

Appendix C

Some specific Cauchy principal-value integrals

In this appendix we give analytical expressions for the following integrals for $0 < s < c$:

$$F_k^{(1)}(s) = \int_0^c \frac{\psi'_k(u)}{(u-s)\sqrt{u(c-u)}} du, \quad (\text{C.1})$$

$$F_k^{(2)}(s) = \int_0^c \frac{\psi_k(u)}{(u-s)\sqrt{u(c-u)}} du, \quad (\text{C.2})$$

$$F_k^{(3)}(s) = \int_0^c \frac{\Psi_k(u)}{(u-s)\sqrt{u(c-u)}} du, \quad (\text{C.3})$$

where $\psi_k(x)$ are the dry normal modes given by equations (3.74) for $k = 0, 1$ and by equations (3.91) and (3.92) for $k \geq 2$. The integrals (C.1) – (C.3) appear in equations (3.138) and (5.39).

For $k = 0$ and $k = 1$, expressions for $F_k^{(i)}$ in (C.1) – (C.3) can be found using the identity (2.35), so that we obtain:

$$F_0^{(1)}(s) = 0, \quad F_1^{(1)}(s) = 0, \quad (\text{C.4})$$

$$F_0^{(2)}(s) = 0, \quad F_1^{(2)}(s) = 2\sqrt{3}\pi, \quad (\text{C.5})$$

$$F_0^{(3)}(s) = \pi, \quad F_1^{(3)}(s) = \pi\sqrt{3}(s + \frac{c}{2} - 1). \quad (\text{C.6})$$

For $k \geq 2$ we can evaluate $F_k^{(i)}(s)$ by writing the right-hand sides of (C.1) – (C.3) as an expansion in terms of Chebyshev polynomials of the second kind, U_j , with the help of the following identity:

$$\int_0^c \frac{e^{ru}}{(u-s)\sqrt{u(c-u)}} du = \frac{4\pi}{c} e^{\frac{rc}{2}} \sum_{j=0}^{\infty} I_{j+1} \left(\frac{rc}{2} \right) U_j(2s/c - 1), \quad (\text{C.7})$$

where I_j are the modified Bessel functions of the first kind. The identity (C.7) is obtained from the expansion $e^{rx} = 2 \sum_{k=0}^{\infty} I_k(r) T_k(x)$ in terms of the Chebyshev polynomials of the first kind, T_n , (see equation (B.23)) and equation (B.24). The identity (C.7) for $r = \pm\lambda_k, \pm i\lambda_k$ together with equations (3.91) and (3.92) for $k \geq 2, 0 < x < c$ and $i = 1, 2, 3$ give

us

$$F_k^{(i)}(x) = \frac{4\pi\lambda_k^{2-i}}{c} \sum_{j=0}^{\infty} \left(A_{kj}^{(i)}(c) I_{j+1}\left(\frac{c}{2}\lambda_k\right) + B_{kj}^{(i)}(c) J_{j+1}\left(\frac{c}{2}\lambda_k\right) \right) U_j(2x/c - 1), \quad (\text{C.8})$$

where the functions $J_j(x)$ are Bessel functions of the first kind. For k even, the coefficients $A_{kj}^{(i)}$ and $B_{kj}^{(i)}$ are defined by $A_{kj}^{(i)} = \alpha_{kj}^{(i)}/\cosh(\lambda_k/2)$ and $B_{kj}^{(i)} = \beta_{kj}^{(i)}/\cos(\lambda_k/2)$. For k even and j even the elements $\alpha_{kj}^{(i)}$ and $\beta_{kj}^{(i)}$ are given by

$$\alpha_{kj}^{(1)}(c) = \cosh(f_k), \quad \beta_{kj}^{(1)}(c) = (-1)^{j/2+1} \cos(f_k), \quad (\text{C.9})$$

$$\alpha_{kj}^{(2)}(c) = -\sinh(f_k), \quad \beta_{kj}^{(2)}(c) = (-1)^{j/2} \sin(f_k), \quad (\text{C.10})$$

$$\alpha_{kj}^{(3)}(c) = \cosh(f_k), \quad \beta_{kj}^{(3)}(c) = (-1)^{j/2} \cos(f_k), \quad (\text{C.11})$$

where $f_k = \frac{1-c}{2}\lambda_k$. For k even and j odd we obtain

$$\alpha_{kj}^{(1)}(c) = -\sinh(f_k), \quad \beta_{kj}^{(1)}(c) = (-1)^{(j+1)/2} \sin(f_k), \quad (\text{C.12})$$

$$\alpha_{kj}^{(2)}(c) = \cosh(f_k), \quad \beta_{kj}^{(2)}(c) = (-1)^{(j+1)/2} \cos(f_k), \quad (\text{C.13})$$

$$\alpha_{kj}^{(3)}(c) = -\sinh(f_k), \quad \beta_{kj}^{(3)}(c) = (-1)^{(j-1)/2} \sin(f_k). \quad (\text{C.14})$$

For k odd we set $A_{kj}^{(i)} = \alpha_{kj}^{(i)}/\sinh(\lambda_k/2)$ and $B_{kj}^{(i)} = \beta_{kj}^{(i)}/\sin(\lambda_k/2)$. For k odd and j even the elements $\alpha_{kj}^{(i)}$ and $\beta_{kj}^{(i)}$ are defined by

$$\alpha_{kj}^{(1)}(c) = \sinh(f_k), \quad \beta_{kj}^{(1)}(c) = (-1)^{j/2+1} \sin(f_k), \quad (\text{C.15})$$

$$\alpha_{kj}^{(2)}(c) = -\cosh(f_k), \quad \beta_{kj}^{(2)}(c) = (-1)^{j/2+1} \cos(f_k), \quad (\text{C.16})$$

$$\alpha_{kj}^{(3)}(c) = \sinh(f_k), \quad \beta_{kj}^{(3)}(c) = (-1)^{j/2} \sin(f_k). \quad (\text{C.17})$$

For k odd and j odd we obtain

$$\alpha_{kj}^{(1)}(c) = -\cosh(f_k), \quad \beta_{kj}^{(1)}(c) = (-1)^{(j-1)/2} \cos(f_k), \quad (\text{C.18})$$

$$\alpha_{kj}^{(2)}(c) = \sinh(f_k), \quad \beta_{kj}^{(2)}(c) = (-1)^{(j+1)/2} \sin(f_k), \quad (\text{C.19})$$

$$\alpha_{kj}^{(3)}(c) = -\cosh(f_k), \quad \beta_{kj}^{(3)}(c) = (-1)^{(j+1)/2} \cos(f_k). \quad (\text{C.20})$$

As to the convergence of the series (C.8), for increasing j the values $I_j(\frac{c}{2}\lambda_k)$ and $J_j(\frac{c}{2}\lambda_k)$ quickly tend to zero as $O(\frac{1}{j!}(\frac{c}{4}\lambda_k)^j)$ for $j > \frac{c}{4}\lambda_k$ and $U_{j-1}(2x/c - 1)$ diverges only weakly and only close to the edges $x = 0$ and $x = c$ as $O(j)$. The convergence of the series is quick, since the series is alternating due to regular sign changes for $A_{kj}^{(i)}$ and $B_{kj}^{(i)}$ and irregular sign change of $U_j(2x/c - 1)$ in j . For evaluations of the pressure in section 3.3 and in section 5.1 we obtained good results for $F_k(x)$ when we truncate the series in (C.8) after the 10th summand.

As to large k , the values $A_{kj}(c)I_{j+1}(\frac{c}{2}\lambda_k)$ and $B_{kj}(c)J_{j+1}(\frac{c}{2}\lambda_k)$ tend to zero as $k \rightarrow \infty$ with order $O(k^{-1/2})$ for fixed j . We found numerically that $F_k^{(i)}(x) = O(k^{2-i})$ as $k \rightarrow \infty$ for fixed x and c . Hence, the series $\sum_k F_k^{(1)}(x)a_k(t)$, $\sum_k F_k^{(2)}(x)\dot{a}_k(t)$ and $\sum_k F_k^{(3)}(x)\ddot{a}_k(t)$ in equations (3.138) and (5.39) converge, since it was shown that the magnitudes of $a_k(t)$, $\dot{a}_k(t)$ and $\ddot{a}_k(t)$ approximately decay as $O(k^{-5})$, $O(k^{-4})$ and $O(k^{-2})$, respectively.

Appendix D

An integral relation

Our expression for the rate of change of the kinetic energy in the fluid bulk, $\frac{d}{dt}E_{\text{bulk}}^{(f)}$, in (4.70) includes, in particular, $\varphi(x, 0, t)$ for $x: t < x < t + c$. Its computation requires the evaluation of $\varphi_x(x, 0, t)$ in (4.24), which involves two integrals (see equation (4.25)) to be computed for every point $t < x < t + c$. The aim of this appendix is to show the following identity

$$\int_0^{d_2} \varphi(x, 0, t) \varphi_{yt}(x, 0, t) dx = - \int_{d_1}^{d_2} p(x, 0, t) \omega_t(x, t) dx - \dot{d}_2 \frac{K^2(d_2, t)}{\pi(d_2 - d_1)}, \quad (\text{D.1})$$

where $K(x, t)$ is defined by equation (4.25). Equation (D.1) helps us in (4.70) to confirm that $E_{\text{jet}}^{(f)}$ and $E_{\text{bulk}}^{(f)}$ make up the total energy of the fluid flow. By computing the left and right-hand sides of (D.1) we can verify the accuracy of the numerical results in chapters 4 and 5. To prove (D.1) we need some properties of the complex velocity potential $F_t(z) = \varphi + i\psi$ and the complex acceleration $f_{tt}(z) = \varphi_{tx} - i\varphi_{ty}$ given in section 4.1: The functions $F_t(z)$ and $f_{tt}(z)$ have the following behaviours at $z = d_1, d_2$ and in the far-field (see also equation (4.34)):

$$F_t(z) = O(1), \quad f_{tt}(z) = O((z - d_1)^{-1/2}) \quad (z \rightarrow d_1), \quad (\text{D.2})$$

$$F_t(z) = i\psi(d_2, 0, t) - i \frac{2K(d_2, t)}{\pi\sqrt{d_2 - d_1}} (z - d_2)^{1/2} + O(z - d_2) \quad (z \rightarrow d_2), \quad (\text{D.3})$$

$$f_{tt}(z) = -i \frac{\dot{d}_2 K(d_2, t)}{2\pi\sqrt{d_2 - d_1}} (z - d_2)^{-3/2} + O((z - d_2)^{-1}) \quad (z \rightarrow d_2), \quad (\text{D.4})$$

$$F_t(z) = O(z^{-1}), \quad f_{tt}(z) = O(z^{-2}) \quad (|z| \rightarrow \infty). \quad (\text{D.5})$$

Furthermore, due to equation (4.15) the real part of $F_t(z)$ is zero for $x < d_0$, $y = 0$ and $x > d_2$, $y = 0$, and the real part of $f_{tt}(z)$ is zero for $x < d_1$, $y = 0$ and $x > d_2$, $y = 0$. Since $F_t(z)$ and $f_{tt}(z)$ are analytic functions, we can apply Cauchy's integral theorem for the function $F_t^*(z)f_{tt}(z)$ where we define $F_t^*(z) = F_t(z) - i\psi(d_2, 0, t)$. We obtain

$$\text{Im} \left(\int_{C_\varepsilon} F_t^*(z) f_{tt}(z) dz \right) = 0, \quad (\text{D.6})$$

where we define the closed contour C_ε (described clockwise) by the four sections of the contour $C_\varepsilon^{(1)}$, $C_\varepsilon^{(2)}$, $C_\varepsilon^{(3)}$ and $C_\varepsilon^{(4)}$, which are sketched in Figure D.1. In particular $C_\varepsilon^{(2)}$ and $C_\varepsilon^{(4)}$ are contours on semi-circles with radius ε and ε^{-1} , correspondingly. By integrating by parts, using the asymptotic behaviours in (D.2) and using $\varphi(x, 0, t) = 0$ for $x < d_0$ and

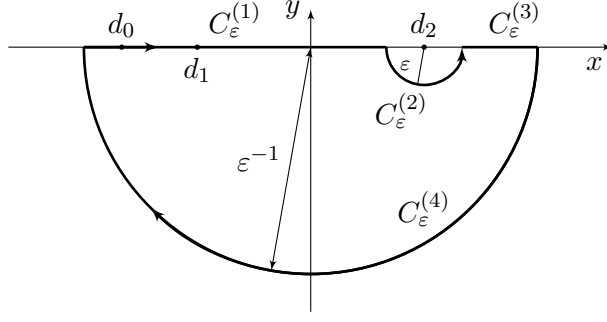


Figure D.1: The contour integral $C_\varepsilon = C_\varepsilon^{(1)} + C_\varepsilon^{(2)} + C_\varepsilon^{(3)} + C_\varepsilon^{(4)}$.

$\varphi_t(x, 0, t) = 0$ for $x < d_1$ we find

$$\lim_{\varepsilon \rightarrow 0} \int_{C_\varepsilon^{(1)}} \text{Im}(F_t^*(z) f_{tt}(z)) \, dz = \int_{d_0}^{d_2} \varphi_y \varphi_t \Big|_{y=0} \, dx - \int_{d_1}^{d_2} \varphi \varphi_{ty} \Big|_{y=0} \, dx. \quad (\text{D.7})$$

For the integral on the contour section $C_\varepsilon^{(2)}$ we use the asymptotic behaviours of $F_t(z)$ and $f_{tt}(z)$ in (D.3) and (D.4) to obtain

$$\lim_{\varepsilon \rightarrow 0} \int_{C_\varepsilon^{(2)}} \text{Im}(F_t^*(z) f_{tt}(z)) \, dz = -\frac{\dot{d}_2 K^2(d_2, t)}{\pi(d_2 - d_1)}. \quad (\text{D.8})$$

Owing to the far-field behaviour of $F_t(z)$ and $f_{tt}(z)$ given by (D.5) and $\varphi(x, 0, t) = \varphi_{tx}(x, 0, t) = 0$ for $x > d_2$, we obtain

$$\lim_{\varepsilon \rightarrow 0} \int_{C_\varepsilon^{(3)} + C_\varepsilon^{(4)}} \text{Im}(F_t^*(z) f_{tt}(z)) \, dz = 0. \quad (\text{D.9})$$

In conclusion, the limits of the integrals in equations (D.7) – (D.9), together with (D.6), the linearised Bernoulli equation (4.17) and the linearised kinematic boundary condition (4.18), give us altogether equation (D.1).

Bibliography

- Abramowitz, M. and Stegun, I. (1965). *Handbook of Mathematical Functions: With Formulas, Graphs, and Mathematical Tables*, volume 55. Dover publications.
- Acheson, D. J. (1990). *Elementary Fluid Dynamics*. Clarendon Press, Oxford.
- Baker, C. T. (1977). *The Numerical Treatment of Integral Equations*. Clarendon Press, Oxford.
- Batchelor, G. K. (1967). *An Introduction to Fluid Dynamics*. Cambridge University Press, New York.
- Bertorelli, P. (1999). Ditching myths torpedoed! <http://www.equipped.com/ditchingmyths.htm>.
- Birkhoff, G. and Zarantonello, E. (1957). *Jets, Wakes, and Cavities*. Academic Press, New York.
- Chuang, S.-L. (1966). Slamming of rigid wedge-shaped bodies with various low deadrise angle. Technical Report 2268, DTMB.
- Cointe, R., Fontaine, E., Molin, B., and Scolan, Y.-M. (2004). On energy arguments applied to the hydrodynamic impact force. *J. Eng. Math.*, 48:305–319.
- Cooker, M. J. (1996). Sudden changes in a potential flow with a free surface due to impact. *Q. J. Mech. Appl. Math.*, 49(4):581–591.
- Crighton, D. G. (1985). The Kutta condition in unsteady flow. *Ann. Rev. Fluid Mech.*, 17:411–445.
- Dobrovol'skaya, Z. N. (1969). On some problems of similarity flow of fluid with a free surface. *J. Fluid Mech.*, 36:805–832.
- Donnell, L. H. (1976). *Beams, Plates and Shells*. McGraw-Hill, New York.
- Dovgiy, S. A., Efremov, I. I., and Makasyeyev, M. V. (2002). Some problems of a planing theory. *The International Summer Scientific School in High Speed Hydrodynamics*.
- Duffy, D. G. (2008). *Mixed Boundary Value Problems*. Boca Raton, Chapman & Hall.
- Faltinsen, O. (1997). The effect of hydroelasticity on ship slamming. *Phil. Trans. R. Soc. Lond. A*, 355(1724):575–591.
- Faltinsen, O. M. (2005). *Hydrodynamics of High-Speed Marine Vehicles*. Cambridge University Press, New York.

- Faltinsen, O. M. and Semenov, Y. A. (2008). Nonlinear problem of flat-plate entry into an incompressible liquid. *J. Fluid Mech.*, 611:151–173.
- Fraenkel, L. E. and McLeod, J. B. (1997). Some results for the entry of a blunt wedge into water. *Phil. Trans. R. Soc. Lond. A*, 355:523–535.
- Gakhov, F. D. (1966). *Boundary Value Problems*. Pergamon, Oxford.
- Gillow, K. (1998). *Codimension-Two Free Boundary Problems*. D.Phil thesis, University of Oxford.
- Gradshteyn, I. S. and Ryzhik, I. M. (1994). *Table of Integrals, Series, and Products, Fifth Edition*. Academic Press, New York.
- Green, A. E. (1936). Note on the gliding of a plate on the surface of a stream. *Proc. Cambridge Phil. Soc.*, 32:248–252.
- Greenhow, M. (1987). Wedge entry into initially calm water. *Appl. Ocean Res.*, 9(4):214–223.
- Hamilton, J. A. (1998). Ethiopian Airlines B767 (ET-AIZ) Aircraft Accident in the Federal Islamic Republic of the Comoros, in the Indian ocean on November 23,1996. Aircraft accident investigation report, Ethiopian Civil Aviation Authority, Addis Ababa. <http://www.fss.aero/accident-reports/dvdfiles/ET/1996-11-23-ET.pdf>.
- Hersman, D. A., Hart, C. A., and Sumwalt, R. L. (2010). Loss of Thrust in Both Engines After Encountering a Flock of Birds and Subsequent Ditching on the Hudson River. Accident Report NTSB/AAR-10/03, National Transportation Safety Board, Washington D.C.
- Hicks, P. D., Ermanyuk, E. V., Gavrilov, N. V., and Purvis, R. (2012). Air trapping at impact of a rigid sphere onto a liquid. *J. Fluid. Mech.*, 695:310–320.
- Hicks, P. D. and Smith, F. T. (2011). Skimming impacts and rebounds on shallow liquid layers. *Proc. R. Soc. A*, 467:653–674.
- Howison, S., Morgan, J., and Ockendon, J. (1994). Patch cavitation in flow past a rigid body. *Bubble Dynamics and Interface Phenomena*, 23:219–226.
- Howison, S. D., Morgan, J. D., and Ockendon, J. R. (1997). A class of codimension-two free boundary problems. *SIAM Review*, 39(2):221–253.
- Howison, S. D., Ockendon, J. R., and Oliver, J. M. (2004). Oblique slamming, planing and skimming. *J. Eng. Math.*, 48:321–337.
- Howison, S. D., Ockendon, J. R., and Wilson, S. K. (1991). Incompressible water-entry problems at small deadrise angles. *J. Fluid Mech.*, 222:215–230.
- Iafrati, A. (2010). Private communication.
- Iafrati, A. and Korobkin, A. A. (2004). Initial stage of flat plate impact onto liquid free surface. *Phys. Fluids*, 16:2215–2227.
- Ionina, M. F. and Korobkin, A. A. (1999). Water impact on cylindrical shells. In *14th International Workshop on Water Waves and Floating Bodies*, Port Huron, USA.

- Johnson, W. (1998). The ricochet of spinning and non-spinning spherical projectiles, mainly from water. Part II: An outline of theory and warlike applications. *Int. J. Impact Eng.*, 21:25–34.
- Judge, C., Troesch, A., and Perlin, M. (2004). Initial water impact of a wedge at vertical and oblique angles. *J. Eng. Math.*, 48:279–303.
- Kapsenberg, G. K. (2011). Slamming of ships: where are we now? *Phil. Trans. R. Soc. A*, 369:2892–2919.
- Khabakhpasheva, T. I. and Korobkin, A. A. (2012). Inclined impact of a smooth body on thin liquid layer. In *27th International Workshop for Water Waves and Floating Bodies*, pages 85–88, Copenhagen. Technical University of Denmark.
- King, F. W. (2009). *Hilbert Transforms. Vol. 1*, volume 124 of *Encyclopedia of Mathematics and its Applications*. Cambridge University Press, Cambridge. 85 pp.
- Korobkin, A. A. (1982). Formulation of penetration problem as a variational inequality. *Din. Sploshnoi Sredi*, 58:73–79.
- Korobkin, A. A. (1988). Inclined entry of a blunt profile into an ideal fluid. *Fluid Dynamics*, 23:443–447.
- Korobkin, A. A. (1992). Blunt-body impact on a compressible liquid surface. *J. Fluid Mech.*, 244:437–453.
- Korobkin, A. A. (1994). Blunt-body penetration into a slightly compressible liquid. In *Proc. 20th Symp. on Naval Hydrodynamics*, volume 3, pages 179–186, Santa Barbara. Office of Naval Research.
- Korobkin, A. A. (1995). Wave impact on the bow end of a catamaran wet deck. *J. Ship Res.*, 39(4):321–327.
- Korobkin, A. A. (1998). Wave impact on the center of an Euler beam. *J. Appl. Mech. Tech. Phys.*, 39:770–781.
- Korobkin, A. A. (2003). Cavitation in liquid impact problems. In *Fifth International Symposium on Cavitation*, pages 1–4, Osaka.
- Korobkin, A. A. (2004). Analytical models of water impact. *Euro. J. Appl. Math.*, 15:821–838.
- Korobkin, A. A. (2007). Second-order Wagner theory of wave impact. *J. Eng. Math.*, 58:121–139.
- Korobkin, A. A. and Khabakhpasheva, T. I. (2006). Regular wave impact onto an elastic plate. *J. Eng. Math.*, 55:127–150.
- Korobkin, A. A., Parau, E. I., and Vanden-Broeck, J.-M. (2011). The mathematical challenges and modelling of hydroelasticity. *Phil. Trans. R. Soc. A*, 369:2803–2812.

- Korobkin, A. A. and Scolan, Y.-M. (2006). Three-dimensional theory of water impact. Part 2. linearized Wagner problem. *J. Fluid Mech.*, 549:343–373.
- Kvåsvold, J. and Faltinsen, O. M. (1993). Hydroelastic modelling of slamming against wetdecks. *8th International Workshop on Water Waves and Floating Bodies*, pages 57–60.
- Lamb, H. (1945). *Hydrodynamics*. Dover Publication, New York.
- Lang, S. (1993). *Complex analysis*. Springer-Verlag, New York.
- Lesser, M. B. and Field, J. E. (1983). The impact of incompressible liquids. *Ann. Rev. Fluid Mech.*, 15:97–122.
- Meyerhoff, W. (1965a). Die Berechnung hydroelastischer Stöße. *Schiffstechnik* 12, 60:18–30.
- Meyerhoff, W. (1965b). Die Berechnung hydroelastischer Stöße. *Schiffstechnik* 12, 61:49–64.
- Milne-Thomson, L. M. (1968). *Theoretical Hydrodynamics*. Dover Publication, New York.
- Miloh, T. (1990). Oblique water entry of spherical shapes with special reference to the ricocheting phenomenon. In *5th International Workshop for Water Waves and Floating Bodies*, Manchester.
- Miloh, T. (1991). On the oblique water-entry problem of a rigid sphere. *J. Eng. Math*, 25:77–92.
- Moore, M. R., Howison, S. D., Ockendon, J. R., and Oliver, J. M. (2012a). A note on oblique water entry. *J. Eng. Math*. DOI 10.1007/s10665-012-9570-0.
- Moore, M. R., Howison, S. D., Ockendon, J. R., and Oliver, J. M. (2012b). Three-dimensional oblique water-entry problems at small deadrise angles. *J. Fluid Mech.*, 711:259–280.
- Nariboli, G. A. (1965). Eigen-function expansions for a fourth order differential equation. *Proc. Nat. Inst. Sci. India*, 31:593–602.
- Newman, J. N. (1977). *Marine Hydrodynamics*. The MIT Press, Cambridge.
- Oliver, J. M. (2002). *Water Entry and Related Problems*. D.Phil thesis, University of Oxford.
- Oliver, J. M. (2007). Second-order wagner theory for two-dimensional water-entry problems at small deadrise angles. *J. Fluid Mech.*, 572:59–85.
- Reinhard, M., Korobkin, A., and Cooker, M. J. (2011). Elastic plate impact into water at high horizontal speed. In *26th International Workshop on Water Waves and Floating Bodies*, pages 157–160, Athens.
- Reinhard, M., Korobkin, A., and Cooker, M. J. (2012a). The bounce of a blunt body from a water surface at high horizontal speed. In *27th International Workshop on Water Waves and Floating Bodies*, pages 153–156, Copenhagen. Technical University of Denmark.
- Reinhard, M., Korobkin, A. A., and Cooker, M. J. (2012b). Elastic plate impact into water at high horizontal speed with early water detachment. In *6th International Conference on Hydroelasticity in Marine Technology 2012*, pages 1–10, Tokyo. University of Tokyo Press.

- Reinhard, M., Korobkin, A. A., and Cooker, M. J. (2013). Water entry of a flat elastic plate at high horizontal speed. *J. Fluid Mech.* (accepted).
- Rosselini, L., Hersen, F., Clanet, C., and Bocquet, L. (2005). Skipping stones. *J. Fluid Mech.*, 543:137–146.
- Scolan, Y.-M. and Korobkin, A. A. (2001). Three-dimensional theory of water impact. Part 1. Inverse Wagner problem. *J. Fluid Mech.*, 440:293–326.
- Scolan, Y.-M. and Korobkin, A. A. (2003). Energy distribution from vertical impact of a three-dimensional solid body onto the flat free surface of an ideal fluid. *J. Fluids Struct.*, 17(2):275–286.
- Seddon, C. M. and Moatamedi, M. (2006). Review of water entry with applications to aerospace structures. *Int. J. Impact Eng.*, 32:1045–1067.
- Sedov, L. I. (1940). On the theory of unsteady planing and the motion of a wing with vortex separation. Technical Report 942, NACA.
- Smiley, R. F. (1951). An experimental study of water-pressure distributions during landings and planing of a heavily loaded rectangular flat-plate model. Technical Report 2453, NACA.
- Sneddon, I. N. (1966). *Mixed Boundary Value Problems in Potential Theory*. New York, North Holland.
- Sun, H. and Faltinsen, O. M. (2007). Water impact of horizontal circular cylinders and cylindrical shells. *Appl. Ocean Res.*, 28:299–311.
- Takagi, K. (2004). Numerical evaluation of three-dimensional water impact by the displacement potential formulation. *J. Eng. Math.*, 48(4):339–352.
- Tassin, A., Jacques, N., El Malki Alaoui, A., Nème, A., and Leblé, B. (2012). Hydrodynamic loads during water impact of three-dimensional solids: Modelling and experiments. *J. Fluids Structures*, 28:211–231.
- The Boeing Company (1999). *737-300/400/500 Flight Crew Training Manual*. <http://www.captainpilot.com/files/B737CL/B737-400g>
- Ting, L. and Keller, J. B. (1974). Planing of a flat plate at high Froude number. *Phys. Fluids*, 17(6):1080–1086.
- Ulstein, T. (1995). *Nonlinear effects of a flexible stern seal bag on cobblestone oscillations of an SES*. PhD thesis, Norwegian Institute of Technology, Trondheim.
- Ulstein, T. and Faltinsen, O. M. (1996). Two-dimensional unsteady planing. *J. Ship Res.*, 40(3):200–210.
- von Karman, T. (1929). The impact of sea planes floats during landing. Technical Report 321, NACA.

- Vorus, W. S. (1996). A flat cylinder theory for vessel impact and steady planing resistance. *J. Ship Res.*, 40(2):89–106.
- Wagner, H. (1932). Über Stoß- und Gleitvorgänge an der Oberfläche von Flüssigkeiten. *ZAMM*, 12:193–215.
- Wilson, S. K. (1991). A mathematical model for the initial stages of fluid impact in the presence of a cushioning fluid layer. *J. Eng. Math.*, 25:265–285.
- Woods, L. C. (1961). *The Theory of Subsonic Plane Flow*. Cambridge University Press.
- Zhao, R. and Faltinsen, O. M. (1993). Water entry of two-dimensional bodies. *J. Fluid Mech.*, 246:593–612.
- Zhao, R., Faltinsen, O. M., and Aarsnes, J. (1996). Water entry of arbitrary two-dimensional sections with and without flow separation. In *Twenty-First Symposium on Naval Hydrodynamics*, pages 408–423, Trondheim. U.S. National Research Council.